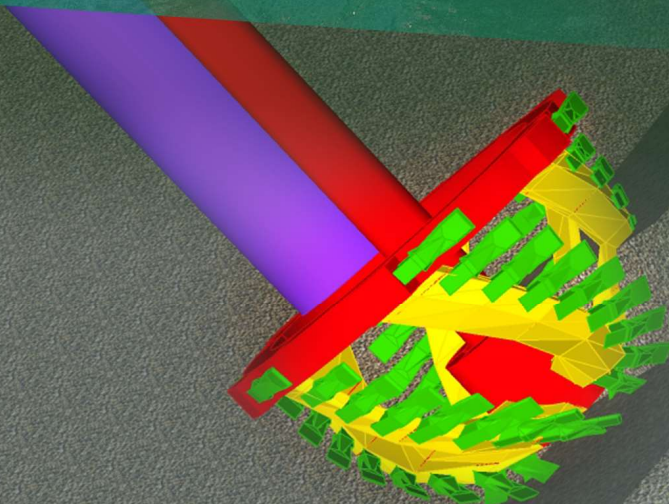


# CSD Spillage Model for Sand and Rock

A Particle Size-Agnostic, Adaptable Engineering Model  
for the Prediction of Cutter Suction Dredge Spillage Rates

J.J. Werkhoven





*On the cover*

The cover shows an image of a cutter head subject to a maintenance inspection. At rock-type projects the large pick points mounted on the cutter head wear off heavily. In the early days of cutter dredging, workers would stand on top of the cutter to replace the pick points. Their only safety line would be a colleague's hand.

With regards to safety, dredging operations at GLDD and other dredging companies have seen a seismic shift. Among other measures, workers can now perform cutter maintenance safely on the cutter platform.

**Safety without compromise.**



A model is never done, it is only due.

# CSD Spillage Model for Sand and Rock

A Particle Size-Agnostic, Adaptable Engineering Model  
for the Prediction of Cutter Suction Dredge Spillage Rates

By

J.J. Werkhoven

in partial fulfilment of the requirements for the degree of

**Master of Science**  
in Offshore and Dredging Engineering

at the Delft University of Technology,  
to be defended publicly on Friday, May 24, 2019, at 15:00 hrs.

Chair:	Dr.ir. S.A. Miedema,	TU Delft
Thesis committee:	Prof.dr.ir. C. van Rhee,	TU Delft
	Ir. B.J. Nieuwboer,	TU Delft
	Dr.ir. M. Van Damme,	TU Delft
	R.C. Ramsdell BA,	GLDD

An electronic version of this thesis is available at  
<http://repository.tudelft.nl/>



 **TU Delft**

## Abstract

CSD spillage is defined as “any soil that is dislodged above the lowest cutter tip trajectory of a single swing, but is not sucked into the suction pipe”. In addition to higher energy consumption and material wear for delivering the targeted depth, spillage can lead to a variety of environmental issues. As of yet, no analytical model exists in literature that can estimate spillage rates for a given set of cutting parameters. This thesis presents the Sand-Rock Cutting Spillage Model (SRCSM), an engineering model that is particle-size agnostic and makes use of cutting parameters that are all available to the dredge operator.

Prediction accuracy of 5 percentage point is achieved with a two-disc potential flow model complemented with empirical closing relationships. A triad of forces governs flow in the cutter head for typical cutting conditions: a centrifugal, suction and gravitational force are considered. For the centrifugal pump effect, and centrifugal pump effect only, the flow inside the cutter is considered steady, non-gravitational, inviscid and non-axial. This allows for the derivation of a pressure-discharge affinity law from the Navier-Stokes. The axial pump effect is governed by the mixture velocity at the suction mouth. It is hypothesized that the pressure difference over the discs drives an inflow at the disc closest to the nose.

Centrifugal advection and rapid redeposition spillage are considered the two most significant spillage types out of the six classified. Centrifugal advection can be determined by identifying the onset of radial outflow at the disc near the cutter ring. The magnitude of rapid redeposition flow and its concentration depend on mixing effects that are proportional to the ratio particle settling velocity and the mixture velocity squared.

The model is calibrated with three coefficients. User input parameters are the cutter geometry, cut-type factor  $f_{d_{type}}$  (-1 for under-cut), bank slope angle  $\xi$ , cutter inclination angle  $\lambda$ , bank height  $h$ , step size  $l_{step}$ , rotational velocity  $\omega$ , settling velocity  $v_{ts}$ , swing velocity  $v_s$ , mixture velocity  $v_m$  and material densities.

$$S = f \left( D_{ring}, D_{nose}, D_{pipe}, b, f_{d_{type}}, \xi, \gamma, h, l_{step}, \omega, v_{ts}, v_s, v_m, \rho_q, \rho_b, \rho_w \right)$$

For calibration, an inverse flow number  $\hat{\theta}$  is used that is proportional to the ratio of centrifugal flow over mixture flow. Spillage rates from SRCSM are in high agreement with reference data for sand (Miltenburg, 1983) and rock (Den Burger, 2003) in an under-cut swing. A sensitivity analysis suggests that most cutter head dynamics are adequately incorporated.

The model is less reliable for (non-typical) inverse flow numbers of  $\hat{\theta} = 6$  [-] and higher due to a mixture velocity that drops below zero. In addition, the model is calibrated for a relatively high cutter inclination angle of 45 [deg] and bank angle of 45 [deg]. Caution should be observed with the results. It is also suggested that mixing effects related to the swing velocity are incorporated more explicitly in the model.

For typical sand cutting conditions, the highest spillage reduction (-4.6%) is achieved by a 1 [%] smaller step size. For rock, the highest spillage reduction (-0.63%) is achieved for a 1 [%] decrease in swing velocity. Spillage appears to follow the theorem of Ellington (1934): it don't mean a thing if it ain't got that swing.

## Preface

As I have just completed writing the conclusions of this thesis, I realize that an engineer's task of building a model is never done. It is only due. By definition, a model can always be improved as a perfect model cannot coexist with reality. The model report that lies before you is due as it concludes the final stage of my graduation. It is the product of an iterative process that comprises of literature reviews, model (re)development, python coding, conference presentations and elaborate discussions with my thesis committee. Although I believe that further model steps can be taken, I take pride in the results that, I hope, will be as interesting to you as they have been for me to obtain.

The foundational flow concept in this model originates from an idea by Sape Miedema who has also supervised this research. Sape is a charismatic supervisor with the ability to fill a meeting with long but fascinating tangents, only to make up for this time with a meticulously devised advice on further steps to take. For these conversations as well as the stimulus to aim for publication I would like to express my sincerest gratitude. The pleasure of doing this research is also highly attributed to the internship opportunity that was provided to me by Robert Ramsdell from Great Lakes Dredge and Dock. Robert and his department created an inspiring environment where I was given the liberty to explore not only the perks and pitfalls of a Dutch mindset, but also the safety culture that comes with a professional team. I owe him many thanks for our elaborate spillage discussions and the warm welcome in Chicago from him and his family. I am grateful for the help I have been given by Cees van Rhee and Bas Nieuwboer who have provided a more scientific due diligence and rigorous reviews. In particular, I would like to thank Bas for his help editing the two conference papers. A special thanks goes to Cees for rearranging his schedule to enable the graduation date of May 24. Lastly, I highly appreciate Myron van Damme for his time and efforts to review this research from a less dredging-dominated mindset. Little did I know that this research would take me to the WEDA and WODCONXXII dredging conferences in Norfolk and Shanghai. The conference attendance and time leading up to them has been monumental for my personal development as I like to think it has made me more confident.

In line with my expectation, the model development came with ups and downs. I have tried to model using a wide variety of parameters and effects. The iteration process and coding process can be slow and tiring. In partial, what kept me going in slow times is the realization that for the first time in my studies I had the chance to make a scientific contribution to the field. Writing the report posed an interesting challenge since I myself know that it can be difficult to grasp the model concept. Putting in words what I had been thinking about for a year has been lonesome at times. I feel lucky to have felt great support from my friends and family. I have received useful help from those with whom I earlier shared a period of research in Indonesia. I am grateful that our past cooperation and bonding has enabled us to speak in terms of our rich imaginations as well as very to the point. Furthermore, I

want to specifically thank the parrot zone pirates. They helped alleviate any stressful moments with the much amusing comment that I should not be worrying about presenting my thesis but what traditionally comes after. In all seriousness, their involvement does not go unnoticed. Especially in the last phase of writing, I have found substantial support from my ever-sharp housemates in Delft. I believe my gratitude for sharing such a positive and entertaining household has so far been least acknowledged of all. Looking back at my studies over the past years, there are two people I want to thank the most who have supported me all along the way. During celebratory times and sorrow, my parents have been an incredible source of inspiration to me. Characteristic of this feeling are the bike rides, whether it be in the Andes mountains of Peru or along our usual ride on the dyke to Wijk bij Duurstede. My father's prompt fascination by the things we see, experience or talk about never ceases to amaze me. From rationally consistent to hypothetical, I have sincere gratitude for the conversations we share and the directions we take. Whenever head winds are strong, I find my mother just behind me. This is mostly true metaphorically. No matter the time, occasion, or cause, my mother's unwavering support is the silent force that helped me finish my graduation.

# Table of contents

	<b>ABSTRACT .....</b>	<b>6</b>
	<b>PREFACE .....</b>	<b>8</b>
	<b>TABLE OF CONTENTS .....</b>	<b>10</b>
	<b>TABLE OF FIGURES .....</b>	<b>13</b>
	<b>TABLE OF TABLES .....</b>	<b>14</b>
	<b>1 INTRODUCTION .....</b>	<b>15</b>
1.1	RESEARCH MOTIVATION .....	15
1.2	RESEARCH OBJECTIVE .....	15
1.3	RESEARCH HYPOTHESIS .....	18
1.4	THESIS OUTLINE AND READING GUIDE .....	18
	<b>2 CUTTER SUCTION DREDGE SPILLAGE .....</b>	<b>19</b>
2.1	CUTTER SUCTION DREDGE .....	19
2.2	SPILLAGE AND ITS IMPLICATIONS .....	21
2.3	SPILLAGE DEFINITION .....	23
2.4	SPILLAGE TYPES .....	23
2.5	SPILLAGE DIAGRAM .....	28
2.6	EMPIRICAL MODELS FOR TOTAL SPILLAGE .....	28
2.7	CONCLUSION .....	29
	<b>3 FUNDAMENTAL PHYSICS .....</b>	<b>31</b>
3.1	CUTTER FLOW CHARACTERIZATION .....	31
3.2	GOVERNING FORCES .....	33
3.3	CYLINDRICAL COORDINATE SYSTEM .....	34
3.4	DERIVATION OF NAVIER-STOKES EQUATIONS .....	34
3.5	VISCOSITY, DENSITY, INERTIA .....	37
3.6	DERIVATION OF EULER EQUATION .....	41
3.7	DERIVATION OF EULER'S PUMP EQUATION .....	41
3.8	CONCLUSION .....	45
	<b>4 MODEL SETUP .....</b>	<b>47</b>
4.1	GEOMETRY .....	48
4.2	POTENTIAL FLOW MODEL .....	53
4.3	SPILLAGE COMPUTATION .....	64
4.4	IMPLEMENTATION TEMPLATE .....	66
4.5	CONCLUSION .....	68
	<b>5 RESULTS AND DISCUSSION .....</b>	<b>70</b>
5.1	CALIBRATION NUMBER .....	70
5.2	CALIBRATION DATA .....	70
5.3	RESULTS FOR SAND .....	72
5.1	RESULTS FOR ROCK .....	74
5.2	EXPRESSION FOR PUMP FLOW NUMBER .....	76
5.3	SENSITIVITY ANALYSIS .....	76

5.4	FURTHER DISCUSSION.....	82
5.5	CONCLUSION.....	83
	<b>6 CONCLUSION AND RECOMMENDATIONS .....</b>	<b>85</b>
6.1	CONCLUSION.....	87
6.2	RECOMMENDATIONS FOR FURTHER RESEARCH .....	88
	<b>7 LIST OF SYMBOLS.....</b>	<b>91</b>
7.1	SYMBOLS.....	91
7.2	INDICES.....	92
	<b>8 GLOSSARY.....</b>	<b>94</b>
	<b>9 BIBLIOGRAPHY.....</b>	<b>96</b>
	<b>A DERIVATION OF BERNOULLI'S PRINCIPLE.....</b>	<b>98</b>
	<b>B VELOCITY TRIANGLES OF A PUMP.....</b>	<b>99</b>
B.1	2D VELOCITY TRIANGLES.....	99
B.2	3D VELOCITY TRIANGLES .....	100
	<b>C DERIVATION OF CENTRIFUGAL PUMP AFFINITY LAWS FROM CAUCHY MOMENTUM EQUATION.....</b>	<b>103</b>
C.1	DERIVATION OF CAUCHY MOMENTUM EQUATION .....	103
C.2	VELOCITIES IN A CYLINDRICAL COORDINATE SYSTEM.....	104
C.3	DERIVATION OF CONTINUITY EQUATION .....	105
C.4	DERIVATION OF DIVERGENCE OF STRESS TENSOR .....	107
C.5	DERIVATION OF STRESS-STRAIN RELATIONSHIPS IN A CYLINDRICAL COORDINATE SYSTEM .....	108
C.6	GRAVITATIONAL ACCELERATION .....	110
C.7	DERIVATION OF NAVIER-STOKES EQUATIONS .....	111
C.8	ALTERNATIVE FORMS OF NAVIER-STOKES EQUATIONS.....	112
C.9	DERIVATION OF EULER EQUATIONS .....	112
C.10	DERIVATION OF EULER'S PUMP EQUATION .....	113
C.11	DERIVATION OF EULER'S PUMP EQUATION .....	116
C.12	DERIVATION OF AFFINITY LAW FOR PRESSURE.....	118
C.13	DERIVATION OF AFFINITY LAW FOR DISCHARGE .....	118
C.14	AFFINITY LAW FOR PUMP POWER.....	119
	<b>D DERIVATION OF PUMP RELATIONSHIPS FOR RADIAL AND AXIAL FLOW IN 3D .....</b>	<b>120</b>
D.1	RADIAL PRESSURE HEAD IN THREE-DIMENSIONAL PHYSICAL DOMAIN .....	120
D.2	AXIAL PRESSURE HEAD IN A THREE-DIMENSIONAL DOMAIN.....	121
	<b>E SIMPLE DERIVATION OF AFFINITY LAW FOR PUMP PRESSURE.....</b>	<b>125</b>
	<b>F EXPANSION OF THE MODEL'S CONTINUITY EQUATION.....</b>	<b>126</b>
F.1	DERIVATION OF ACTUAL RADIAL SPECIFIC FLOW FOR DISC 1 AND 2.....	126
F.2	DERIVATION OF POLYNOMIAL FOR DISC HEIGHT 1.....	127
	<b>G GEOMETRY DESCRIPTIONS.....</b>	<b>132</b>
G.1	CUTTER (PRELIMINARY) .....	132
G.2	BANK (PRELIMINARY) .....	133
G.3	CUTTER (ADVANCED).....	134

	<b>H LITERATURE NOTES.....</b>	<b>135</b>
H.1	DEN BURGER (2003) .....	135
H.2	SLOTTA (1976) .....	140
H.3	JOANKNECHT (1976).....	140
H.4	STEINBUSCH (1999).....	141
H.5	HAYES (2000).....	144
H.6	ANDRASSY AND HERBICH (1988) .....	145
H.7	EMPERICAL RELATIONS FOR SPILLAGE ESTIMATION TYPE 1.....	150
	<b>I CUTTER TIP TRAJECTORY.....</b>	<b>151</b>
	<b>J REFERENCE IMPLEMENTATION (PYTHON) .....</b>	<b>152</b>
	<b>K MODEL ANALYSIS TOOL (PYTHON) .....</b>	<b>158</b>

## Table of figures

FIGURE 2.1: CSD WITH LADDER DEPLOYED (LEFT) AND CUTTING TERMINOLOGY (RIGHT). .....	19
FIGURE 2.2: UNDER-CUTTING AND OVER-CUTTING (LEFT) AND TYPICAL CSD CUTTING PATTERN (RIGHT). .....	20
FIGURE 2.3: NAMES OF DEVICES AND ELEMENTS FOR A CUTTER EQUIPPED TO CUT SAND. ....	20
FIGURE 2.4: COMMON DEFINITIONS FOR CSD CUTTING. ....	22
FIGURE 2.5: CENTRIFUGAL ADVECTION-INDUCED SPILLAGE FOR OVER-CUTTING (LEFT) AND UNDER-CUTTING (RIGHT). ....	24
FIGURE 2.6: RAPID REDEPOSITION-INDUCED SPILLAGE FOR OVER-CUTTING (LEFT) AND UNDER-CUTTING (RIGHT). ....	25
FIGURE 2.7: SPILLAGE DUE TO BURIED CUTTING (LEFT) AND SPILLAGE DUE TO VIOLENT CUTTING (RIGHT) FOR AN UNDER-CUTTING. ....	25
FIGURE 2.8: SPILLAGE DUE TO BANK INSTABILITY (LEFT) AND SPILLAGE DUE TO CUTTER GEOMETRY (RIGHT). ....	26
FIGURE 2.9: SPILLAGE TYPE DIAGRAM. ....	28
FIGURE 3.1: DERIVATION STEPS FOR EULER’S PUMP EQUATION. ....	31
FIGURE 3.2: CENTRIFUGAL PUMP EFFECT CHARACTERIZATION BY MILTENBURG (1983, LEFT) AND DEN BURGER (2003, RIGHT). ....	32
FIGURE 3.3: CONTINUITY (LEFT) AND STRESS BALANCE (RIGHT) FOR AN INFINITESIMALLY SMALL CONTROL VOLUME. ....	35
FIGURE 3.4: GRAVITATIONAL ACCELERATION IN A CYLINDRICAL COORDINATE SYSTEM. ....	37
FIGURE 3.5: BLADE-INDUCED VELOCITIES OF AN INFINITESIMALLY SMALL FLUID VOLUME. ....	42
FIGURE 4.1: TYPICAL GEOMETRY APPROXIMATION OF A RELATIVELY LARGE CUTTER HEAD. ....	48
FIGURE 4.2: ADVANCED GEOMETRY DESCRIPTION FOR CUTTER-BANK INTERACTION. ....	49
FIGURE 4.3: SCHEMATIC DEPICTION OF THE BANK CONTACT ANGLE (LEFT) AND DISC DIVISION OF THE CUTTER HEAD (RIGHT). ....	53
FIGURE 4.4: SCHEMATIC 3D VIEW OF THE CUTTER HEAD DIVISION IN DISC 1 AND 2 WITH RELEVANT PARAMETERS. ....	55
FIGURE 4.5: APPROXIMATED 2-DIMENSIONAL VELOCITY TRIANGLES AT THE BLADES FOR DISC 1 (LEFT) AND DISC 2 (RIGHT). ....	56
FIGURE 4.6: PRESSURE EXPECTATIONS (LEFT) AND ASSUMPTIONS (RIGHT) FROM THE CUTTER HEAD. ....	59
FIGURE 4.7: REFERENCE POINT FOR RAPID REDEPOSITION FROM FRONTAL (LEFT) AND LATERAL PERSPECTIVE (RIGHT). ....	61
FIGURE 4.8: VELOCITY APPROXIMATIONS FOR A FLUID ELEMENT AT THE CUTTER BOTTOM (LEFT) AND CONCENTRATION SCALING FOR RAPID REDEPOSITION (RIGHT). ....	65
FIGURE 4.9: IMPLEMENTATION TEMPLATE. ....	67
FIGURE 5.1: PHOTO OF EXPERIMENTAL CUTTER HEAD (LEFT) AND PRODUCTION CURVE (RIGHT). ....	72
FIGURE 5.2: SAND SPILLAGE RESULTS (LEFT) AND MAGNITUDE OF ERROR (RIGHT). ....	72
FIGURE 5.3 VOLUMETRIC FLOW RATES (LEFT) AND CONCENTRATIONS (RIGHT) FOR SAND. ....	73
FIGURE 5.4 VOLUMETRIC FLOW RATES (LEFT) AND SAND SPILLAGE RESULTS FOR SAND (RIGHT) WITH AXIAL FLOW THROUGH THE NOSE. ....	74
FIGURE 5.5: ROCK SPILLAGE RESULTS (LEFT) AND MAGNITUDE OF ERROR (RIGHT). ....	75
FIGURE 5.6 VOLUMETRIC FLOW RATES (LEFT) AND CONCENTRATIONS (RIGHT) FOR ROCK. ....	76
FIGURE 5.7: MODEL SENSITIVITY TO SWING VELOCITY FOR CENTRIFUGAL ADVECTION FOR SAND (LEFT) AND ROCK (RIGHT). ....	77
FIGURE 5.8: MODEL SENSITIVITY TO STEP LENGTH FOR CENTRIFUGAL ADVECTION (LEFT) AND RAPID REDEPOSITION (RIGHT) FOR ROCK. ....	78
FIGURE 5.9: MODEL SENSITIVITY TO CUTTER INCLINATION ANGLE FOR CENTRIFUGAL ADVECTION (LEFT) AND RAPID REDEPOSITION (RIGHT) FOR ROCK. ....	79
FIGURE 5.10: MODEL SENSITIVITY TO THE SLOPE ANGLE FOR CENTRIFUGAL ADVECTION (LEFT) AND RAPID REDEPOSITION (RIGHT) FOR ROCK. ....	80
FIGURE 5.11: MODEL SENSITIVITY TO THE BANK HEIGHT FOR CENTRIFUGAL ADVECTION FOR SAND. ....	81
FIGURE 5.12: SENSITIVITY OF OVER-CUT SCENARIO TO CUTTER INCLINATION ANGLE (LEFT) AND RESPECTIVE ERRORS (RIGHT). ....	82
FIGURE 6.1 OVERVIEW OF FLOWS FOR N-SLICE MODEL. ....	89
FIGURE B.1: VELOCITY TRIANGLES IN 2D .....	99
FIGURE B.2: VELOCITY TRIANGLES IN 3D AND 2D .....	101
FIGURE C.1: VELOCITY COMPONENTS OF AN INFINITESIMALLY SMALL CONTROL VOLUME .....	105
FIGURE C.2: STRESSES ON AN INFINITESIMALLY SMALL CONTROL VOLUME. ....	107
FIGURE C.3: GRAVITATIONAL ACCELERATION ACTING ON AN INFINITESIMALLY SMALL CONTROL VOLUME. ....	111
FIGURE G.1: SIMPLIFICATION OF THE CUTTER GEOMETRY. ....	132
FIGURE G.2: SCHEMATIC VISUALIZATION OF THE BANK CONTACT ANGLE (LEFT) AND THE RELATION BETWEEN BANK HEIGHT AND EFFECTIVE BANK HEIGHT (RIGHT). ....	133

## Table of tables

TABLE 1.1: FOCUS POINTS WITHIN THE RESEARCH OBJECTIVE. ....	16
TABLE 2.1: CUTTER SUCTION DREDGE TERMINOLOGY. ....	20
TABLE 3.1: ASSUMPTIONS RELEVANT TO THE PHYSICAL PARAMETERS IN THE MODEL. ....	46
TABLE 4.1: OVERVIEW OF INPUT PARAMETERS ....	68
TABLE 5.1: EXPERIMENT PARAMETERS FOR MILTENBURG (1983) AND DEN BURGER (2003). ....	71
TABLE 5.2: SENSITIVITY TO RELEVANT PARAMETERS AT $\theta = 2.77$ . ....	81

# 1 Introduction

This chapter focuses on formulating a research overview. First, a short introduction is given that establishes the motivation for spillage modeling. Next, a research objective and sub-questions are presented. Last, a thesis outline and reading guide is given.

This thesis was commissioned by the research department at Great Lakes Dredge and Dock (GLDD) and carried out in partial fulfilment of the requirements for Master of Science in Offshore and Dredging Engineering at the TU Delft. The model presented in this research was first conceptualized by Dr.Ir. Sape Miedema (2017). Louis (2017) demonstrated a conceptual implementation for sand. This research aims to presents an upgraded model that is calibrated for Sand and Rock.

## 1.1 Research motivation

Depending on its size and installed power, a Cutter Suction Dredge (CSD) is capable of cutting a wide range of soil types from silts and clays to fractured or solid rocks. Its high precision allows for utilization in a variety of dredge operations including navigational channel deepening, port construction and pipeline trenching. In spite of being considered relatively efficient, a CSD can spill significantly. In rock, wear of dredge material is based on the amount cut while contractors are only paid for amount removed. Spillage is therefore a primary driver of operating cost. In sand, accurately predicting and controlling the yield of a borrow area is crucial to planning works. A lack of prediction methods thus indirectly adds to the cost.

A typical larger dredging contract is the \$47 million Charleston I Deepening contract, awarded in 2017 (GLDD, 2019). The contract was awarded to GLDD and comprised the cutting 4.7 million cubic meters of soil by CSDs primarily. According to company planning, the project is to be executed over a period of approximately two and a half years. From a broad perspective, it can be estimated that each 1% increase in CSD efficiency may reduce the project cost by \$1 million and approximately 9 days. Any reduction in spillage rates can thus significantly contribute to improved project economics and execution speed.

Moreover, safety considerations and environmental implications provide ample motivation for industry-participants to desire a spillage model that supports risk-mitigation.

---

**As of yet, no analytical engineering model exists in literature that is capable of predicting spillage.**

---

## 1.2 Research objective

The objective of this thesis is formulated as:

---

**Develop a particle size-agnostic, adaptable engineering model for the prediction of spillage rates for Cutter Suction Dredge cutting.**

---

The objective properties are further elaborated upon in the scope of this research. It was chosen that the objective is theoretical and does not involve experiments.

### 1.2.1 Research scope

Three foci of the research objective are the properties *particle-size agnostic*, *adaptable* and *engineering*. To increase the applicability of the model it was chosen to develop a model that applies for sand and rock particles, hence the model should be *particle-size agnostic*.

The author desires to promote the use and further work on the model. Therefore, modularity of the model will be enabled where possible. This property makes the model *adaptable*.

In “Principles of Production Engineering Models”, Ramsdell et al. (2019) propose a framework of *engineering* model classifications. Engineering models must have three properties that are shown in Table 1.1 under “engineering”. Models that fit the three requirements are most likely analytical models. This research aims to make substantial use of equations derived “from the underlying physical science” as well as empirical observations. According to the proposed engineering model framework, this model will qualify as both fundamental and empirical.

**Table 1.1: Focus points within the research objective.**

<i>Property</i>	<i>Sub-property</i>	<i>Property description</i>
Particle-size agnostic		Is applicable for the cutting of sand as well as rock particles.
Adaptable		Is easily expandable for further improvements.
“Engineering”	“Tractable”	“[is] Quick to set up and run.” Project-specific inputs should be easily changeable, and iterations should be fast enough to support decision making.
	“Discernible”	“[makes use] Of inputs that are likely to be known to the engineer.”
	“Informative”	“Provide outputs of direct interest to the engineer and that are valid across a wide range of typical cases.”

The scope of the research is limited by looking solely at spillage generation during a single cutter head swing. Interactions between consecutive swings are not considered. The “tractability” of the model is maintained by designing the model such that it can be called upon as a function within other models that look at wider cutting patterns.

The model can be made “discernible” by relying on well-known parameters such as mixture velocity, rotational velocity, bank height, step size and particle size distribution. A discernible and intuitive model is of paramount importance for its adoption.

The “informative” property can be achieved by providing the spillage percentage as a direct output of the model. Ideally, the model enables an easy sensitivity analysis to dominant process parameters such as the mixture velocity and swing speed.

Furthermore, it is planned to design the model in an “informative” way by making it sufficiently generic to cutter sizes. When references to cutter scale are made a cutter head diameter of 3.11 meter is considered.

#### *Outside the scope*

A classification of spillage types will be performed, and their significance will be evaluated. It is expected that the model will exclude negligible spillage types. Along with this evaluation, the influence of non-characteristic variables such as the radius of the drive axis of the cutter will be excluded. More cutting variables will be assumed negligible as the model fully develops.

#### 1.2.2 *Main research question*

The objective can be reformulated to the research question:

---

**What are physical parameters, model concepts and assumptions that give rise to an adaptable, particle size-agnostic engineering model for CSD spillage rates within 5 percentage point accuracy?**

---

#### 1.2.3 *Research sub-questions*

To support the research goal, a series of research questions is formulated.

---

**1. What is CSD spillage and what types of spillage can be identified?**

---

The first part of this question may appear trivial. In practice, a large variation of dredging terminology and spillage definitions can be observed. In addition, the aim of this question is to classify spillage types which are often conflated.

---

**2. What formulations are fundamental to the motion and behaviour of a fluid substance in the physical domain of the cutter head?**

---

This question’s goal is to provide insight into the origin of the fluid equations that form the fundamental fluid relationships that will be used in the model.

---

**3. In conjunction with the relevant physical parameters, what concepts and assumptions enable a CSD spillage engineering model?**

---

An ideal model would comprehend all fluid, sediment and cutter head properties and their respective interactions. This research question aims to present compelling arguments for the model concepts as well as some nuance for the assumptions that come with it.

---

**4. Based on the identified physical parameters, concepts and assumptions, how does the model perform relative to experimental data?**

---

Validation of the model proves difficult in an engineering field where data sharing is scarce. Openly available experimental data will be used to calibrate the model and the results will be evaluated to help initiate further research.

### 1.3 Research hypothesis

In the field of dredging, empirical models tend to predict spillage within 10 to 20 percentage points accuracy. For an analytical model, the accuracy is estimated higher.

---

**A potential flow model with empirical closing relations that capture the dynamics of gravitational, centrifugal and suction forcing give rise to a spillage rate prediction within 5 percentage point accuracy.**

---

### 1.4 Thesis outline and reading guide

The main concepts in this thesis report have been published over the course of writing it. The author of this report is first author of the following three co-publications:

1. Werkhoven, J. J., Nieuwboer, B.J., Louis, A.A., Ramsdell, R.C., and Miedema, S.A. "A pseudo-analytical model for CSD spillage due to rotational velocity-induced flow," *Proceedings of the Western Dredging Association Dredging Summit & Expo '18*, Norfolk, VA, USA, June 25-28, 2018.
2. Werkhoven, J. J., Nieuwboer, B.J., Louis, A.A., Ramsdell, R.C., and Miedema, S.A. (2019a) "Can a preliminary model describe CSD Spillage due to centrifugal advection?" *Terra & Aqua*, 153, pp 23-35
3. Werkhoven, J. J., Nieuwboer, B.J., Ramsdell, R.C., and Miedema, S.A. (2019b) "CSD Spillage Model for Sand and Rock," *Proceedings of the Twenty-Second World Dredging Congress, WODCON XXII*, Shanghai, China, April 22-25, 2019.

Where the second publication is an adapted version of the first with permission of the copyright holder. This thesis draws significantly on texts and figures from these publications. Since multiple authors are involved in all papers, *copied* as well as *adapted* parts are referred to in a structural manner.

Items of text highlighted with a dotted line on the right side are references to Werkhoven et al. (2018). This paper introduces a spillage model that works for sand and will be referred to as the Sand Cutting Spillage Model (SCSM).

The paper by Werkhoven et al. (2019b) is referenced using a dashed line on the right side of the paragraph. This paper proposes a spillage model for sand and rock and will be referred to as the Sand-Rock Cutting Spillage Model (SRCSM).

A glossary of terms and symbols used in this report is provided in the back. Figures that contain a visualization of the cutter head have an overview legend in the corner that shows how the viewing angle of the figure.

## 2 Cutter Suction Dredge spillage

This chapter answers the question:

---

### What is CSD spillage and what types of spillage can be identified?

---

The focus of this chapter is on industry observations rather than mathematical descriptions.

### 2.1 Cutter Suction Dredge

A CSD is equipped with a rotating cutter head that is mounted in front of a suction mouth. A hoistable ladder carries the installation and along with a set of swing winches, provides sufficient weight and force to laterally maneuver the rotating cutter head through the soil. Cutter suction dredges can typically reach depths of 30 meter in a very precise pattern. This depth is considered relatively limited in comparison with Trailing Suction Hopper Dredges (TSHD). The maximum ladder angle is approximately 45 degrees.

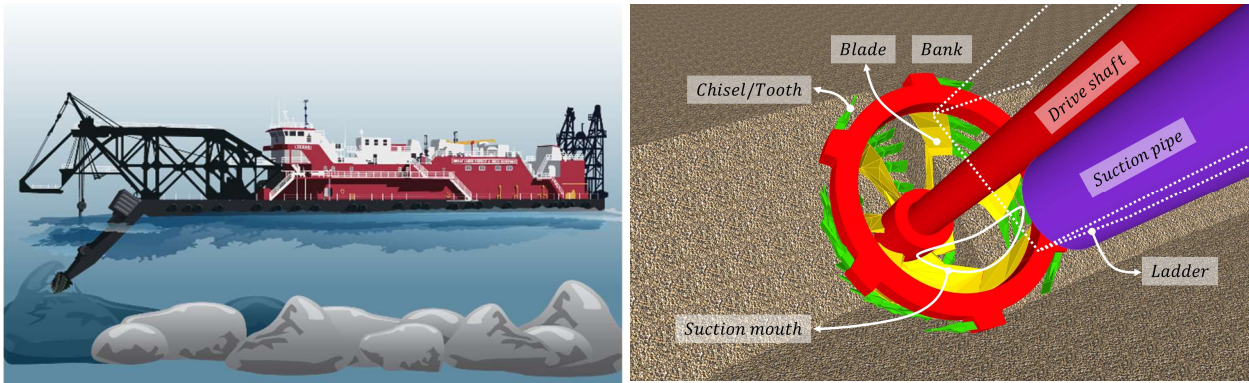
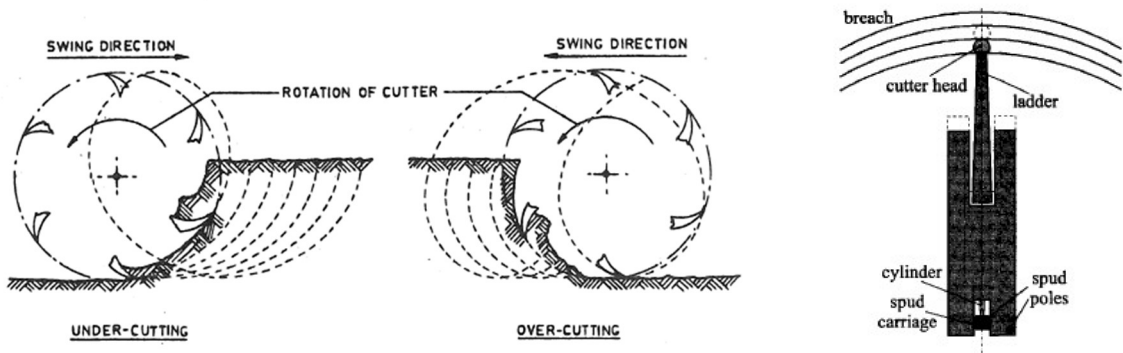


Figure 2.1: CSD with ladder deployed (left) and cutting terminology (right).

Typically, the axi-symmetrical cutterhead of a CSD consists of 5 or 6 blades with a series of teeth that mechanically excavate and suspend bank sediment in order to be sucked up by the suction mouth (see Figure 2.1). The cutter head trails along an arc-shaped path centered on a carrier spud pole. The maximum rotation angle is usually 30 degrees from the centerline.

#### 2.1.1 Dig Swing and Back Swing

The circular arc the cutter makes from either port-side to starboard-side or reverse is defined as a swing. When the swing velocity and the tangential velocity at the top of the cutter align, a scenario arises that is referred to as “over-cutting” (back swinging), while opposing vectors render an “under-cutting” (dig swinging) scenario. See Figure 2.2 for a visual representation of these scenarios.



**Figure 2.2: Under-cutting and over-cutting (left) and typical CSD cutting pattern (right).**  
 Left image is taken from Joanknecht (1976). Right image is taken from Den Burger (2003).

### 2.1.2 Cutter head terminology

Upon entering the bank, an opening is created by the cutter head that is referred to as the breach. The penetration depth into the bank depends on the preferred step size and the height of the bank. Large step sizes are common for soft, small-grained materials. Smaller step sizes are chosen when cutting rock to ensure the cutter has sufficient power to penetrate the material.

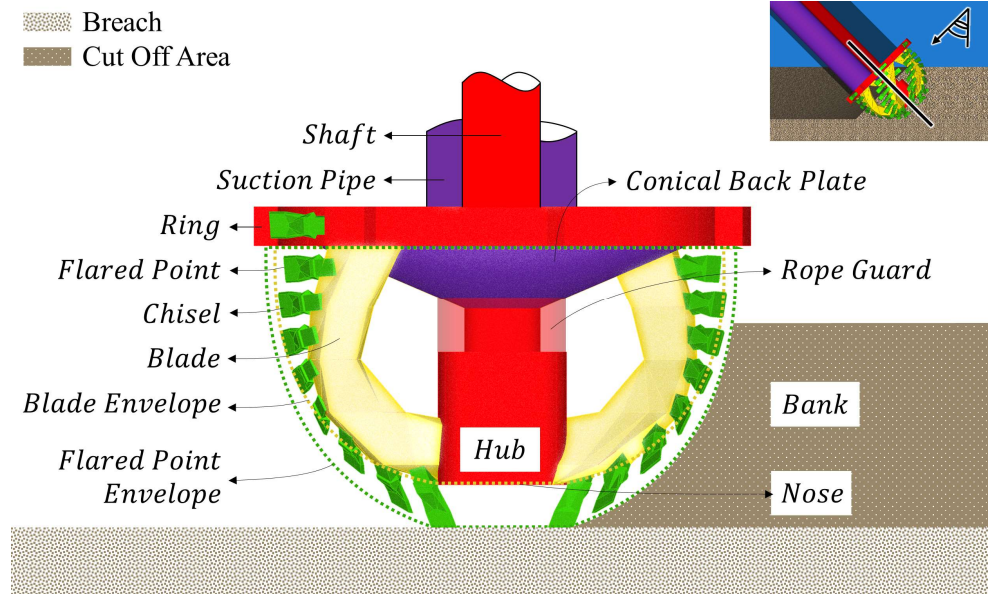


**Figure 2.3: Names of devices and elements for a cutter equipped to cut sand.**

An overview of CSD components is given in Table 2.1. The blades are mounted with adapters to enable easy replacement of teeth/pick-points that are worn out. In addition, adapters enable that the teeth or pick-points are always positioned correctly. The blades are thick to ensure high cutting forces.

**Table 2.1: Cutter Suction Dredge Terminology.**

Name	Function
Anchor	Device that hooks into the bed for holding power to achieve cable tension
Adapter	Connection device for chisels/pick-points and the blades

Blade	Core element of the cutter head (synonym: arm)
Blade envelope	Envelope of the blade rotation around the cutter axis
BOS	Bottom Of Suction: lowest point of the suction mouth
Chisel	Intermediate width steel cutting tool for sand (synonyms: knife, edge)
Conical back plate	Steel plate that directs flow towards the suction mouth
Flared-point	Tip of the flare
Flared-point Envelope	Envelope of the flared point of the blade rotation
Hub	Steel three threaded screw connection between the cutter head and shaft
Ladder	Construction upon which the cutter head is mounted
Nose	Name of the top of the cutter head
Pick-point	Short, strong cutting tool for rock
Ring	Steel ring for structural integrity
Rope guard	Drive axis protection (synonym: rubber bearing)
Shaft	Ladder element that transmits torque
Skirts	Optional steel plates welded onto the blades to extend the blades
Spade	Wide-bladed steel cutting tool that enables a continuous cutter envelope
Spud (auxiliary)	Spud that moves the spud carriage back to its start position
Spud (carrier)	Spud that serves as center of rotation during a swing
Spud carriage	Spud moving system at the stern of the cutter
Suction mouth	Cutout in the back plate that forms the entrance of the suction pipe
Tooth	Steel pick-point for the cutting of rock
TOC	Tip Of Cutter: Location of the lowest point of the cutter envelope
Winch	Mechanical device that connects the pulling cables from the vessel to the anchors, providing sufficient tension on the cables.

## 2.2 Spillage and its implications

Many different standards are used within the industry to describe spillage. An intuitive measure of spillage is to compare the post-passage bed depth to the deepest bed depth during passage. In accordance with this characterization, spillage rates are found of around 25% for sand cutting projects. The cutting of gravel or rock-type projects is more difficult to predict. The reason being that with hard rock cutting, the dredge operator (see Figure 2.1) may prioritize wear prevention of the pick-points over spillage reduction in some situations.

### 2.2.1 Spillage schools of thought

Discussions about spillage are impeded because of different interpretations and therefore conflicting data. There are generally two schools of thought with regards to spillage. One assumes that only the remaining soil above the bottom of the suction mouth (BOS) amounts to spillage, making this a convenient metric for the operator. The other is to consider spillage as all of the remaining soil above the height of the tip of the cutter (TOC). Figure 2.4 (Left) illustrates these different ideas by means of the terms  $S_{suc}$  [-] and  $S_{tot}$  [-] respectively.

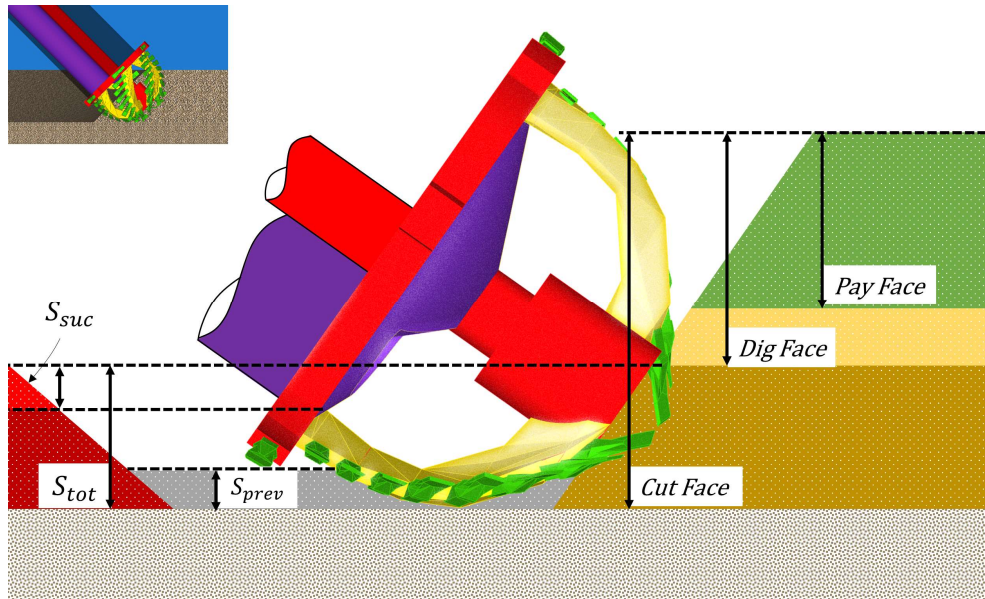


Figure 2.4: Common definitions for CSD cutting.

### 2.2.2 Spillage in dredge contracts

In Figure 2.4 (Left) the commonly used terms “Pay Face”, “Dig Face” and “Cut Face” are visualized. For a typical contract, the dredger is be paid to deepen a certain waterway or port. A minimal depth is often demanded and penalties for violating the contract are significant. For this reason, the dredger will decide to estimate a certain dig face that serves as a safety buffer to achieve the pay face. The dig face is estimated by the difference in cut face and predicted spillage. The cut face is defined as the vertical distance between the TOC and the top of the bank. The method to compensate for reduced depth due to spillage is often referred to as “overdepth cutting”.

### 2.2.3 Economic implications of spillage

Overdepth cutting has a number of consequences. In stiff or hard material, the CSD spends additional energy cutting more material than it excavates, leading to reduced efficiency and greater wear. In areas where the cut depth is restricted, spillage limits the borrow area yield or requires costly cleanup to leave grade.

The reduction of spillage rates is not always a priority. For example, with land winning projects the final depth of the borrow area may not be critical. A larger spillage rate may be accepted in return for very high mixture volumes.

In general, many CSDs are deployed to dredging projects where the limiting production factor is density. Dredging conditions where the pump limit is not exceeded is a priority for operators. A careful consideration must be made between spillage optimization and the pump’s sensitivity to changes in density. In an ideal project, spillage is minimized without changing pump configurations.

#### 2.2.4 *Environmental implications of spillage*

In the water column, plumes resulting from spillage may cause environmental loss as light reduction and sedimentation affect sensitive receptors (Becker et al., 2014; Nakai, 1978). Also, turbidity plumes can reduce oxygen levels and interfere with fish respiration and feeding. Furthermore, the release of adsorbed pesticides, herbicides, toxic metals and synthetic organic compounds may contaminate the water column (Nakai, 1978). Simultaneously, environmental gains are to be expected from the release of nutrients and the supply of fine sediments to silt rich habitats (Becker et al., 2014).

### 2.3 **Spillage definition**

In accordance with the *informative* property of an engineering model, it is chosen to define spillage as a *relative* quantity.

#### 2.3.1 *Single swing VS cutting pattern*

An important differentiator in the determination of spillage is whether a cutting pattern is considered or a single swing only. Swing-swing interactions may be very complex and difficult to validate. For example, suspended sediment from a prior swing may have redeposited or still be in suspension. Consequently, flume concentration, dispersion and porosity of the bed is highly unpredictable. Such a bed is illustrated in Figure 2.4. The increased face due to a previous swing is called  $S_{prev}$  [-]. Overcutting losses from increased bed are mostly not taken into account because only general spillage rates are considered.

A second example of swing-swing interactions is double cutting, where a large face is cut in two-fold. Experimental data for spillage is not available for swing-swing interactions. Calibration of the model is therefore unrealistic. It is decided to define spillage for a *single swing*.

#### 2.3.2 *Scientific definition*

In his PhD dissertation, Den Burger (2003) defines spillage broadly as “the soil that is cut during the dredging process, but is not sucked up by the suction pipe”. This research approaches defines spillage more precisely as

---

**“any soil that is dislodged above the lowest cutter tip trajectory of a single swing, but is not sucked into the suction pipe”**

---

In contrast to Den Burger’s definition, this includes any soil in the vicinity of the cutter and above the cutter profile, but not directly in contact with the cutting equipment. It will be shown that this broader definition includes spillage due to the geometry of the cutter.

### 2.4 **Spillage Types**

According to Den Burger, spillage can be attributed to the cutting process as well as the mixture forming process. Six types of spillage sources pertaining to CSD cutting are identified. A brief overview of the types of spillage is given in this

section. A detailed discussion of the types centrifugal advection, rapid redeposition, and buried cutting is described in later sections.

#### 2.4.1 Centrifugal Advection

Centrifugal advection causes spillage due to high rotational velocity-induced advection in the cutter. High rotational velocity-induced spillage is a primary spillage source for CSD cutting. In its axial trajectory towards the suction mouth, entrained aggregates are accelerated by a centrifugal force induced by the rotational moment of the cutter, resulting in centrifugal advection along the cutter contour. Centrifugal advection leads to a plume in the water column before sediment redeposits into the bed. This type of spillage is most pronounced with small grain sizes, high rotation velocities and low mixture velocities. Figure 2.5 schematically depicts the trajectory of a single particle for the over- (left) and under-cut (right) scenario. Although not identical, centrifugal advection spillage of similar magnitude is observed for each flow pattern (den Burger, 2003). This type of spillage  $S_1$  [-] is considered most significant in this research.

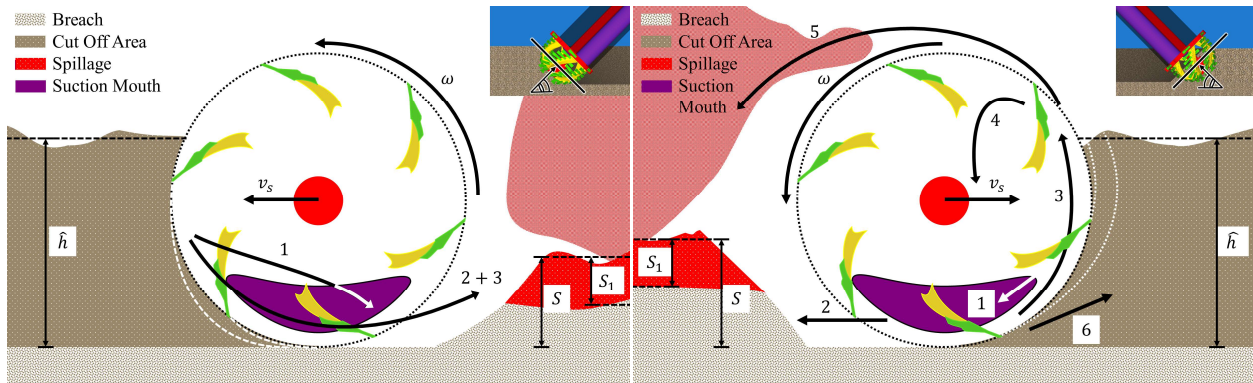


**Figure 2.5: Centrifugal advection-induced spillage for over-cutting (left) and under-cutting (right).**

Particle trajectories are taken from experiments by Den Burger (2003). Trajectories relevant to high rotational velocities are denoted with numbers 1,2,3,5,6. A fourth trajectory was neglected at higher velocities.

#### 2.4.2 Rapid Redeposition

The suspension acceleration resulting from mechanical excavation of the blades may be offset by the influence of gravity. Therefore, solids that are suspended from the bank may rapidly redeposit. Spillage from rapid redeposition  $S_2$  [-] is highly dependent on particle size and rotational velocity. This can be explained by the higher inertia of larger particles that are more difficult to suspend. Furthermore, rapid redeposition mostly occurs with cohesive soils such as clay and rock (Vlasblom, 2003). In practice, when cutting rock in the under-cut mode, the production is “about two to three times higher than in over-cut mode” (Den Burger, 2003).

Industry observations indicate a significantly lower production rate for over-cutting scenarios. In over-cutting, the tangential velocities of the front and top blades coincide with the gravity vector and swing velocity respectively. Dislodged sediment will therefore accelerate downwards and through the suction zone of influence to redeposit immediately (see Figure 2.6, left). In under-cut mode, the

opposing rotational and gravitational force vectors result in a particle trajectory characterized by relatively high suspension rates and improved mixing in the cutter as depicted in Figure 2.6 (right). Sediment passes through the suction zone of influence with lower velocity.

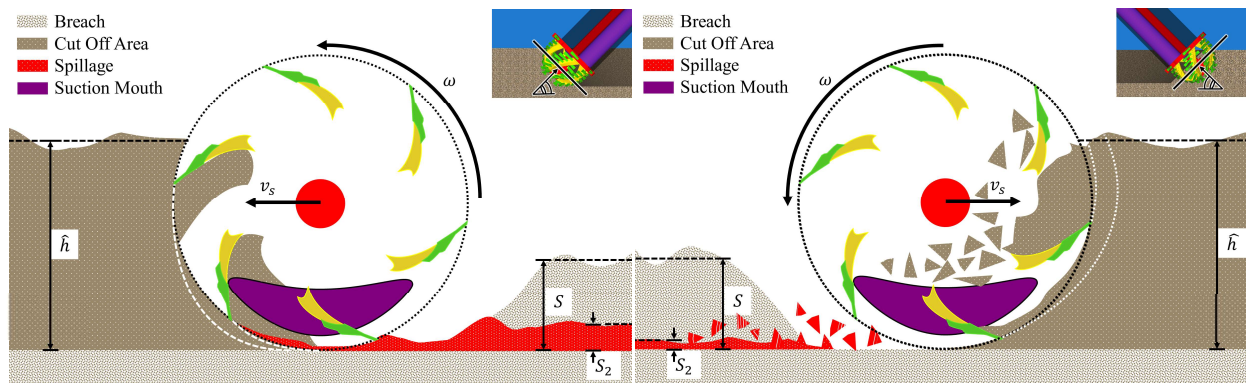


Figure 2.6: Rapid redeposition-induced spillage for over-cutting (left) and under-cutting (right).

#### 2.4.1 Buried Cutting

When dredging a bank height that exceeds the effective height of the cutter head, the undermined soil will fail and rest onto the cutter head. Generally, this soil volume will be entrained into the cutter head, thereby increasing production. However, the cutter head might reach saturation, upon which remaining particles will move past the cutter head and fall behind the cutter head as illustrated in Figure 2.7 (left). Spillage due to buried cutting  $S_3$  [-] is generally determined by the height of the bank and the swing speed.

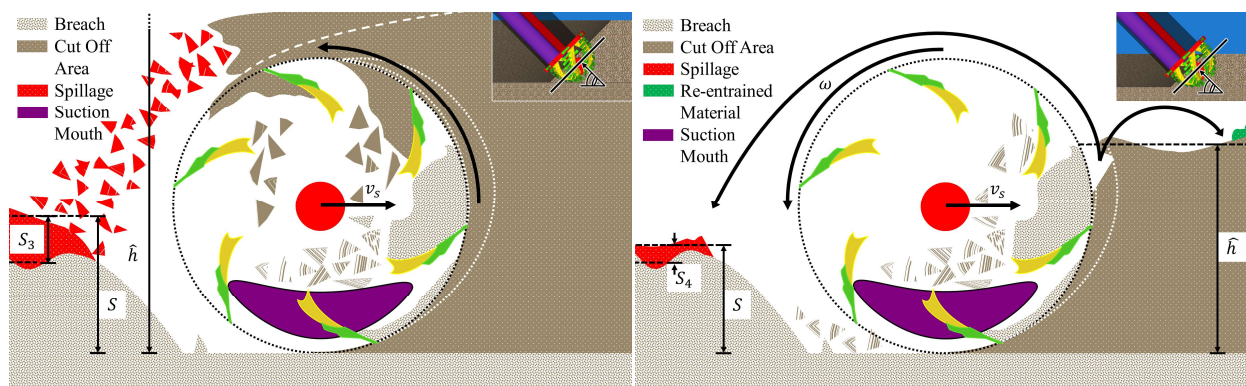


Figure 2.7: Spillage due to buried cutting (left) and spillage due to violent cutting (right) for an under-cutting.

#### Ploughing

A second effect that relates to the saturation of the cutter head is ploughing. When the swing velocity relative to the cutter rotation is too high, uncut material may be diverted collinearly with the cutter axis past the cutter ring. This material will not enter the cutter head and is considered spillage.

### 2.4.2 Violent Cutting

Violent cutting  $S_4$  is a CSD aspect that pertains to particle suspension and subsequent transportation to an area beyond the reach of the CSD head. As the blades and teeth (or chisels for sand cutting) of the cutter head penetrate the bank, soil disintegrates in front of the cutter and some particles will be lifted due to the rotational motion of the cutter head as depicted in Figure 2.7 (right). Moreover, a high swing velocity can cause a bull-dozing effect on the bank which lifts and suspends particles. Particles that redeposit in front of the cutter may be encountered by the cutter head again. Particles that settle behind the cutter contribute to spillage. This type of spillage is most visible when digging rock and cemented material.

#### Breaching

When the cutter head breaches the bank, the slope angle of the breach may be larger than the internal friction angle of the bank material. With the absence of capillary forces below the water line, the steep slope will cause bank instability for granular materials. Van Rhee et al. (1998) describes that the bank wall following a dredger passage can be temporarily steep for sand due to dilatancy-induced plastic deformation of the breach. Shear deformation increases the pore volume of sand and an increased dilatancy causes an under-pressure in the pores resulting in an inflow of water. This process temporarily increases the effective pressure on the bank, yielding a temporarily stable bank slope. The slope will collapse when the maximum possible dilatancy is reached.

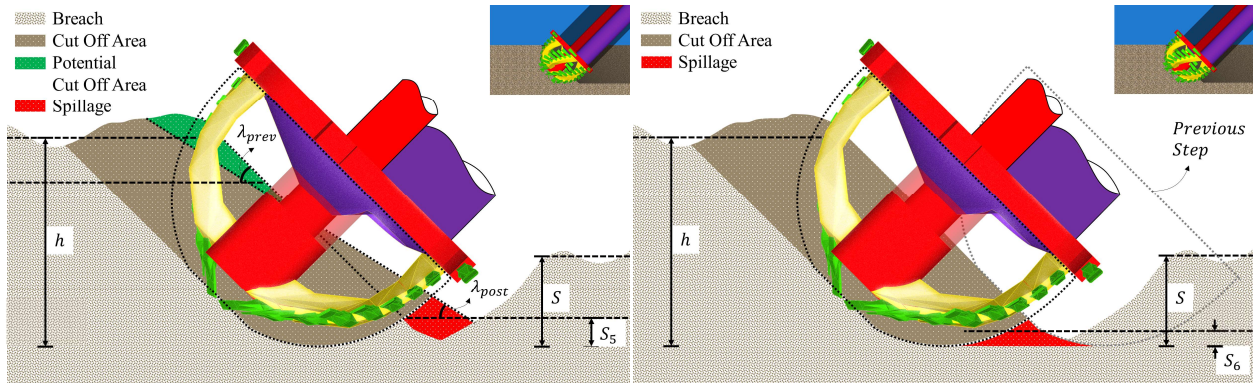


Figure 2.8: Spillage due to bank instability (left) and spillage due to cutter geometry (right).

Figure 2.8 (left) depicts a situation in which the bank wall has collapsed after the cutter passes. It can be seen that the newly created slope extends towards the area that has already been dredged. Hence, this soil remains on the seabed and is considered spillage. Spillage due to bank instability  $S_5$  [-] is mostly dependent on the porosity, particle size and the swing speed.

Since breaching mostly occurs between swings, at the starting point of the cutting pattern breaching effects are neglected for this research.

### *Unstable Breaching*

When the slope angle below a temporary stable wall is smaller than the existing slope angle, the breaching process is considered unstable (van Rhee et al., 1998). According to Van Rhee (2018), unstable breaching may occur at stationary bulk dredging operations with large face where spillage is less relevant.

#### 2.4.3 *Cutter Geometry*

Inherent to the geometry of the cutter head, a relatively small spillage source  $S_6$  [-] can be observed. As the cutter travels forward in discrete step sizes, a portion of the soil above the lower cutter tip depth is undisturbed (see Figure 2.8, right). Based on tradeoffs between the magnitude of inertia and the irregularity of cut areas, cutter geometry has evolved from cylindrically-shaped heads to parabolically-shaped heads (Vlasblom et al., 2006). In lateral direction, spillage due to the cutter geometry exists but is considered negligible. Appendix I illustrates why this is a reasonable assumption.

#### *Cutter height*

The cutter height is highly influential with regards to spillage rates. Taller heads are less productive due to the distance of the suction mouth to the breach (Slotta, 1984).

#### *Suction mouth*

Industry observations indicate that the spillage also results from the shape and rotation of the suction mouth. The entrance of the suction pipe can be rotated backwards or forwards to more directly entrain the mixture flow. Improvement of the geometry is very much an iterative process due to the interaction of cutter components.

#### *Skirts*

For sand cutting projects, dredgers may make use of skirts. Skirts are steel plates welded to the trailing edge of the blades in the vicinity of the cutter mouth. This decreases the probability of particles leaving the cutter head.

#### 2.4.4 *Other factors (single swing)*

Operations in ports, canals, rivers and offshore locations make the CSD subject to a variety of environmental conditions. Translational and rotational vessel movements such as surge, heave and pitch result in unexpected cutter head movements. Furthermore, soil type estimations and bathymetry measurements are complex and prone to errors. The effect of vessel movement and erroneous estimations are inherently difficult to measure directly and can magnify other spillage sources. For this reason, other factors for a single swing are neglected in this research.

#### 2.4.5 *Other factors (Swing-swing)*

Spillage from one swing may be cut in a consecutive swing. When the spillage of a consecutive swing is increased because of its previous swing. this process may be called recycling. The consequences of swing-swing spillage interactions are non-

linear and can be computed when spillage models for individual swings are of sufficient quality.

## 2.5 Spillage diagram

The spillage sources identified in this research can be partitioned in single swing and swing-swing types as presented in Figure 2.9. The spillage types can be differentiated with respect to the ratio of forces that govern a particle motion inside the cutter head. The relevant forces are the gravitational acceleration  $F_g$ , the centrifugal force  $F_{cf}$  and the suction force  $F_s$ . Pumping dynamics are governed by the ratio  $F_{cf}/F_s$  and is relevant to the centrifugal advection as well as the remaining single-swing spillage types. Gravitating effects are governed by  $F_g/F_s$  and is relevant for rapid redeposition. The ratio  $F_{cf}/F_g$  is relevant for mixing effects inside the cutter, which are not seldomly also referred to as “cutting effects”. Section 4 further discusses these force ratios.

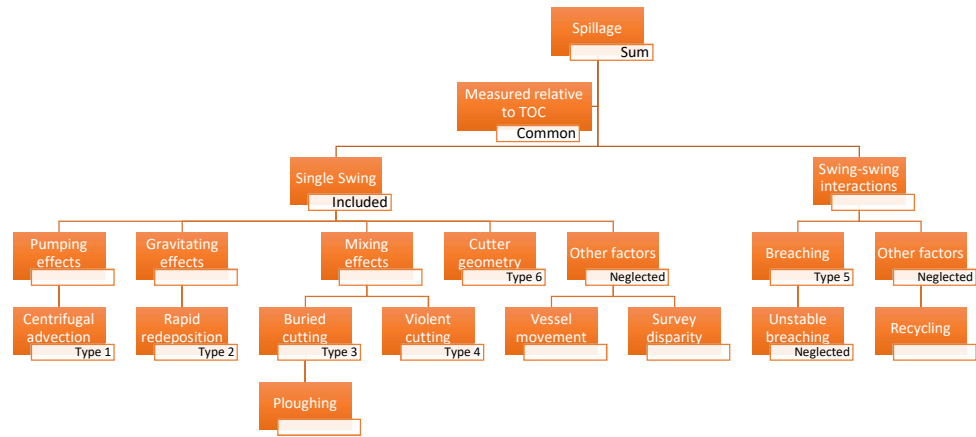


Figure 2.9: Spillage type diagram.

The two considered spillage types in this research are centrifugal advection and rapid redeposition.

## 2.6 Empirical models for total spillage

As of yet, no analytical model exists in literature that can provide an estimate of spillage rates given a set of cutting parameters. Industry practices commonly estimate spillage by linearly scaling the total amount of fines subject to dislodgement by an empirically-derived coefficient as evidenced by equation (1) (Becker et al. 2014). This expression presumes that a certain fraction of fines is representative or in its entirety responsible for spillage due to centrifugal advection.

$$m_{eq} = \Xi_{eq} \rho_{ar} \hat{V}_{cf < 63\mu m} \quad (1)$$

Where  $m_{eq}$  is the total cutter head related mass of fines (dry solids) brought into suspension [kg],  $\Xi_{eq}$  is an empirical source term fraction associated with cutter

head spillage [-],  $\rho_{dr}$  is the dry solids density [ $\text{kg}/\text{m}^3$ ],  $\hat{V}_{situ}$  is the in situ dredge volume [ $\text{m}^3$ ] and  $f_{<63}$  is the fraction of fines smaller than  $63 \mu\text{m}$  [-]. The fraction of fines during the dredge operation may increase due to degradation (Ngan-Tillard et al, 2009). Empirical source term fractions are typically proprietary data.

### 2.6.1 Regression Analyses

Joanknecht (1976) found empirical relations for dimensionless similitude criteria obtained from experimental data for a cylindrical cutter head. It was observed that Froude scaling complemented with the ratio of the terminal settling velocity and the mixture velocity resulted in appropriate scaling. The experiments indicated that over-cutting spillage was positively correlated with the ratio of the swing velocity  $v_s$  and the tangential velocity, whereas under-cutting spillage remained insensitive to this ratio.

Slotta (1978) utilized the Buckingham  $\Pi$  theorem to find empirical relations with the Euler, Reynolds and Froude numbers as well as a diameter ratio and a ratio of the rotational velocity and the mixture velocity. Experimental data indicated that Reynolds scaling should be applied for the suction inlet.

Hayes (1986) performed a linear regression study for dimensionless variable groups obtained from observed suspended sediment concentrations resulting from CSD operations at Calumet harbour (Hayes et al. 1988). Collins (1995) expanded this dataset with three field operations and two experimental studies and performed a similar linear regression. The improved empirical model could, however, “not explain suspended sediment variations very well” (Hayes et al., 2000). Earlier research by Andrassy et al. (1988) in which CSD operation parameters were used in a correlation study for a similar dataset, was unable to identify statistically significant relationships.

Hayes et al. (2000) performed a dimensional criteria study to support a dimensionless regression analysis based on the Buckingham  $\Pi$  theorem to find spillage correlations. The “106 observation data set used in this study represents a too limited range of operating parameters to generate a model applicable to a wider variety of conditions”, however, reasonable accuracy was obtained for spillage data. Additional validation is needed to substantiate the model.

## 2.7 Conclusion

### What is CSD spillage and what types of spillage can be identified?

In this research, CSD spillage is defined as “any soil that is dislodged above the lowest cutter tip trajectory of a single swing, but is not sucked into the suction pipe”. A classification of spillage based on pumping, mixing and gravitating effects results in six distinct spillage types. It is reasoned that four types can be considered negligible under typical cutting circumstances. The first significant type is named centrifugal advection and is defined as the radial outflow of suspended particles in close proximity to the cutter ring and is driven by high rotational velocity of the

cutter. Centrifugal advection affects spillage rates for all particle sizes but is most pronounced for fine particles such as sand. The second, concurrent spillage type is referred to as rapid redeposition and is governed by the ratio of the particle settling velocity over the mixture velocity.

### 3 Fundamental physics

This chapter focuses on the physics that govern cutter head flows and aims to answer the question:

---

**What formulations are fundamental to the motion and behaviour of a fluid substance in the physical domain of the cutter head?**

---

First, cutter flow observations are presented based on a literature review. Second, the governing forces inside the cutter are identified. Motivation is given for the use of a cylindrical coordinate system of Navier-Stokes equations for the considered cutter head.

In search of an expression for flow inside the cutter, a series of assumptions is provided that reduce the Navier-Stokes equations to Euler's Equations. These can be further simplified to find Euler's pump equation for centrifugal pumps. It is demonstrated that Bernoulli's principle can be used to establish Euler's pump equation. An overview of derivation steps is given in Figure 3.1. A full derivation is provided in Appendix C.

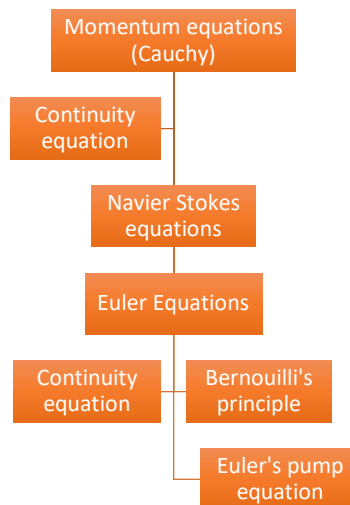


Figure 3.1: Derivation steps for Euler's pump equation.

#### 3.1 Cutter flow characterization

In the 1970s, a joint research effort from a group of Dutch contractors united under the name Combinatie Speurwerk Baggertechniek (CSB), Ministerial Agency of Public Works Rijkswaterstaat and research institute WL|Delft Hydraulics conducted a series of experiments to gain a better understanding of the internal flows in and around the cutter. The conducted experiments considered only water.

As summarized by Den Burger (2003), the experimental results indicate that the cutter head resembles a combination of an axial pump as well as a centrifugal pump.

This dual phenomenon of an axial and a centrifugal pump effect was first noticed by Miltenburg (1983). Figure 3.2 displays the observations from these sources.

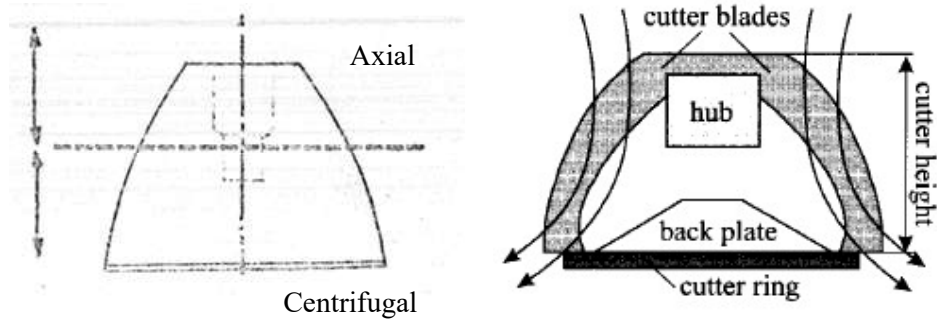


**Figure 3.2: Centrifugal pump effect characterization by Miltenburg (1983, left) and Den Burger (2003, right).**

Figures are adapted.

A numerical model based on Unsteady Reynolds Averaged Navier Stokes equations by Nieuwboer et al. (2017) indicates that “water movement caused by the passing of the blades does accelerate the particles outward” with spillage as a consequence.

The mixture velocity was varied in the experiments at WL|Delft Hydraulics. Depending on the mixture velocity, a transition value was observed for the rotational velocity. The data showed that there is an inward flow along the entire contour of the cutter head for rotational velocities below the transition value.

However, above this threshold an outwards flow near the back plate was observed that increased with rotational velocity. This outward flow contains suspended particles which may not re-enter the cutter head. Figure 3.2 (right) schematically depicts the flow that is generated by these pump effects as well as the location along the contour line of the cutter head where inflow reverses to outflow.

Particle trajectories in the under-cut and over-cut situation appeared very different. However, for both situations they appeared insensitive to variations of the rotational velocity and mixture velocity. Also, the ratio of the transition value for the rotational velocity and the mixture velocity appeared relatively constant and identical for the under-cut and over-cut situation. For a 0.6 [m] cutter head this ratio was approximately 0.42 [-], hence

$$\frac{\omega}{v_m} \approx \frac{v_{ratio}}{R_{ring}} = \frac{0.42}{0.6} = 0.7 \quad (2)$$

Den Burger describes that the rotational velocity and mixture velocity do influence the magnitude of the velocities in both situations as was found by Moret (1977a). The outflow is also confirmed by Steinbusch (1999). Further literature observations are given in Appendix G.

### 3.2 Governing forces

The effects described in section 3.1 suggest that particle trajectories in a CSD are governed by the centrifugal force  $F_{cf}$  in the cutter [N], the gravitational force  $F_g$  [N] and the product of the particle volume and radial pressure gradient in the suction mouth  $F_s$  [N]. The ratios between these terms provide convenient indicators for the governing motion of a fluid substance inside the cutter head.

#### 3.2.1 Inertial force vs gravitational force

A typical ratio for the cutting-related forces can be found by dividing the centrifugal force over the gravitational force as demonstrated in equation (3).

$$\frac{F_{cf}}{F_g} \propto \frac{m_p R_{ring} \omega^2}{(\rho_q - \rho_w) V_p g} = \frac{\rho_q}{(\rho_q - \rho_w)} \frac{R_{ring} \omega^2}{g} \quad (3)$$

Where  $m_p$  is the particle mass [kg],  $V_p$  is the particle volume [m<sup>3</sup>] and  $g$  the gravitational acceleration [m/s<sup>2</sup>]. This ratio is representative of the degree of mixing of in situ dredge material inside the cutter. When particles are not mixed into the cutter head, they will not be entrained in the axial flow towards the suction mouth. A lack of mixing directly contributes to spillage. The ratio between the inertial and gravitational force is significantly different for the under-cut and over-cut mode.

#### 3.2.2 Inertial force vs suction force

Of equal interest is the ratio of centrifugal force and suction force. The suction force is proportional to the product of the pressure gradient and the volume of the particle, i.e. the volume-pressure gradient product. The ratio is presented in equation (4).

$$\frac{F_{cf}}{F_s} \propto \frac{\rho_q}{\rho_w} \left( \frac{\omega R_{ring}^3}{v_m R_{pipe}^2} \right)^2 \quad (4)$$

Where  $\rho_q$  is the particle density [kg/m<sup>3</sup>],  $\rho_w$  is the water density [kg/m<sup>3</sup>],  $R_{ring}$  and  $R_{pipe}$  are the cutter ring and pipe radii [m] and  $v_m$  is the mixture velocity [m/s]. This ratio is a governing metric for the process that takes place near the suction mouth. A high ratio indicates a small influence from the suction mouth. Den burger (2003) noted that “there is a distinct relationship between the productivity of the cutter head and the ratio of the suction flow and the rotational velocity of the cutter head”. This ratio is expected to be governing for centrifugal advection.

#### 3.2.3 Gravitational force vs suction force

The gravitational force can be divided over the volume-pressure gradient product as demonstrated in equation (5).

$$\frac{F_g}{F_s} \propto \frac{\rho_w}{(\rho_q - \rho_w)} \frac{v_m R_{pipe}^2}{V_p g} \quad (5)$$

This ratio provides insights into the dynamics of rapid redeposition. If the gravitational force is stronger in comparison to the suction force then the influence

of the suction mouth is insignificant and particles will redeposit onto the bank. Coarser material such as rock is more subject to gravitational acceleration since it has a higher terminal settling velocity.

### 3.3 Cylindrical coordinate system

In the scope of this research (Section 1.2.1) it was determined that an analytical model is desired. Analytical models highly benefit from a coordinate system that is in accordance with the physical domain. The hemiellipsoidal shape of the cutter head prescribes a cylindrical coordinate system. Cylindrical coordinates have the advantage of symmetry, which will later prove useful to eliminate a velocity component in the Navier-Stokes equations.

The velocity of a fluid is then given by its radial distance, azimuthal angle and axial distance, as shown in equation (6).

$$\mathbf{v}(r, \theta, z, t) = v_r(r, \theta, z, t)\mathbf{e}_r + v_\theta(r, \theta, z, t)\mathbf{e}_\theta + v_z(r, \theta, z, t)\mathbf{e}_z \quad (6)$$

Where  $\{\mathbf{e}_r, \mathbf{e}_\theta, \mathbf{e}_z\}$  is a triad of unit vectors. These velocities will prove to be helpful in the derivation of the continuity equation.

### 3.4 Derivation of Navier-Stokes equations

The movement of fluid in the physical domain of the cutter head is driven by velocity, pressure, density, viscosity and to a lesser extent, temperature. The dynamics between these properties are based on the principles of conservation of energy, mass and momentum.

#### 3.4.1 Conservation of energy

Since the cutter flows consist of water and suspension flows, it can be assumed that the fluids are *incompressible*. Incompressible flows are energy conserving.

#### 3.4.2 Conservation of mass: continuity equation

Conservation of mass is governed by the *continuity* equation. Let us consider an infinitesimally small control volume as visualized in Figure 3.3 (left).

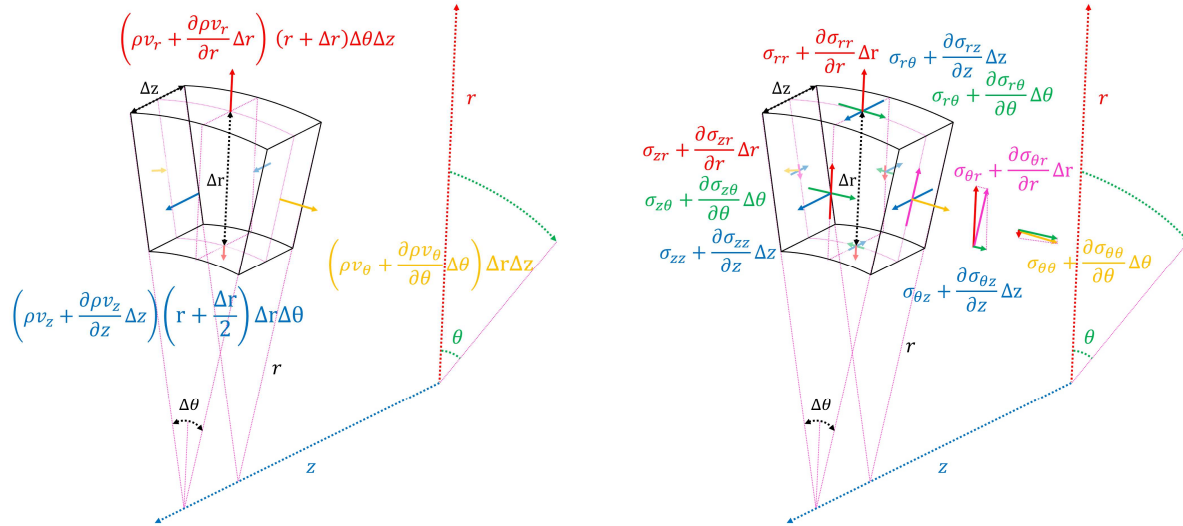


Figure 3.3: Continuity (left) and stress balance (right) for an infinitesimally small control volume.

It can be assumed that the cutter head is in *steady state*, hence all temporal terms in the derivation can be set to zero. It can be demonstrated that the continuity equation then reduces to equation (7).

$$\frac{1}{r} \frac{\partial(rv_r)}{\partial r} + \frac{1}{r} \frac{\partial v_\theta}{\partial \theta} + \frac{\partial v_z}{\partial z} = 0 \quad (7)$$

### 3.4.3 Conservation of momentum: Cauchy

The total force per infinitesimally small element within the cutter equal to the sum of molecular forces and body forces. The continuity equation holds within the cutter and the velocity order of the magnitudes suggests *non-relativistic* momentum transport. The Cauchy momentum equation can therefore be written as presented in equation (8).

$$\rho \frac{D\mathbf{v}}{Dt} = \nabla \cdot \boldsymbol{\sigma} + \rho \cdot \mathbf{g} \quad (8)$$

Where *gravity* is the only body force considered. Again, the time-rated change in velocity is zero which sets the time-rated changes of the unit vector according to equation (9).

$$\frac{\partial \mathbf{v}}{\partial t} = \frac{\partial v_r}{\partial t} \mathbf{e}_r + \frac{\partial v_\theta}{\partial t} \mathbf{e}_\theta + \frac{\partial v_z}{\partial t} \mathbf{e}_z \quad (9)$$

#### Material derivative of velocity

It can be demonstrated that the material derivative from equation (8) reduces to

$$\begin{aligned} \frac{D\mathbf{v}}{Dt} &= \left[ \frac{\partial v_r}{\partial t} + v_r \frac{\partial v_r}{\partial r} + \frac{v_\theta}{r} \frac{\partial v_r}{\partial \theta} - \frac{v_\theta^2}{r} + v_z \frac{\partial v_r}{\partial z} \right] \mathbf{e}_r \\ &+ \left[ \frac{\partial v_\theta}{\partial t} + v_r \frac{\partial v_\theta}{\partial r} + \frac{v_\theta}{r} \frac{\partial v_\theta}{\partial \theta} + \frac{v_\theta v_r}{r} + v_z \frac{\partial v_\theta}{\partial z} \right] \mathbf{e}_\theta \\ &+ \left[ \frac{\partial v_z}{\partial t} + v_r \frac{\partial v_z}{\partial r} + \frac{v_\theta}{r} \frac{\partial v_z}{\partial \theta} + v_z \frac{\partial v_z}{\partial z} \right] \mathbf{e}_z \end{aligned} \quad (10)$$

### Stress tensor

Figure 3.3 displays the stresses present on an infinitesimally small control volume. By summing the radial, azimuthal and axial stresses it can be shown that the stress divergence term from equation (11) arises.

$$\begin{aligned}\nabla \cdot \boldsymbol{\sigma} = & \left[ \frac{\sigma_{rr}}{r} + \frac{\partial \sigma_{rr}}{\partial r} + \frac{1}{r} \frac{\partial \sigma_{r\theta}}{\partial \theta} + \frac{\partial \sigma_{rz}}{\partial z} - \sigma_{\theta\theta} r \right] \mathbf{e}_r \\ & + \left[ \frac{2\sigma_{r\theta}}{r} + \frac{\sigma_{r\theta}}{\partial r} + \frac{1}{r} \frac{\partial \sigma_{\theta\theta}}{\partial \theta} + \frac{\partial \sigma_{\theta z}}{\partial z} \right] \mathbf{e}_\theta \\ & + \left[ \frac{\sigma_{rz}}{r} + \frac{\partial \sigma_{rz}}{\partial r} + \frac{1}{r} \frac{\partial \sigma_{\theta z}}{\partial \theta} + \frac{\partial \sigma_{zz}}{\partial z} \right] \mathbf{e}_z\end{aligned}\quad (11)$$

The stress effect on the control volume is represented by the sum of the isotropic and anisotropic part of the stress tensor, i.e.

$$\boldsymbol{\sigma} = -p\mathbf{I} + \boldsymbol{\tau} \quad (12)$$

The viscous forces are captured by the anisotropic stress tensor ( $\nabla \cdot \boldsymbol{\sigma}$ ) while the pressure gradient makes up the isotropic stress tensor ( $\nabla p$ ). Since the fluid is considered incompressible, the only viscous forces are shear. A series of operations including equation (13) can be performed to find stresses required to solve equation (11).

$$\boldsymbol{\tau} = \mu(\nabla \mathbf{v} + \nabla \mathbf{v}^T) \quad (13)$$

where  $\mu$  is the viscosity [Pa·s]. In the radial direction, the result is given in equation (14)

$$\begin{aligned}-\frac{\partial p}{\partial r} + \mu \left[ -\frac{u_r}{r^2} + \frac{\partial}{\partial r} \left( \frac{1}{r} \frac{\partial (rv_r)}{\partial r} + \frac{1}{r} \frac{\partial u_\theta}{\partial \theta} + \frac{\partial v_z}{\partial z} \right) \right. \\ \left. + \frac{1}{r} \frac{\partial}{\partial r} \left( r \frac{\partial v_r}{\partial r} \right) + \frac{1}{r^2} \frac{\partial^2 v_r}{\partial \theta^2} + \frac{\partial^2 v_r}{\partial z^2} - \frac{2}{r^2} \frac{\partial v_\theta}{\partial \theta} \right]\end{aligned}\quad (14)$$

As demonstrated in equation (7) of the continuity equation derivation, the terms between the first parentheses, the radial derivative, is equal to zero.

### Gravitational acceleration

Suppose a unit mass is inclined under an angle  $\lambda$  [rad] with respect to a reference frame aligned with the seabed as depicted in Figure 3.4.

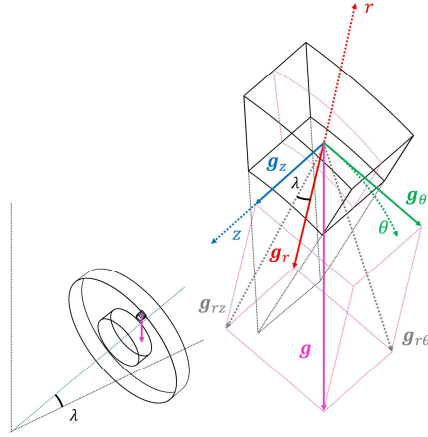


**Figure 3.4: Gravitational acceleration in a cylindrical coordinate system.**

The gravitational accelerations in the  $r$ -,  $\theta$ - and  $z$ -direction can then be found according to the formulations given in equation (15).

$$\begin{aligned} g_r &= g \cos \theta \cos \lambda \\ g_\theta &= g \sin \theta \cos \lambda \\ g_z &= g \sin \lambda \end{aligned} \quad (15)$$

The Navier-Stokes (NS) equation in the radial direction can be obtained from the Cauchy Momentum equation (8) by substitution of equations found for the velocities (10), the stress tensor (14) and the gravitational acceleration (15).

$$\begin{aligned} & \rho \left[ \underbrace{\frac{\partial v_r}{\partial t}}_{\text{variation}} + \underbrace{v_r \frac{\partial v_r}{\partial r} + \frac{v_\theta}{r} \frac{\partial v_r}{\partial \theta} - \frac{v_\theta^2}{r} + v_z \frac{\partial v_r}{\partial z}}_{\text{convection}} \right] \\ &= - \underbrace{\frac{\partial p}{\partial r}}_{\substack{\text{pressure} \\ \text{gain}}} + \mu \underbrace{\left[ -\frac{u_r}{r^2} + \frac{1}{r} \frac{\partial}{\partial r} \left( r \frac{\partial v_r}{\partial r} \right) + \frac{1}{r^2} \frac{\partial^2 v_r}{\partial \theta^2} + \frac{\partial^2 v_r}{\partial z^2} - \frac{2}{r^2} \frac{\partial v_\theta}{\partial \theta} \right]}_{\text{diffusion}} + \underbrace{\rho g_r}_{\substack{\text{external} \\ \text{source}}} \end{aligned} \quad (16)$$

The NS components of the azimuthal and axial direction are presented in Appendix C.

### 3.5 Viscosity, density, inertia

The three-dimensional nature and complex geometry of the cutter head, combined with the difficulty of accurately quantifying spillage types, encumber CSD spillage modeling and validation. Additionally, observations from experiments and empirical models are subject to scaling difficulties. In order to assess the influence of viscosity, density and inertia in the cutter head, A few dimensionless numbers are evaluated, namely

$$\begin{aligned}
\text{Reynolds number} &= \frac{\text{inertia}}{\text{viscous force}} \\
\text{Euler number} &= \frac{\text{pressure}}{\text{inertia}} \\
\text{Strouhal number} &= \frac{\text{local acceleration}}{\text{convective acceleration}} \\
\text{Froude number}^2_{\text{densimetric}} &= \frac{\text{inertia}}{\text{gravity}}
\end{aligned} \tag{17}$$

The general relevance of these numbers for the proposed model can be derived from the NS equations, which can be generalized from equation (14) and further derivations in Appendix C.7, to the form

$$\underbrace{\rho \frac{\partial \mathbf{v}}{\partial t} + \rho \mathbf{v} \cdot \nabla \mathbf{v}}_{\text{acceleration}} = - \underbrace{\nabla p}_{\text{pressure gradient}} + \underbrace{\mu \nabla^2 \mathbf{v}}_{\text{shear stresses}} + \underbrace{\rho \mathbf{g}}_{\text{gravitational acceleration}} \tag{18}$$

To derive the dimensionless numbers, it is sought to make the NS equations dimensionless. As a first step, it is realized that the fluid density in the cutter comprises a hydrostatic and a hydrodynamic part ( $\rho = \rho_0 + \Delta\rho$ ). For the pressure gradient, the NS equations can be made more insightful by considering only the dynamic pressure ( $p_{dyn} = p - p_s$ ). The generalized NS can be rewritten and divided by  $\rho_0$  to find

$$\left(1 + \frac{\Delta\rho}{\rho_0}\right) \left(\frac{\partial \mathbf{v}}{\partial t} + \mathbf{v} \cdot \nabla \mathbf{v}\right) = -\frac{1}{\rho_0} \nabla p_d + \frac{\mu}{\rho_0} \nabla^2 \mathbf{v} + \left(1 + \frac{\Delta\rho}{\rho_0}\right) \mathbf{g} \tag{19}$$

The relative importance of the dimensionless coefficients can be found by normalizing equation (19) to relevant scales. To this end, the following definitions are introduced

$$\begin{aligned}
\mathbf{v}' &= \frac{\mathbf{v}}{V} \\
t' &= \frac{t}{T} \\
\mathbf{l}' &= \frac{\mathbf{l}}{L} \\
p'_{dyn} &= \frac{p_{dyn}}{\hat{P}_{dyn}} \\
\mathbf{g}' &= \frac{\mathbf{g}}{G}
\end{aligned} \tag{20}$$

Where the pressure scale  $\hat{P}_{dyn}$  is yet to be estimated. The normalized NS equations are

$$\left(1 + \frac{\Delta\rho}{\rho_0}\right) \left(\frac{L}{TV} \frac{\partial \mathbf{v}}{\partial t} + \mathbf{v}' \cdot \nabla \mathbf{v}'\right) = -\frac{P_d}{V^2} \frac{1}{\rho_0} \nabla' p'_d + \frac{1}{VL} \mu \nabla'^2 \mathbf{v}' + \frac{gL}{V^2} \frac{\Delta\rho}{\rho_0} \mathbf{g}' \tag{21}$$

In which the following dimensionless numbers can be identified

$$\begin{aligned}
Re &= \frac{LV}{\nu} \\
Eu &= \frac{P_d}{\rho_0 V^2} \\
St &= \frac{L}{TV} \\
Fr^2 &= \frac{\rho_0 V^2}{\Delta\rho g L}
\end{aligned} \tag{22}$$

### 3.5.1 Reynolds number

The flow regime is determined by the Reynolds number. As mentioned in the research scope (section 1.2.1), a cutter head of 3.12 [m] is chosen as a characteristic length scale. Furthermore, a very common 30 revolutions per minute [rpm] for the cutter and a suction flow of 6 [m/s] are considered. The Reynolds number can be found as

$$Re = 0.7 \cdot 10^7 \approx 1 \cdot 10^7 \tag{23}$$

The Reynolds number is large enough to conclude that viscosity can be neglected.

### 3.5.2 Euler number

The Euler number provides a ratio between the pressure and inertia forces. An indication of the dynamic pressure  $P_d$  is found in Bernoulli's principle (see Appendix A).

$$P_d \propto \frac{1}{2} \rho V^2 \tag{24}$$

From equation (22) the Euler number can thus be obtained

$$Eu = \frac{P_d}{\rho_0 V^2} = \frac{1}{2} \frac{\rho}{\rho_0} \approx 1 \tag{25}$$

It can be concluded that an Euler number corresponding to approximately 1 represents a cutter head with frictionless flow.

### 3.5.3 Strouhal number

The Strouhal number for the acceleration ratio is used to assess whether viscosity dominates the cutter flow. A case is considered for laminar flow and for flow with high rotational velocity.

#### *Laminar flow*

Again, an estimate of the time-scale  $T$  is to be made. The cutter head volume is approximated by taking half of a sphere volume and then scaling the volume with a common cutter height  $b$  of 2.50 [m]. The volume is then found as

$$Volume = \frac{2.5}{L} \cdot \frac{1}{2} \cdot \frac{1}{6} \pi D^3 \approx 6.4 \tag{26}$$

Again, the characteristic length scale is the diameter of the cutter head of 3.12 [m]. Next, the flow through the cutter head needs to be estimated. For this estimation the volumetric flow rate  $Q_{a_m}$  [m<sup>3</sup>/s] through the cutter head can be used. A

common value of 4 cubic meters per second is chosen. The time-scale is then approximated by the retention time in the cutter, i.e.

$$T = \frac{V}{Q_{a_m}} = \frac{6.4}{4} = 1.6 \quad (27)$$

This time-scale from equation (27), the diameter length scale and a velocity scale of  $V = \omega D/2 = 4.9$  [m/s] is substituted in equation (22) to find

$$St = \frac{L}{TV} = \frac{3.12}{1.6 \cdot 4.9} = 0.4 \approx 0.1 \quad (28)$$

#### *High rotational velocity*

A high rotational velocity is considered of 40 [rpm]. For this velocity, a more appropriate time-scale is estimated by Den Burger (2003). It is proposed that a six-bladed cutter head has a cycle time of 0.25 [s]. The Strouhal number then becomes

$$St = \frac{L}{TV} = \frac{3.12}{0.25 \cdot 4.9} = 2.54 \approx 3 \quad (29)$$

This order of magnitude suggests that for higher rotational velocities the Strouhal number is more significant and that viscosity would have to be included.

#### 3.5.4 *Froude number (densimetric)*

The Froude number is indicative of the influence of density differences in the cutter head. With rapid redeposition present in the cutter head, the density differences between the top and bottom of the cutter head can be high and lead to density currents.

Equation (22) requires an estimation of the fluid density with suspended material. A dredge pump transports a typical density of 1200 [kg/m<sup>3</sup>]. The hydrodynamic density in the cutter is found through subtraction of the static density ( $\Delta\rho = \rho - \rho_0 = 1200 - 1000 = 200$  [kg/m<sup>3</sup>]). Secondly, an approximation should be made for the characteristic length scale. It is assumed that half the cutter is penetrated into the bank, thus the length scale  $L$  is set at  $b/2$ . The densimetric Froude number is therefore

$$Fr = \frac{\rho_0 V^2}{\Delta\rho g \frac{b}{2}} = \frac{1000 \cdot 4.9^2}{200 \cdot 9.81 \cdot \frac{2.5}{2}} = 9.79 \approx 10 \quad (30)$$

A Froude number of 10 suggest that the inertial forces are dominant over the gravitational body force. The influence of gravity is can be considered negligible.

#### *Density error*

The model assumes uniform density in the cutter, whereas in reality the density varies between 1000 and 1200 [kg/m<sup>3</sup>], an thus error is to be expected. The maximum size of the error is estimated using equation (26).

$$\frac{\Delta\rho}{\rho_0} = \frac{200}{1000} = 0.2 \quad (31)$$

The dominance of inertial forces indicates that the assumption of uniform density introduces a maximum error of 20%. The error is acceptable for dredging standards.

#### *Dominant scaling parameters*

The dominant scaling parameters for the cutting process, flow within the cutter and influence of the suction mouth are now considered. The mechanical *excavation* of the cutter scales according to Froude's number since inertial and gravitational forces are governing. The *suction* mouth process is characterized by dominant inertial and viscous forces, rendering Reynolds scaling most appropriate. When gravity and viscosity dominate, the particle trajectories become more sensitive to the viscosity and density (Slotta, 1978).

From the Reynolds and Euler number, it was concluded that the viscosity in the cutter head can be neglected. The Strouhal number consists of a length scale, time-scale and velocity scale. It can be reasoned that these numbers scale linearly and therefore do not significantly impose restrictions on scaling. The Euler number is thus rendered the most important dimensionless scaling number for *flow*. In other words, the pressure is considered the most dominant contribution to the dynamic of flows in the cutter.

### 3.6 Derivation of Euler equation

From the dimensionless number analysis, it is assumed that fluid is *inviscid*. With the absence of shear stresses, the fluid is also *irrotational*. Setting  $\mu = 0$  gives the Euler Equation as shown in equation (32) for the radial direction. In conjunction with the axial and azimuthal components, this equation is known as the Euler equation.

$$\rho \left[ \frac{\partial v_r}{\partial t} + v_r \frac{\partial v_r}{\partial r} + \frac{v_\theta}{r} \frac{\partial v_r}{\partial \theta} - \frac{v_\theta^2}{r} + v_z \frac{\partial v_r}{\partial z} \right] = -\frac{\partial p}{\partial r} + \rho g_r \quad (32)$$

### 3.7 Derivation of Euler's pump equation

Let us assume that the fluid flows *axisymmetrically*, i.e. any change in velocity with respect to  $\theta$  is zero. It was assumed that the physical domain of the cutter is in a steady state that will remove any temporal change from the NS equations. In the radial direction, the following assumptions are imposed

$$\frac{v_\theta}{r} \frac{\partial v_r}{\partial \theta} = 0, \quad \frac{\partial v_r}{\partial t} = 0 \quad (33)$$

The Euler equation in radial direction (32) can therefore be substituted with the assumptions from equation (33). The result is given in equation (34) and serves as a basis for Euler's pump equation.

$$\rho \left( v_r \frac{\partial v_r}{\partial r} - \frac{v_\theta^2}{r} + v_z \frac{\partial v_r}{\partial z} \right) - \rho g_r = -\frac{\partial p}{\partial r} \quad (34)$$

The velocities in equation (34) are the absolute velocities  $v_{r_i}$  and  $v_{\theta_i}$  at axial location  $i$  in radial and tangential direction respectively [m/s]. Equation (32) is

known in the field of pump design. Since the cutter head highly resembles that of a centrifugal pump, it is assumed that Euler's pump equation is suitable for flow descriptions of the centrifugal kind. The blades of the cutter head can be compared to the vanes of a centrifugal pump. For this reason, the following derivation draws heavily on the analogy that can be made with a centrifugal pump.

### 3.7.1 Velocity triangles

The derivation is continued by considering a streamline within a cylinder. In 3D space, the pressure on an infinitesimally small element with respect to the radius at location  $r\theta z = \{r, \theta, z\}$  along a section of the streamline, can be found as

$$\frac{dp}{dr}\bigg|_{r\theta z} = \frac{\partial p}{\partial r} + \frac{\partial p}{\partial \theta} \frac{d\theta}{dr}\bigg|_{r\theta z} + \frac{\partial p}{\partial z} \frac{dz}{dr}\bigg|_{r\theta z} \quad (35)$$

A unit mass, in a cylindrical coordinate system, travels along a blade (depicted in yellow) with a velocity  $w$  [m/s] relative to the blade. Since the blade has absolute velocity  $u$  [m/s], the sum of  $u$  and  $w$  yields the absolute velocity  $v$  [m/s] of the unit mass. Here,  $u$  is depicted in green and  $v$  is depicted in grey, with components  $v_\theta$  (azimuthal) in grey and  $v_r$  (radial) in red. Figure 3.5 visualizes the vectors in the cylindrical coordinate system.

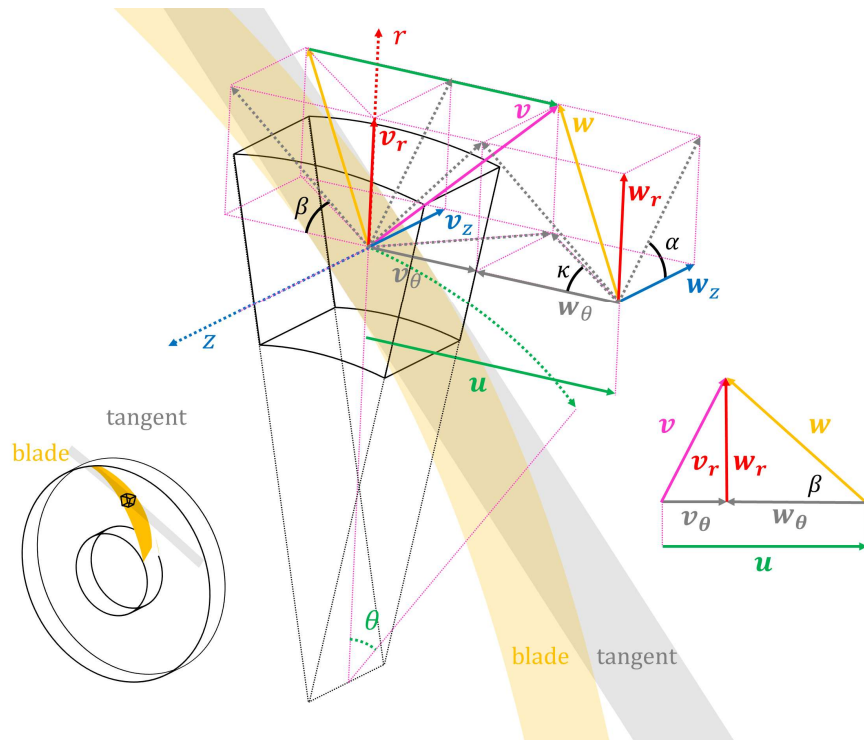


Figure 3.5: Blade-induced velocities of an infinitesimally small fluid volume.

As can be seen in the figure, a two-dimensional velocity triangle would simplify the velocity triangles found in the figure significantly. In reality, axial flow is an important component that is induced by the suction pressure as well as the curvature of blades near the nose. However, if axial flow is incorporated in the

derivation of the radial pressure gradient, then the equations become significantly more complex which introduces the risk of compromising on tractability.

**For the derivation of the radial pressure gradient of the centrifugal pump effect, flow velocities in the axial direction are neglected.**

The velocities in the axial direction at the leading and trailing edge of the blade set to zero. The effect of axial flow is incorporated in the volumetric flow rate balance later.

$$v_z \frac{\partial v_r}{\partial z} = 0 \quad (36)$$

All presented velocity triangles for  $v$  are now subject to the goniometric rules as presented in equation (37), (38) and (39).

$$u_i = \omega r_{t_i} \quad (37)$$

$$w_{r_i} = w_i \cdot \sin \beta_i \quad (38)$$

$$v_i^2 = u_i^2 + w_i^2 - 2u_i w_i \cos \beta_i \quad (39)$$

Where  $\beta_i$  is the blade (vane) angle of the supposed centrifugal pump [rad],  $w_i$  is the velocity of the fluid relative to the blade [m/s] and  $u_i$  is the azimuthal (tangential) velocity of the blade [m/s]. A comprehensive list of velocity triangle relationships is provided in appendix B.

From the shape of the linearized velocity triangle, which is valid for an infinitesimally small element, the angle  $\beta$  between the tangential and relative velocities is given in equation (40).

$$\left. \frac{dr}{rd\theta} \right|_{r\theta z} = \tan \beta \quad (40)$$

It is also known that this angle equals the ratio of radial and azimuthal velocities, hence the following relations hold

$$\begin{aligned} \frac{w_r}{w_\theta} &= \frac{v_r}{w_\theta} = \tan \beta \\ \Leftrightarrow \cot \beta &= \frac{w_\theta}{w_r} \end{aligned} \quad (41)$$

Equations (40) and (41) can be combined to find the angular change with respect to the radius along a streamline as shown in equation (42).

$$\left. \frac{d\theta}{dr} \right|_{r\theta z} = \frac{w_\theta}{rv_r} \quad (42)$$

We also know that the discharge that is delivered by a pump must be in accordance with equation (43).

$$w_r = \frac{Q}{f_y 2\pi r b} \quad (43)$$

Where  $f_\gamma$  is a factor that limits the outflow area of the centrifugal pump. With the assumption of axisymmetrical flow, the radial and azimuthal velocities are now a two-dimensional approximation of what was considered a three-dimensional physical domain.

#### *Linearization*

The pressure and the velocity in Equation (34) can be linearized as shown in section C.10.1. The pressure that results from these operations is given in equation (44).

$$-\frac{dp}{dr}\Big|_{r\theta z} = \rho \left[ -\omega^2 r + \frac{1}{2} \frac{dw^2}{dr} - gf_{g_r} \right] \quad (44)$$

It can be demonstrated that equation (44) can be rewritten and integrated to find equation (45) where indications for the leading edge and trailing edge are abbreviated to  $t$  and  $l$  respectively.

$$p_2 - p_1 = \rho \left[ \omega^2 \frac{r_{t,i}^2 - r_{l,i}^2}{2} + \frac{w_{l,i}^2 - w_{t,i}^2}{2} + gf_{g_r}(r_{t,i} - r_{l,i}) \right] \quad (45)$$

#### *Notation*

From here, the denotations  $\{\dots\}_1$  and  $\{\dots\}_2$  of the velocities  $\mathbf{w}$ ,  $\mathbf{u}$  and  $\mathbf{v}$  in equation (48) will be replaced by  $\{\dots\}_{l,i}$  and  $\{\dots\}_{t,i}$  to reflect their location at the leading and trailing edge of the blade respectively. See chapter 7 for further details.

#### 3.7.2 *Gravitational acceleration*

In equation (45) a gravity constant is introduced as  $f_{g_r} = \csc \beta \cos \lambda \sin(\beta + \theta) + \cot \alpha \sin \lambda$ , in which the cosecant is used ( $\csc \beta = \frac{1}{\sin \beta}$ ). A derivation of this formulation for the gravity is provided in appendix B, section C.7 by means of equation (199).

The effect of gravitational acceleration is especially important when cutting rock, however, it is neglected for the derivation of the affinity laws. Since gravity is the driving mechanism behind rapid redeposition, its effect is approximated in chapter 4. For Euler's pump equation derivation, the fluid is assumed *non-gravitational*.

#### 3.7.3 *Bernoulli's Principle for energy conservation*

Bernoulli's principle states that a fluid's potential head and pressure are inversely related to the fluid velocity. Incorporating this relationship is the next step in the derivation of Euler's pump equation. For Bernoulli's principle to hold, a steady flow along a streamline is assumed with negligible shear stress influence. This restriction is in accordance with earlier assumptions in the derivation of the NS equations.

Again, the density of the fluid is constant for the considered domain and the fluid is considered incompressible. Lastly, the flow is required to be irrotational with respect to the streamline. Bernoulli's principle is then found as presented in equation (46). A derivation of this equation is demonstrated in Appendix A.

$$\frac{h_{t,i} - h_{l,i}}{\substack{\text{elevation} \\ \text{head}}} - \frac{p_{t,i} - p_{l,i}}{\substack{\rho g \\ \text{pressure} \\ \text{head}}} = - \frac{v_{t,i}^2 - v_{l,i}^2}{\substack{2g \\ \text{velocity} \\ \text{head}}} \quad (46)$$

Combining equation (37), (38), (39), (45) and subsequent substitution in the formulation of Bernoulli's principle of equation (46) yields equation (47) for the elevation head generated by a centrifugal pump.

$$h_{t,i} - h_{l,i} = \omega^2 \frac{r_{t,i}^2 - r_{l,i}^2}{g} + \frac{r_{l,i} \omega w_{r_{l,i}} \cot \beta_{l,i} - r_{t,i} \omega w_{r_{t,i}} \cot \beta_{t,i}}{g} \quad (47)$$

More commonly, equation (47) is expressed in terms of pressure difference through  $\Delta p = \Delta h_i \rho_i g$ . This relationship can be substituted, and the equation can be rewritten. These operations give rise to what is commonly referred to as Euler's pump equation as displayed in equation (220). The pressure gain is a result of both static and kinematic contributions.

$$p_2 - p_1 = \underbrace{\rho \omega^2 (r_{t,i}^2 - r_{l,i}^2)}_{\text{static}} + \underbrace{\omega \rho \frac{Q}{f_y 2\pi b} (\cot \beta_{l,i} - \cot \beta_{t,i})}_{\text{kinematic}} \quad (48)$$

### 3.8 Conclusion

#### What formulations are fundamental to the motion and behaviour of a fluid substance in the physical domain of the cutter head?

Experimental and analytical research provides substantial evidence to confirm that cutter flow resembles a combination of an axial pump near the nose and a centrifugal pump effect near the ring (Miltenburg (1983); Den Burger (2003); Nieuwboer et al. (2017)). From the characteristic Reynolds and Euler numbers, it can be concluded that the inertial forces render viscosity in the cutter head negligible. For the centrifugal pump dynamics, the flow inside the cutter is considered steady, non-gravitational, inviscid and non-axial. It can be demonstrated that the Navier-Stokes equations therefore reduce to Euler's pump equation. The axial flow dynamics are governed by the product of the particle volume and radial pressure gradient in the suction mouth. Den Burger observed that there is an inward flow along the entire contour of the cutter head for rotational velocities below a certain ratio of the rotational to the mixture velocity. Above this ratio, the cutter dynamics give rise to a radial outflow that increases with rotational velocity.

Table 3.1 presents an overview of the assumptions that underpin the potential flow model.

**Table 3.1: Assumptions relevant to the physical parameters in the model.**

<i>Property</i>	<i>Definition</i>
Axisymmetrical	No change in velocity with respect to the azimuthal axis
Non-cavitation	No presence of voids causing cavitation
Continuous	No internal source terms
(Non-)gravitational	Gravity is neglected.
Incompressible	Conservation of energy
Inviscid	Viscosity effects are neglected (ideal fluid)
Irrotational	No net rotation with respect to the cylindrical coordinate system (follows from inviscid fluid)
(Non-)relativistic	Velocities are considered less than relativistic velocities
Steady (state)	No temporal change of magnitude or direction with time
Two-dimensional	No velocity components in the axial direction

## 4 Model setup

In chapter 1 it was decided that model should be analytical. From the spillage classification of chapter 2 it was concluded that the most prominent spillage types are centrifugal advection and rapid redeposition. Chapter 3 provides the relevant assertions that give rise to a spillage model. This chapter aims to answer the sub-question:

---

**In conjunction with the relevant physical parameters, what concepts and assumptions enable a CSD spillage engineering model?**

---

From this chapter forward, the model proposed in this research is referred to as the Sand-Rock Cutting Spillage Model (SRCSM). SRCSM is an analytical potential flow model with several empirical closing relations. All subsequent model steps are described in this chapter. First, the geometry of the cutter head is described.

---

### 4.1 Geometry

#### 4.1.1 Cutter head

#### 4.1.2 Bank

---

Next, it is explained how the volumetric flow rates that underlie a potential flow model can be obtained. An iterative solution method is provided in section 4.2.7.

---

### 4.2 Potential flow model

#### 4.2.1 Continuity

#### 4.2.2 Centrifugal advection

#### 4.2.3 Radial inflow at nose

#### 4.2.4 Axial inflow at nose

#### 4.2.5 Rapid redeposition

#### 4.2.6 Mixture flow

#### 4.2.7 In situ dredge flow

#### 4.2.8 Solving for continuity

---

In order to compute spillage rates, the concentrations of the respective flows are computed.

---

### 4.3 Spillage computation

#### 4.3.2 Average concentration

#### 4.3.2 Rapid redeposition concentration

#### 4.3.4 Spillage numbers

---

The chapter also provides an implementation template (section 4.4) to help set up the model. A reference implementation in Python is given in Appendix I. The model can be analyzed using a Python tool that is presented in Appendix K.

---

### 4.4 Implementation template

---

## 4.1 Geometry

First, a geometrical description of the cutter head should be obtained. Subsequently, the cutter head geometry can be placed into the bank. This section provides an advanced geometrical description. Alternatively, a more simple approximation for the geometry is provided in Appendix E.

### 4.1.1 Cutter head

A representative large cutter head is chosen for which the radii and blade angles are approximated with second-degree polynomials. Figure 4.1 (left) displays a series of plots for the trailing edge and leading edge radii of the envelope of the cutter head as well as the radius of the plate  $r_{plate}$  [m] and the drive shaft  $r_{shaft}$  [m]. Figure 4.1 (right) provides an estimate of representative trailing and leading edge blade angles  $\beta_{t,i}$  and  $\beta_{l,i}$  [deg]. It should be noted that this envelope does not include the reach of the cutter teeth or chisels, which typically increase the envelope size.

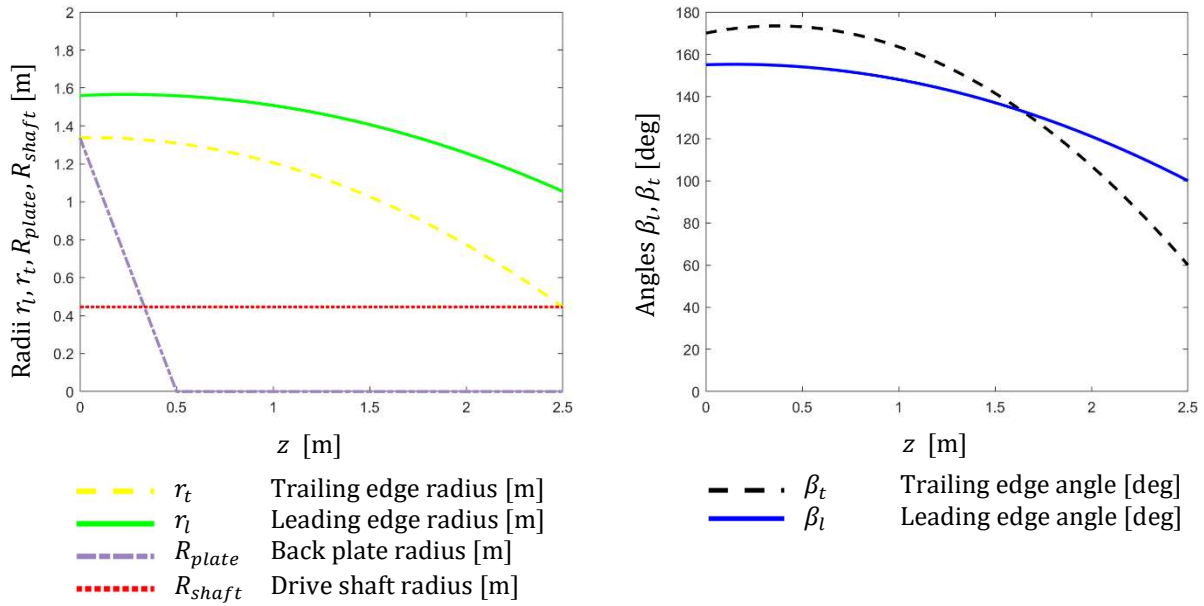


Figure 4.1: Typical geometry approximation of a relatively large cutter head.

An analytical description of the cutter head geometry is given in equation (49) and equation (302), (303) and (304) of Appendix G. These equations are for the trailing and leading edge radii as well as the trailing and leading edge blades angles respectively.

$$\begin{aligned}
r_t &= r_{t,z_0} + f_{rt_1} z^2 + f_{rt_2} z \\
f_{rt_2} &= -\frac{r_{t,z_0} - r_{t,z_b}}{b} - f_{rt_1} b \\
f_{rt_1} &= -0.1 \\
r_{t,z_0} &= \frac{D_{ring}}{2} \\
r_{t,z_b} &= \frac{D_{nose}}{2}
\end{aligned} \tag{49}$$

#### 4.1.2 Bank

The placement of the cutter in the bank is described according to the schematic representation of Figure 4.2. The origin of the axes in this figure is located at the intersection of the z-axis and the cutter ring.

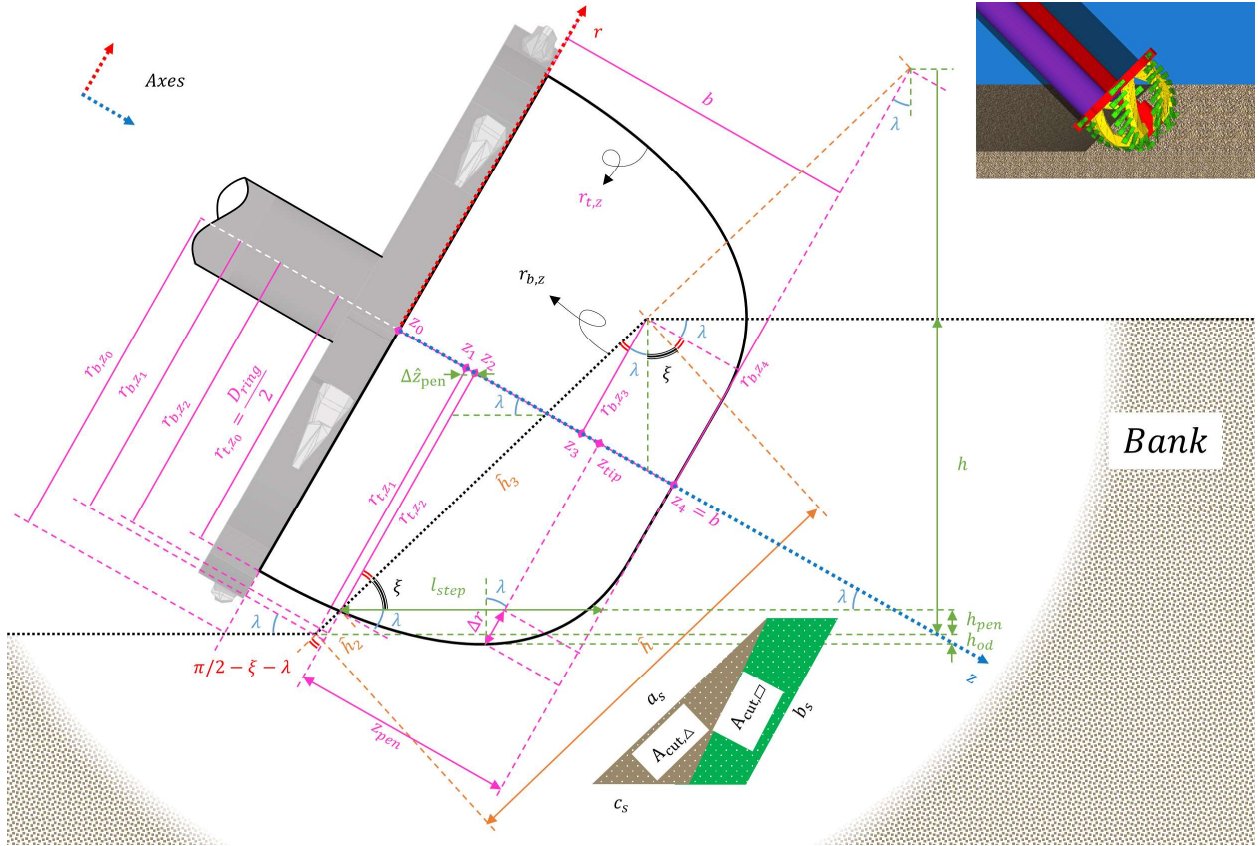


Figure 4.2: Advanced geometry description for cutter-bank interaction.

In the spillage type classification of chapter 2, it was concluded that spillage due to swing interactions is neglected in this model. With no redeposited particles from a previous swing, hence no spillage height  $h_{od}$  [m], the following formulation can be made

$$h_{pen} = h_{pen} + h_{od} \tag{50}$$

For the interaction of the cutter head with the bank, the cutter inclination angle  $\lambda$  [rad] and slope angle  $\xi$  [rad] should be chosen. The location of the tip of the cutter (TOC),  $z_{tip}$  [m], is found by taking the derivative of the lower trailing edge radius

equal to the inclination of the cutter. The derivative of the trailing edge radius and the inclination angle is given as:

$$\begin{aligned}\frac{d}{dz}(-r_t) &= \frac{d}{dz} - (r_{t,z_0} + f_{r_{t_1}} z^2 + f_{r_{t_2}} z) \\ \frac{d}{dz}(-r_t) &= -2f_{r_{t_1}} z - f_{r_{t_2}}\end{aligned}\quad (51)$$

Setting the latter part of equation (51) equal to  $\tan \lambda$  yields the desired location of TOC in the reference frame of the cutter head.

$$z_{tip} = \begin{cases} -\frac{1}{2} \frac{\tan \lambda + f_{r_{t_2}}}{f_{r_{t_1}}}, & z_{tip} \leq b \\ b, & b < z_{tip} \end{cases}\quad (52)$$

This formulation is subject to the condition that  $z_{tip}$  is limited to the height  $b$ , hence the conditional format. Next, a parameter is introduced for the penetration depth  $z_{pen}$  [m] that is linearly related with the chosen step size  $l_{step}$  [m].

$$z_{pen} = l_{step} \cos \lambda \quad (53)$$

With the penetration depth known, the cutter-bank characteristics from equation (54) can be computed consecutively.

$$\begin{aligned}z_2 &= b - z_{pen} \\ r_{t,z_2} &= r_t|_{z_2} \\ r_{t,z_{pen}} &= r_t|_{z_{pen}} \\ r_{t,z_{tip}} &= r_t|_{z_{tip}} \\ \Delta r &= \left| -r_{t,z_{pen}} - (-r_{t,z_2} + (z_{tip} - z_2) \tan \lambda) \right| \\ h_{pen} &= \Delta r \cos \lambda \\ z_1 &= z_2 - \Delta r \tan \left( \frac{\pi}{2} - \xi - \lambda \right) \\ r_{b,z_2} &= -r_{t,z_2} \\ r_{b,z_1} &= r_{t,z_2} - \Delta r \\ r_{b,z_0} &= r_{b,z_1} - z_1 \sin \lambda \\ \hat{h} &= \frac{h}{\sin \xi} \\ \hat{h}_2 &= \frac{h_{pen}}{\sin \xi} \\ \hat{h}_3 &= \hat{h} - \hat{h}_2 \\ z_3 &= \begin{cases} b, & z_3 \leq b \\ \hat{h}_3 \sin \left( \frac{\pi}{2} - \xi - \lambda \right) + z_2, & b < z_3 \end{cases} \\ r_{b,z_3} &= -r_{t,z_2} + \sqrt{\hat{h}_3^2 + (z_3 - z_2)^2} \\ z_4 &= b \\ r_{b,z_4} &= r_{b,z_3} + (z_4 - z_3) \tan \lambda \\ \Delta \hat{z}_{pen} &= \frac{z_2 - z_1}{\cos \lambda}\end{aligned}\quad (54)$$

A conditional function can be found for the computation of the bank height in the reference frame of the cutter.

$$r_{b,z} = \begin{cases} r_{b,z_0} + z \tan \lambda, & z < z_1 \\ r_{b,z_2} + (z - z_2) \tan(\lambda + \xi), & z_1 \leq z < z_3 \\ r_{b,z_3} + (z - z_3) \tan \lambda, & z_3 \leq z \end{cases} \quad (55)$$

#### Cut area

Basis geometrical rules now prescribe a series of operations that enable the computation of the total cut area  $A_{cut}$  [m<sup>2</sup>]. Figure 4.2 provides an overview of the calculated surfaces. It should be noted that spillage due to cutter geometry was neglected. Equation (56) provides a basis for the development of a spillage computation for this type.

$$\begin{aligned} a_s &= \hat{h} \\ b_s &= \frac{h}{\cos\left(\frac{\pi}{2} - \lambda\right)} \\ c_s &= \frac{z_3 - z_1}{\cos \lambda} \\ s &= \frac{a_s + b_s + c_s}{2} \end{aligned} \quad (56)$$

$$A_{cut,\Delta} = \begin{cases} 0, & c_s = 0 \\ \sqrt{s(s-a)(s-b)(s-c)}, & 0 < c_s \end{cases}$$

$$A_{cut,\square} = h \frac{z_4 - z_3}{\cos \lambda}$$

$$A_{cut} = A_{cut,\Delta} + A_{cut,\square}$$

A relevant parameter for the cutter-bank interaction is the bank contact angle  $\gamma_z$  [rad]. Figure 4.3 (left) depicts the relevance of this variable for a small and large bank height  $r_{b,z}$  [m]. This angle can be found using the goniometrical relationships of a circle with chord  $k_z$  as shown in equation equations (57). The length of the chord can also be computed with the Pythagorean theorem as presented in equation (58). The angle  $\frac{\gamma}{2}$  can also be found as

$$k_z = 2r_{t,z} \sin \frac{\gamma_z}{2} \quad (57)$$

$$k_z = \sqrt{x_z^2 + \Delta r_{b,z}^2} \quad (58)$$

$$\tan \frac{\gamma}{2} = \frac{\Delta r_{b,z}}{x_z} \quad (59)$$

Where  $x_z$  is the horizontal component of  $r_{t,z}$  [m] (in the reference frame of section cut) and  $\Delta r_{b,z}$  is the absolute height of the bank at location  $z$  [m]. The absolute length depends on whether the bank contact angle exceeds  $\pi/2$ , which can be formulated as:

$$\Delta r_{b,z} = \begin{cases} r_{t,z} - |r_{b,z}|, & r_{b,z} \leq 0 \\ r_{t,z} + r_{b,z}, & 0 < r_{b,z} \end{cases} \quad (60)$$

Equations (57), (58), (59) and (60) can now be combined according to the steps given in equation (61).

$$\begin{aligned}
x_z^2 + \Delta r_b^2 &= \left(2r_{t,z} \sin \frac{\gamma_z}{2}\right)^2 \\
x_z^2 + \Delta r_b^2 &= \left(2r_{t,z} \sin \left(\tan^{-1} \left(\frac{\Delta r_b}{x_z}\right)\right)\right)^2 \\
x_z^2 + \Delta r_b^2 &= \left(2r_{t,z} \frac{\frac{\Delta r_b}{x_z}}{\sqrt{\left(\frac{\Delta r_b}{x_z}\right)^2 + 1}}\right)^2 \\
x_z^2 + \Delta r_b^2 &= 4r_{t,z}^2 \frac{\left(\frac{\Delta r_b}{x_z}\right)^2}{\left(\frac{\Delta r_b}{x_z}\right)^2 + 1} \tag{61} \\
\left(\left(\frac{\Delta r_b}{x_z}\right)^2 + 1\right)(x_z^2 + \Delta r_b^2) &= 4r_{t,z}^2 \left(\frac{\Delta r_b}{x_z}\right)^2 \\
\frac{\Delta r_b^2}{x_z^2}(x_z^2 + \Delta r_b^2) + (x_z^2 + \Delta r_b^2) &= 4r_{t,z}^2 \frac{\Delta r_b^2}{x_z^2} \\
(x_z^2)^2 + 2\Delta r_b^2 x_z^2 + (\Delta r_b^2)^2 - 4r_{t,z}^2 \Delta r_b^2 &= 0 \\
x_z^2 &= \frac{-2\Delta r_b^2 \pm \sqrt{2\Delta r_b^2 - 4(-4r_{t,z}^2 \Delta r_b^2)}}{2} \\
x_z^2 &= -\Delta r_b^2 \pm \sqrt{\frac{1}{2}\Delta r_b^2 + 4r_{t,z}^2 \Delta r_b^2}
\end{aligned}$$

The value of the horizontal length is easily found as the positive result from the quadratic method. Subsequently, the bank contact angle is found according to equation (62). The bank contact angle can be transformed to a dimensionless coefficient named the outflow factor which is given in equation (63).

$$\tan \frac{\gamma_z}{2} = \frac{\Delta r_{b,z}}{x_z} \Leftrightarrow \gamma_z = 2 \tan^{-1} \frac{\Delta r_{b,z}}{x_z} \tag{62}$$

$$f_{\gamma_z} = 1 - \frac{\gamma_z}{2\pi} \tag{63}$$

It is assumed that the shaft radius  $r_{shaft}$  and the back plate radius  $r_{plate}$  in Figure 4.2 negligible.



With varying heights for  $b_1$  and  $b_2$  [m] it is beneficial to make use of specific flow instead of volumetric flow, hence equation (65) can be rewritten to:

$$\rho_2 Q_{a_{nose}} + \rho_c Q_c + \rho_2 q_{r_2} b_2 - \rho_1 q_{r_1} b_1 - \rho_1 Q_d - \rho_1 Q_{a_m} = 0 \quad (66)$$

Where  $Q_{a_{nose}}$  is an axial flow rate (assumed positive) through the cutter nose [m<sup>3</sup>/s],  $Q_c$  the incoming volumetric flow rate of dislodged bank material [m<sup>3</sup>/s],  $q_{r_2}$  the specific radial flow rate of water entering the cutter (assumed positive) through the peripheral boundary of disc 2 [m<sup>2</sup>/s],  $q_{r_1}$  the specific radial flow rate of material leaving the cutter through the peripheral boundary of disc 1 (assumed negative) [m<sup>2</sup>/s],  $Q_d$  the rapid redeposition flow rate [m<sup>3</sup>/s] and  $Q_{a_m}$  the axial mixture flow rate through the suction pipe [m<sup>3</sup>/s]. The inclusion of an axial flow rate through the nose is hypothetical and may be discarded in a later stage.

Suppose that the density of fluid in disc 1  $\rho_m$  is uniform for any outflow term and that sediment concentration around the cutter is negligible, i.e. the incoming flow density is equal to the density of water. The bulk density at the bank is an input parameter to the model and is computed using the estimated or known concentration of the material. Equations (67)-(71) summarize the abovementioned assumptions.

$$\rho_c = \rho_q c_c + \rho_w (1 - c_c) \quad (67)$$

$$\rho_a = \rho_w \quad (68)$$

$$\rho_2 = \rho_w \quad (69)$$

$$\rho_1 = \rho_m \quad (70)$$

$$\rho_m = c_{vs} (\rho_q - \rho_w) + \rho_w \quad (71)$$

Where  $c_c$  is the spatial concentration of solids in the bank [-],  $c_{vs}$  is the spatial concentration of solids in the cutter [-],  $\rho_q$  is the particle quartz density [kg/m<sup>3</sup>],  $\rho_w$  the density (= 1025) of water [kg/m<sup>3</sup>] and  $\rho_m$  the density inside disc 1 and 2 [kg/m<sup>3</sup>].

#### *Volumetric flow rate balance*

The volumetric flow rate balance also holds for the cutter head. Substitution of equation (72) in the mass flow rate balance of particles yields an expression for the spatial concentration  $c_{vs}$  [-] of disc 1 and disc 2 as shown in equation (73).

$$Q_{a_{nose}} + Q_c + Q_{r_2} - Q_{r_1} - Q_d - Q_{a_m} = 0 \quad (72)$$

$$c_{vs} = \frac{c_c Q_c}{Q_{r_1} + Q_d + Q_{a_m}} \quad (73)$$

Substitution of equation (73) in equation (71) yields for the internal density of fluids in the cutter:

$$\rho_m = c_{vs}(\rho_q - \rho_w) + \rho_w = \left( \frac{c_c Q_c}{Q_{r1} + Q_d + Q_{am}} (\rho_q - \rho_w) + \rho_w \right) \quad (74)$$

Figure 4.4 provides a 3D overview of the components of the volumetric flow rate balance. This section continues with the establishment of the volumetric flow rates outlined in the flow rate balances.

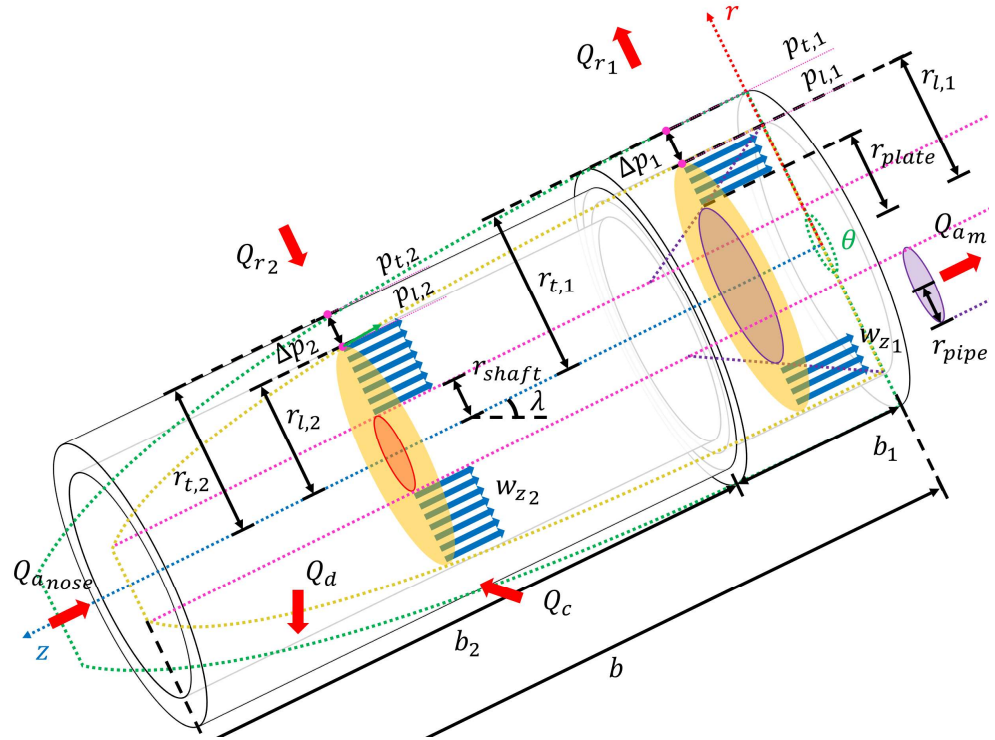


Figure 4.4: Schematic 3D view of the cutter head division in disc 1 and 2 with relevant parameters.

#### 4.2.2 Centrifugal advection

Centrifugal advection occurs near the back ring and is therefore designed to occur in disc 1. Based on the findings in chapter 3.1, centrifugal advection is predominantly a function of the mixture velocity and the rotational velocity.

$$Q_{r1} = f(v_m, \omega)$$

This section will proceed to find an expression for the flow induced by the rotational velocity of the cutter. Influence of the mixture velocity will be incorporated in through the mixture flow rate in the continuity equation. Section 3.7 provides a derivation of Euler's pump equation. The applicability of this equation for centrifugal advection flow is evaluated for the cutter. Euler's pump equation, as derived from equation (48), reads

$$p_2 - p_1 = \underbrace{\rho \omega^2 (r_2^2 - r_1^2)}_{\text{static}} + \underbrace{\omega \rho \frac{Q}{f_y 2\pi b} (\cot \beta_1 - \cot \beta_2)}_{\text{kinematic}} \quad (75)$$

The geometry of the cutter head dictates that the implied impeller vanes are forward bladed and that the 2-dimensional velocity triangles that underpin Euler's pump equation can be found as shown in Figure 4.5.

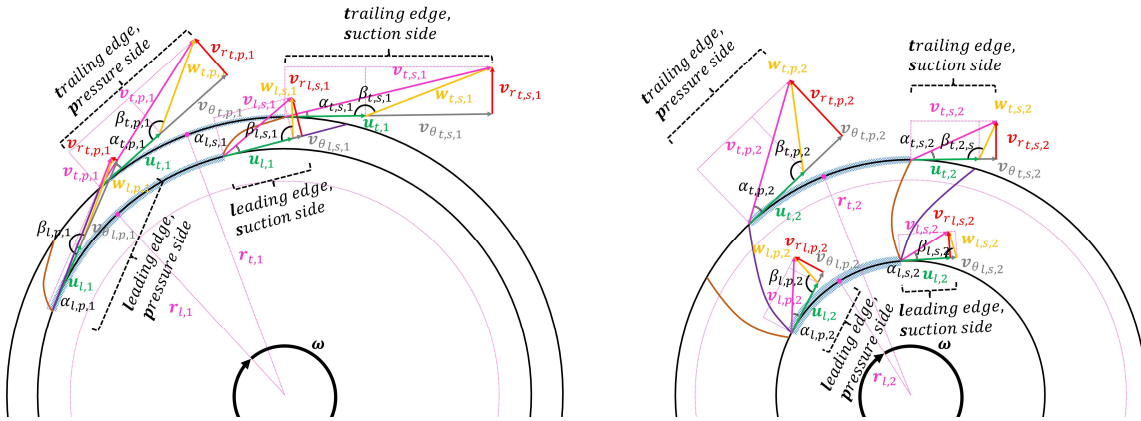


**Figure 4.5: Approximated 2-dimensional velocity triangles at the blades for disc 1 (left) and disc 2 (right).**

The pressure side of the blade is colored in purple and the suction side is colored in brown.

For a 6-bladed cutter head, a small fluid volume (highlighted in blue) has widths ranging between  $\frac{\pi}{3}r_{l,i}$  and  $\frac{\pi}{3}r_{t,i}$ . The velocity triangles are slightly different between the pressure (s) and suction (p) side of the blades. An approximation of a typical cutter head suggests that the blade thickness in the cross-sectional plane is small near the back ring and relatively large near the nose.

Application of Euler's pump equation to the cutter is subject to certain assumptions. First, the impeller passages are filled with the flowing fluid at all time (no void spaces and *non-cavitating* conditions).

Second, an infinite number of blades is assumed. Therefore, it is reasoned that the outflow velocity profile is linear between blades (aligns with the irrotational property during the derivation). The velocities, as well as blade angles, can be found by computing the average of the suction and pressure side of the blades, i.e.  $v_{r_{t,i}} = (v_{r_{t,p,i}} + v_{r_{t,s,i}})/2$ .

Third, work transfer of the blades is considered frictionless (aligns with the assumption of an inviscid fluid). Also, flow between two adjacent streams does not disturb each other.

#### *Establishing the affinity law for pressure*

The use of Euler's pump equation would introduce the unknowns  $p_{t,i}$  and  $p_{l,i}$  into the model. Analogous to the affinity that are used for centrifugal pumps, an important assumption is made.

**The affinity law for pressure for centrifugal advection can be obtained by assuming that the inner radius in Euler's pump equation is equal to zero.**

Consequently, there cannot be a radial velocity at the origin of the cylindrical coordinate system. Euler's pump equation then simplifies to equation (76) when the dimensionless head of the considered disc,  $\Psi_i$ , is taken in accordance with equation (77).

$$\Delta p_i = \Psi_i \rho_i \omega^2 r_{t,i}^2 \quad (76)$$

$$\Psi_i = 1 - \frac{w_{r,i}}{\omega r_i} \cot \beta_i \quad (77)$$

Where  $\Delta p_i$  is the pressure difference for the considered streamline, or  $p_{t,i} - p_{l,i}$ , for the pressures at the trailing and leading radii of the cutter head. The derivation of equation (76) and the value for  $\Psi$  is given in Appendix C, section C.12.

#### *Establishing the affinity law for discharge*

Let us consider flow similitude for both discs, i.e. the ratio of the average fluid velocity  $v_r$  [m/s] and the tangential impeller velocity  $u$  [m/s] equals a constant dimensionless flow number

$$\frac{v_r}{u} = \Phi \quad (78)$$

Where  $\Phi$  is known as the pump flow number [-]. The average fluid velocity exits the cutter over an area equal to the circumference of the cutter, multiplied by the disc height and limited by the outflow factor  $f_\gamma$  [-] that accounts for limitations to the outflow area, i.e.  $f_\gamma 2\pi r b$ . The outflow factor is introduced in equation (63). Again, assuming incompressible flow and flow equilibrium, the fluid velocity inside the cutter follows from volume continuity and reads

$$v_r = \frac{Q_r}{f_\gamma 2\pi r b} \quad (79)$$

Where  $Q_r$  is the disc discharge [m<sup>3</sup>/s],  $r$  is the cutter radius [m] and  $b$  the blade width [m]. The tangential velocity of the blade is found through multiplication of the angular velocity  $\omega$  [rad/s] and the cutter radius [m] ( $u = \omega r$ ). Substitution of the velocity ratio in equation (79) and subsequent reordering yields an expression for the discharge as a function of the angular velocity as evidenced in equation (227).

$$Q_r = \Phi f_\gamma 2\pi b \omega r^2 = \widehat{\Phi} f_\gamma b \omega r^2 \quad (80)$$

Physically, the coefficient  $\widehat{\Phi}$  can be considered a dimensionless ratio of the velocity components in the radial direction and the tangential (azimuthal) direction. The effect of fluid viscosity is captured by this dimensionless measure. Equation (80) can be referred to as the affinity law for cutter discharge. In terms of specific flow, the affinity law at location  $i$  is found through  $q_{r,i} = Q_{r,i}/b_i$ .

$$q_r = \Phi f_\gamma 2\pi b \omega r^2 = \widehat{\Phi} f_\gamma \omega r^2 \quad (81)$$

The affinity laws for pressure (76) and discharge (81) can be combined to compute a second expression for the pressure-generating specific outflow  $q_{r_i}$  [ $\text{m}^2/\text{s}$ ] using a pump flow number  $\Phi_i$ , [-] and dimensionless head  $\Psi_i$  [-].

$$q_{r_i} = \frac{\Phi_i}{\Psi_i} 2\pi \frac{1}{\omega \rho_i} f_{\gamma_i} \Delta p_i \quad (82)$$

Where  $\rho_i$  is the density [ $\text{kg}/\text{m}^3$ ],  $\omega$  the angular velocity of the cutter head [ $\text{rad}/\text{s}$ ] and  $r_{t,i}$  the representative outer radius [m] (trailing edge of the blades) at axial location  $z = i$ . Expressed as a volumetric flow rate, the centrifugal flow at disc 1 is found in two ways. The first equation is based on equation (80) and is used to compute  $Q_{r_1}$ . The second equation is based on equation (82) and is used in the computation of the radial inflow at the nose.

$$\begin{aligned} Q_{r_1} &= \hat{\Phi} f_{\gamma_1} b_1 \omega r_{t,1}^2 \\ Q_{r_1} &= \frac{\Phi_1}{\Psi_1} 2\pi b_1 \frac{1}{\omega \rho_1} f_{\gamma_1} \Delta p_1 \end{aligned} \quad (83)$$

#### 4.2.3 Radial inflow at nose

Miedema (2017) and Nieuwboer (2018) conceptualized that any flow leaving the cutter head near the back ring may return near the nose. This implied that the flow pattern exhibits a (partial) return flow of some magnitude.

The pressure along the outside contour of the cutter head is initially assumed to be equal to the ambient pressure. The pressure inside the cutter is driven by the centrifugal force. Since this force is proportional to the distance to the rotational axis, the centrifugal force is larger at the blades near the ring of the cutter than at the blades near the nose. From the trailing edge onwards, the pressure is expected to drop with the distance to the cutter squared. Figure 4.6 (left) depicts the expected pressure drops from the contours of disc 1 and 2 independently. Miedema and Nieuwboer hypothesized that the flow from disc 1 may return in full or partially at disc 2. Since the pump affinity law is used to compute the pressure gradient inside the cutter, the leading edge pressures in each disc are equal to zero.

**The assumption is made that the true pressure at the trailing edge of the cutter is equal to the pressure that is generated in disc 1. As a consequence, the difference in estimated pressure gradients between the discs drives an inflow at disc 2.**

Figure 4.6 (right) depicts this assumption. The inflow at the disc is found as

$$\Delta p_{discs_2} = \Delta p_1 - \Delta \hat{p}_2 \quad (84)$$

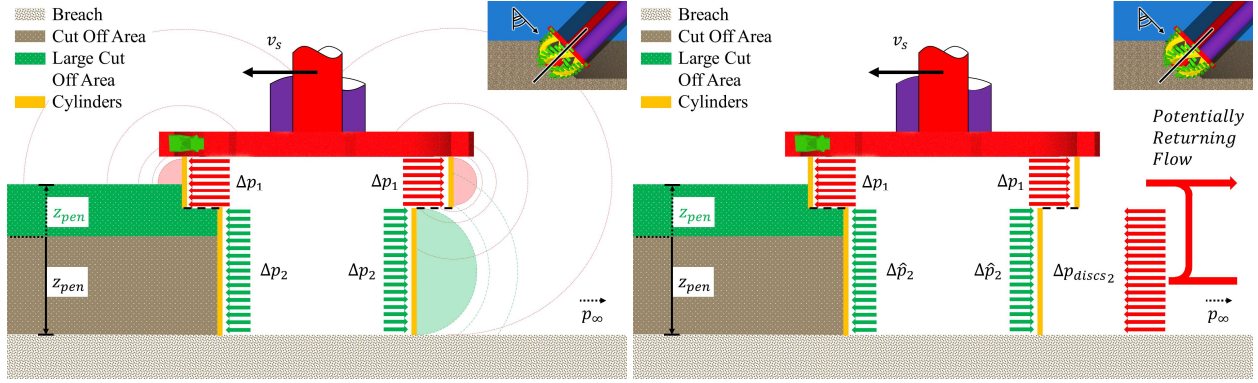


Figure 4.6: Pressure expectations (left) and assumptions (right) from the cutter head.

The magnitude of the specific flow rate of radial inflow at the nose can be computed as follows. First, the affinity laws for centrifugal pumps are used to calculate the pressure-generating outflow  $q_{r_1}$  and to estimate  $\hat{q}_{r_2}$ . Please note the hat notation for *estimate*. Equation (82) is used to provide the estimate.

$$\hat{q}_{r_2} = \frac{\Phi_2}{\Psi_2} 2\pi \frac{1}{\omega \rho_2} f_{\gamma_2} \Delta \hat{p}_2 \quad (85)$$

The *actual* value of the specific radial outflow  $q_{r_2}$  [m<sup>2</sup>/s] is obtained by combining equation (82) in equation (84). Subsequently, the estimated pressure difference that drives outflow is substituted from equation (85) and rewritten to obtain

$$\begin{aligned} q_{r_2} &= \frac{\Phi_2}{\Psi_2} 2\pi \frac{1}{\omega \rho_w} f_{\gamma_2} \Delta p_{discs_2} \\ &= \frac{\Phi_2}{\Psi_2} 2\pi \frac{1}{\omega \rho_w} f_{\gamma_2} (\Delta p_1 - \Delta \hat{p}_2) \\ &= \frac{\Phi_2}{\Psi_2} 2\pi \frac{1}{\omega \rho_w} f_{\gamma_2} \left( \frac{\Psi_1}{\Phi_1} \frac{1}{2\pi f_{\gamma_1}} \omega \rho_m q_{r_1} - \frac{\Psi_2}{\Phi_2} \frac{1}{2\pi f_{\gamma_2}} \omega \rho_m \hat{q}_{r_2} \right) \\ &= \frac{\Psi_1 \rho_m \Phi_2 f_{\gamma_2}}{\Psi_2 \rho_w \Phi_1 f_{\gamma_1}} q_{r_1} - \hat{q}_{r_2} \end{aligned} \quad (86)$$

Appendix F.1 provides a full derivation of this assertion. The mixture density  $\rho_m$  can now be substituted from equation (74). Also, the affinity law for cutter discharge from equation (81) can be used to compute  $q_{r_1}$  and  $\hat{q}_{r_2}$ . This results in a new expression for the specific inflow rate at disc 2.

$$q_{r_2} = 2\pi\omega \left[ \frac{\Psi_1 \Phi_2}{\Psi_2 \Phi_1} \left( \frac{c_c Q_c}{\hat{\Phi}_1 2\pi\omega r_{t,1}^2 f_{\gamma_1} b_1 + Q_d + Q_{am}} \left( \frac{\rho_q}{\rho_w} - 1 \right) + 1 \right) f_{\gamma_2} \Phi_1 r_{t,1}^2 - \Phi_2 r_{t,2}^2 f_{\gamma_2} \right] \quad (87)$$

**The pump flow number and dimensionless head are assumed equal for disc 1 and 2.**

In equation (87) the variables  $\Phi_1 = \Phi_2$  cancel out the influence of the flow number. The physical interpretation of this cancellation is that the velocity components in the radial direction and the tangential (azimuthal) direction are equal. This is a heavy simplification of reality since the discs are divided based on their typical flow

direction (axial versus centrifugal). However, it can be reasoned that the respective changes in pump flow number scale similarly for both discs. The actual ratio of these numbers can therefore be captured by a dimensionless scaling coefficient that is added later.

The value of dimensionless head  $\Psi_1, \Psi_2$  was found in equation (77). The assumption that the dimensionless head is equal for both discs implies that the ratio of the blade angles is constant.

$$\Psi_i = 1 - \frac{w_{r_i}}{\omega r_i} \cot \beta_i \quad (88)$$

The radial inflow at the nose is now obtained by multiplication of equation (87) by the disc height  $b_2$  as shown in equation (89). Section F.1 provides a full derivation of the volumetric flow rate for radial flow at the nose.

$$Q_{r_2} = 2\pi\omega \left( \frac{f_{\gamma_2} c_c Q_c}{2\pi\omega f_{\gamma_1} b_1 + \frac{Q_d}{\Phi_1 r_{t,1}^2} + \frac{Q_{a_m}}{\Phi_1 r_{t,1}^2}} \left( \frac{\rho_q}{\rho_w} - 1 \right) + f_{\gamma_2} \Phi_1 r_{t,1}^2 - \Phi_2 r_{t,2}^2 f_{\gamma_2} \right) b_2 \quad (89)$$

#### *Influence of density difference between in- and outflow*

The pressure outside disc 1 is generated by an outflow containing suspended sediment. In contrast, the inflow at disc 2 consists of water only. The affinity laws from equation (85) therefore dictate that the reduction in density is counteracted by an increase in specific flow rate. However, the latter term of equation (86) shows that the actual radial inflow increases with increasing cutter density  $\rho_m$ . This actual inflow reduces the density inside the cutter. Therefore it is expected that the addition of density differences does not significantly change the behavior of the model.

#### 4.2.4 *Axial inflow at nose*

Section 3.1 highlights substantial evidence that suggests that an axial flow is present in disc 2. The axial flow may partially originate through the nose. An axial flow  $Q_{a_{nose}}$  [m<sup>3</sup>/s] is introduced to simulate the axial pump effect. Den Burger (2003) argues that, in a freely spinning cutter, axial flow is generated by the curvature of the blades near the hub which suck in water through the nose. Also, a large under pressure caused by the suction flow will most likely dominate axial flow.

To study the effect of the axial flow through the cutter, the flow rate is initially estimated as half of the axial mixture flow rate near the back ring, i.e.

$$Q_{a_{nose}} = \frac{Q_{a_m}}{2} \quad (90)$$

Upon placement of the cutter in the bank, the nose is fully covered. This implies that only a limited flow rate is entrained through the nose. It is hypothesized that this flow can be therefore be neglected at a later stage.

#### 4.2.5 Rapid redeposition

Rapid redeposition flow is a function of the following variables

$$Q_d = f(v_{ts}, v_m, \omega, \lambda, f_{d_{type}}, z_{pen}, h)$$

Where  $v_{ts}$  is the particle terminal settling velocity [m/s],  $f_{d_{type}}$  is a cutting scenario factor [-] that indicates whether the cutter is in under-cut mode ( $f_{d_{type}} = -1$ ) or over-cut mode ( $f_{d_{type}} = 1$ ).

**A reference point in the cutter is chosen that is assumed to best represent the dynamics relevant to rapid redeposition.**

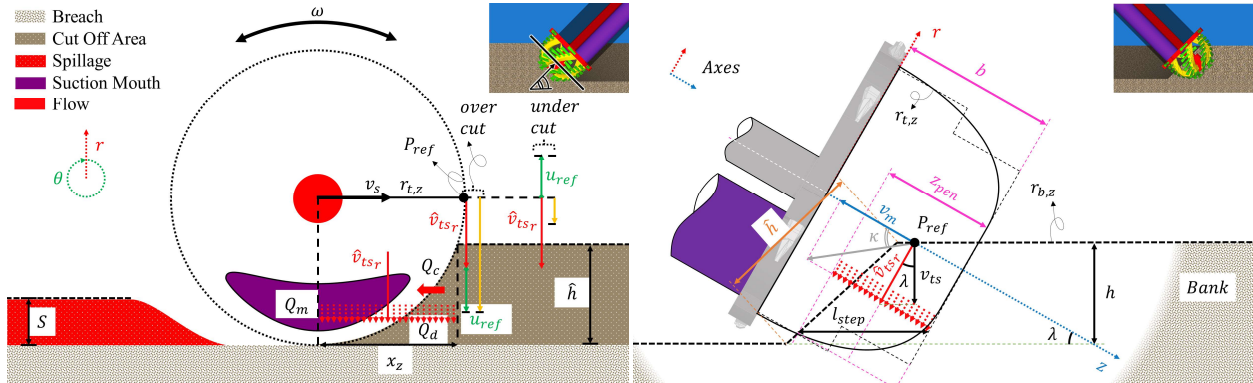


Figure 4.7: Reference point for rapid redeposition from frontal (left) and lateral perspective (right).

The reference point is taken on the axial location at  $z = b - z_{pen}/2$ . This is an approximation of the axial location of the centroid of the bank surface  $A_{cut}$ . On the azimuthal axis, the location  $\theta = \pi/2$  is chosen. This is the location of the front of the cutter, hence this location is in contact with the bank. On the radial axis, the trailing edge  $r = r_t$  is chosen since this radius is best representative of the magnitude of the rotational velocity.

#### Notation

From this point onwards, the approximate location (hence the hat notation) of rapid redeposition reference point is denoted as

$$\hat{v}_{\{\dots\}_t, \frac{\pi}{2}, b - \frac{z_{pen}}{2}} = \hat{v}_{\{\dots\}_{ref}} \quad (91)$$

In accordance with Figure 4.7 (left and right), the following formulations are found that *approximate* (hence the hat notation) the relevant velocities at the bank reference point.

$$\hat{v}_{\theta_{ref}} = \hat{v}_{ts_r} + f_{d_{type}} f_d u_{ref} \quad (92)$$

Where  $\hat{v}_{ts_r}$  is the representative radial component of the terminal settling velocity and  $f_d$  is a dimensionless rapid redeposition factor [-]. It should be observed that the tangential velocity at the reference point may be positive or negative, depending on the cutting scenario. In an under-cut scenario  $f_{d_{type}} = -1$ , resulting

in a negative value for  $\hat{v}_{\theta_{ref}}$ . To prevent negative values for rapid redeposition, a limitation is set such that the tangential velocity will always remain positive ( $\hat{v}_{\theta_{ref}} > 0$ ). The value of  $\hat{v}_{tsr}$  is determined such that an increase in the cutter inclination angle increases the radial component of the settling velocity as shown in equation (93). The radius that gives the tangential velocity  $u_{ref}$  is chosen as  $r_{t,2}$  since rapid redeposition effects will be governing in disc 2.

$$\hat{v}_{tsr} = \frac{v_{ts}}{\cos \lambda} \quad (93)$$

$$u_{ref} = \omega r_{t,ref} = \omega r_{t,2} \quad (94)$$

The tangential velocity from equation (92) is be used to determine the velocity of the rapid redeposition flow. To determine the outflow area for rapid redeposition, the horizontal length  $x_2$  is used that was introduced in equation (61). The disc height  $b_2$  is the second metric that enables the computation of a surface plan orthogonal to the radial component of the settling velocity.

$$A_d = x_2 b_2 \quad (95)$$

#### *Velocity ratio*

The governing forces for rapid redeposition are the suction force and gravitational force. A characteristic velocity ratio can be established that represents the dynamics between these forces in the form

$$\hat{v}_{ratio} = \frac{v_m}{\hat{v}_{tsr}} \quad (96)$$

The axial component of the terminal settling velocity is considered negligible since this component is generally much smaller than the mixture velocity. The square of the velocity ratio can be taken as a representation of the dynamics introduced by the suction and gravitational force. The volumetric flow rate for rapid redeposition is established by taking an estimate of redepositing material and subsequent scaling with the velocity ratio squared. The result is multiplied by a dimensionless factor that incorporates the height of the bank and the distance of the bank to the suction mouth. The result is given in equation (97).

$$Q_d = \hat{v}_{\theta_{ref}} A_d \left( \frac{v_m}{\hat{v}_{tsr}} \right)^2 \frac{b - \frac{z_{pen}}{2}}{h} \quad (97)$$

#### 4.2.6 *Mixture flow*

The mixture flow rate is trivially found through multiplication of the suction pipe area and the mixture velocity

$$Q_{a_m} = \pi R_{pipe}^2 v_m \quad (98)$$

Where  $R_{pipe}$  is the radius of the suction pipe [m],  $v_m$  the mixture velocity measured in the suction pipe [m/s].

#### 4.2.7 *In situ dredge flow*

Equation (99) demonstrates a straight forward method to calculate the flow that enters the cutter head.

$$Q_c = A_{cut} v_s \quad (99)$$

Where  $A_{cut}$  the projected bank surface from equation (56) and  $v_s$  the swing speed of the cutter [m/s].

#### *Neglected flow terms*

In reality, the lateral movement of the cutter head implies a flow of water from the front to the back of the cutter. It is assumed that these flows cancel out and do not contribute significantly to the mass balance.

#### 4.2.8 *Solving continuity of volume*

The volumetric flow rate balance of equation (72) can be substituted with the volumetric flow rates found in equations (83), (89), (90), (97), (98) and (99) which are repeated for clarity.

$$\begin{aligned} Q_{r_1} &= \hat{\Phi} f_{\gamma_1} b_1 \omega r^2 \\ Q_{r_2} &= 2\pi\omega \left( \frac{f_{\gamma_2} c_c Q_c}{2\pi\omega f_{\gamma_1} b_1 + \frac{Q_d}{\Phi_1 r_{t,1}^2} + \frac{Q_{a_m}}{\Phi_1 r_{t,1}^2}} \left( \frac{\rho_q}{\rho_w} - 1 \right) + f_{\gamma_2} \Phi_1 r_{t,1}^2 - \Phi_2 r_{t,2}^2 f_{\gamma_2} \right) b_2 \\ Q_{a_{nose}} &= \frac{\pi}{2} R_{pipe}^2 v_m \\ Q_d &= \hat{v}_{\theta_{ref}} x_2 b_2 \left( \frac{v_m}{\hat{v}_{tsr}} \right)^2 b - \frac{z_{pen}}{2} \\ Q_{a_m} &= \pi R_{pipe}^2 v_m \\ Q_c &= A_{cut} v_s \end{aligned} \quad (100)$$

Substitution of the volumetric flow rates in the continuity equation results in a laborious equation. The equation can be reorganized to express the cutter height  $b_1$  in the form of a quadratic polynomial as shown in equation (101). A full derivation of equation (101) is provided in section Appendix F.3. The height of disc 1 cannot drop below zero hence a condition is set for  $b_1 \geq 0$  in the model.

$$\begin{aligned} &\Phi 2\pi\omega \left[ (f_{\gamma_2} f_{\gamma_1} + f_{\gamma_1}^2) r_{t,1}^2 - f_{\gamma_2} f_{\gamma_1} r_{t,2}^2 \right] b_1^2 \\ &- 2\pi\omega f_{\gamma_1} \left[ \Phi f_{\gamma_2} (r_{t,1}^2 - r_{t,2}^2) b + (Q_{a_{nose}} + Q_c - Q_d - Q_{a_m}) \right] b_1 \\ &+ \left[ f_{\gamma_2} c_c Q_c \left( \frac{\rho_q}{\rho_w} - 1 \right) + \left( f_{\gamma_1} + f_{\gamma_2} \left( 1 - \frac{r_{t,2}^2}{r_{t,1}^2} \right) \right) (Q_d + Q_{a_m}) \right] b_1 \\ &- f_{\gamma_2} \left[ \left( \frac{\rho_q}{\rho_w} - 1 \right) c_c Q_c + \left( 1 - \frac{r_{t,2}^2}{r_{t,1}^2} \right) (Q_d + Q_{a_m}) \right] b \\ &- \frac{1}{\Phi 2\pi\omega r_{t,1}^2} (Q_{a_{nose}} + Q_c - Q_d - Q_{a_m}) (Q_d + Q_{a_m}) \\ &= 0 \end{aligned} \quad (101)$$

Should all parameters in the above equation be known, then quadratic polynomial can be solved using the quadratic formula. An interpretation of the dynamics that result from this polynomial is difficult. Let us consider the case where only water is flowing through the cutter head, i.e.  $\rho_q = \rho_w$ . The above equation then reduces to a less complex equation where the width  $b_1$  can be computed directly.

$$b_1 = \begin{cases} \frac{\widehat{\Phi} f_{\gamma_2} (r_{t,1}^2 - r_{t,2}^2) b \omega + Q_c + Q_{a_m} - Q_{a_{nose}} - Q_d}{\widehat{\Phi} (f_{\gamma_1} + f_{\gamma_2}) r_{t,1}^2 \omega - \widehat{\Phi} f_{\gamma_2} r_{t,2}^2 \omega}, & b_1 \geq 0 \\ 0, & b_1 < 0 \end{cases} \quad (102)$$

This formulation suggests that an increase in the mixture velocity  $v_m$  results in a decrease of the width  $b_1$  and therefore a decrease in centrifugal advection spillage. Likewise, according to the model, an increase in the swing speed  $v_s$  leads to an increase in spillage in this spillage type.

#### *Implicit problem*

Equations (101) and (102) are implicit because the radii  $r_{t,1}^2$  and  $r_{t,2}^2$  of the cutter depend on the disc height  $b_1$  and  $b_2$  respectively. The solution to this implicit problem is found by iteratively evaluating to approximate  $b_1$ .

### **4.3 Spillage computation**

When the disc height  $b_1$  is known, the spillage results in the model can be obtained. Spillage  $S$  is a dimensionless number [-] which is often expressed in terms of a percentage. For the computation of spillage, the concentrations of the respective flows is to be obtained.

#### *4.3.1 Centrifugal advection concentration*

It was assumed that the concentration inside the cutter is homogenous. Since the density of centrifugal advection  $Q_{r_1}$  is essential to the pressure and thereby density assumptions, it is evident that the concentration  $c_r$  for centrifugal advection should not be adapted ( $c_r = c_{vs}$ ). The concentration of centrifugal advection is equal to the average concentration. Hence, equation (73) for the spatial concentration inside disc 1

$$c_r = c_{vs} = \frac{c_c Q_c}{Q_{r_1} + Q_d + Q_{a_m}} \quad (103)$$

#### *4.3.2 Rapid redeposition concentration*

It can be reasoned that the volumetric flow rate of rapid redeposition is of similar magnitude as the in situ dredge flow rate. Therefore, heterogeneous concentration is obtained by adapting the concentration  $c_d$  [-]. The dredge flow rate concentration is an order higher than the spatial concentration and can be obtained from equation (104).

$$c_c = \frac{\rho_b - \rho_w}{\rho_q - \rho_w} \quad (104)$$

Figure 4.8 (left) schematically depicts the relevant velocities that determine the concentration of rapid redeposition. The concentration of rapid redeposition is approximated by considering a minimum concentration equal to  $c_{d,min}$  [-] and a maximum concentration equal to  $c_{d,max}$  [-]. The location of the spectrum between these concentrations is found by the velocity ratio  $\hat{v}_{ratio}$  which was also found in equation (96). Figure 4.8 (right) depicts this method.

**It is assumed that the ratio of a particle's terminal settling velocity over its velocity provides a useful dimensionless coefficient that scales the concentration of the rapidly redepositing flow.**

The concentration of rapid redeposition  $c_d$  is obtained through

$$c_d = c_{vs} + f_{c_d}(c_{d,max} - c_{d,min}) \left( \frac{v_m}{\hat{v}_{tsr}} \right)^2 \quad (105)$$

Where  $f_{c_d}$  is the rapid redeposition concentration factor [-]. The concentration is limited by the magnitude of  $c_c$  since the particles cannot be packed tighter than in the bank. The maximum concentration  $c_{d,max}$  is obtained by setting the mixture velocity to zero in the mass flow rate balance. The ends of the spectrum are determined as

$$c_{d,max} = \begin{cases} \frac{c_c Q_c - c_r Q_{r1}}{Q_d}, & c_{d,max} \leq c_c \\ c_c, & c_c < c_{d,max} \end{cases} \quad (106)$$

$$c_{d,min} = c_{vs} \quad (107)$$

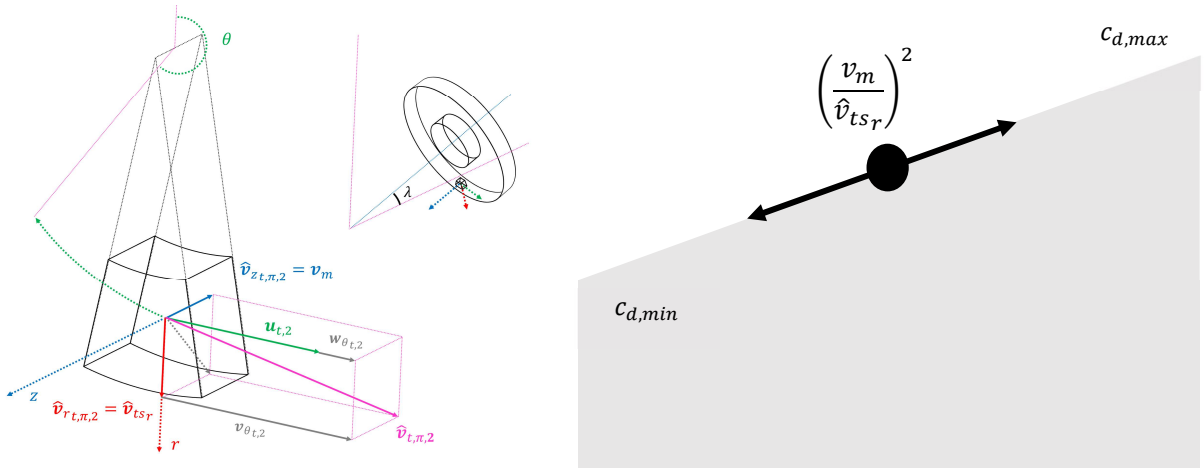


**Figure 4.8: Velocity approximations for a fluid element at the cutter bottom (left) and concentration scaling for rapid redeposition (right).**

With the special concentration  $c_{vs}$  unchanged, the increase in rapid redeposition concentration can only be explained by a drop in the concentration of solids in the mixture flow. Therefore, it is of interest to monitor the concentration  $c_m$  as shown in equation (106).

$$c_m = \frac{c_c Q_c - c_r Q_{r_1} - c_d Q_d}{Q_m} \quad (108)$$

#### 4.3.3 Spillage numbers

In accordance with the assumptions of the model, the two types that contribute to spillage as centrifugal advection  $S_1$  [-] and rapid redeposition [ $S_2$ ]. The total spillage rate  $S$  and its components are found as given in equations (109)-(111).

$$S_1 = \frac{c_r Q_{r_1}}{c_c Q_c} \quad (109)$$

$$S_2 = \frac{c_d Q_d}{c_c Q_c} \quad (110)$$

$$S = S_1 + S_2 \quad (111)$$

#### 4.4 Implementation template

The objective of the model is to compute the volumetric flow rates that underlie the continuity equation. For continuity to hold, the correct value of  $b_1$  is to be found. This section provides an overview of the chronological steps a user can take to find a solution for  $b_1$  and subsequently to compute spillage rates. The essence of the solution is to iterate over the value of  $b_1$  until an accuracy threshold is met. Straight forward spillage rate computations then complement the model. The template is given in Figure 4.9. A reference is given for equations.

- 1 Input  $D_{ring}$
- 2 Input  $D_{nose}$
- 3 Input  $D_{pipe}$
- 4 Input  $b$
- 5 Define function for  $r_{t,z}$  (49)
- 6 Input  $\xi$
- 7 Input  $\lambda$
- 8 Input  $h$
- 9 Input  $l_{step}$
- 10 Compute  $z_{tip}$  (52)
- 11 Compute  $z_{pen}$  (53)
- 12 Compute geometry (54)
- 13 Define function for  $r_{b,z}$  (55)
- 14 Define function for  $\Delta r_{b,z}$  (60)
- 15 Define function for  $x_z$  (61)
- 16 Define function for  $\gamma_z$  (62)
- 17 Input initial  $\hat{b}_1$  estimate
- 18 Set convergence coefficient  $relax = 1E-2$
- 19 Set accuracy coefficient  $threshold = 1E-4$
- 20 While  $error > threshold$
- 21     Compute  $b_2$  63
- 22     Input  $\omega$

23	Input $\hat{\Phi}$	
24	Compute $r_{t,1}$ and $r_{t,2}$	Step 5
25	Compute $\gamma_1$ and $\gamma_2$	Step 16
26	Compute $f_{\gamma_1}$ and $f_{\gamma_2}$	(63)
27	Compute $Q_{r_1}$	(83)
28	Input $Q_{a,nose}$	(90) estimate
29	Input $v_{ts}$	
30	Compute $\hat{v}_{tsr}$	(93)
31	Input $f_d$	
32	Input $f_{d,type}$	
33	Compute $u_{ref}$	(94)
34	Compute $\hat{v}_{\theta,ref}$	(92)
35	Compute $x_2$	Step 15
36	Compute $A_d$	(95)
37	Compute $\hat{v}_{ratio}$	(96)
38	Compute $Q_d$	(97)
39	Input $v_s$	
40	Compute $A_{cut}$	(56)
41	Input $v_m$	
42	Compute $Q_{a,m}$	(98)
43	Compute $Q_c$	(99)
44	Compute $b_1$	(101)
45	$error =  b_1 - \hat{b}_1 $	
46	$\hat{b}_1 = \hat{b}_1(1 - relax) + b_1(relax)$	
47	Compute $Q_{r_2} = Q_d + Q_{a,m} + Q_{r_1} - Q_{a,nose} - Q_c$	
48	Input $\rho_q$	
49	Input $\rho_b$	
50	Input $\rho_w$	
51	Compute $c_c$	(104)
52	Compute $c_r$	
53	Compute $c_{d,max}$	(106)
54	Compute $c_{d,min}$	(107)
55	Input $f_{c_d}$	
56	Compute $c_d$	(105)
57	Compute $c_m$	(108)
58	Compute $S_1$	(109)
59	Compute $S_2$	(110)
60	Compute $S$	(111)
61	End	

Figure 4.9: Implementation template.

## 4.5 Conclusion

---

### In conjunction with the relevant physical parameters, what concepts and assumptions enable a CSD spillage engineering model?

---

A spillage model can be set up by taking three steps. First, an advanced geometrical description of the cutter head-bank interface can be derived. Important parameters are the cutter radius and curvature, cutter height, bank height, bank slope angle, cutter inclination angle and the step size of the cutting pattern. Second, a potential flow model can be set up based on flow continuity in the cutter. The cutter is split into two discs with disc 1 at the cutter ring and disc 2 at the nose. Volumetric flow rates are determined for centrifugal advection flow, radial as well as axial inflow through the nose, rapid redeposition flow, mixture flow and an in situ dredge flow. The model strategy is outlined below

1. Among other assumptions, the pump effects of the leading edge of the cutter blade are considered negligible. This allows for the simplification of Euler's pump equation to a pump affinity law that expresses discharge as a function of radial pressure difference. This affinity law and the height of disc 1 are used to approximate centrifugal advection flow near the ring.
2. For the radial inflow at the nose, the assumption is made that the true pressure at the trailing edge of the cutter is equal to the pressure that is generated in disc 1. As a consequence, the difference in estimated pressure gradients between the discs drives an inflow at disc 2. Again, the pump affinity law is used in conjunction with density considerations to provide an estimate of the flow rate into disc 2.
3. Axial inflow at the nose is added as an optional component in the flow balance but is assumed negligible due to geometrical considerations.
4. A spillage flow for rapid redeposition is found as a function of the rotational velocity, cutting scenario, particle settling velocity, mixture velocity and geometrical parameters for a reference point in the cutter.
5. Straight forward expressions are obtained for the mixture flow rate where the user inputs the mixture velocity.
6. The swing velocity is an input parameter to determine the in situ dredge flow rate.

The resulting continuity balance poses an implicit problem and is solved iteratively. The third step in the model is to rewrite the mass flow rate balance to find the concentrations of outgoing flows. Gravitational acceleration is expected to affect the entrainment rate of particles into the axial flow and increases the concentration of rapid redeposition. Spillage is computed as the mass flow ratios of the spillage components to the mass flow rate of incoming bank material. Table 4.1 provides an overview of the user input parameters as well as model coefficients.

**Table 4.1: Overview of input parameters**

<i>Parameter</i>	<i>Symbol</i>	<i>Unit</i>	<i>General estimate</i>
Diameter of the cutter ring	$D_{ring}$	m	3

Diameter of the cutter nose	$D_{nose}$	m	2.5
Diameter of the suction pipe	$D_{pipe}$	m	1
Height of the cutter head	$b$	m	2.5
Bank slope angle	$\xi$	rad	30 deg $\approx$ 0.5 rad
Cutter inclination angle	$\gamma$	rad	30 deg $\approx$ 0.5 rad
Bank height	$h$	m	1
Step size	$l_{step}$	m	1.5
Rotational velocity	$\omega$	rad/s	30 rpm = $\pi$ rad/s
Terminal settling velocity	$v_{ts}$	m/s	$f(d_{50})$
Swing velocity	$v_s$	m/s	0.2
Mixture velocity	$v_m$	m/s	1
Quartz density	$\rho_q$	Kg/m <sup>3</sup>	2650
Bulk density (wet)	$\rho_b$	Kg/m <sup>3</sup>	1700
Water density	$\rho_w$	Kg/m <sup>3</sup>	1025
Pump flow number	$\hat{\Phi}$	[-]	$f(d_{50})$
Rapid redeposition factor	$f_d$	-	0.012
Cutting scenario factor	$f_{d_{type}}$	-	-1 (under cut) 1 (over cut)
Rapid redeposition concentration factor	$f_{c_d}$	-	20

## 5 Results and discussion

This research aims to find a grain size-agnostic model. Previous chapters have presented a series of derivations, model concepts and assumptions. These findings culminated in an engineering model named the Sand-Rock Cutting Spillage Model (SRCSM). In essence, SRCSM is a potential flow model with empirical closing relations based on the assumptions from chapter 4. The last sub-question in this research reads

---

**Based on the identified physical parameters, concepts and assumptions, how does the model perform relative to experimental data?**

---

The first iteration of the results is focused on fitting the model for sand. Next, the calibration is performed for rock. For all calibration, the dig-swing is considered.

### 5.1 Calibration number

The pressure gradient is considered the most dominant force in the model (see section 0). In section 3.2.2 it was described that particle trajectories in a cutter are in part governed by the centrifugal force  $F_{cf}$  in the cutter [N] and the product of the particle volume and radial pressure gradient in the suction mouth  $F_s$  [N]. Equation (4) was derived and is repeated here for clarity

$$\frac{F_{cf}}{F_s} \propto \frac{\rho_p}{\rho_w} \left( \frac{\omega R_{ring}^3}{v_m R_{pipe}^2} \right)^2 \quad (112)$$

Where  $\rho_p$  is the particle density [kg/m<sup>3</sup>],  $\rho_w$  is the water density [kg/m<sup>3</sup>],  $R_{ring}$  and  $R_{pipe}$  are the cutter ring and pipe radii [m] and  $v_m$  is the mixture velocity [m/s]. In work by Steinbusch et al. (1999) and Dekker et al. (2003), the inverse term of the expression between brackets in equation (112) was identified as a characteristic flow number for the ratio of the cutter-induced velocity and the suction velocity. This term was named a *flow number* and denoted as  $\theta$  (please note this number is different from the *pump flow number*  $\hat{\Phi}$ ). Similar versions have been used for spillage and flow phenomena (Mol (1977a); Miltenburg (1983); Den Burger (2003); Nieuwboer et al. (2017)). Calibration of the SRCSM is chosen to be performed using the inverse of the flow number, defined as

$$\hat{\theta} = \theta^{-1} = \frac{\omega R_{ring}^3}{Q_{a_m}} \quad (113)$$

Nieuwboer et al. (2017) suggest that typical inverse flow numbers in the industry lie between 1.6 and 3.7.

### 5.2 Calibration data

Data from the cutters in the field is difficult to obtain. Density meters in the suction pipe only indicate production. Since the meters are typically located far from the cutter head there is increased uncertainty and a delay in feedback.

The SRCSM is evaluated using comprehensively upscaled experimental data from Miltenburg (1983, as cited in Den Burger (2003)) for prototype sand particles ( $d_{50}=180E^{-3}$  [mm]) and Den Burger (2003) for prototype rock particles ( $d_{50}=80$  [mm]).

Caution should be observed since the spillage data for rock are obtained synthetically. The method is pictured in Figure 5.1 (right). First, Den Burger set the angular velocity of the cutter at a 30 [rpm] equivalent. Then, the mixture velocities were varied between 2 and 5 [m/s] and production was measured. The spillage rates were set out against the inverse flow number. Several polynomials were fitted through the production rates  $P$  [%] which exhibited a maximum spill rate for each mixture velocity. The production curve for rock was then determined by curvefitting a line tangential to the polynomials that exhibit maximums of the individual mixture velocity curves. In this research, spillage is computed from the production as  $S = 1 - P$  and is therefore measured in [%]. The spillage data for the experiments with sand were measured directly.

**Table 5.1: Experiment parameters for Miltenburg (1983) and Den Burger (2003).**

<sup>1</sup>Estimated value.

Parameter	Symbol	Sand (Miltenburg, 1983)		Rock (Den Burger, 2003)		Units
		Prototype	Experiment	Prototype	Experiment	
Particle diameter	$d_{50}$	180E-3 <sup>(1)</sup>	180E-3	80	10	mm
Bed concentration	$c_c$	0.4	0.4	0.42	0.42	-
Quartz density	$\rho_q$	2650	2650	2200	2650	Kg/m <sup>3</sup>
Bulk density (wet)	$\rho_{b,wet}$	2000	2000	2200	2200	Kg/m <sup>3</sup>
Settling velocity	$v_{ts}$	0.02	0.02 <sup>1</sup>	0.73	0.73	m/s
Drag coefficient	$C_{drag}$	9	9 <sup>1</sup>	0.4	0.4	-
Diameter of the cutter ring	$D_{ring}$	2.80	0.40	3.12	0.4	m
Diameter of the cutter nose	$D_{nose}$	2.11 <sup>(1)</sup>	0.18	2.11 <sup>(1)</sup>	0.28	m
Diameter of the suction pipe	$D_{pipe}$	0.7	0.1	0.95	0.1	m
Height of the cutter head	$b$	2.5 <sup>(1)</sup>	0.265	2.50 <sup>(1)</sup>	0.265	m
Swing velocity	$v_s$	0.2	0.1	0.2	0.1	m/s
Cutoff area	$A_{cut}$	1.4	0.023	1.4	0.03	m <sup>2</sup>
Bank contact angle	$\gamma$	$\pi/2$	$\pi/2$	$\pi/2$	$\pi/2$	rad
Cutter inclination angle	$\lambda$	45	45	45	45	deg
Rotational velocity	$\omega$	30	100	30	90	rpm
Cutting scenario	$f_{d_{type}}$	Under-cut ( $f_{d_{type}} = -1$ )				-

For calibration of the model,  $R_{ring}$  is chosen as 3.12 [m] and the bank cut off area is set at  $A_{cut} = 1.4$  [m<sup>2</sup>]. The shape of the bank is determined such that the experiment cross section is approximated. Spillage data is highly scarce for over-cut scenarios; hence the under-cut scenario is chosen for calibration. It should be noted that the cutter inclination angle is relatively large at 45 degrees. Typical cutter angles are 30 degrees. Additional caution should therefore be observed when applying the model for small cutter inclination angles.

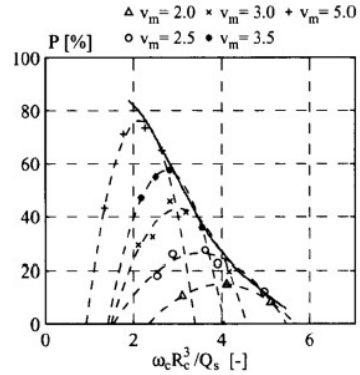


**Figure 5.1: Photo of experimental cutter head (left) and production curve (right).**

From top left to bottom right in the left image: open cutter, closed cutter, short back plate and long back plate used by Miltenburg (1983). The right plot depicts the synthetic production curve approximation for rock by Den Burger (2003).

### 5.3 Results for sand

The settling velocity for sand is equal to 0.02 [m/s] and is therefore of negligible influence for sand with a  $d_{50}$  of 180 micron. For this reason, the effect of rapid redeposition can be neglected. With spillage reduced to centrifugal advection only, the relevant calibration parameter is the pump flow number  $\hat{\Phi}$ . The pump flow number was found to be 0.58. The spillage results for sand are presented in Figure 5.2 (left).

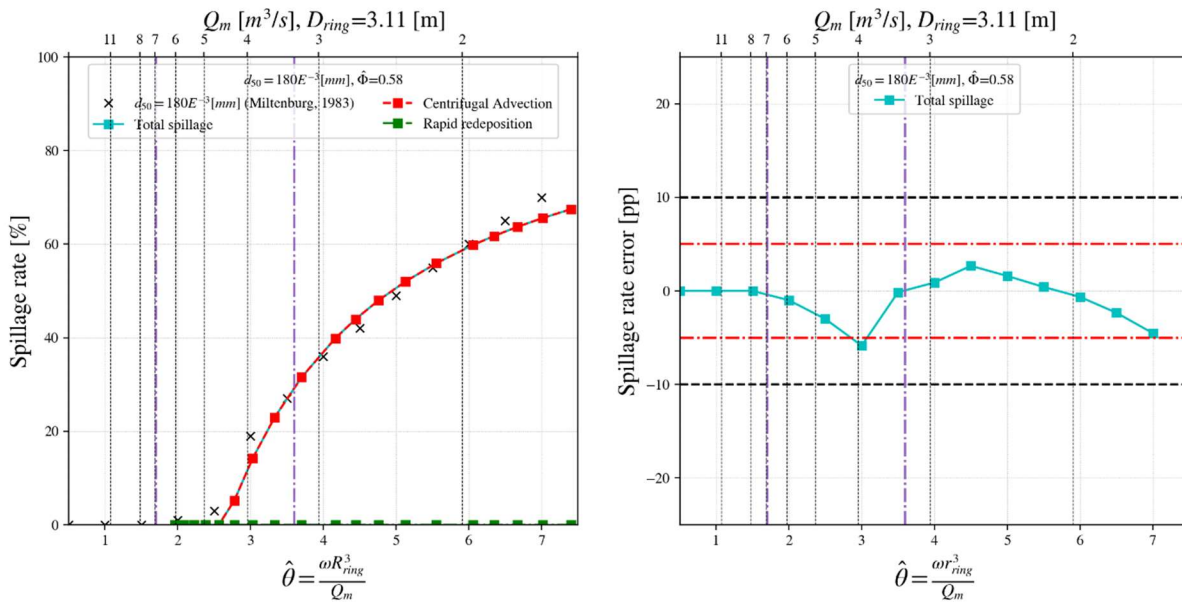


**Figure 5.2: Sand spillage results (left) and magnitude of error (right).**

Reference data is obtained from laboratory experiments by Miltenburg (1983). Typical operation range is indicated with the purple dash-dotted line.

A high similarity can be observed between the curvature of SRCSM and the experimental data. The dynamics of centrifugal advection appear to be adequately captured by the model. For a cutter with a diameter of 3.11 [m] the onset of spillage occurs at a mixture flow of around 5 [m<sup>3</sup>/s]. The model error is given in the right

plot of Figure 5.2 and is expressed in percentage point [pp]. A large error can be observed at  $\hat{\theta} = 3$ . The curvature of the calibration data suggests that the experimental data exhibits an outlier at this inverse flow number. The model deviation is therefore neglected. The remaining errors, especially within the region of interest, are all within the 5 [pp] bandwidth, indicating that the model is in agreement with the data.

### 5.3.1 Flow Rates and concentrations for sand

Figure 5.3 displays the volumetric flow rates and concentrations for sand. In accordance with expectations, centrifugal advection flow increases for higher inverse flow numbers. Centrifugal advection significantly increases the total in- and outflow of the cutter, which would otherwise be dominated by the mixture flow. At  $\hat{\theta} = 2.5$  an interesting onset of  $Q_{r_1}$  can be observed. There appears to be a smooth transition from inflow to outflow at the cutter ring which is also visible at the experimental data. The model captures the dynamics of centrifugal advection fittingly. The concentration inside the cutter is stable at approximately 0.025 with an associated cutter density and mixture density of 1065 [kg/m<sup>3</sup>].

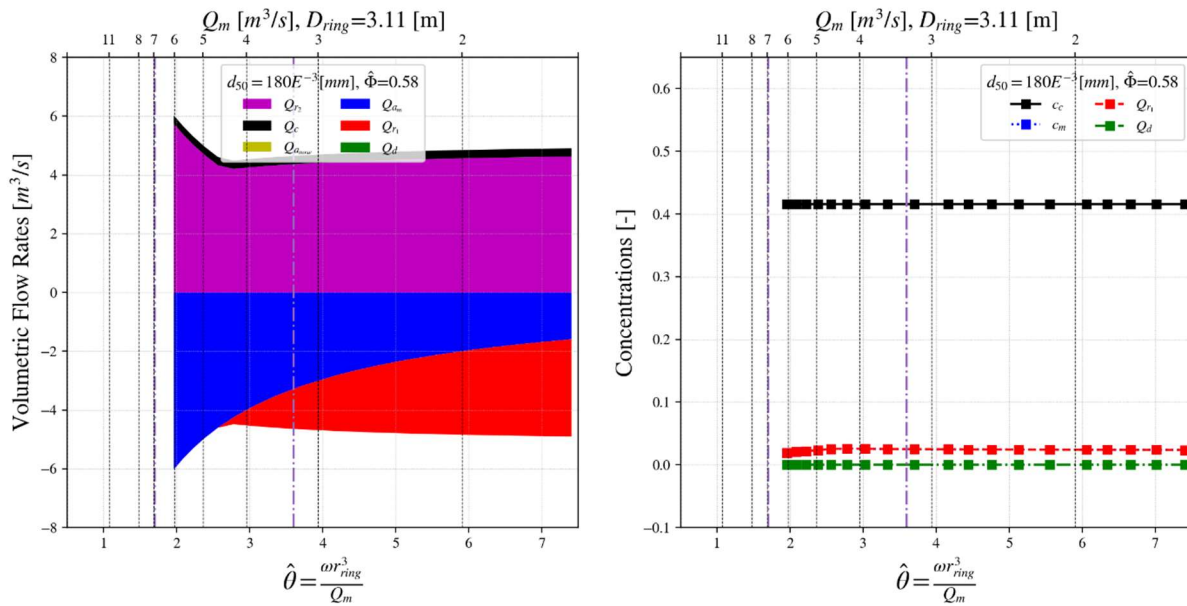


**Figure 5.3 Volumetric flow rates (left) and concentrations (right) for sand.**  
Typical operation range is indicated with the purple dash-dotted line.

### 5.3.2 Axial flow through the nose

The model enables the addition of an axial flow through the nose. It was hypothesized however that this flow only exists when the cutter rotates in water. Low through the nose is heavily impeached by the breach as well as the compact geometry of the cutter. Axial flow is detrimental to the model's performance as can be seen in Figure 5.4. The increase in axial flow induces more radial advection at low inverse flow numbers because the dredge pump is not capable of entraining this additional flow. The right plot clearly demonstrates that axial flow should be neglected.

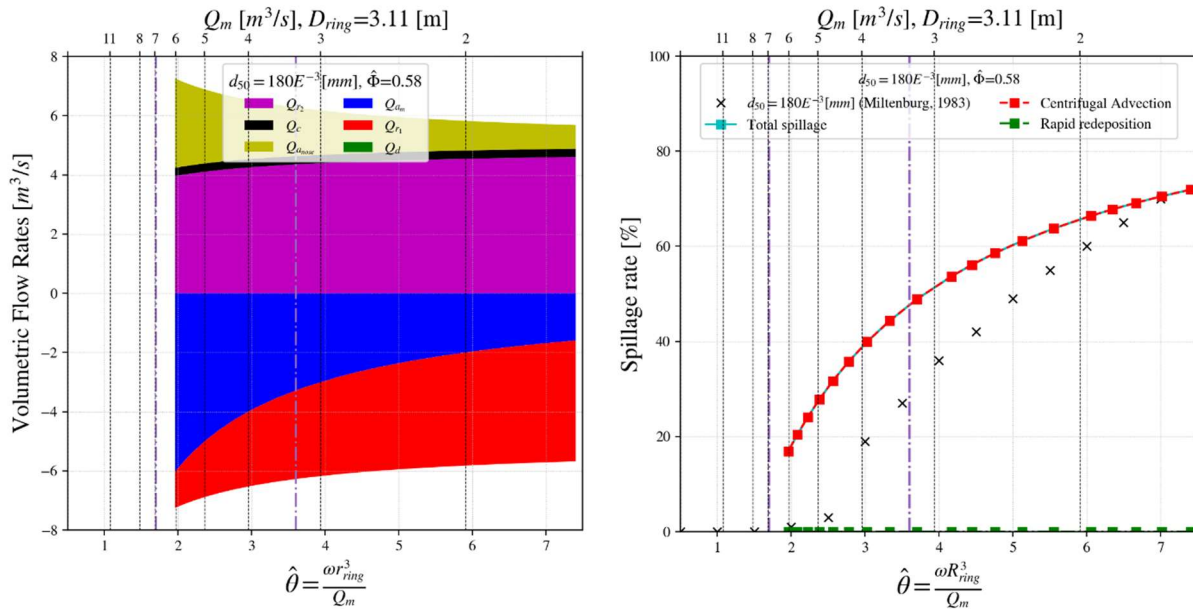


Figure 5.4 Volumetric flow rates (left) and sand spillage results for sand (right) with axial flow through the nose.

Typical operation range is indicated with the purple dash-dotted line.

### 5.1 Results for rock

The results for rock are presented in Figure 5.5 (left). Rapid redeposition is to be calibrated for rock. In addition to the pump flow number, the model requires a value for the rapid redeposition factor and the rapid redeposition concentration factor. The primer scales the influence of the rotational velocity of the cutter. The latter scales the magnitude of the redeposition concentration between the average spatial concentration and bank concentration. These factors and the pump flow number are found to be

$$\begin{aligned} f_d &= 0.012 \\ f_{c,d} &= 20 \\ \hat{\theta} &= 0.92 \end{aligned}$$

Rapid redeposition proves significant for high values of the inverse flow number, associated with low mixture velocities in the suction pipe, which was hypothesized during development. Contrary to centrifugal advection, the rate of change of rapid

redeposition rises with increasing inverse flow numbers. Rapid redeposition appears to be inversely proportional to the mixture velocity. The model is in high agreement with the calibration data. The rapid redeposition component complements centrifugal advection satisfactorily as the plot fits the curvature of the spillage data. The errors that are displayed in Figure 5.5 (right) are within the 5 percentage point margins.

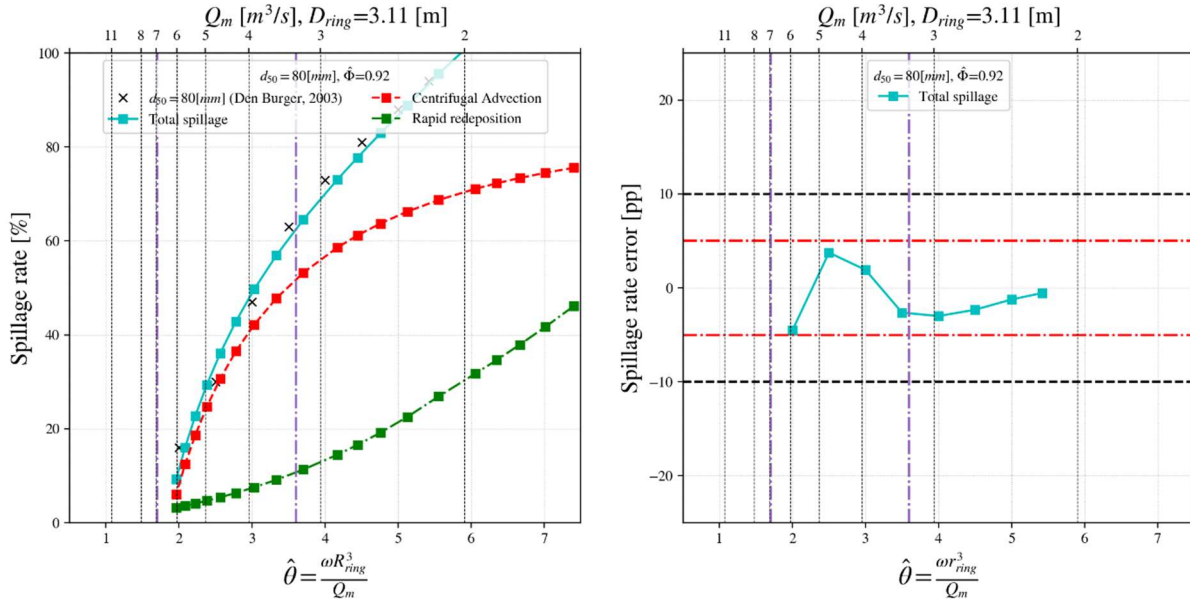


**Figure 5.5: Rock Spillage results (left) and magnitude of error (right).**

Reference data is obtained from laboratory experiments by Den Burger (2003). Typical operation range is indicated with the purple dash-dotted line.

### 5.1.1 Flow rates and concentrations for rock

The results for the flow rates and concentrations when cutting rock are given in Figure 5.6. The onset for centrifugal advection is at  $\hat{\theta} = 2$  despite the hypothesis that rock particles are less impacted by drag in the centrifugal direction. High centrifugal advection for rock-type particles may be explained by arguing that these particles are also less affected by drag induced by the mixture velocity. Centrifugal advection for rock may take place relatively close to the suction mouth. With the given redeposition factors, the volumetric flow rate for redeposition is small. However, Figure 5.6 (indicates) that the concentration is relatively high in comparison to the spatial concentration in the cutter. It can be seen that the concentration of the bank is higher for rock than for sand. At  $\hat{\theta} = 5.5$ , the model exhibits a small discontinuity in the redeposition concentration. This can be explained by the method used to calculate the redeposition concentration from equation (106). The model approaches the value of  $c_{d,max}$  which is equal to the bank concentration. As a result, the concentration increase is limited. In spite of this limit, the amount of solids that is modelled downwards is so large that this would only be possible if solids would be flowing out of the mixture pipe. Hence the proximity with  $\hat{\theta} = 6$  where mixture concentration drops below zero. The model

concentrations for the mixture are similar to concentrations found in experiments by Den Burger (0.01 – 0.05 [-]).

Potentially, the volumetric flow rate can be adapted to further detail. Since this model artifact is outside the region of interest, the relatively small discontinuity is accepted.

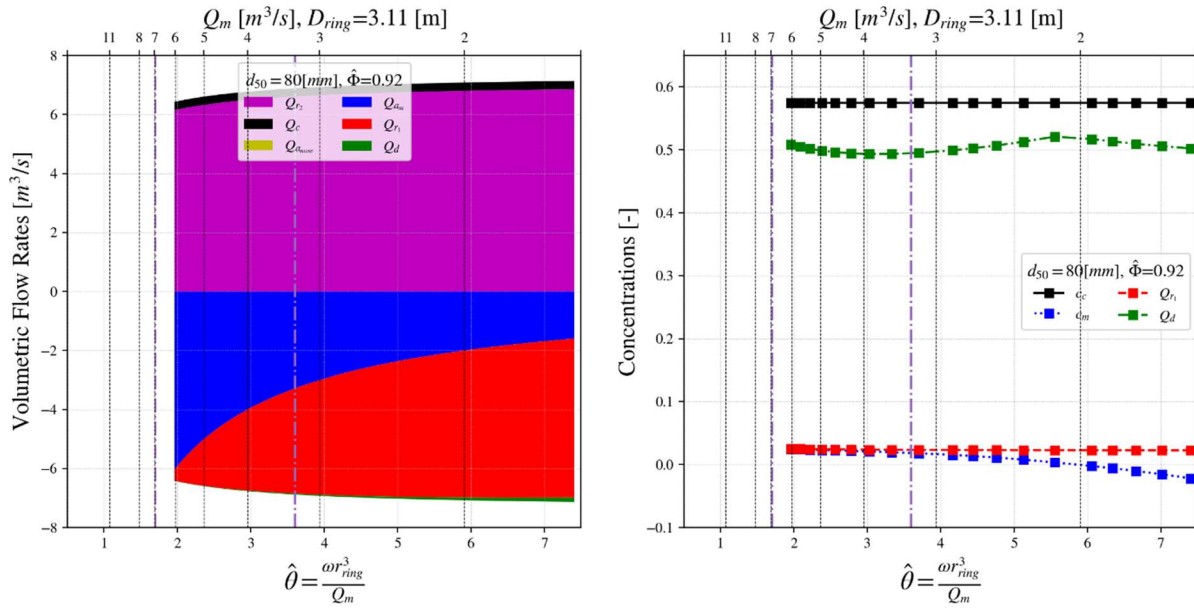


**Figure 5.6 Volumetric flow rates (left) and concentrations (right) for rock.**  
Typical operation range is indicated with the purple dash-dotted line.

## 5.2 Expression for pump flow number

Based on calibration of the Sand-Rock Cutting Spillage Model for sand and rock data, the results indicate that the pump (cutter) flow number can be related to a relevant particle property. This is the last parameter that is unknown to the user and can be calculated according to, for instance

$$\hat{\Phi} = 0.57 + 0.48v_{ts}$$

The pump flow number is higher for larger particles. The physical interpretation of this relationship is that rock particles are less subject to drag forces in the radial direction. Therefore, the ratio of the radial velocity over the axial velocity must be larger for rock for the model to be in agreement with the data.

## 5.3 Sensitivity analysis

In alignment with the model property to be informative to its user, a sensitivity analysis is performed. Important user parameters are the swing velocity, step size and cutter inclination angle.

### 5.3.1 Spillage sensitivity to swing velocity

The model's sensitivity to swing velocity is evaluated. An increase in swing velocity typically increases spillage rates since adequate mixing is impeded. This is not explicitly modeled; its implied effect however was noticed in equation (102). Figure 5.7 displays the spillage centrifugal advection sensitivity to swing velocity for sand and rock. The plots demonstrate that for relevant inverse flow numbers, a 1 [%] increase in swing velocity may result in more than 3 (sand) or 4 (rock) [%] increments in spillage. The reverse effect is observed for a drop in swing velocity. The symmetry of this sensitivity indicates that the model functions well. The effect for sand is higher than for rock. This can be explained by the fact that sand particles may now be more heavily advected out of the cutter in the lateral direction. It was found that that rapid redeposition was not significantly affected by the swing velocity. It will be recommended to adapt the model to better incorporate the effects of mixing to rapid redeposition.

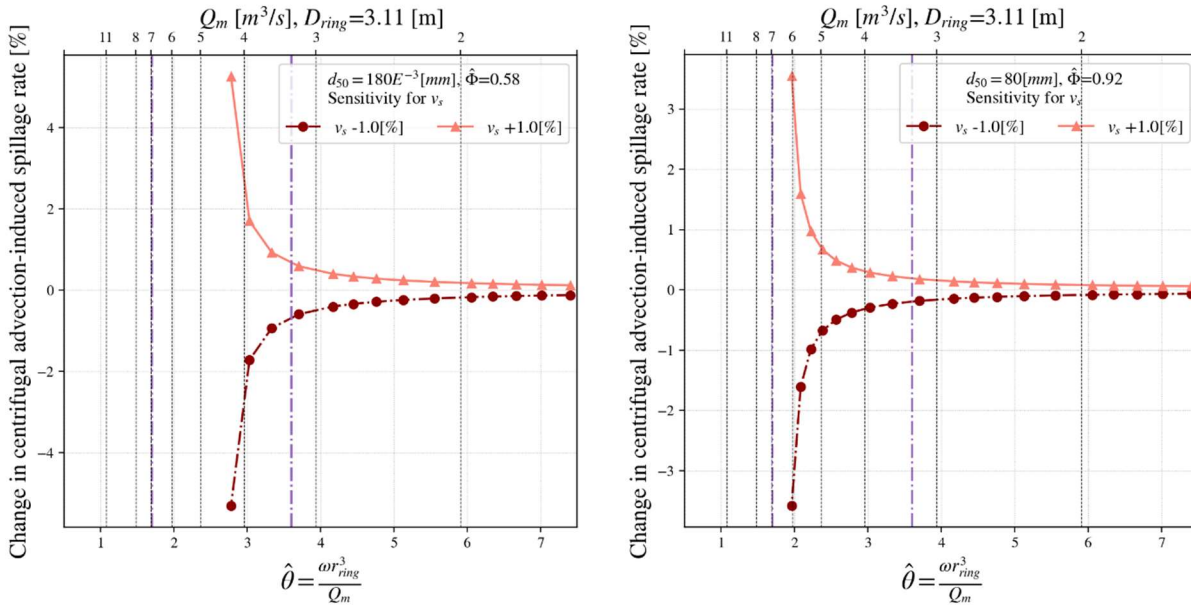


**Figure 5.7: Model sensitivity to swing velocity for centrifugal advection for sand (left) and rock (right).**

Typical operation range is indicated with the purple dash-dotted line. The reference swing velocity  $v_s = 0.2 [m/s]$  and is increased and decreased with 1 [%].

### 5.3.1 Spillage sensitivity to step size

An increase of the step size implies a deeper penetration into the bank. The spatial concentration in the cutter increases. The dynamics of the pressure assumption from section 4.2.3 can be used to explain how this effects spillage. The density ratio in equation (86) suggest that the *actual* specific flow rate  $q_{r2}$  at disc 2 increases when the higher concentrations.

$$q_{r2} = \frac{\hat{\Psi}_1 \rho_m \hat{\Phi}_2 f_{y2}}{\hat{\Psi}_2 \rho_w \hat{\Phi}_1 f_{y1}} q_{r1} - \hat{q}_{r2}$$

From axial inflow at the nose it was concluded that a larger inflow increases centrifugal advection for low inverse flow numbers. Figure 5.8 (left) indicates that cutting 20 [%] deeper does increase spillage rates for centrifugal advection with potentially more than 20 [%]. The right plot indicates that rapid redeposition increases decreases for longer step sizes. Equation (97) is repeated for clarity.

$$Q_d = \hat{v}_{\theta_{ref}} A_d \left( \frac{v_m}{\hat{v}_{tsr}} \right)^2 b - \frac{z_{pen}}{2}$$

The latter ratio is indicative of the distance to the cutter mouth versus the bank height. With the penetration depth  $z_{pen}$  proportional to the step length, it can be concluded that rapid redeposition rates should drop with increasing step size. The model appears to exhibit this behavior well, as shown in Figure 5.8 (right). An increase in step size of 20 [%] results in a decrease of the spillage rates of about 6 [%]. The large sensitivity step of 20 [%] is chosen to demonstrate the non-linear results that are obtained from the advanced geometrical description of the cutter head. For different bank parameters, the curvature of the sensitivity for rapid redeposition may differ.

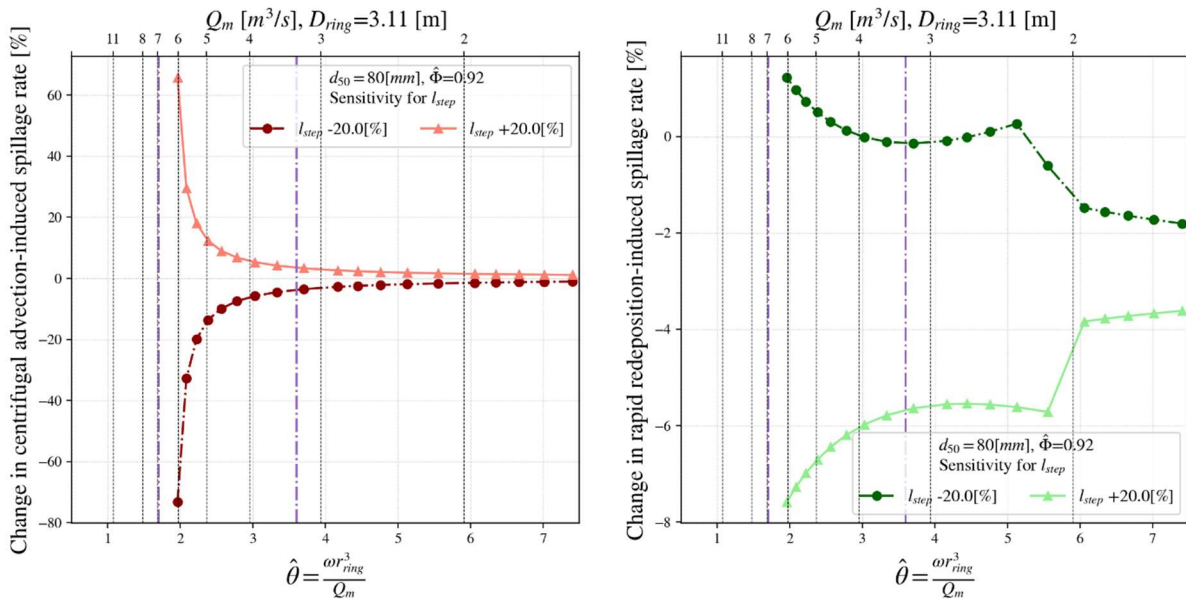


**Figure 5.8: Model sensitivity to step length for centrifugal advection (left) and rapid redeposition (right) for rock.** Typical operation range is indicated with the purple dash-dotted line. The reference swing velocity  $l_{step} = 0.2$  [m/s] and is increased and decreased with 20 [%].

### 5.3.2 Spillage sensitivity to cutter inclination angle

Large inclination angles increase the vertical distance of particles to the suction mouth. Figure 5.9 depicts the sensitivity analysis for the cutter inclination angle. For centrifugal advection (left), the sensitivity to small changes of the cutter inclination angle is considered negligible since this effect is not incorporated. For rapid redeposition (right) the results indicate that a minor 1 [%] increase in inclination

angle leads to more than 6 [%] more spillage. These effects are significant and in accordance with the hypothesis that was made in section 3.2.3.

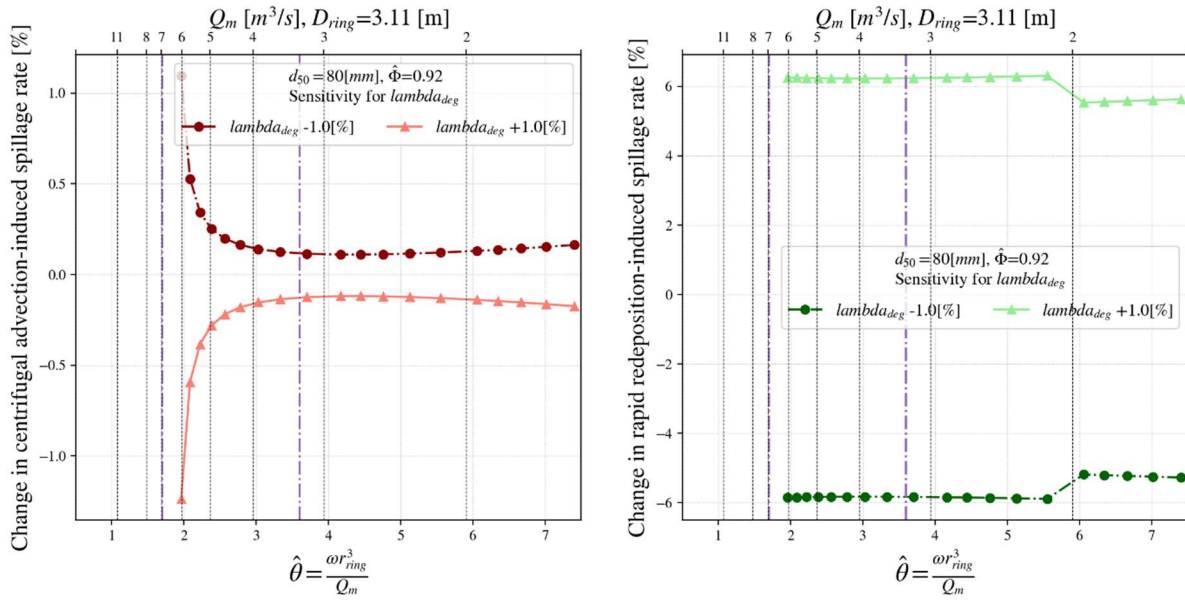


**Figure 5.9: Model sensitivity to cutter inclination angle for centrifugal advection (left) and rapid redeposition (right) for rock.** Typical operation range is indicated with the purple dash-dotted line. The reference inclination angle  $\lambda = 45$  [deg] and is increased and decreased with 1 [%].

### 5.3.1 Spillage sensitivity to slope angle

The slope angle  $\xi$  of the bank determines the size of  $A_{cut}$ . Figure 5.12 depicts the 1 [%] sensitivity of the model to the slope angle. Most interesting, an increase in slope angle reduce spillage for redeposition. The center of gravity of the cut surface is removed further from the cutter for increasing inclination angles. This dynamic appears to be adequately captured by the geometrical description of the bank.

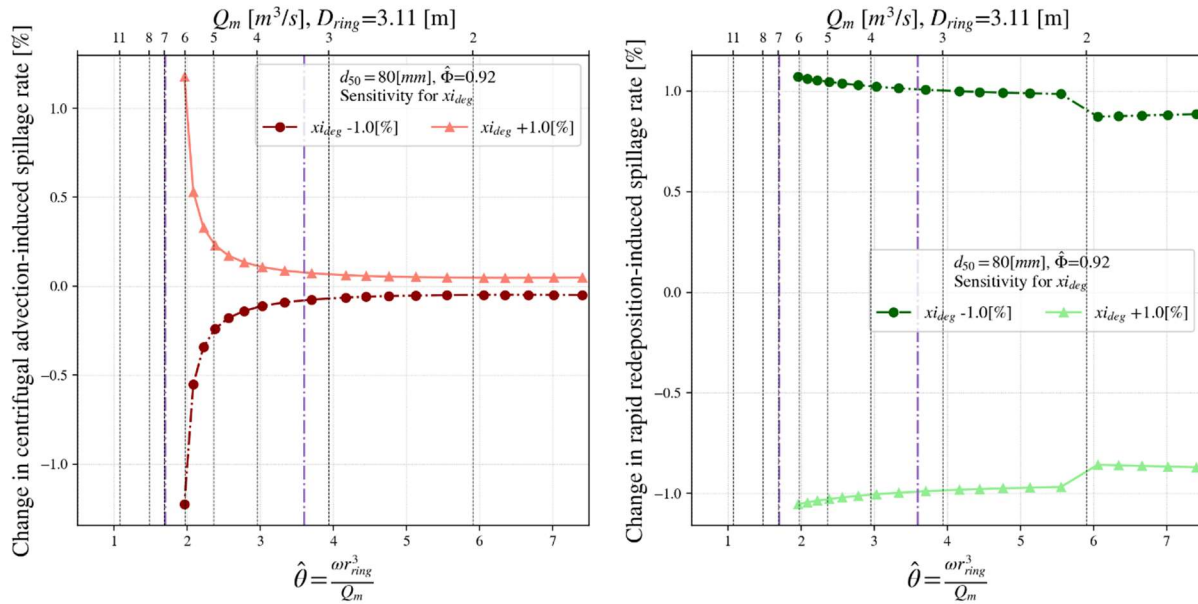


**Figure 5.10: Model sensitivity to the slope angle for centrifugal advection (left) and rapid redeposition (right) for rock.** Typical operation range is indicated with the purple dash-dotted line. The reference swing velocity  $\xi = 45$  [deg] and is increased and decreased with 1 [%].

### 5.3.1 Spillage sensitivity to bank height

In certain occasions, dredge operators will have to determine optimal productivity for cutting large bank heights. A choice can be made between swinging either once or twice per step. Larger bank heights are exclusive for sand cutting since due to the torque limitations of the cutter and for wear considerations. For this decision an analysis of the sensitivity to the bank height  $h$  is provided in Figure 5.12. The total spillage rate and sensitivity for sand equals that of the centrifugal advection component. It can be observed that a 20 [%] increase in bank height increases spillage with approximately 5 to 40 [%] in the region of interest.

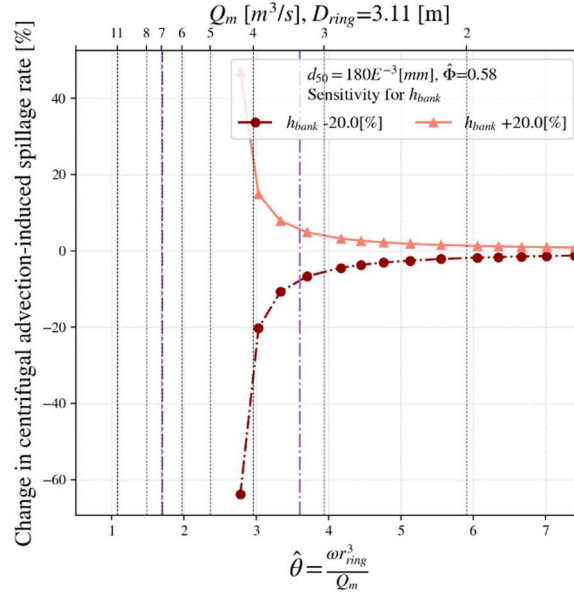


**Figure 5.11: Model sensitivity to the bank height for centrifugal advection for sand.**

Typical operation range is indicated with the purple dash-dotted line. The reference swing velocity  $h = 1$  [m] and is increased and decreased with 1 [%].

### 5.3.2 Sensitivity overview

An overview of the overall sensitivity to cutting parameters is given in Table 5.2. When cutting with a ring radius  $r_{ring} = 3.11$  [m], a representative mixture flow rate of 4.5 [m3/s] is chosen which corresponds to an inverse flow number of  $\hat{\theta} = 2.77$ .

**Table 5.2: Sensitivity to relevant parameters at  $\hat{\theta} = 2.77$ .**

<sup>1</sup>Considered a model artifact. Sensitivity measured at.

Parameter	Sand, $d_{50}=180E-3$ [mm]			Rock, $d_{50}=80$ [mm]			Ref. value
	-1 [%]	Symbol	+1 [%]	-1 [%]	Symbol	+1 [%]	
Swing velocity	-2.80	$v_s$	2.73	-0.63	$v_s$	0.62	0.2 m/s
Step size	-4.64	$l_{step}$	4.60	-0.37	$l_{step}$	0.37	1.4 m
Cutter angle	0.87 <sup>1</sup>	$\lambda$	-1.04 <sup>1</sup>	-0.62	$\lambda$	0.65	45 deg
Slope angle	-1.43	$\xi$	1.37	0,03	$\xi$	-0.03	45 deg
Bank height	-2.8	$h$	2.76	-0.63	$h$	0.62	1 m

### 5.3.3 Over-cut vs under-cut

The lack of over-cutting spillage data impedes adequate calibration for the over-cut mode. To demonstrate the effect of cutter rotation direction, a qualitative evaluation is performed. For over-cutting ( $f_{d_{type}} = 1$ ), the following parameters are chosen where  $f_d$  is relatively arbitrary.

$$\begin{aligned} f_d &= 0.05 \\ f_{cd} &= 20 \\ \hat{\theta} &= 0.92 \end{aligned}$$

The model results are plotted in Figure 5.12. Reference data is given for under-cut mode and only serves as a qualitative reference. In over-cut mode, spillage rates

are higher for the broad range of inverse flow numbers. The rapid redeposition effect is the highest contributor to this spillage rate increase. Caution should be observed with the interpretation of these results, since the computed spillage rates are unrealistic in practice. This is mostly due to the very high cutter inclination angle.

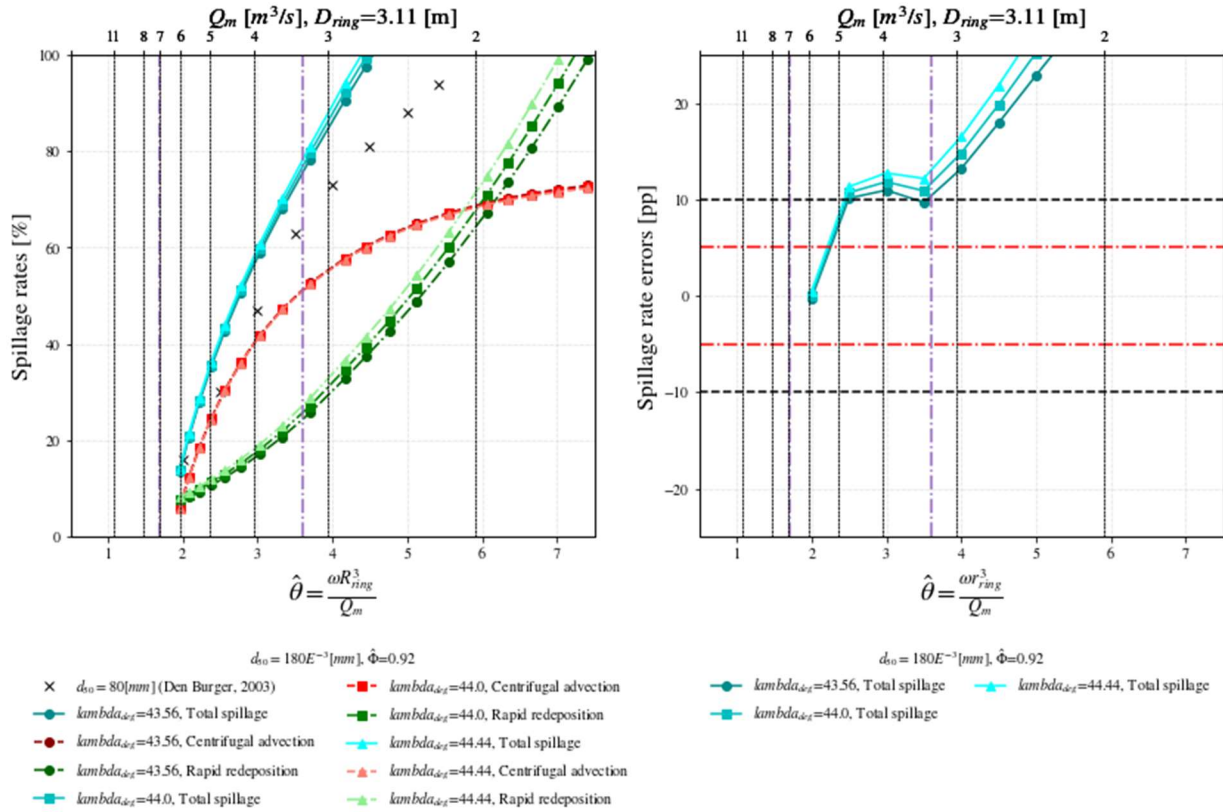


Figure 5.12: Sensitivity of over-cut scenario to cutter inclination angle (left) and respective errors (right).

Typical operation range is indicated with the purple dash-dotted line. The reference inclination angle  $\lambda = 45$  [deg] and is increased and decreased with 1 [%]. Reference data is given for under-cut mode and only serves as a qualitative reference.

## 5.4 Further discussion

This section evaluates certain assumptions and model concepts and sets limits to the applicability of the presented SRCSM.

### 5.4.1 Strouhal number

For the Strouhal number of equation (28), it was assumed that the volumetric flow rate through the cutter is approximately 4 [m<sup>3</sup>/s]. This assumption seems in line with the range of volumetric flow rates in the SRCSM that are relevant. The Strouhal number for lower rotational velocity indicates that viscosity at this flow rate can be neglected. It can be concluded that the assumptions hold.

### 5.4.2 Pressure considerations

The foundational concept of the model is the assumption that the pressure difference between disc 1 and 2 at the trailing edge drives an inflow at disc 2.

Justification of this assumption is subject to discussion. In favor of the assumption, it can be argued that the square relation between the pressure and the disc diameter allows for a significantly larger pressure generation at disc 1, rendering the generated pressure at disc 2 negligible. Also, in reality, the dimensionless head  $\hat{\Phi}_i$  will be larger for disc 2 due to the fact that larger impellers (and blades also) are more efficient. These blades are also more curved outwards and therefore axial flow can be considered smaller in comparison to the nose.

In contrast, the volumetric flow rate  $Q_{r_1}$  is found to be up to an order of magnitude smaller compared to  $Q_{r_2}$  (see Figure 5.3, left). The extent to which such a small flow rate is able to drive an inflow may be smaller than assumed. However, it can be reasoned that the squared ratio of the cutter radii are highly representative for overall flow entrainment and therefore this assumption may hold.

#### 5.4.3 *Limits to applicability*

The model is presented based on the dimensionless inverse flow number. This suggests that the model is applicable for small to large cutters. Since many assumptions were made about the dimensionless scaling coefficients, caution should be taken when interpreting the model results for a prototype scale.

For non-relevant inverse flow numbers of 6 and higher, the concentration of the mixture velocity drops below zero. This suggests that the model is less reliable at high inverse flow numbers. However, this range is not *informative* to the end user and is thus not relevant for the model. In addition, the model is calibrated for very high cutter inclination angles. It has therefore been calibrated using data that is less realistic.

## 5.5 Conclusion

---

### **Based on the identified physical parameters, concepts and assumptions, how does the model perform relative to experimental data?**

---

The performance of the model can be evaluated using a dimensionless flow number  $\hat{\theta}$  that incorporates the cutter radius, angular velocity and mixture velocity. Two particle sizes are chosen for calibration and only the under-cut mode is considered. The data for sand ( $d_{50} = 180 \text{ E-3 [mm]}$ ) proves useful for the determination of the pump affinity law number since the low settling velocity for sand eliminates the effect of rapid redeposition. Model parameters can be identified for which both sand and rock ( $d_{50} = 80 \text{ [mm]}$ ) spillage is estimated within a 5 [pp] accuracy over the available range of  $\hat{\theta} = \langle 2,6 \rangle [-]$ . Moreover, the plot curvature exhibits a large resemblance with the experimental data for sand as well as rock. For rock, the rapid redeposition component appears to be inversely proportional to the mixture velocity. The relevant flow number for the dredge industry equals  $\hat{\theta} = 2.7 [-]$  for which a sensitivity analysis is performed. The dynamics of the governing ratios between centrifugal force, suction force and gravitational force appear to be captured adequately by the model. The influence of the cutter inclination angle appears arbitrary for sand cutting. This is ascribed to a model artefact that is linked

to the absence of rapid redeposition where cutter inclination becomes is of higher significance. The model exhibits correct behaviour for a qualitative simulation of over-cutting. For sand cutting, spillage is reduced for a 1 [%] reduction of the step size (-4.6%), swing velocity (-2.8%), bank height (-2.8%) or bank slope angle (-1.43%). For rock, spillage is reduced for a 1 [%] reduction of the swing velocity (-0.63%), bank height (-0.63%), cutter inclination angle (-0.62%) or step size (-0.37%). It is suggested that mixing effects related to the swing velocity are incorporated more explicitly in the model. To conclude, the model is in high agreement with calibration data and the SRCSM pump flow number  $\hat{\Phi}$  can be expressed as a function of particle properties such as the settling velocity.

## 6 Conclusion and recommendations

This chapter provides an overview of the conclusions from the sub-questions to formulate a conclusion for the main research question. The intermediate conclusions for the research sub-questions are repeated for clarity.

---

### **What is CSD spillage and what types of spillage can be identified?**

---

In this research, CSD spillage is defined as “any soil that is dislodged above the lowest cutter tip trajectory of a single swing, but is not sucked into the suction pipe”. A classification of spillage based on pumping, mixing and gravitating effects results in six distinct spillage types. It is reasoned that four types can be considered negligible under typical cutting circumstances. The first significant type is named centrifugal advection and is proportional to the radial outflow of suspended particles in close proximity to the cutter ring and is driven by high rotational velocity of the cutter. Centrifugal advection affects spillage rates for all particle sizes but is most pronounced for fine particles such as sand. The second, concurrent spillage type is referred to as rapid redeposition and is governed by the ratio of the particle settling velocity over the mixture velocity.

---

### **What formulations are fundamental to the motion and behaviour of a fluid substance in the physical domain of the cutter head?**

---

Experimental and analytical research provides substantial evidence to confirm that cutter flow resembles a combination of an axial pump near the nose as well as a centrifugal pump effect near the ring (Miltenburg (1983); Den Burger (2003); Nieuwboer et al. (2017)). From the characteristic Reynolds and Euler numbers it can be concluded that the inertial forces render viscosity in the cutter head negligible. For the centrifugal pump dynamics, the flow inside the cutter is considered steady, non-gravitational, inviscid and non-axial. It can be demonstrated that the Navier-Stokes equations therefore reduce to Euler’s pump equation. The axial flow dynamics are governed by the product of the particle volume and radial pressure gradient in the suction mouth. Den Burger observed that there is an inward flow along the entire contour of the cutter head for rotational velocities below a certain ratio of the rotational to the mixture velocity. Above this ratio, the cutter dynamics give rise to a radial outflow that increases with rotational velocity.

---

### **In conjunction with the relevant physical parameters, what concepts and assumptions enable a CSD spillage engineering model?**

---

A spillage model can be set up by taking three steps. First, an advanced geometrical description of the cutter head-bank interface can be derived. Important parameters are the cutter radius and curvature, cutter height, bank height, bank slope angle, cutter inclination angle and the step size of the cutting pattern. Second, a potential flow model can be set up based on flow continuity in the cutter. The cutter is split into two discs with disc 1 at the cutter ring and disc 2 at the nose. Volumetric flow rates are determined for centrifugal advection flow, radial as well as axial inflow

through the nose, rapid redeposition flow, mixture flow and an in situ dredge flow. The model strategy is outlined below

1. Among other assumptions, the pump effects of the leading edge of the cutter blade are considered negligible. This allows for the simplification of Euler's pump equation to a pump affinity law that expresses discharge as a function of radial pressure difference. This affinity law and the height of disc 1 are used to approximate centrifugal advection flow near the ring.
2. For the radial inflow at the nose, the assumption is made that the true pressure at the trailing edge of the cutter is equal to the pressure that is generated in disc 1. As a consequence, the difference in estimated pressure gradients between the discs drives an inflow at disc 2. Again, the pump affinity law is used in conjunction with density considerations to provide an estimate of the flow rate into disc 2.
3. Axial inflow at the nose is added as an optional component in the flow balance but is assumed negligible due to geometrical considerations.
4. A spillage flow for rapid redeposition is found as a function of the rotational velocity, cutting scenario, particle settling velocity, mixture velocity and geometrical parameters for a reference point in the cutter.
5. Straight forward expressions are obtained for the mixture flow rate where the user inputs the mixture velocity.
6. The swing velocity is an input parameter to determine the in situ dredge flow rate.

The resulting continuity balance poses an implicit problem and is solved iteratively. The third step in the model is to rewrite the mass flow rate balance to find the concentrations of outgoing flows. Gravitational acceleration is expected to affect the entrainment rate of particles into the axial flow and increases the concentration of rapid redeposition. Spillage is computed as the mass flow ratios of the spillage components to the mass flow rate of incoming bank material. The resulting continuity balance poses an implicit problem and is solved iteratively. The third step in the model is to rewrite the mass flow rate balance to find the concentrations of outgoing flows. Gravitational acceleration is expected to affect the entrainment rate of particles into the axial flow and increases the concentration of rapid redeposition. Spillage is computed as the mass flow ratios of the spillage components to the mass flow rate of incoming bank material.

---

**Based on the identified physical parameters, concepts and assumptions, how does the model perform relative to experimental data?**

---

The performance of the model can be evaluated using a dimensionless flow number  $\hat{\theta}$  that incorporates the cutter radius, angular velocity and mixture velocity. Two particle sizes are chosen for calibration and only the under-cut mode is considered. The data for sand ( $d_{50} = 180 \text{ E-3 [mm]}$ ) proves useful for the determination of the pump affinity law number since the low settling velocity for sand eliminates the effect of rapid redeposition. Model parameters can be identified for which both

sand and rock ( $d_{50} = 80$  [mm]) spillage is estimated within a 5 [pp] accuracy over the available range of  $\hat{\theta} = \langle 2,6 \rangle$  [-]. Moreover, the plot curvature exhibits a large resemblance with the experimental data for sand as well as rock. For rock, the rapid redeposition component appears to be inversely proportional to the mixture velocity. The relevant flow number for the dredging industry equals  $\hat{\theta} = 2.7$  [-] for which a sensitivity analysis is performed. The dynamics of the governing ratios between centrifugal force, suction force and gravitational force appear to be captured adequately by the model. The influence of the cutter inclination angle appears arbitrary for sand cutting. This is ascribed to a model artefact that is linked to the absence of rapid redeposition where cutter inclination becomes is of higher significance. The model exhibits correct behaviour for a qualitative simulation of over-cutting. For sand cutting, spillage is reduced for a 1 [%] reduction of the step size (-4.6%), swing velocity (-2.8%), bank height (-2.8%) or bank slope angle (-1.43%). For rock, spillage is reduced for a 1 [%] reduction of the swing velocity (-0.63%), bank height (-0.63%), cutter inclination angle (-0.62%) or step size (-0.37%). It is suggested that mixing effects related to the swing velocity should be incorporated more explicitly in the model. To conclude, the model is in high agreement with calibration data and the SRCSM pump flow number  $\hat{\Phi}$  can be expressed as a function of particle properties such as the settling velocity. In conclusion, the research sub-questions have culminated in sufficient results in order to answer the main research question.

## 6.1 Conclusion

---

**What are physical parameters, model concepts and assumptions that give rise to an adaptable, particle size-agnostic engineering model for CSD spillage rates within 5 percentage point accuracy?**

---

The effects of CSD spillage can be adequately captured by a potential flow model with empirical closing relations. Essential spillage flows are centrifugal advection due to radial outflow at the ring and rapid redeposition caused by the settling velocity of the particles. The SRCSM can be set up with only three coefficients that follow from scaling: the pump flow number  $\hat{\Phi}$  (0.58 for sand, 0.92 for rock), for centrifugal flow and the coefficients for rapid redeposition  $f_d$  and its concentration  $f_{cd}$ .

A sensitivity analysis suggests that most cutter head dynamics are adequately incorporated. For typical sand cutting conditions, the highest spillage reduction (-4.6%) is achieved by a 1 [%] smaller step size. For rock, the highest spillage reduction (-0.63%) is achieved for a 1 [%] decrease in swing velocity. The model is less reliable for (non-typical) inverse flow numbers of  $\hat{\theta} = 6$  [-] and higher due to a mixture velocity that drops below zero. In addition, the model is calibrated for a relatively high cutter inclination angle of 45 [deg] and bank angle of 45 [deg]. Caution should be observed with the results. It is also suggested that mixing effects related to the swing velocity are incorporated more explicitly in the model.

A high degree of model *adaptability* is enabled through the modularity of the continuity equation and dimensionless coefficients. The *engineering* requirement of the model is preserved in three ways. First, the implicit analytical model is computable within seconds and the relevant parameters are easily changeable. This contributes to the *tractability* of the model. Second, the assumptions have led to an intuitive model that makes use of realistically known parameters, giving rise to a *discernible* model. Last, the model provides accurate spillage sensitivity feedback for relevant cutting variables. This *informative* feature concludes the engineering property of the model.

## 6.2 Recommendations for further research

This section provides the author's recommendations for further research. It is stressed that the usability of the model should remain focused on its tractability, discernibility and informative value. It is not recommended to perform analyses in the category of computational fluid dynamics for this model.

### 6.2.1 *Mixing effects*

Mixing effects were assumed to relate to the ratio of the centrifugal force and gravitational force. The current model does only incorporates mixing effects through rapid redeposition. For future iterations, it is suggested to make the effects of mixing more prominent. A more elaborate function for the rapid redeposition coefficient  $f_d$  could be established for future development of the model. Mixing dynamics are also an important driver of the spillage mechanism behind violent cutting and buried cutting. For these spillage types a, filling degree of the cutterhead can be found through the ratio of the rotational velocity to the swing velocity. Ploughing was considered a second effect that is related to the saturation of the cutter. The effect of ploughing may be incorporated by evaluating the ratio of rotational velocity over the swing velocity.

### 6.2.2 *Cut surface and teeth contour*

In the current calibration, the bank-cutter interaction is modeled with very high slope and cutter inclination angles. It can be shown that these values would render spillage from the shape of the cutter head significant while it was assumed negligible. It is advised to use more realistic calibration data or to derive a spillage expression for losses due to the bank geometry.

In the current model, the cutter radii have been chosen to represent the radius of the contour that the cutter teeth follow during the rotation. When using flared points (or chisels) for sand cutting, the actual flared-point envelope may be significantly wider than the cutter ring. For rock, the pick-points are stronger and smaller. The pick points will have a limited effect on cutter envelope radius. It is suggested to consider these envelope effects in future model iterations.

### 6.2.3 *Rotation of the cutter head*

Industry observations suggest that the orientation of the suction mouth in terms of angular offset can play an important role for spillage. A parameter that incorporates

this effect may be of great benefit to helping reduce spillage. Implementation of the cutter head rotation seems trivial for the model.

#### 6.2.4 Experimental data

It is strongly recommended to conduct experiments for two reasons. First, experimental data for spillage will enable further model calibration and improve sensitivity correctness to the model parameters. Second, the physical working of the model can be more closely analyzed with experimental data. For example, a freely rotating cutter in water can be mounted with pressure sensors. The results may substantiate the assumptions underlying the SRCSM. The location of the pressure sensors would have to be chosen correctly. For this, section the derivation of Euler’s pump equation in section 3.7 provides a useful foundation.

#### 6.2.5 N-slice model

The SRCSM is based on a 2-disc model for the cutter head shape. This assumption is ideal to determine the inflow at the nose. A further, more advanced flow model can be set up by dividing the cutter in  $n$  slices. This would provide more insight into the flow dynamics but is significantly more complex to solve because more assumptions are to be made for the boundary condition of pressure inside and outside of the cutter. Figure 6.1 depicts a schematic representation this suggestion.

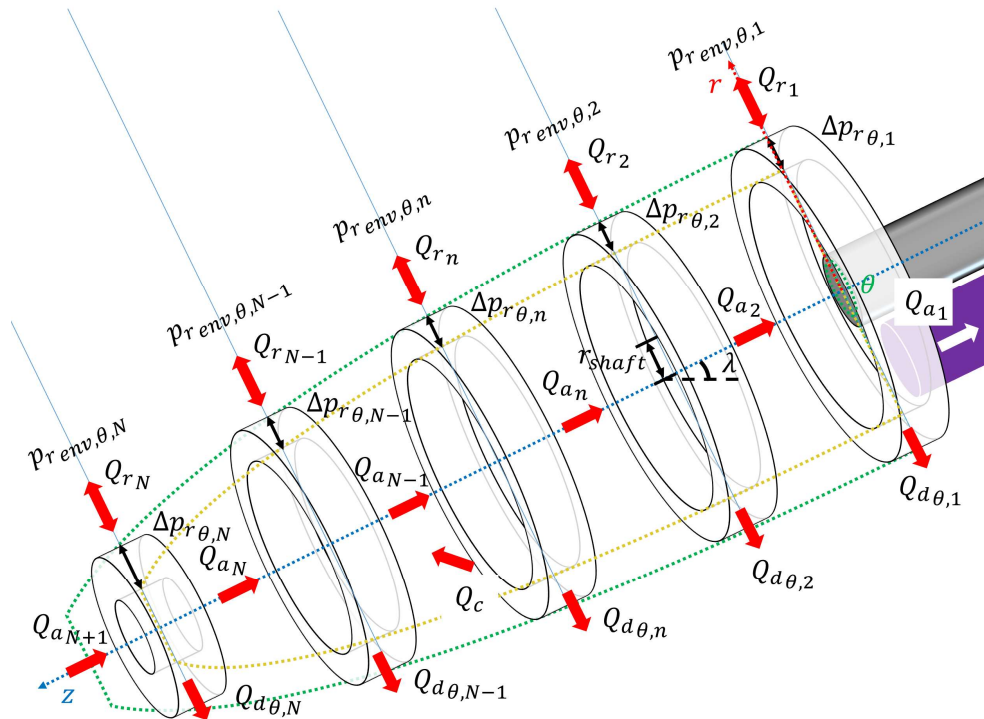


Figure 6.1 Overview of flows for n-slice model

An outflow  $Q_{r_i}$  can be positive or negative for a slice. This results in  $N$  equations for radial flow. If  $Q_{a_{N+1}}$  is assumed negligible, the axial flow rates comprise of  $N - 1$  equations. A solution of the model is proposed to make use of a pressure correction method (van Rhee, 2018) and may take the following steps.

1. First, pressures outside the cutter ( $p_{env,i}$ ) are assumed zero. The pressure gradient now requires  $N$  assumptions for the blade-induced pressures.
2. An average of the trailing edge pressures ( $p_{t,i}$ ) and leading edge ( $p_{l,i}$ ) is estimated  $p_{disc,i}$ . A proportionality with the tangential velocity of the cutter may be assumed.
3. The in situ dredge flow rate  $Q_{c_i}$  per slice is determined based on the cutter geometry.
4. The rapid redeposition flow rate  $Q_{d,i}$  per slice can be estimated similar to the SRCSM model.
5. The volumetric flow rates  $Q_{a,i}$  can be determined using Bernoulli's principle and the pressure gradient between slices  $\Delta p_{a,\theta,i}$ . Energy losses may be accounted for in this step.
6. The volumetric flow rates of radial flow  $Q_{r,i}$  are similarly determined with the pressure gradient  $\Delta p_{r,\theta,i}$ .
7. The obtained volumetric flow rate may violate the continuity equation per disc for the initial pressure assumptions. The initial pressure assumptions  $p_{disc,i}$  is now adapted by iterating over the pressure assumption. Where inflow is too small, the disc pressures are lowered and reversely. An accuracy threshold can be set to find the pressure profile in the cutter for which the continuity balance holds.
8. Spillage can be computed based on the mass flow rate balance per disc.

As mentioned earlier, the SRCSM model performs well. An N-slice spillage model may compromise on calculation speed to improve the model accuracy. A careful consideration should be made to evaluate the added value of the model for engineering purposes.

## 7 List of symbols

### 7.1 Symbols

<i>Symbol</i>	<i>Unit</i>	<i>Description</i>
$A$	$m^2$	area
$Eu$	-	euler number
$Fr$	-	froude number
$D$	m	diameter
$G$	$m/s^2$	characteristic gravitation-scale
$P$	-	production rate
$L$	m	characteristic length-scale
$P$	-	production rate
$\hat{P}$	$n/m^2$	characteristic pressure-scale
$Q$	$m^3/s$	flow
$R$	m	radius
$Re$	-	reynolds number
$S$	-	spillage rate
$St$	-	strouhal number
$T$	s	characteristic time-scale
$\hat{V}$	$m^3$	volume
$V$	m/s	characteristic velocity-scale
$b$	m	height
$c$	-	concentration
$e$	-	unity vector
$f$	-	factor
$g$	$m/s^2$	gravitational acceleration
$h$	m	height (of the bank)
$k$	m	chord
$l$	m	length
$m$	kg	mass
$n$	rpm	rotational velocity of the cutter head
$p$	$n/m^2$	pressure
$r$	m	radius
$s$	m	characteristic triangle scale
$u$	m/s	azimuthal (tangential) velocity
$v$	m/s	absolute velocity
$w$	m/s	relative velocity
$x$	m	orthogonal distance of cutter centroid to bank top
$\Delta$	-	difference
$\Phi$	-	dimensionless head
$\hat{\Phi}$	-	pump flow number
$\alpha$	rad	angle between radial and axial component
$\beta$	rad	blade angle
$\lambda$	rad	cutter inclination angle
$\hat{\theta}$	-	inverse flow number / adapted flow number
$\kappa$	rad	angle between radial and azimuthal component
$\gamma$	rad	cutter inclination angle
$\mu$	$m^2/s$	kinematic viscosity

$\xi$	rad	bank slope angle
$\rho$	kg/m <sup>3</sup>	density
$\sigma$	kg/(m s <sup>2</sup> )	stress
$\omega$	rad/s	rotational velocity

## 7.2

### Indices

<i>Indice</i>	<i>Description</i>
0 (zero)	origin
1	disc 1 / centrifugal advection
2	disc 2 / rapid redeposition
3	buried cutting
4	violent cutting
5	bank instability
6	geometry
<i>a</i>	axial
<i>b</i>	bank
<i>c</i>	in situ
<i>cf</i>	centrifugal
<i>cut</i>	cut surface
<i>d</i>	(re)deposition
<i>dr</i>	dry
<i>dyn</i>	dynamic
<i>eq</i>	equivalent
<i>g</i>	gravitation
<i>i</i>	indicator for element number
<i>l</i>	leading edge
<i>m</i>	mixture
<i>max</i>	max
<i>min</i>	min
<i>nose</i>	cutter nose location
<i>od</i>	over depth
<i>p</i>	particle
<i>pen</i>	penetration
<i>pipe</i>	pipe
<i>plate</i>	plate
<i>prev</i>	previous
<i>post</i>	posterior
<i>q</i>	quartz
<i>r</i>	radial
<i>ratio</i>	ratio
<i>ref</i>	reference
<i>ring</i>	cutter ring location
<i>s</i>	swing
<i>shaft</i>	shaft
<i>step</i>	step
<i>suc</i>	suction
<i>t</i>	trailing edge
<i>tip</i>	tip of cutter (toc)
<i>tot</i>	total
<i>ts</i>	terminal settling

<i>type</i>	cutting scenario
<i>vs</i>	spatial
<i>w</i>	water
<i>wet</i>	submerged
$\theta$	azimuthal

## 8 Glossary

<i>Word</i>	<i>Synonym(s)</i>	<i>Description</i>
Blade	Arm	Core element of the cutter head
Blade envelope		Envelope of the blade rotation around the cutter axis
Borrow Area		Area from which material is excavated by the cutter
BOS		Bottom Of Suction: lowest point of the suction mouth
Centrifugal Advection	High rotational velocity-induction	Process in which suspended particles are transported in radial direction through the flow of water
Chisel	knife, edge	Medium-size cutting tool for granular material
CSD		Cutter Suction Dredge
Cut face	Bank height	Depth of the tip of the cutter into the bank
Cutter head	Cutter	Synonym for cutter head
Back Swing	Over-cut	Cutter head swing in over-cut mode
Dig face		Net dredge depth
Dig Swing	Under-cut	Cutter head swing in under-cut mode
Euler Equations		Form of Navier-Stokes equations governing inviscid (and adiabatic) flow
Navier Stokes Equations	NS equations	Equations governing the motion of fluid flow
Euler's Pump Equation		Equation that governs the pressure head, fluid velocities and geometry of centrifugal pumps
Flared-point		Tip of the flare
Flared-point Envelope		Envelope of the flared point of the blade rotation
Hub		Steel three threaded screw connection between the cutter head and shaft
Ladder		Construction upon which the cutter head is mounted
Nose		Name of the top of the cutter head
Pay face		Depth that dredgers are paid for
Pick-point		Short, strong cutting tool for rock
Rapid Redeposition		Spillage type where suspended sediment settles back onto the bank before reaching the suction mouth
Ring		Steel ring for structural integrity
Rope guard	Rubber bearing	Drive axis protection
Sand Cutting Spillage Model	SCSM	Reference to the model for cutting of sand (Werkhoven et al., 2018)
Sand-Rock Cutting Spillage Model	SRCSM	Reference to the model for cutting of sand and rock as presented in this thesis and in (Werkhoven et al., 2019b)
Shaft		Ladder element that transmits torque
Skirts		Optional steel plates welded onto the blades to extend the blades
Spade		Wide-bladed steel cutting tool that enables a continuous cutter envelope
Spud (auxiliary)		Spud that moves the spud carriage back to its start position
Spud (carrier)		Spud that serves as center of rotation during a swing
Spud carriage		Spud moving system at the stern of the cutter
Suction mouth		Cutout in the back plate that forms the entrance of the suction pipe

Swing velocity	Haul velocity	Velocity of the cutter head in lateral direction
Tooth		Steel pick-point for the cutting of rock
TOC		Tip Of Cutter: Location of the lowest point of the cutter envelope
Winch		Mechanical device that connects the pulling cables from the vessel to the anchors, providing sufficient tension on the cables

## 9 Bibliography

- Andrassy, C. and Herbich, J. (1988). "Generation of resuspended sediment at the cutterhead." *The Dock and Harbour Authority*, 68(797), pp. 207–216.
- Burger, M. den. (2003). "Mixture forming processes in dredge cutter heads." *Ph.D. Dissertation*, Delft University of Technology, The Netherlands.
- Becker, J., van Eekelen, E., van Wiechen, J., de Lange, W., Damsma, T., Smolders, T. and van Koningsveld, M. (2015). "Estimating source terms for far field dredge plume modelling." *Journal of Environmental Management*, 149, pp. 282-293.
- Collins, M. A. (1995). "Dredging-induced near-field resuspended sediment concentrations and source strengths." *Miscellaneous Paper D-95-2*, U.S. Army Engineer Waterways Experiment Station, Vicksburg, Miss.
- Dekker, M. A., den Burger, M., Kruyt, N. P., and Vlasblom, W. J. (2003). "Experimental and numerical investigation of cutter head dredging flows." *Journal of Waterway, Port, Coastal and Ocean Engineering*, ASCE, Vol. 129, No. 5, pp. 203-209.
- GLDD, accessed 21 March  
<<https://www.gldd.com/great-lakes-announces-receipt-87-million-awarded-work-including-47-million-award-charleston-deepening/>>
- Hayes, D. (1986). "Development of a near field source strength model to predict sediment resuspension from cutter suction dredges." *MS thesis*, Mississippi State University, Mississippi State, Miss.
- Hayes, D. F., Crockett, T. R., Ward, T. J., and Averett, D. (2000). "Sediment Resuspension during Cutterhead Dredging Operations." *Journal of Waterway, Port, Coastal, and Ocean Engineering*, 126(3), pp. 153-161
- Hayes, D., McLellan, T., and Truitt, C. (1988). "Demonstrations of innovative and conventional dredging equipment at Calumet Harbor, Illinois." *Miscellaneous Paper EL-88-1*, U.S. Army Engineer Waterways Experiment Station, Vicksburg, Miss.
- Nakai, O. (1978). "Turbidity generated by dredging projects." *Proc., 3<sup>rd</sup> U.S./Japan Experts Meeting*, U.S. Army Engineer Water Resources Support Center, Ft. Belvoir, Va.
- Joanknecht L.W.F., (1976). "A review of Dredge Cutter Head Modeling & Performance." *Proceedings WODCON VII*, San Francisco, California, USA, pp. 995-1016.
- Miedema, S.A. (2017, November 11). Personal correspondence.
- Miltenburg, C.J.M. (1983). "Stroming en mengselvorming in grote snijkoppen (Flow and Mixture Forming in large cutterheads)." *Laboratoriumopdracht La0/8/101*, Laboratory of Soil Transportation, Delft University of Technology, Delft, The Netherlands. (in Dutch).
- Mol, A. (1977a). "Stroombeeld rond en in Cutter deel II: vrij in water draaiend; injecties met kleurstof (Flow around and in a cutter head part II: freely rotating in water; injections with dye)." *WL/Delft Hydraulics BAGT 236*, The Netherlands. (in Dutch).
- Moret, G.E. (1977a). "Stroombeeld rond en in Cutter deel I: Stroombeeld rondom cutter bij kunstmatige taluds; injecties met kleurstof (Flow around and in a cutter head part II: flow around cutter head placed in an artificial bank; injections with dye)." *WL/Delft Hydraulics BAGT 235*, The Netherlands. (in Dutch).
- Ngan-Tillard, D., Haan, J., Laughton, D., Mulder, A. and Nooy van der Kolff, A. (2009). "Index test for the degradation potential of carbonate sands during hydraulic transportation." *Eng. Geol.*, 108(1-2), pp. 54-64
- Nakai, O. (1978). "Turbidity generated by dredging projects." *Proc., 3<sup>rd</sup> U.S./Japan Experts Meeting*, U.S. Army Engineer Water Resources Support Center, Ft. Belvoir, Va.

- Nieuwboer, B.J. (2018, March 6). Personal correspondence.
- Ramsdell, R. C., Miedema, S. A., Remme, J. J. "Principles of Production Engineering Models," *Proceedings of the Twenty- Second World Dredging Congress, WODCON XXII, Shanghai, China, April 22-25, 2019.*
- Nieuwboer, B.J., Keetels, G.H., van Rhee., C. (2017). "Flow velocities in an axi-symmetrical rotating cutter suction head" . *18<sup>th</sup> International Conference on Transport and Sedimentation of Solid Particles, Prague, Czech Republic*
- Slota, L.S. (1968). "Flow visualization techniques used in dredge cutter head evaluation." *Proceedings of WODCON II 1968, Rotterdam, The Netherlands, pp. 56-77.*
- Steinbusch, P.J., Vlasblom, W.J., den Burger, M. and Kruyt, N.P. (1999). "Numerical Simulation of the Flow Generated by Cutter Heads." *Slurry Handling and Pipeline Transport, 14<sup>th</sup> International conference, Hydrotransport 14, Maastricht, The Netherlands.*
- van Rhee (2018, April 09). Personal Correspondence.
- van Rhee, C., & Bezuijen, A. (2001). "The breaching of sand investigated in large-scale model tests." *Coastal Engineering Proceedings, 1(26).*
- Van Rhee, C. (2018, September 13). Personal Correspondence.
- Vlasblom, W.J. and van Hemmen, A.J.M. (2006) "The Shape of and the Position of Teeth on a Cutter Head. The background information." *CEDA Dredging Days 2006 - Protection of the Coastline. Dredging and Sustainable Development, Tangier, Morocco*
- Werkhoven, J. J., Nieuwboer, B.J., Louis, A.A., Ramsdell, R.C., and Miedema, S.A. (2018) "A pseudo-analytical model for CSD spillage due to rotational velocity-induced flow," *Proceedings of the Western Dredging Association Dredging Summit & Expo '18, Norfolk, VA, USA, June 25-28, 2018.*
- Werkhoven, J. J., Nieuwboer, B.J., Louis, A.A., Ramsdell, R.C., and Miedema, S.A. (2019a) "Can a preliminary model describe CSD Spillage due to centrifugal advection?" *Terra & Aqua, 153, pp 23-35*
- Werkhoven, J. J., Nieuwboer, B.J., Ramsdell, R.C., and Miedema, S.A. (2019b) "CSD Spillage Model for Sand and Rock," *Proceedings of the Twenty-Second World Dredging Congress, WODCON XXII, Shanghai, China, April 22-25, 2019.*
- Vlasblom, W.J (2003) "Lecture Notes Wb3408b" *Version 2003, TU Delft, Dredging equipment, ch-3*

## A Derivation of Bernoulli's principle

A derivation is provided that demonstrates how Bernoulli's principle is found from an energy balance for a fluid mass. Work and Energy relation to power according to equation (114)

$$W = E_2 - E_1 = (p_2 - p_1)V \quad (114)$$

Neglecting friction, for net Work (Energy) we find for a fluid section of mass  $m$  traveling along a streamline in a 3-dimensional space

$$E_2 - E_1 = \left( mgh_2 + \frac{mv_2^2}{2} \right) - \left( \rho Vgh_1 + \frac{mv_1^2}{2} \right) \quad (115)$$

Where  $v_z, z$  equals the velocity in  $z$ -direction at location  $i$ . Equations (114) and (115) are combined to obtain

$$(p_2 - p_1)V = \left( mgh_1 + \frac{mv_1^2}{2} \right) - \left( mgh_2 + \frac{mv_2^2}{2} \right) \quad (116)$$

Or using  $m = \rho V$  and reorganizing to find for the elevation head gain

$$\underbrace{h_2 - h_1}_{\text{elevation head}} = \underbrace{\frac{p_1 - p_2}{\rho g}}_{\text{pressure head}} - \underbrace{\frac{v_2^2 - v_1^2}{2g}}_{\text{velocity head}} \quad (117)$$

The latter ratio is defined as the velocity head. Bernoulli becomes useful for the derivation of the Euler pump equation after the static pressure has been found. The elevation head is a representation of the fluids weight. The pressure head is a result of static pressure; the pressure the fluid exerts on its environment. Lastly, the velocity head results from kinetic energy and relates to dynamic pressure.

## B Velocity triangles of a pump

This appendix elaborates on the goniometric properties of velocity triangles that are used for the calculation of pump power.

### B.1 2D Velocity triangles

Let us consider two-dimensional fluid velocity vectors of a unit mass in the  $r\theta$ -plane. Velocities in the  $z$ -direction are neglected in this section.

A unit mass, in a cylindrical coordinate system, travels along a blade (depicted in yellow) with a velocity  $\mathbf{w}$  [m/s] relative to the blade. Since the blade has absolute velocity  $\mathbf{u}$  [m/s], the sum of  $\mathbf{u}$  and  $\mathbf{w}$  yields the absolute velocity  $\mathbf{v}$  [m/s] of the unit mass. Here,  $\mathbf{u}$  is depicted in green and  $\mathbf{v}$  is depicted in grey, with components  $v_\theta$  (azimuthal) in grey and  $v_r$  (radial) in red.

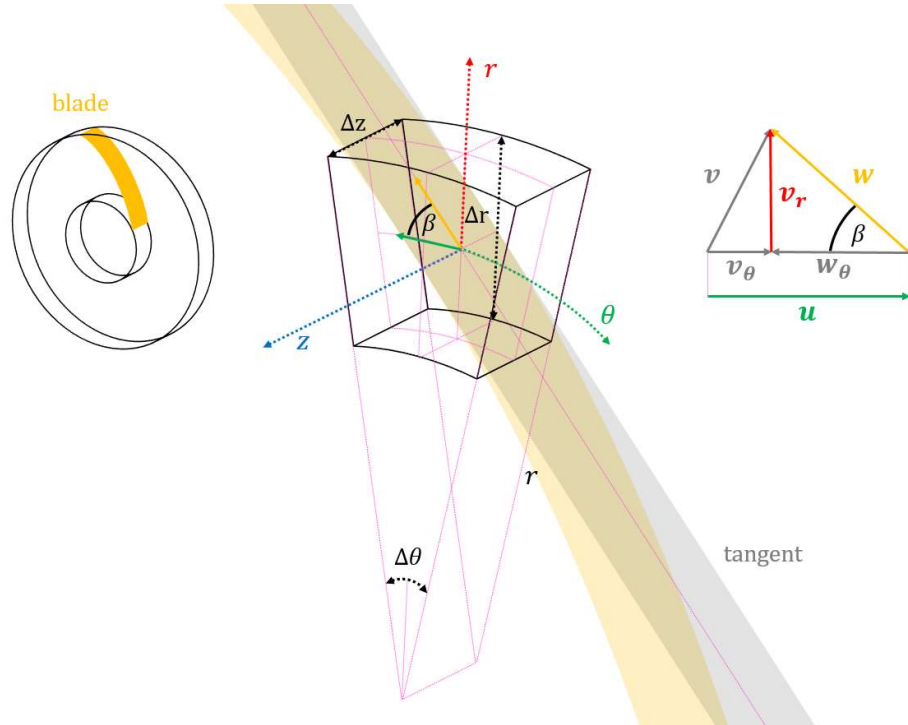


Figure B.1: Velocity Triangles in 2D

From the triangle  $\Delta uvw$  and vector length  $x \stackrel{\text{def}}{=} \|\mathbf{x}\|$ , a series of geometric relationships can be formulated as shown in equation (118).

$$\begin{aligned}
 w^2 &= w_r^2 + w_\theta^2 \\
 w_\theta = \|\mathbf{w}_\theta\| &= \|\mathbf{w}\| \cdot \cos \beta = v_\theta + \omega r \\
 w_r = \|\mathbf{w}_r\| &= \|\mathbf{w}\| \cdot \sin \beta \\
 v_\theta = \|\mathbf{v}_\theta\| &= \|\mathbf{u}\| + \|\mathbf{w}_\theta\| = -\omega r + w_\theta \\
 v_r = \|\mathbf{v}_r\| &= \|\mathbf{w}_r\| \\
 u = -\|\mathbf{u}\| &= -\|\boldsymbol{\omega} \cdot \mathbf{r}\|
 \end{aligned} \tag{118}$$

The geometrical relationships in the velocity triangle dictate that

$$\begin{aligned} v_1^2 &= \|\mathbf{u}_1\|^2 + \|\mathbf{w}_1\|^2 - 2 \cdot \|\mathbf{u}_1\| \cdot \|\mathbf{w}_1\| \cdot \cos \beta_1 \\ v_2^2 &= \|\mathbf{u}_2\|^2 + \|\mathbf{w}_2\|^2 - 2 \cdot \|\mathbf{u}_2\| \cdot \|\mathbf{w}_2\| \cdot \cos \beta_2 \end{aligned} \quad (119)$$

Or rewritten to alternative forms

$$\begin{aligned} v_1^2 &= u_1^2 + w_1^2 - 2u_1w_1 \cos \beta_1 \\ v_2^2 &= u_2^2 + w_2^2 - 2u_2w_2 \cos \beta_2 \end{aligned} \quad (120)$$

From the shape of the linearized velocity triangle, which is valid for an infinitesimally small element, the angle  $\beta$  between the tangential and relative velocities is given in equation (121).

$$\left. \frac{dr}{r d\theta} \right|_{r\theta z} = \tan \beta \quad (121)$$

It is also known that this angle equals the ratio of radial and azimuthal velocities, hence the following relations are true

$$\begin{aligned} \frac{w_r}{w_\theta} &= \frac{v_r}{w_\theta} = \tan \beta \\ \Leftrightarrow \cot \beta &= \frac{w_\theta}{w_r} \end{aligned} \quad (122)$$

Equations (121) and (122) can be combined to find the angular change with respect to the radius along a streamline as shown in equation (123).

$$\left. \frac{d\theta}{dr} \right|_{r\theta z} = \frac{w_\theta}{r v_r} \quad (123)$$

We also know that the discharge that is delivered by a pump must be in accordance with equation (124).

$$w_r = \frac{Q}{f_\gamma 2\pi r b} \quad (124)$$

Where  $f_\gamma$  is a factor that limits the outflow area of the centrifugal pump.

## B.2 3D Velocity Triangles

When considering a blade that is curved in the axial direction too, the velocity triangles become more complex. The absolute and relative fluid velocities can now be decomposed in three directions.

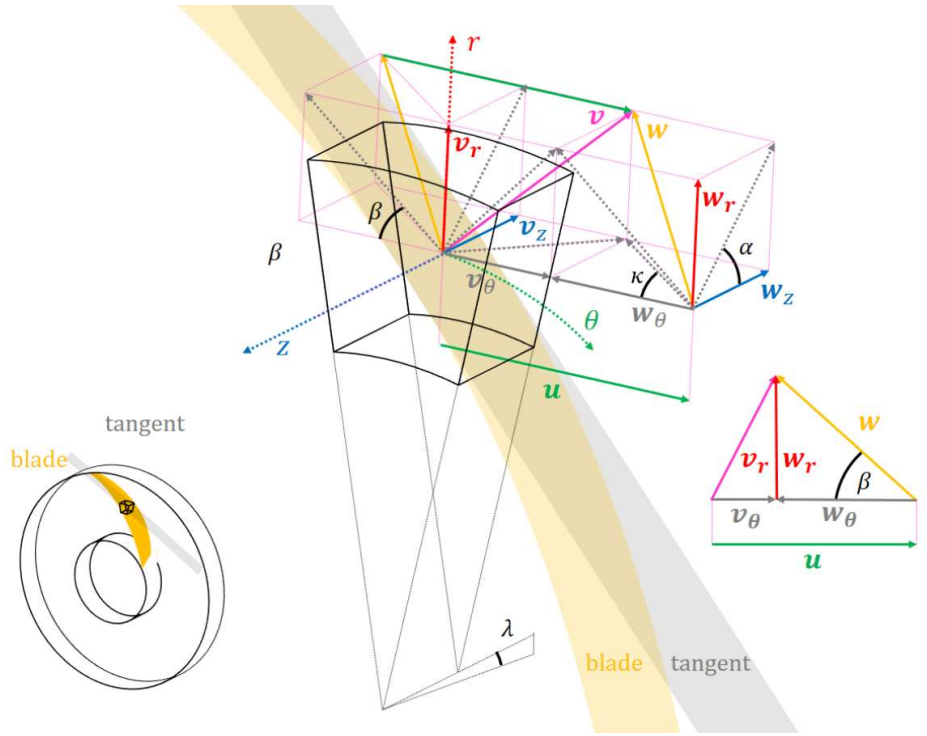


**Figure B.2: Velocity Triangles in 3D and 2D**

An angle  $\alpha$  can be presumed that represents the curvature of the blade in the  $z$ -direction

$$\left. \frac{dr}{dz} \right|_{r\theta z} = \tan \alpha \quad (125)$$

And this angle equals the ratio of radial and axial velocities, which are given in two forms in equation (126).

$$\begin{aligned} \frac{w_r}{w_z} &= \frac{v_r}{w_z} = \tan \alpha \\ \Leftrightarrow \cot \alpha &= \frac{w_z}{w_r} \end{aligned} \quad (126)$$

Combining equations (125) and (126) yields

$$\left. \frac{dr}{dz} \right|_{r\theta z} = \frac{w_r}{w_z} \quad (127)$$

Similarly, an angle  $\kappa$  can be presumed that represents the curvature of the blade in the  $z$ -direction

$$\left. \frac{dz}{rd\theta} \right|_{r\theta z} = \tan \kappa \quad (128)$$

By definition, this angle equals the ratio of radial and axial velocities as given in equation (129).

$$\frac{w_z}{w_\theta} = \frac{v_z}{w_\theta} = \tan \kappa \quad (129)$$

Combining equations (128) and (129) gives a relationship that can be used in a three-dimensional derivation of pressure-discharge relationships of a pump.

$$\left. \frac{d\theta}{dz} \right|_{r\theta z} = \frac{w_\theta}{rw_z} \quad (130)$$

## C Derivation of centrifugal pump affinity laws from Cauchy momentum equation

This appendix demonstrates how the pump affinity laws can be derived in a cylindrical coordinate system. For this, the Cauchy momentum equation and Bernoulli's principle are used, among other relationships.

### C.1 Derivation of Cauchy momentum equation

Consider a constant mass. The rate of change in momentum equals the net force on an element with volume  $V$  [m<sup>3</sup>]

$$\frac{d}{dt} \int_V \rho \cdot \mathbf{v} dV = \int_V \rho \cdot \frac{D\mathbf{v}}{Dt} dV \quad (131)$$

Where  $\mathbf{v}$  [m/s] is the flow velocity vector field,  $\rho$  equals the density [kg/m<sup>3</sup>] and  $t$  represents time [s]. The net molecular force acts within a thin surface layer of the control volume. In a three-dimensional space, each of the 3 sets of surface planes experiences a 3-component force, giving rise to 9 components in all. These form the stress tensor  $\boldsymbol{\sigma}$  [N/m<sup>2</sup>] so that the force exerted per unit area across a surface element, or  $d\mathbf{S} = \hat{\mathbf{n}} \cdot dS$ , reads

$$\mathbf{f}_\sigma = \boldsymbol{\sigma} \cdot \hat{\mathbf{n}} \Rightarrow \mathbf{F}_\sigma = \int_S \boldsymbol{\sigma} \cdot d\mathbf{S} \quad (132)$$

Where  $\mathbf{n}$  points on the fluid on the other side. The net force consists of body forces and molecular forces internal to the fluid. The only body force assumed here is gravity as given in equation (132).

$$\mathbf{F}_g = \int_V \rho \cdot \mathbf{g} dV \quad (133)$$

The total force per element is therefore the sum of molecular forces and body forces

$$\int_V \rho \cdot \frac{D\mathbf{v}}{Dt} dV = \int_S \boldsymbol{\sigma} \cdot d\mathbf{S} + \int_V \rho \cdot \mathbf{g} dV \quad (134)$$

Which can be rewritten using the divergence of sigma ( $\nabla \cdot \boldsymbol{\sigma}$ )

$$\int_V \rho \cdot \frac{D\mathbf{v}}{Dt} dV = \int_V \nabla \cdot \boldsymbol{\sigma} \cdot d\mathbf{V} + \int_V \rho \cdot \mathbf{g} dV \quad (135)$$

Equation (135) can be reduced to find the Cauchy momentum equation as presented in equation (136).

$$\rho \frac{D\mathbf{v}}{Dt} = \nabla \cdot \boldsymbol{\sigma} + \rho \cdot \mathbf{g} \quad (136)$$

This equation is valid provided that the continuity equation holds. For completeness it should be noted that this equation is valid for non-relativistic momentum transport.

## C.2 Velocities In a cylindrical coordinate system

The material derivative on the left-hand side of Eq. (136) equals

$$\frac{D\mathbf{v}}{Dt} = \frac{\partial \mathbf{v}}{\partial t} + \frac{\partial \mathbf{v}}{\partial r} \frac{dr}{dt} + \frac{\partial \mathbf{v}}{\partial \theta} \frac{d\theta}{dt} + \frac{\partial \mathbf{v}}{\partial z} \frac{dz}{dt} \quad (137)$$

Since unit vectors in a cylindrical coordinate system are not fixed, the unit vectors should also be differentiated. Unit vectors with respect to the radius are constant. The azimuthal rate of change of the radial unit vector  $\mathbf{e}_r$  is equal to the azimuthal unit vector  $\mathbf{e}_\theta$ , while the azimuthal rate of change of the azimuthal unit vector is the negative radial unit vector. These relations are given in equation (138), (139) and (140).

$$\frac{\partial \mathbf{e}_r}{\partial r} = \frac{\partial \mathbf{e}_\theta}{\partial r} = \frac{\partial \mathbf{e}_z}{\partial r} = 0 \quad (138)$$

$$\frac{\partial \mathbf{e}_r}{\partial \theta} = \mathbf{e}_\theta \quad (139)$$

$$\frac{\partial \mathbf{e}_\theta}{\partial \theta} = -\mathbf{e}_r \quad (140)$$

The partial derivative at right-hand side of eq. (137) is located at fixed position hence unit vectors are not subject to temporal change and can be set to zero.

$$\frac{\partial \mathbf{v}}{\partial t} = \frac{\partial v_r}{\partial t} \mathbf{e}_r + \frac{\partial v_\theta}{\partial t} \mathbf{e}_\theta + \frac{\partial v_z}{\partial t} \mathbf{e}_z \quad (141)$$

The remaining terms at the right hand side of equation (137) can be rewritten by making use of the definitions in equation (142).

$$v_r \stackrel{\text{def}}{=} \frac{dr}{dt}, \quad \frac{v_\theta}{r} \stackrel{\text{def}}{=} \frac{d\theta}{dt}, \quad v_z \stackrel{\text{def}}{=} \frac{dz}{dt} \quad (142)$$

Substitution in equation (137) yields equation (143), (144) and (145) for the partial derivatives of the radial, azimuthal and axial axes respectively.

$$\begin{aligned} \frac{dr}{dt} \frac{\partial \mathbf{v}}{\partial r} &= v_r \frac{\partial \mathbf{v}}{\partial r} \\ &= v_r \left[ \frac{\partial v_r}{\partial r} \mathbf{e}_r + v_r \frac{\partial \mathbf{e}_r}{\partial r} + \frac{\partial v_\theta}{\partial r} \mathbf{e}_\theta + v_\theta \frac{\partial \mathbf{e}_\theta}{\partial r} + \frac{\partial v_z}{\partial r} \mathbf{e}_z + v_z \frac{\partial \mathbf{e}_z}{\partial r} \right] \\ &= v_r \left[ \frac{\partial v_r}{\partial r} \mathbf{e}_r + \frac{\partial v_\theta}{\partial r} \mathbf{e}_\theta + \frac{\partial v_z}{\partial r} \mathbf{e}_z \right] \end{aligned} \quad (143)$$

$$\begin{aligned} \frac{d\theta}{dt} \frac{\partial \mathbf{v}}{\partial \theta} &= \frac{v_\theta}{r} \frac{\partial \mathbf{v}}{\partial \theta} \\ &= \frac{v_\theta}{r} \left[ \frac{\partial v_r}{\partial \theta} \mathbf{e}_r + v_r \frac{\partial \mathbf{e}_r}{\partial \theta} + \frac{\partial v_\theta}{\partial \theta} \mathbf{e}_\theta + v_\theta \frac{\partial \mathbf{e}_\theta}{\partial \theta} + \frac{\partial v_z}{\partial \theta} \mathbf{e}_z + v_z \frac{\partial \mathbf{e}_z}{\partial \theta} \right] \\ &= \frac{v_\theta}{r} \left[ \frac{\partial v_r}{\partial \theta} \mathbf{e}_r + v_r \mathbf{e}_\theta + \frac{\partial v_\theta}{\partial \theta} \mathbf{e}_\theta + v_\theta (-\mathbf{e}_\theta) + \frac{\partial v_z}{\partial \theta} \mathbf{e}_z \right] \\ &= \frac{v_\theta}{r} \left[ \left( \frac{\partial v_r}{\partial \theta} - v_\theta \right) \mathbf{e}_r + \left( \frac{\partial v_\theta}{\partial \theta} + v_r \right) \mathbf{e}_\theta + \frac{\partial v_z}{\partial \theta} \mathbf{e}_z \right] \end{aligned} \quad (144)$$

$$\begin{aligned}
\frac{dz}{dt} \frac{\partial \mathbf{v}}{\partial z} &= v_z \frac{\partial \mathbf{v}}{\partial z} \\
&= v_r \left[ \frac{\partial v_r}{\partial z} \mathbf{e}_r + v_r \frac{\partial \mathbf{e}_r}{\partial z} + \frac{\partial v_\theta}{\partial z} \mathbf{e}_\theta + v_\theta \frac{\partial \mathbf{e}_\theta}{\partial z} + \frac{\partial v_z}{\partial z} \mathbf{e}_z + v_z \frac{\partial \mathbf{e}_z}{\partial z} \right] \\
&= v_r \left[ \frac{\partial v_r}{\partial z} \mathbf{e}_r + \frac{\partial v_\theta}{\partial z} \mathbf{e}_\theta + \frac{\partial v_z}{\partial z} \mathbf{e}_z \right]
\end{aligned} \tag{145}$$

Equation (141), (143), (144) and (145) can now be accumulated by unit vector products and substituted in equation (137) to find the material derivative.

$$\begin{aligned}
\frac{D\mathbf{v}}{Dt} &= \left[ \frac{\partial v_r}{\partial t} + v_r \frac{\partial v_r}{\partial r} + \frac{v_\theta}{r} \frac{\partial v_r}{\partial \theta} - \frac{v_\theta^2}{r} + v_z \frac{\partial v_r}{\partial z} \right] \mathbf{e}_r \\
&+ \left[ \frac{\partial v_\theta}{\partial t} + v_r \frac{\partial v_\theta}{\partial r} + \frac{v_\theta}{r} \frac{\partial v_\theta}{\partial \theta} + \frac{v_\theta v_r}{r} + v_z \frac{\partial v_\theta}{\partial z} \right] \mathbf{e}_\theta \\
&+ \left[ \frac{\partial v_z}{\partial t} + v_r \frac{\partial v_z}{\partial r} + \frac{v_\theta}{r} \frac{\partial v_z}{\partial \theta} + v_z \frac{\partial v_z}{\partial z} \right] \mathbf{e}_z
\end{aligned} \tag{146}$$

### C.3 Derivation of continuity equation

The continuity equation for a cylindrical coordinate system is found by considering an infinitesimally small control volume as depicted in Figure C.1.

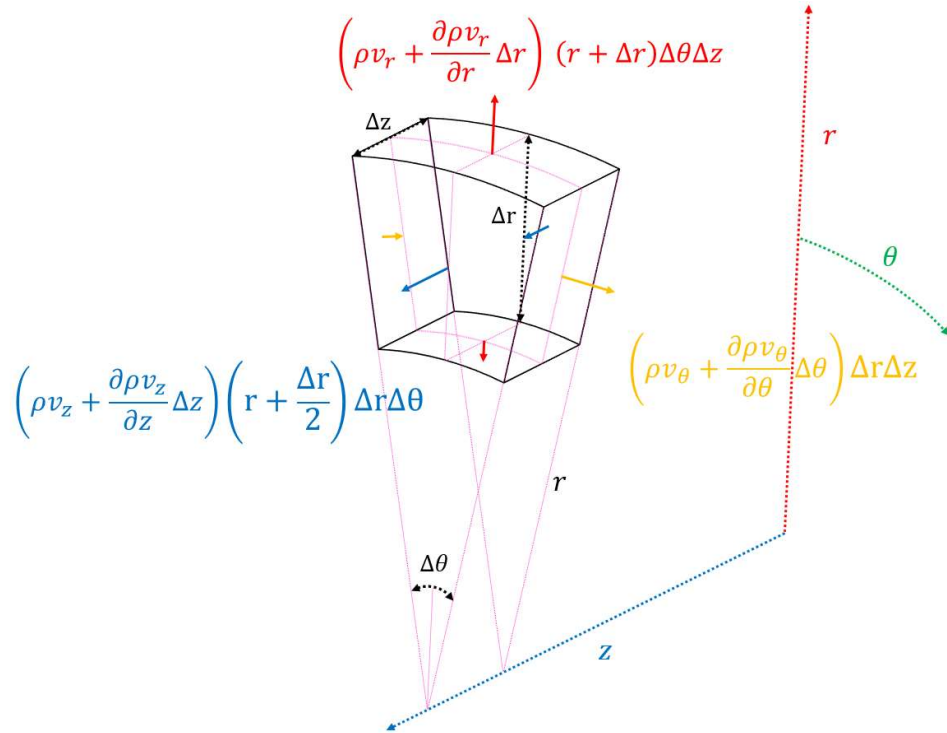


Figure C.1: Velocity components of an infinitesimally small control volume .

The differential control volume is bound as given in equation (147).

$$dV = \left( r + \frac{\Delta r}{2} \right) \Delta r \Delta \theta \Delta z \tag{147}$$

The radial rate change of the mass balance can be found by summing all contributions in the radial direction.

$$\left(\rho v_r + \frac{\partial \rho v_r}{\partial r} \Delta r\right)(r + \Delta r)\Delta\theta\Delta z - \rho v_r r \Delta\theta\Delta z \quad (148)$$

Equation (148) can be rewritten through division by  $\Delta r \Delta\theta \Delta z$  to find that the first and last terms cancel out. Additionally,  $\Delta r$ ,  $\Delta\theta$ ,  $\Delta z$  are let to zero so that in the fourth term in equation (149),  $\partial \rho v_r$ , can be considered negligible.

$$\rho \frac{v_r}{\Delta r} r + \frac{\partial \rho v_r}{\partial r} r + \rho \frac{v_r}{\Delta r} \Delta r + \frac{\partial \rho v_r}{\partial r} \Delta r - \rho \frac{v_r}{\Delta r} r \quad (149)$$

The result is equation (149).

$$\frac{1}{r} \rho v_r + \frac{\partial \rho v_r}{\partial r} \quad (150)$$

A similar procedure is performed in the  $\theta$ -direction and  $z$ -direction that yields the terms from equation (151) and (152).

$$\frac{1}{r} \frac{\partial \rho v_\theta}{\partial \theta} \quad (151)$$

$$\frac{\partial \rho v_z}{\partial z} \quad (152)$$

The rate of change of mass is

$$\frac{\partial \rho}{\partial t} \quad (153)$$

Combining terms (153), (150), (151) and (152) respectively we find for the continuity equation

$$\frac{\partial \rho}{\partial t} + \frac{1}{r} \rho v_r + \frac{\partial \rho v_r}{\partial r} + \frac{1}{r} \frac{\partial \rho v_\theta}{\partial \theta} + \frac{\partial \rho v_z}{\partial z} = 0 \quad (154)$$

Let us consider a fluid that is incompressible. Assuming this steady state, i.e.  $\frac{\partial \rho}{\partial t} = 0$ , division by  $\rho$  and rearrangement of the radial components of the velocity by making use of the product rule, gives equation (155).

$$\frac{1}{r} \frac{\partial (r v_r)}{\partial r} + \frac{1}{r} \frac{\partial v_\theta}{\partial \theta} + \frac{\partial v_z}{\partial z} = 0 \quad (155)$$

#### C.4 Derivation of divergence of stress tensor

Again, an infinitesimally small control volume is considered with the aim to find the divergence of the stress tensor in the Cauchy momentum equation (136).

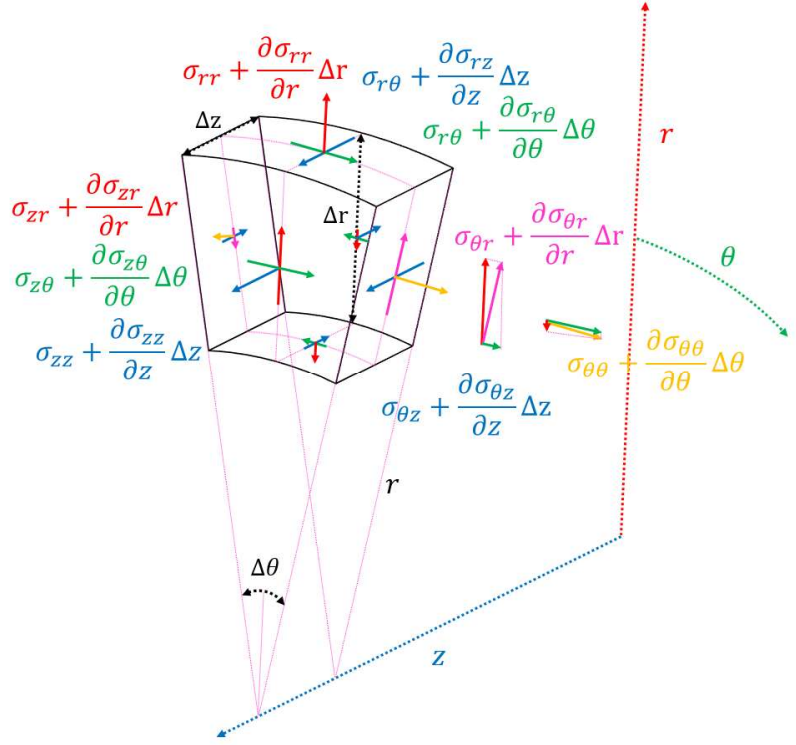


Figure C.2: Stresses on an infinitesimally small control volume.

Assume an infinitesimally small control volume with an approximate volume from equation (147). Summing all the contributions in the radial direction, it can be found that

$$\begin{aligned}
 & \left( \sigma_{rr} + \frac{\partial \sigma_{rr}}{\partial r} \Delta r \right) (r + \Delta r) \Delta \theta \Delta z - \sigma_{rr} r \Delta \theta \Delta z \\
 & + \left( \sigma_{r\theta} + \frac{\partial \sigma_{r\theta}}{\partial \theta} \Delta \theta \right) \Delta r \Delta z \cos \frac{\Delta \theta}{2} - \sigma_{r\theta} \Delta r \Delta z \cos \frac{\Delta \theta}{2} \\
 & + \left( \sigma_{rz} + \frac{\partial \sigma_{rz}}{\partial z} \Delta z \right) \left( r + \frac{\Delta r}{2} \right) \Delta r \Delta \theta - \sigma_{rz} \left( r + \frac{\Delta r}{2} \right) \Delta r \Delta \theta \\
 & - \left( \sigma_{\theta\theta} + \frac{\partial \sigma_{\theta\theta}}{\partial \theta} \Delta \theta \right) \Delta r \Delta z \sin \frac{\Delta \theta}{2} - \sigma_{\theta\theta} \Delta r \Delta z \sin \frac{\Delta \theta}{2}
 \end{aligned} \tag{156}$$

Equation (156) can be rewritten through division by  $r \Delta r \Delta \theta \Delta z$ . This allows for the cancellation of negligible terms analogous to the rewriting of equation (149). The differential magnitudes  $\Delta r$ ,  $\Delta \theta$ ,  $\Delta z$  are let to zero to find equation (157).

$$\frac{\sigma_{rr}}{r} + \frac{\partial \sigma_{rr}}{\partial r} + \frac{1}{r} \frac{\partial \sigma_{r\theta}}{\partial \theta} + \frac{\partial \sigma_{rz}}{\partial z} - \sigma_{\theta\theta} r \tag{157}$$

This procedure can be repeated for the  $\theta$ -direction and  $z$ -direction, for which the result is presented in equation (158) and (159) respectively.

$$\frac{2\sigma_{r\theta}}{r} + \frac{\sigma_{r\theta}}{\partial r} + \frac{1}{r} \frac{\partial \sigma_{\theta\theta}}{\partial \theta} + \frac{\partial \sigma_{\theta z}}{\partial z} \quad (158)$$

$$\frac{\sigma_{rz}}{r} + \frac{\partial \sigma_{rz}}{\partial r} + \frac{1}{r} \frac{\partial \sigma_{\theta z}}{\partial \theta} + \frac{\partial \sigma_{zz}}{\partial z} \quad (159)$$

The results from equation (157), (158) and (159) can be substituted in equation (137) so that the first right hand term in the Cauchy momentum equation is elaborated upon as demonstrated in equation (160).

$$\begin{aligned} \nabla \cdot \boldsymbol{\sigma} &= \left[ \frac{\sigma_{rr}}{r} + \frac{\partial \sigma_{rr}}{\partial r} + \frac{1}{r} \frac{\partial \sigma_{r\theta}}{\partial \theta} + \frac{\partial \sigma_{rz}}{\partial z} - \sigma_{\theta\theta} r \right] \mathbf{e}_r \\ &+ \left[ \frac{2\sigma_{r\theta}}{r} + \frac{\sigma_{r\theta}}{\partial r} + \frac{1}{r} \frac{\partial \sigma_{\theta\theta}}{\partial \theta} + \frac{\partial \sigma_{\theta z}}{\partial z} \right] \mathbf{e}_\theta \\ &+ \left[ \frac{\sigma_{rz}}{r} + \frac{\partial \sigma_{rz}}{\partial r} + \frac{1}{r} \frac{\partial \sigma_{\theta z}}{\partial \theta} + \frac{\partial \sigma_{zz}}{\partial z} \right] \mathbf{e}_z \end{aligned} \quad (160)$$

### C.5 Derivation of stress-strain relationships in a cylindrical coordinate system

The stress tensor can be represented by the addition of the pressure gradient to the deviatoric (shear) stress tensor.

$$\boldsymbol{\sigma} = -p\mathbf{I} + \boldsymbol{\tau} \quad (161)$$

The pressure gradient  $\nabla p$  arises from isotropic part of the Cauchy Stress tensor. Viscous forces give rise to  $\nabla \cdot \boldsymbol{\tau}$  which is the anisotropic part of the Cauchy stress tensor. For incompressible flow this is only a shear effect. Therefore  $\boldsymbol{\tau}$  is the deviatoric stress tensor, i.e. the stress tensor for a system which consists of unequal principal-stresses. From equation (136) we know

$$\rho \frac{D\mathbf{v}}{Dt} = \nabla \cdot \boldsymbol{\sigma} + \rho \mathbf{g} \quad (162)$$

Where the shear tensor can be written as

$$\boldsymbol{\tau} = \mu(\nabla \mathbf{v} + \nabla \mathbf{v}^T) \quad (163)$$

Which means the gradient of the vector and the gradient of its transpose vector. These gradients are tensors (higher order). The control volume has six sides. The gradients can be represented by the dyadic product of the vector with the gradient operator

$$\mathbf{v} \otimes \nabla = \mu(v_r \mathbf{e}_r + v_\theta \mathbf{e}_\theta + v_z \mathbf{e}_z) \otimes \left( \mathbf{e}_r \frac{\partial}{\partial r} + \mathbf{e}_\theta \frac{1}{r} \frac{\partial}{\partial \theta} + \mathbf{e}_z \frac{\partial}{\partial z} \right) \quad (164)$$

When evaluating the derivatives, the basic vectors are functions of the azimuthal coordinate  $\theta$  and therefore their derivatives may not vanish. E.g.

$$\begin{aligned} \frac{1}{r} \frac{\partial}{\partial \theta} (v_r \mathbf{e}_r) \otimes \mathbf{e}_\theta &= \frac{1}{r} \frac{\partial v_r}{\partial \theta} \mathbf{e}_r \otimes \mathbf{e}_\theta + \frac{v_r}{r} \frac{\partial \mathbf{e}_r}{\partial \theta} \otimes \mathbf{e}_\theta \\ &= \frac{1}{r} \frac{\partial v_r}{\partial \theta} \mathbf{e}_r \otimes \mathbf{e}_\theta + \frac{v_r}{r} \mathbf{e}_\theta \otimes \mathbf{e}_\theta \end{aligned} \quad (165)$$

Equation (165) can be rewritten to represent  $\nabla \mathbf{v}$  as shown in equation (166).

$$\nabla \mathbf{v} = \begin{bmatrix} \frac{\partial v_r}{\partial r} & \frac{1}{r} \frac{\partial v_r}{\partial \theta} - \frac{v_\theta}{r} & \frac{\partial v_r}{\partial z} \\ \frac{\partial v_\theta}{\partial r} & \frac{1}{r} \frac{\partial v_\theta}{\partial \theta} + \frac{v_r}{r} & \frac{\partial v_\theta}{\partial z} \\ \frac{\partial v_z}{\partial r} & \frac{1}{r} \frac{\partial v_z}{\partial \theta} & \frac{\partial v_z}{\partial z} \end{bmatrix} \quad (166)$$

The transpose of this matrix is given in equation (167).

$$\nabla \mathbf{v} = \begin{bmatrix} \frac{\partial v_r}{\partial r} & \frac{\partial v_\theta}{\partial r} & \frac{\partial v_z}{\partial r} \\ \frac{1}{r} \frac{\partial v_r}{\partial \theta} - \frac{v_\theta}{r} & \frac{1}{r} \frac{\partial v_\theta}{\partial \theta} + \frac{v_r}{r} & \frac{1}{r} \frac{\partial v_z}{\partial \theta} \\ \frac{\partial v_r}{\partial z} & \frac{\partial v_\theta}{\partial z} & \frac{\partial v_z}{\partial z} \end{bmatrix} \quad (167)$$

Combining equations (163), (166) and (167) allows for substitution in equation (161). Equation (168) demonstrates the stress terms resulting from this operation.

$$\begin{aligned} \sigma_{rr} &= -p + 2\mu \frac{\partial v_r}{\partial r} \\ \sigma_{\theta\theta} &= -p + 2\mu \left( \frac{1}{r} \frac{\partial v_\theta}{\partial \theta} + \frac{v_r}{r} \right) \\ \sigma_{zz} &= -p + 2\mu \frac{\partial v_z}{\partial z} \\ \sigma_{r\theta} = \sigma_{\theta r} &= \mu \left( \frac{1}{r} \frac{\partial v_r}{\partial \theta} + \frac{\partial v_\theta}{\partial r} - \frac{v_\theta}{r} \right) \\ \sigma_{rz} = \sigma_{zr} &= \mu \left( \frac{\partial v_r}{\partial z} + \frac{\partial v_z}{\partial r} \right) \\ \sigma_{\theta z} = \sigma_{z\theta} &= \mu \left( \frac{1}{r} \frac{\partial v_z}{\partial \theta} + \frac{\partial v_\theta}{\partial z} \right) \end{aligned} \quad (168)$$

Substitution of the stress terms in equation (160) renders, for the radial component

$$\begin{aligned} \left[ \frac{\sigma_{rr}}{r} + \frac{\partial \sigma_{rr}}{\partial r} + \frac{1}{r} \frac{\partial \sigma_{r\theta}}{\partial \theta} + \frac{\partial \sigma_{rz}}{\partial z} - \sigma_{\theta\theta} r \right] \mathbf{e}_r &= \left[ \left( -p + 2\mu \frac{\partial v_r}{\partial r} \right) + \left( -\frac{\partial p}{\partial r} + 2\mu \frac{\partial^2 v_r}{\partial r^2} \right) \right. \\ &\quad + \mu \left( \frac{1}{r^2} \frac{\partial^2 v_r}{\partial \theta^2} + \frac{\mu}{r} \frac{\partial^2 v_\theta}{\partial r \partial \theta} - \frac{v_\theta}{r^2} \frac{\partial v_\theta}{\partial \theta} \right) \\ &\quad \left. + \mu \left( \frac{\partial^2 v_r}{\partial z^2} + \frac{\partial^2 v_z}{\partial r \partial z} \right) - \left( -\frac{p}{r} + \frac{2\mu}{r^2} \frac{\partial v_\theta}{\partial \theta} + 2\mu \frac{v_r}{r^2} \right) \right] \mathbf{e}_r \quad (169) \\ &= -\frac{\partial p}{\partial r} + \mu \left[ \frac{2}{r} \frac{\partial v_r}{\partial r} + 2 \frac{\partial^2 v_r}{\partial r^2} + \frac{1}{r} \frac{\partial^2 v_\theta}{\partial r \partial \theta} + \frac{1}{r^2} \frac{\partial^2 v_r}{\partial \theta^2} - \frac{1}{r^2} \frac{\partial v_\theta}{\partial \theta} \right. \\ &\quad \left. + \left( \frac{\partial^2 v_r}{\partial z^2} + \frac{\partial^2 v_z}{\partial r \partial z} \right) - \frac{2}{r^2} \frac{\partial v_\theta}{\partial \theta} - \frac{2}{r^2} u_r \right] \end{aligned}$$

In the result of equation (169), the first two terms between the square brackets are rewritten as demonstrated in equation (170).

$$\begin{aligned} \frac{2}{r} \frac{\partial v_r}{\partial r} + 2 \frac{\partial^2 v_r}{\partial r^2} &= \frac{1}{r} \frac{\partial}{\partial r} \left( r \frac{\partial v_r}{\partial r} \right) + \frac{1}{r} \frac{\partial v_r}{\partial r} + \frac{\partial^2 v_r}{\partial r^2} \\ &= \frac{1}{r} \frac{\partial}{\partial r} \left( r \frac{\partial v_r}{\partial r} \right) + \frac{u_r^2}{r^2} + \frac{\partial}{\partial r} \left( \frac{1}{r} \frac{\partial (rv_r)}{\partial r} \right) \end{aligned} \quad (170)$$

The chain rule is applied to the third term between square brackets to obtain

$$\frac{1}{r} \frac{\partial^2 v_\theta}{\partial r \partial \theta} = \frac{\partial}{\partial r} \left( \frac{1}{r} \frac{\partial v_\theta}{\partial \theta} \right) + \frac{1}{r^2} \frac{\partial v_\theta}{\partial \theta} \quad (171)$$

We can now find the radial component by substitution of equation (170) and (171) in the result of equation (169). This resulting expression for the stress tensor in radial direction is therefore given in equation (172).

$$\begin{aligned} & -\frac{\partial p}{\partial r} + \mu \left[ \frac{1}{r} \frac{\partial}{\partial r} \left( r \frac{\partial v_r}{\partial r} \right) + \frac{u_r^2}{r^2} + \frac{\partial}{\partial r} \left( \frac{1}{r} \frac{\partial (r v_r)}{\partial r} \right) + \frac{\partial}{\partial r} \left( \frac{1}{r} \frac{\partial u_\theta}{\partial \theta} \right) + \frac{1}{r^2} \frac{\partial v_\theta}{\partial \theta} \right. \\ & \left. + \frac{1}{r^2} \frac{\partial^2 v_r}{\partial \theta^2} - \frac{1}{r^2} \frac{\partial v_\theta}{\partial \theta} + \left( \frac{\partial^2 v_r}{\partial z^2} + \frac{\partial^2 v_z}{\partial r \partial z} \right) - \frac{2}{r^2} \frac{\partial v_\theta}{\partial \theta} - \frac{2}{r^2} u_r \right] \end{aligned} \quad (172)$$

Grouping relevant terms and reorganizing yields

$$\begin{aligned} & -\frac{\partial p}{\partial r} + \mu \left[ -\frac{u_r}{r^2} + \frac{\partial}{\partial r} \left( \frac{1}{r} \frac{\partial (r v_r)}{\partial r} + \frac{1}{r} \frac{\partial u_\theta}{\partial \theta} + \frac{\partial v_z}{\partial z} \right) \right. \\ & \left. + \frac{1}{r} \frac{\partial}{\partial r} \left( r \frac{\partial v_r}{\partial r} \right) + \frac{1}{r^2} \frac{\partial^2 v_r}{\partial \theta^2} + \frac{\partial^2 v_r}{\partial z^2} - \frac{2}{r^2} \frac{\partial v_\theta}{\partial \theta} \right] \end{aligned} \quad (173)$$

As demonstrated in equation (155) of the continuity equation derivation, the terms between the first parentheses, the radial derivative, is equal to zero. In the radial direction, the right side of the momentum equation therefore reduces to equation (174).

$$-\frac{\partial p}{\partial r} + \mu \left[ -\frac{u_r}{r^2} + \frac{1}{r} \frac{\partial}{\partial r} \left( r \frac{\partial v_r}{\partial r} \right) + \frac{1}{r^2} \frac{\partial^2 v_r}{\partial \theta^2} + \frac{\partial^2 v_r}{\partial z^2} - \frac{2}{r^2} \frac{\partial v_\theta}{\partial \theta} \right] \quad (174)$$

## C.6 Gravitational acceleration

Suppose a unit mass is inclined under an angle  $\lambda$  [rad] with respect to a reference frame aligned with the seabed as depicted in Figure C.3. The gravitational accelerations in the  $r$ -,  $\theta$ - and  $z$ -direction can then be found according to the formulations given in equation (175).

$$\begin{aligned} g_{r\theta} &= g \cos \lambda \\ g_z &= g \sin \lambda \end{aligned} \quad (175)$$

Gravitational acceleration in the radial and azimuthal direction is found in accordance with Figure C.3.

$$\begin{aligned} g_r &= g_{r\theta} \cos \theta \\ g_\theta &= g_{r\theta} \sin \theta \end{aligned} \quad (176)$$

Hence

$$\begin{aligned} g_r &= g \cos \theta \cos \lambda \\ g_\theta &= g \sin \theta \cos \lambda \\ g_z &= g \sin \lambda \end{aligned} \quad (177)$$

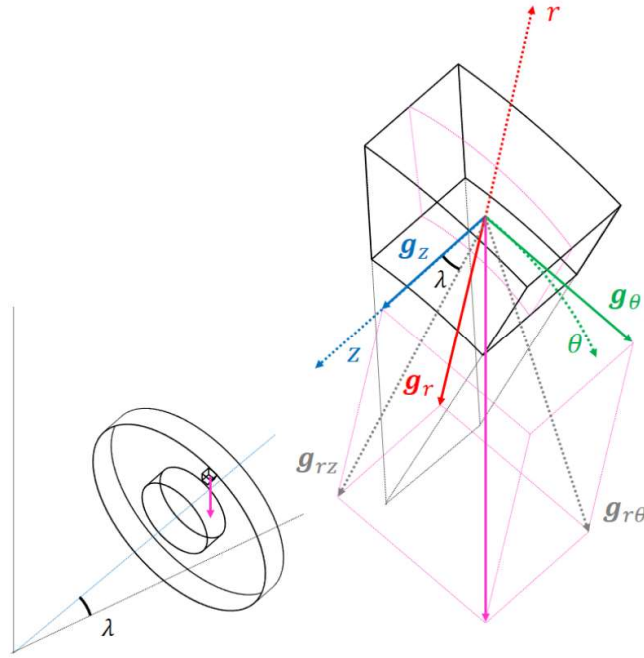


Figure C.3: Gravitational acceleration acting on an infinitesimally small control volume.

### C.7 Derivation of Navier-Stokes equations

The Navier-Stokes equations can be obtained from the Cauchy Momentum equation (162) by substitution of equations found for the velocities (146), the stress tensor (174) and the gravitational acceleration (177).

$$\begin{aligned} & \rho \left[ \frac{\partial v_r}{\partial t} + v_r \frac{\partial v_r}{\partial r} + \frac{v_\theta}{r} \frac{\partial v_r}{\partial \theta} - \frac{v_\theta^2}{r} + v_z \frac{\partial v_r}{\partial z} \right] \\ &= -\frac{\partial p}{\partial r} + \mu \left[ -\frac{u_r}{r^2} + \frac{1}{r} \frac{\partial}{\partial r} \left( r \frac{\partial v_r}{\partial r} \right) + \frac{1}{r^2} \frac{\partial^2 v_r}{\partial \theta^2} + \frac{\partial^2 v_r}{\partial z^2} - \frac{2}{r^2} \frac{\partial v_\theta}{\partial \theta} \right] + \rho g_r \end{aligned} \quad (178)$$

In a similar fashion, Navier-Stokes for the  $\theta$ -component is given in equation (179).

$$\begin{aligned} & \rho \left[ \frac{\partial v_\theta}{\partial t} + v_r \frac{\partial v_\theta}{\partial r} + \frac{v_\theta}{r} \frac{\partial v_\theta}{\partial \theta} + \frac{v_\theta v_r}{r} + v_z \frac{\partial v_\theta}{\partial z} \right] \\ &= -\frac{1}{r} \frac{\partial p}{\partial \theta} + \mu \left[ -\frac{u_\theta}{r^2} + \frac{1}{r} \frac{\partial}{\partial r} \left( r \frac{\partial v_\theta}{\partial r} \right) + \frac{1}{r^2} \frac{\partial^2 v_\theta}{\partial \theta^2} + \frac{\partial^2 v_\theta}{\partial z^2} + \frac{2}{r^2} \frac{\partial v_r}{\partial \theta} \right] + \rho g_\theta \end{aligned} \quad (179)$$

Lastly, for the axial  $z$ -component, the Navier-Stokes are given in equation (180).

$$\begin{aligned} & \rho \left[ \frac{\partial v_z}{\partial t} + v_r \frac{\partial v_z}{\partial r} + \frac{v_\theta}{r} \frac{\partial v_z}{\partial \theta} + v_z \frac{\partial v_z}{\partial z} \right] \\ &= -\frac{\partial p}{\partial z} + \mu \left[ \frac{1}{r} \frac{\partial}{\partial r} \left( r \frac{\partial v_z}{\partial r} \right) + \frac{1}{r^2} \frac{\partial^2 v_z}{\partial \theta^2} + \frac{\partial^2 v_z}{\partial z^2} \right] + \rho g_z \end{aligned} \quad (180)$$

### C.8 Alternative forms of Navier-Stokes equations

The Navier-Stokes equations can be rewritten in alternate forms using Newton's law of viscosity. A Newtonian fluid is assumed

$$\boldsymbol{\tau} \stackrel{\text{def}}{=} \mu \nabla \mathbf{v} \quad (181)$$

Using the above definition, equations (178), (179) and (180) can be transformed to equations (181), (182) and (183) respectively. For the radial component

$$\begin{aligned} & \rho \left[ \frac{\partial v_r}{\partial t} + v_r \frac{\partial v_r}{\partial r} + \frac{v_\theta}{r} \frac{\partial v_r}{\partial \theta} - \frac{v_\theta^2}{r} + v_z \frac{\partial v_r}{\partial z} \right] \\ &= -\frac{\partial p}{\partial r} + \mu \left[ -\frac{u_r}{r^2} + \frac{1}{r} \frac{\partial}{\partial r} \left( r \frac{\partial v_r}{\partial r} \right) + \frac{1}{r^2} \frac{\partial^2 v_r}{\partial \theta^2} + \frac{\partial^2 v_r}{\partial z^2} - \frac{2}{r^2} \frac{\partial v_\theta}{\partial \theta} \right] + \rho g_r \\ &= -\frac{\partial p}{\partial r} + \left[ -\mu \frac{u_r}{r^2} + \frac{1}{r} \frac{\partial}{\partial r} \left( r \mu \frac{\partial v_r}{\partial r} \right) + \frac{1}{r^2} \mu \frac{\partial^2 v_r}{\partial \theta^2} + \mu \frac{\partial^2 v_r}{\partial z^2} - \frac{2}{r^2} \mu \frac{\partial v_\theta}{\partial \theta} \right] + \rho g_r \\ &= -\frac{\partial p}{\partial r} + \left[ -\mu \frac{u_r}{r^2} + \frac{1}{r} \frac{\partial}{\partial r} (r \tau_{rr}) + \frac{1}{r} \frac{\partial \tau_{r\theta}}{\partial \theta} + \frac{\partial \tau_{rz}}{\partial z} - \frac{2}{r} \tau_{\theta\theta} \right] + \rho g_r \end{aligned} \quad (182)$$

In a similar fashion, the Navier-Stokes equation for the  $\theta$ -component is

$$\begin{aligned} & \rho \left[ \frac{\partial v_\theta}{\partial t} + v_r \frac{\partial v_\theta}{\partial r} + \frac{v_\theta}{r} \frac{\partial v_\theta}{\partial \theta} + \frac{v_\theta v_r}{r} + v_z \frac{\partial v_\theta}{\partial z} \right] \\ &= -\frac{1}{r} \frac{\partial p}{\partial \theta} + \mu \left[ -\frac{u_\theta}{r^2} + \frac{1}{r} \frac{\partial}{\partial r} \left( r \frac{\partial v_\theta}{\partial r} \right) + \frac{1}{r^2} \frac{\partial^2 v_\theta}{\partial \theta^2} + \frac{\partial^2 v_\theta}{\partial z^2} + \frac{2}{r^2} \frac{\partial v_r}{\partial \theta} \right] + \rho g_\theta \\ &= -\frac{1}{r} \frac{\partial p}{\partial \theta} + \left[ -\mu \frac{u_\theta}{r^2} + \frac{1}{r} \frac{\partial}{\partial r} \left( r \mu \frac{\partial v_\theta}{\partial r} \right) + \frac{1}{r^2} \mu \frac{\partial^2 v_\theta}{\partial \theta^2} + \mu \frac{\partial^2 v_\theta}{\partial z^2} + \frac{2}{r^2} \mu \frac{\partial v_r}{\partial \theta} \right] + \rho g_\theta \\ &= -\frac{1}{r} \frac{\partial p}{\partial \theta} + \left[ -\mu \frac{u_\theta}{r^2} + \frac{1}{r} \frac{\partial}{\partial r} (r \tau_{\theta r}) + \frac{1}{r} \frac{\partial \tau_{\theta\theta}}{\partial \theta} + \frac{\partial \tau_{\theta z}}{\partial z} + \frac{2}{r^2} \tau_{r\theta} \right] + \rho g_\theta \end{aligned} \quad (183)$$

And Navier-Stokes equation for the z-component equals

$$\begin{aligned} & \rho \left[ \frac{\partial v_z}{\partial t} + v_r \frac{\partial v_z}{\partial r} + \frac{v_\theta}{r} \frac{\partial v_z}{\partial \theta} + v_z \frac{\partial v_z}{\partial z} \right] \\ &= -\frac{\partial p}{\partial z} + \mu \left[ \frac{1}{r} \frac{\partial}{\partial r} \left( r \frac{\partial v_z}{\partial r} \right) + \frac{1}{r^2} \frac{\partial^2 v_z}{\partial \theta^2} + \frac{\partial^2 v_z}{\partial z^2} \right] + \rho g_z \\ &= -\frac{\partial p}{\partial z} + \left[ \frac{1}{r} \frac{\partial}{\partial r} \left( r \mu \frac{\partial v_z}{\partial r} \right) + \frac{1}{r^2} \mu \frac{\partial^2 v_z}{\partial \theta^2} + \mu \frac{\partial^2 v_z}{\partial z^2} \right] + \rho g_z \\ &= -\frac{\partial p}{\partial z} + \left[ \frac{1}{r} \frac{\partial}{\partial r} (r \tau_{zr}) + \frac{1}{r} \frac{\partial \tau_{z\theta}}{\partial \theta} + \frac{\partial \tau_{zz}}{\partial z} \right] + \rho g_z \end{aligned} \quad (184)$$

### C.9 Derivation of Euler equations

In accordance with equation (155), the fluid is considered incompressible. The Euler equations can be obtained by assuming an inviscid fluid, i.e. the viscosity of the fluid is to be neglected.

$$\mu = 0 \quad (185)$$

Neglecting the viscosity yields the Euler equations in Lagrangian form, as shown in equation (186), where the first constraint follows from the continuity equation.

$$\begin{aligned}
\frac{D\rho}{Dt} &= 0 \\
\frac{D\mathbf{u}}{Dt} &= -\frac{\nabla p}{\rho} + \mathbf{g} \\
\nabla \cdot \mathbf{u} &= 0
\end{aligned} \tag{186}$$

Alternatively written, the Euler equations for incompressible fluids in a cylindrical coordinate system are given in equation (182), (183) and (184). For the  $r$ -component

$$\rho \left[ \frac{\partial v_r}{\partial t} + v_r \frac{\partial v_r}{\partial r} + \frac{v_\theta}{r} \frac{\partial v_r}{\partial \theta} - \frac{v_\theta^2}{r} + v_z \frac{\partial v_r}{\partial z} \right] = -\frac{\partial p}{\partial r} + \rho g_r \tag{187}$$

For the  $\theta$ -component

$$\rho \left[ \frac{\partial v_\theta}{\partial t} + v_r \frac{\partial v_\theta}{\partial r} + \frac{v_\theta}{r} \frac{\partial v_\theta}{\partial \theta} + \frac{v_\theta v_r}{r} + v_z \frac{\partial v_\theta}{\partial z} \right] = -\frac{1}{r} \frac{\partial p}{\partial \theta} + \rho g_\theta \tag{188}$$

For the  $z$ -component

$$\rho \left[ \frac{\partial v_z}{\partial t} + v_r \frac{\partial v_z}{\partial r} + \frac{v_\theta}{r} \frac{\partial v_z}{\partial \theta} + v_z \frac{\partial v_z}{\partial z} \right] = -\frac{\partial p}{\partial z} + \rho g_z \tag{189}$$

#### C.10 Derivation of Euler's pump equation

It is assumed that the fluid is flowing axisymmetrically within the physical domain of the cutter head. Therefore, any change in velocity with respect to the azimuth  $\theta$  is zero.

$$\begin{aligned}
\frac{v_\theta}{r} \frac{\partial v_r}{\partial \theta} &= 0 \\
\frac{v_\theta}{r} \frac{\partial v_\theta}{\partial \theta} &= 0 \\
\frac{v_\theta}{r} \frac{\partial v_z}{\partial \theta} &= 0
\end{aligned} \tag{190}$$

Furthermore, the fluid within the domain is considered to be in a steady state. This allows for the simplifications presented in equation (191).

$$\begin{aligned}
\frac{\partial v_r}{\partial t} &= 0 \\
\frac{\partial v_\theta}{\partial t} &= 0 \\
\frac{\partial v_z}{\partial t} &= 0
\end{aligned} \tag{191}$$

Euler's equations from (187), (188) and (189) can now be reduced to equation (192), (193) and (194) respectively.

$$\rho \left( v_r \frac{\partial v_r}{\partial r} - \frac{v_\theta^2}{r} + v_z \frac{\partial v_r}{\partial z} \right) - \rho g_r = -\frac{\partial p}{\partial r} \tag{192}$$

In a similar fashion, for the  $\theta$ -component

$$\begin{aligned} \rho \left( v_r \frac{\partial v_\theta}{\partial r} + \frac{v_\theta v_r}{r} + v_z \frac{\partial v_\theta}{\partial z} \right) - \rho g_z &= -\frac{1}{r} \frac{\partial p}{\partial \theta} \\ \Leftrightarrow r\rho \left( v_r \frac{\partial v_\theta}{\partial r} + \frac{v_\theta v_r}{r} + v_z \frac{\partial v_\theta}{\partial z} \right) - r\rho g_\theta &= -\frac{\partial p}{\partial \theta} \end{aligned} \quad (193)$$

And for the z-component

$$\rho \left( v_r \frac{\partial v_z}{\partial r} + v_z \frac{\partial v_z}{\partial z} \right) - \rho g_z = -\frac{\partial p}{\partial z} \quad (194)$$

### C.10.1 Implementing boundary conditions

The derivation of Euler's pump equation is continued by considering a streamline within a cylinder. In 3D space, the pressure on an infinitesimally small element with respect to the radius at location  $r\theta z = \{r, \theta, z\}$  along a section of the streamline equals

$$\frac{dp}{dr} \Big|_{r\theta z} = \frac{\partial p}{\partial r} + \frac{\partial p}{\partial \theta} \frac{d\theta}{dr} \Big|_{r\theta z} + \frac{\partial p}{\partial z} \frac{dz}{dr} \Big|_{r\theta z} \quad (195)$$

Substitution of equations (192), (193) and (194) yields

$$\begin{aligned} -\frac{dp}{dr} \Big|_{r\theta z} &= \rho \left( v_r \frac{\partial v_r}{\partial r} - \frac{v_\theta^2}{r} + v_z \frac{\partial v_r}{\partial z} \right) - \rho g_r \\ &+ \left[ r\rho \left( v_r \frac{\partial v_\theta}{\partial r} + \frac{v_\theta v_r}{r} + v_z \frac{\partial v_\theta}{\partial z} \right) - r\rho g_\theta \right] \frac{d\theta}{dr} \Big|_{r\theta z} \\ &+ \left[ \rho \left( v_r \frac{\partial v_z}{\partial r} + v_z \frac{\partial v_z}{\partial z} \right) - \rho g_z \right] \frac{dz}{dr} \Big|_{r\theta z} \end{aligned} \quad (196)$$

Further substitution of equations (123) and (126) in equation (196) results in

$$\begin{aligned} -\frac{dp}{dr} \Big|_{r\theta z} &= \rho \left( v_r \frac{\partial v_r}{\partial r} - \frac{v_\theta^2}{r} + v_z \frac{\partial v_r}{\partial z} \right) - \rho g_r \\ &+ \left[ \rho \left( v_r \frac{\partial v_\theta}{\partial r} + \frac{v_\theta v_r}{r} + v_z \frac{\partial v_\theta}{\partial z} \right) - \rho g_\theta \right] \frac{w_\theta}{v_r} \\ &+ \left[ \rho \left( v_r \frac{\partial v_z}{\partial r} + v_z \frac{\partial v_z}{\partial z} \right) - \rho g_z \right] \frac{w_z}{w_r} \end{aligned} \quad (197)$$

Equation (197) can be rewritten to group variables. For convenience, some relative velocities are interchanged with absolute velocities. Where applicable,  $v_r = w_r$  and  $v_z = w_z$  in the top row, and  $w_r = v_r$  and  $w_z = v_z$  in the center and bottom row.

$$\begin{aligned} -\frac{dp}{dr} \Big|_{r\theta z} &= \rho \left[ v_r \frac{\partial v_r}{\partial r} - \frac{v_\theta^2}{r} + w_\theta \frac{\partial v_\theta}{\partial r} + w_\theta \frac{v_\theta}{r} + w_z \frac{\partial v_z}{\partial r} \right. \\ &+ v_z \frac{\partial v_r}{\partial z} + v_z \frac{\partial v_\theta}{\partial z} \frac{w_\theta}{v_r} + v_z \frac{\partial v_z}{\partial z} \frac{w_z}{w_r} \\ &\left. - \left( g_r + \frac{w_\theta}{w_r} g_\theta + \frac{w_z}{w_r} g_z \right) \right] \end{aligned} \quad (198)$$

Next,, we know that gravity can be rewritten by substituting Eq. (122) and (126) in the gravity formulations of Eq. (177). The result is demonstrated in equation (199).

$$\begin{aligned}
-\left(g_r + \frac{w_\theta}{w_r} g_\theta + \frac{w_z}{w_r} g_z\right) &= -\left(g \cos \theta \cos \lambda + \frac{w_\theta}{w_r} g \sin \theta \cos \lambda + \frac{w_z}{w_r} g \sin \lambda\right) \\
&= -(g \cos \theta \cos \lambda + \cot \beta g \sin \theta \cos \lambda + \cot \alpha g \sin \lambda) \\
&= -g(\cos \theta \cos \lambda + \cot \beta \sin \theta \cos \lambda + \cot \alpha \sin \lambda) \\
&= -g(\csc \beta \cos \lambda \sin(\beta + \theta) + \cot \alpha \sin \lambda) \\
&= -gf_{g_r}
\end{aligned} \tag{199}$$

Where  $f_{g_r} = \csc \beta \cos \lambda \sin(\beta + \theta) + \cot \alpha \sin \lambda$ , a gravity constant, in which the cosecant is used ( $\csc \beta = \frac{1}{\sin \beta}$ ). Combining equation (198) and (199) results in

$$\begin{aligned}
-\frac{dp}{dr}\Big|_{r\theta z} &= \rho \left[ w_r \frac{\partial w_r}{\partial r} - \frac{v_\theta^2}{r} + w_\theta \frac{\partial v_\theta}{\partial r} + w_\theta \frac{v_\theta}{r} + w_z \frac{\partial w_z}{\partial r} \right. \\
&\quad \left. + v_z \frac{\partial v_r}{\partial z} + v_z \frac{\partial v_\theta}{\partial z} \frac{w_\theta}{v_r} + v_z \frac{\partial v_z}{\partial z} \frac{v_z}{v_r} \right. \\
&\quad \left. - gf_{g_r} \right]
\end{aligned} \tag{200}$$

Substitution of terms from equation (118) in Eq. (200) yields

$$\begin{aligned}
-\frac{dp}{dr}\Big|_{r\theta z} &= \rho \left[ w_r \frac{\partial w_r}{\partial r} - \frac{(-\omega r + w_\theta)^2}{r} + w_\theta \frac{\partial(-\omega r + w_\theta)}{\partial r} + w_\theta \frac{(-\omega r + w_\theta)}{r} + w_z \frac{\partial w_z}{\partial r} \right. \\
&\quad \left. + v_z \frac{\partial v_r}{\partial z} + v_z \frac{\partial v_\theta}{\partial z} \frac{(v_\theta + \omega r)}{v_r} + w_z \frac{\partial v_z}{\partial z} \frac{v_z}{v_r} \right. \\
&\quad \left. - \left( g_r + \frac{w_\theta}{w_r} g_\theta + \frac{w_z}{w_r} g_z \right) \right]
\end{aligned} \tag{201}$$

Simplifying top and center line of Eq. (201)

$$\begin{aligned}
-\frac{dp}{dr}\Big|_{r\theta z} &= \rho \left[ -\omega^2 r + w_r \frac{\partial w_r}{\partial r} + w_\theta \frac{\partial w_\theta}{\partial r} + w_z \frac{\partial w_z}{\partial r} \right. \\
&\quad \left. + \omega r \frac{v_z}{v_r} \frac{\partial v_\theta}{\partial z} + \frac{v_z}{v_r} \left( +v_r \frac{\partial v_r}{\partial z} + v_\theta \frac{\partial v_\theta}{\partial z} + v_z \frac{\partial v_z}{\partial z} \right) \right. \\
&\quad \left. - gf_{g_r} \right]
\end{aligned} \tag{202}$$

By making use of the product rule this can be written as

$$\begin{aligned}
-\frac{dp}{dr}\Big|_{r\theta z} &= \rho \left[ -\omega^2 r + \frac{1}{2} \frac{\partial(w_r^2 + w_\theta^2 + w_z^2)}{\partial r} \right. \\
&\quad \left. + \omega r \frac{v_z}{v_r} \frac{\partial v_\theta}{\partial z} + \frac{v_z}{v_r} \frac{1}{2} \frac{\partial(v_r^2 + v_\theta^2 + v_z^2)}{\partial z} \right. \\
&\quad \left. - gf_{g_r} \right]
\end{aligned} \tag{203}$$

### C.10.2 Axisymmetrical flow (2D)

Further operations on equation (203) are highly complex because the physical domain is three-dimensional. A 3D domain becomes particularly problematic upon linearization of the velocities.

Since the flow is assumed axisymmetrical, the axial rated change of the velocities on the right-hand side (the azimuthal velocity and the velocity), are set to zero, i.e.  $\frac{\partial v_\theta}{\partial z} = 0$  and  $v_r^2 + v_\theta^2 + v_z^2 = 0$ . Equation (203) therefore reduces to equation (204).

$$-\frac{dp}{dr}\Big|_{r\theta z} = \rho \left[ -\omega^2 r + \frac{1}{2} \frac{\partial w^2}{\partial r} - g f_g \right] \quad (204)$$

With the assumption of axisymmetrical flow, the radial and azimuthal velocities now a two-dimensional approximation of what was considered a three-dimensional physical domain. A 2D linearization for the velocity is considered in equation (205).

$$\Delta w^2 \stackrel{\text{def}}{=} \frac{\partial w^2}{\partial r} \Delta r + \frac{\partial w^2}{\partial \theta} \Delta \theta \quad (205)$$

We divide by  $\Delta r$ , assume  $\frac{\Delta \theta}{\Delta r} = 0$  and let  $\Delta$  go to zero to find

$$\frac{dw^2}{dr} = \frac{\partial w^2}{\partial r} \quad (206)$$

Equation (204) can be substituted with the result from equation (206) to obtain

$$-\frac{dp}{dr}\Big|_{r\theta z} = \rho \left[ -\omega^2 r + \frac{1}{2} \frac{dw^2}{dr} - g f_g \right] \quad (207)$$

For ease of use the sign of the above equation is changed

$$\frac{dp}{dr}\Big|_{r\theta z} = \rho \left[ \omega^2 r - \frac{1}{2} \frac{dw^2}{dr} + g f_g \right] \quad (208)$$

The pressure along a stage of the streamline from  $r_1$  to  $r_2$  can be found as

$$\int_{stage} dp = \rho \left[ \omega^2 \int_{stage} r dr - \frac{1}{2} \int_{stage} dw^2 + \int_{stage} g f_g dr \right] \quad (209)$$

Which yields for the increase in pressure over the given stage

$$p_2 - p_1 = \rho \left[ \omega^2 \frac{r_2^2 - r_1^2}{2} + \frac{w_1^2 - w_2^2}{2} + g f_g (r_2 - r_1) \right] \quad (210)$$

### C.11 Derivation of Euler's pump equation

In appendix A, the derivation of Bernoulli's principle is given, which proves useful in the further derivation. In the derivation of Euler's pump equation, the gravitational acceleration is neglected

$$g f_g (r_2 - r_1) = 0 \quad (211)$$

It is fair to neglect gravity since the Froude number for the cutter head is estimated at 10 [-] (See section 3.5.4).

After taking into account the restriction of equation (211), Equation (210) and (117) can be combined to obtain a formulation for the elevation head gain. It should be

noted that the friction head is neglected because viscosity was considered negligible.

$$h_2 - h_1 = \omega^2 \frac{r_2^2 - r_1^2}{2g} + \frac{w_1^2 - w_2^2}{2g} + \frac{v_2^2 - v_1^2}{2g} \quad (212)$$

Appendix B provides an overview of a selection of velocity triangle relationships. Substitutions of the equations from (119) in equation (212) yields

$$h_2 - h_1 = \omega^2 \frac{r_2^2 - r_1^2}{2g} + \frac{w_1^2 - w_2^2}{2g} + \frac{u_2^2 + w_2^2 - 2u_2w_2 \cos \beta_2 - (u_1^2 + w_1^2 - 2u_1w_1 \cos \beta_1)}{2g} \quad (213)$$

Where some variables are cancelled out to find

$$h_2 - h_1 = \omega^2 \frac{r_2^2 - r_1^2}{2g} + \frac{u_2^2 - 2u_2w_2 \cos \beta_2 - u_1^2 + 2u_1w_1 \cos \beta_1}{2g} \quad (214)$$

Realizing that  $u = r\omega$  and  $u^2 = r^2\omega^2$  from equation (118), it can be demonstrated that a further cancellation of terms results in equation (215). In this operation, notice the switch in radii in the latter term.

$$h_2 - h_1 = \omega^2 \frac{r_2^2 - r_1^2}{g} + \frac{r_1\omega w_1 \cos \beta_1 - r_2\omega w_2 \cos \beta_2}{g} \quad (215)$$

Rewriting the above formulation using  $w_r = \|\mathbf{w}\| \cdot \sin \beta$  from equation (118) yields

$$h_2 - h_1 = \omega^2 \frac{r_2^2 - r_1^2}{g} + \frac{r_1\omega \frac{w_{r1}}{\sin \beta_1} \cos \beta_1 - r_2\omega \frac{w_{r2}}{\sin \beta_2} \cos \beta_2}{g} \quad (216)$$

By using the definition  $\cot \beta \stackrel{\text{def}}{=} \frac{\cos \beta}{\sin \beta}$  equation (217) can be obtained.

$$h_2 - h_1 = \omega^2 \frac{r_2^2 - r_1^2}{g} + \frac{r_1\omega w_{r1} \cot \beta_1 - r_2\omega w_{r2} \cot \beta_2}{g} \quad (217)$$

Subsequent substitution of equation (124) gives

$$h_2 - h_1 = \omega^2 \frac{r_2^2 - r_1^2}{g} + \omega \frac{Q}{f_\gamma 2\pi b} \frac{(\cot \beta_1 - \cot \beta_2)}{g} \quad (218)$$

Where  $f_\gamma$  is a factor that limits the outflow area of the pump. For clarity, the elevation height in the equation above is replaced with the more commonly used metric of pressure gain (see below)

$$h_2 - h_1 = \frac{p_2 - p_1}{g\rho} \quad (219)$$

The use of pressure gain on the left-hand side gives rise to what is commonly referred to as Euler's pump equation as displayed in equation (220). The pressure gain is a result of both static and kinematic contributions.

$$p_2 - p_1 = \underbrace{\rho\omega^2(r_2^2 - r_1^2)}_{static} + \underbrace{\omega\rho\frac{Q}{f_\gamma 2\pi b}(\cot\beta_1 - \cot\beta_2)}_{kinematic} \quad (220)$$

### C.12 Derivation of affinity law for pressure

With Euler's pump equation fully derived, further assumptions can be made to establish the affinity laws for centrifugal pumps. Continuing with equation (220), it can be assumed that the inner radius equals zero. Consequently, there cannot be a radial velocity at the origin. The equation simplifies to

$$p_2 - p_1 = \rho\omega^2 r_2^2 - \omega\rho\frac{Q}{f_\gamma 2\pi b} \cot\beta_2 \quad (221)$$

The relationship between discharge  $Q$  and radial velocity is given according to equation (124) and can be used to rewrite equation (221) into

$$p_2 - p_1 = \rho\omega^2 r_2^2 - \omega\rho w_{r_2} \cot\beta_2 \quad (222)$$

Which can be rewritten to find an expression for the pressure gain as a function of the dimensionless head, rotational velocity and trailing point radius of the pump and the fluid's velocity

$$p_2 - p_1 = \left(1 - \frac{w_{r_2}}{\omega r_2} \cot\beta_2\right) \rho\omega^2 r_2^2 = \hat{\Psi} \rho\omega^2 r_2^2 \quad (223)$$

Where the dimensionless head equals

$$\hat{\Psi} = 1 - \frac{w_{r_2}}{\omega r_2} \cot\beta_2 \quad (224)$$

Equation (223) is known as the affinity law for pressure of a centrifugal pump.

### C.13 Derivation of affinity law for discharge

Let us consider flow similitude for a centrifugal pump, i.e. the ratio of the average fluid velocity  $v_r$  [m/s] and the tangential impeller velocity  $u$  [m/s] equals a constant dimensionless flow number

$$\frac{v_r}{u} = \Phi \quad (225)$$

Where  $\Phi$  represents the flow number [-]. The average fluid velocity exits the pump over an area equal to the circumference of the pump, multiplied by the impeller width and limited by a factor  $f_\gamma$  [-] that accounts for limitations to the outflow area, i.e.  $f_\gamma 2\pi r b$ . Assuming incompressible flow and flow equilibrium, the fluid velocity inside the volute chamber follows from volume continuity and reads

$$v_r = \frac{Q}{f_\gamma 2\pi r_2 b} \quad (226)$$

Where  $Q$  is the pump discharge [m<sup>3</sup>/s],  $r$  is the pump radius [m] and  $b$  the impeller width [m]. The tangential velocity of the impeller is found through multiplication of

the angular velocity  $\omega$  [rad/s] and the cutter radius [m] ( $u = \omega r$ ). Substitution of the velocity ratio in equation (226) and subsequent reordering yields an expression for the discharge as a function of the angular velocity as evidenced in equation (227).

$$Q = \Phi \pi b \omega r_2^2 = \hat{\Phi} f_v b \omega r_2^2 \quad (227)$$

Where  $\hat{\Phi}$  is an adapted flow number [-]. Physically, the coefficient  $\hat{\Phi}$  can be considered a dimensionless ratio of the velocity components in the tangential (azimuthal) direction and the radial direction. The effect of fluid viscosity is captured by this dimensionless measure. Equation (227) can be referred to as the affinity law for pump discharge.

#### C.14 Affinity law for pump power

By definition, the energy head gain  $\Delta H = H_2 - H_1$  at a given discharge of fluid with density  $\rho$  [kg/m<sup>3</sup>] can be obtained from the pump power  $P$  [kg·m<sup>2</sup>/s<sup>3</sup>] as shown in equation (228).

$$\Delta P = \left. \begin{array}{l} \text{pressure gain} \times \text{volumetric flow rate} \\ \text{energy head gain} \times \text{mass flow rate} \\ \text{elevation head gain} \times \text{gravimetric flow rate} \end{array} \right\} \begin{array}{l} \Delta p Q \\ \Delta H \rho Q \\ \Delta h g \rho Q \end{array} \Rightarrow \Delta H = \frac{\Delta P}{\rho Q} \quad (228)$$

## D Derivation of pump relationships for radial and axial flow in 3D

This section demonstrates that a derivation of pump relationships is significantly more complicated in three dimensions and serves as a justification to assume axisymmetrical flow in order to obtain Euler's pump equation (see Appendix C). The derivation is open ended.

### D.1 Radial pressure head in three-dimensional physical domain

A linearization for the differential velocity is considered

$$\Delta w^2 \stackrel{\text{def}}{=} \frac{\partial w^2}{\partial r} \Delta r + \frac{\partial w^2}{\partial \theta} \Delta \theta + \frac{\partial w^2}{\partial z} \Delta z \quad (229)$$

We divide by  $\Delta r$ , assume  $\frac{\Delta \theta}{\Delta r} = 0$  and let  $\Delta$  go to zero to find

$$\frac{dw^2}{dr} = \frac{\partial w^2}{\partial r} + \frac{\partial w^2}{\partial z} \frac{dz}{dr} \quad (230)$$

Similarly, for  $v$

$$\Delta v^2 \stackrel{\text{def}}{=} \frac{\partial v^2}{\partial r} \Delta r + \frac{\partial v^2}{\partial \theta} \Delta \theta + \frac{\partial v^2}{\partial z} \Delta z \quad (231)$$

We divide by  $\Delta z$ , assume  $\frac{\Delta \theta}{\Delta z} = 0$  and let  $\Delta$  go to zero to find

$$\frac{dv^2}{dz} = \frac{\partial v^2}{\partial r} \frac{dr}{dz} + \frac{\partial v^2}{\partial z} \quad (232)$$

Hence substitutions reduce Eq. (204) to (using  $\frac{w_z}{w_r} = \frac{dz}{dr}$ )

$$-\frac{dp}{dr}\Big|_{r\theta z} = \rho \left[ -\omega^2 r + \left( \frac{1}{2} \frac{dw^2}{dr} - \frac{1}{2} \frac{\partial w^2}{\partial z} \frac{dz}{dr} \right) + \frac{dz}{dr} \left( \frac{1}{2} \frac{dv^2}{dz} - \frac{1}{2} \frac{\partial v^2}{\partial r} \frac{dr}{dz} \right) - g f_g \right] \quad (233)$$

Rewriting and changing sign (!)

$$\frac{dp}{dr}\Big|_{r\theta z} = \rho \left[ \omega^2 r - \frac{1}{2} \frac{dw^2}{dr} - \frac{1}{2} \frac{dv^2}{dr} + \frac{1}{2} \frac{\partial w^2}{\partial z} \frac{dz}{dr} + \frac{1}{2} \frac{\partial v^2}{\partial r} + g f_g \right] \quad (234)$$

The pressure along a stage of the streamline from  $r_1$  to  $r_2$  can be found as

$$\int_{stage} dp = \rho \left[ \omega^2 \int_{stage} r dr - \frac{1}{2} \int_{stage} dw^2 - \frac{1}{2} \int_{stage} dv^2 + \frac{1}{2} \int_{stage} \frac{\partial w^2}{\partial z} dz + \frac{1}{2} \int_{stage} \frac{\partial v^2}{\partial r} dr + \int_{stage} g f_g dr \right] \quad (235)$$

Which yields for the pressure related to the potential head along one streamline stage in the radial direction

$$p_2 - p_1 = \rho \left[ \omega^2 \frac{r_2^2 - r_1^2}{2} + \frac{w_1^2 - w_2^2}{2} + \frac{v_1^2 - v_2^2}{2} + g f_g(r_2 - r_1) \right] \quad (236)$$

Substitution in (117) helps us find the elevation head gain, which is the sum of the potential head and the velocity head

$$h_2 - h_1 = \underbrace{\omega^2 \frac{r_2^2 - r_1^2}{2g}}_{\text{pressure head?}} + \frac{w_1^2 - w_2^2}{2g} + \frac{v_1^2 - v_2^2}{2g} + \underbrace{f_g(r_2 - r_1)}_{\text{elevation head?}} + \underbrace{\frac{v_2^2 - v_1^2}{2g}}_{\text{velocity head}} \quad (237)$$

## D.2 Axial pressure head in a three-dimensional domain

$$\frac{dp}{dz} \Big|_{r\theta z} = \frac{\partial p}{\partial r} \frac{dr}{dz} \Big|_{r\theta z} + \frac{\partial p}{\partial \theta} \frac{d\theta}{dz} \Big|_{r\theta z} + \frac{\partial p}{\partial z} \quad (238)$$

Substitution yields

$$\begin{aligned} -\frac{dp}{dz} \Big|_{r\theta z} = & \left[ \rho \left( v_r \frac{\partial v_r}{\partial r} - \frac{v_\theta^2}{r} + v_z \frac{\partial v_r}{\partial z} \right) - \rho g_r \right] \frac{dr}{dz} \Big|_{r\theta z} \\ & + \left[ r \rho \left( v_r \frac{\partial v_\theta}{\partial r} + \frac{v_\theta v_r}{r} + v_z \frac{\partial v_\theta}{\partial z} \right) - r \rho g_\theta \right] \frac{d\theta}{dz} \Big|_{r\theta z} \\ & + \rho \left( v_r \frac{\partial v_z}{\partial r} + v_z \frac{\partial v_z}{\partial z} \right) - \rho g_z \end{aligned} \quad (239)$$

Substitution of Eq. XX and Eq. (123) in Eq. (196) results in

$$\begin{aligned} -\frac{dp}{dz} \Big|_{r\theta z} = & \left[ \rho \left( v_r \frac{\partial v_r}{\partial r} - \frac{v_\theta^2}{r} + v_z \frac{\partial v_r}{\partial z} \right) - \rho g_r \right] \frac{w_r}{w_z} \\ & + \left[ \rho \left( v_r \frac{\partial v_\theta}{\partial r} + \frac{v_\theta v_r}{r} + v_z \frac{\partial v_\theta}{\partial z} \right) - \rho g_\theta \right] \frac{w_\theta}{v_z} \\ & + \rho \left( v_r \frac{\partial v_z}{\partial r} + v_z \frac{\partial v_z}{\partial z} \right) - \rho g_z \end{aligned} \quad (240)$$

Grouping terms

$$\begin{aligned} -\frac{dp}{dz} \Big|_{r\theta z} = & \rho \left[ \frac{w_r}{w_z} v_r \frac{\partial v_r}{\partial r} - \frac{w_r}{w_z} \frac{v_\theta^2}{r} + \frac{w_\theta}{v_z} v_r \frac{\partial v_\theta}{\partial r} + \frac{w_\theta}{v_z} \frac{v_\theta v_r}{r} + v_r \frac{\partial v_z}{\partial r} \right. \\ & + \frac{w_r}{w_z} v_z \frac{\partial v_r}{\partial z} + \frac{w_\theta}{v_z} \frac{\partial v_\theta}{\partial z} + v_z \frac{\partial v_z}{\partial z} \\ & \left. - \left( \frac{w_r}{w_z} g_r + \frac{w_\theta}{v_z} g_\theta + g_z \right) \right] \end{aligned} \quad (241)$$

and  $v_r = w_r$  and  $v_z = w_z$  in the top row,  $w_r = v_r$  and  $w_z = v_z$  in the center and bottom row. In the bottom row, we know that gravity can be rewritten by substituting Eq. (122) and (126) in the gravity formulations and  $\cot \kappa = \frac{w_\theta}{w_z}$  and

$$\tan \alpha = \frac{w_r}{w_z}$$

$$\begin{aligned}
-\left(\frac{w_r}{w_z}g_r + \frac{w_\theta}{v_z}g_\theta + g_z\right) &= -\left(\frac{w_r}{w_z}g \cos \theta \cos \lambda + \frac{w_\theta}{w_z}g \sin \theta \cos \lambda + g \sin \lambda\right) \\
&= -(\tan \alpha g \cos \theta \cos \lambda + \cot \kappa g \sin \theta \cos \lambda + g \sin \lambda) \\
&= -g(\tan \alpha \cos \theta \cos \lambda + \cot \kappa \sin \theta \cos \lambda + \sin \lambda) \\
&= -g(\cos \lambda (\tan \alpha \cos \theta + \sin \theta \cot \kappa) + \sin \lambda) \\
&= -gf_{g_z}
\end{aligned} \tag{242}$$

Where  $f_{g_z} = \cos \lambda (\tan \alpha \cos \theta + \sin \theta \cot \kappa) + \sin \lambda$ . This yields

$$\begin{aligned}
-\frac{dp}{dz}\Big|_{r\theta z} &= \rho \left[ \frac{w_r^2}{w_z} \frac{\partial w_r}{\partial r} - \frac{w_r}{w_z} \frac{v_\theta^2}{r} + \frac{w_\theta}{w_z} w_r \frac{\partial v_\theta}{\partial r} + \frac{w_\theta}{w_z} \frac{v_\theta w_r}{r} + w_r \frac{\partial w_z}{\partial r} \right. \\
&\quad \left. + v_r \frac{\partial v_r}{\partial z} + w_\theta \frac{\partial v_\theta}{\partial z} + v_z \frac{\partial v_z}{\partial z} - gf_{g_z} \right]
\end{aligned} \tag{243}$$

Substitution of terms from Eq. (118) (also  $w_\theta = v_\theta + \omega r$ ) in Eq. (200) yields

$$\begin{aligned}
-\frac{dp}{dz}\Big|_{r\theta z} &= \rho \left[ \frac{w_r^2}{w_z} \frac{\partial w_r}{\partial r} - \frac{w_r}{w_z} \frac{(-\omega r + w_\theta)^2}{r} + \frac{w_\theta}{w_z} w_r \frac{\partial(-\omega r + w_\theta)}{\partial r} + \frac{w_\theta}{w_z} \frac{(-\omega r + w_\theta)w_r}{r} + w_r \frac{\partial w_z}{\partial r} \right. \\
&\quad \left. + v_r \frac{\partial v_r}{\partial z} + (v_\theta + \omega r) \frac{\partial v_\theta}{\partial z} + v_z \frac{\partial v_z}{\partial z} - gf_{g_z} \right]
\end{aligned} \tag{244}$$

Simplifying top and center line of Eq. (201)

$$\begin{aligned}
-\frac{dp}{dz}\Big|_{r\theta z} &= \rho \left[ \frac{w_r}{w_z} \left( -\omega^2 r + \left( \frac{1}{r} - 1 \right) w_\theta^2 + w_r \frac{\partial w_r}{\partial r} + w_\theta \frac{\partial w_\theta}{\partial r} \right) + w_r \frac{\partial w_z}{\partial r} \right. \\
&\quad \left. + \omega r \frac{\partial v_\theta}{\partial z} + \left( v_r \frac{\partial v_r}{\partial z} + v_\theta \frac{\partial v_\theta}{\partial z} + v_z \frac{\partial v_z}{\partial z} \right) - gf_{g_z} \right]
\end{aligned} \tag{245}$$

By making use of the product rule this can be written as (basis for further development)

$$\begin{aligned}
-\frac{dp}{dz}\Big|_{r\theta z} &= \rho \left[ \frac{w_r}{w_z} \left( -\omega^2 r + \left( \frac{1}{r} - 1 \right) w_\theta^2 + w_r \frac{\partial w_r}{\partial r} + w_\theta \frac{\partial w_\theta}{\partial r} \right) + w_r \frac{\partial w_z}{\partial r} \right. \\
&\quad \left. + \omega r \frac{\partial v_\theta}{\partial z} + \frac{1}{2} \frac{\partial (v_r^2 + v_\theta^2 + v_z^2)}{\partial z} - gf_{g_z} \right]
\end{aligned} \tag{246}$$

The latter term on the first row can be rewritten to

$$w_r \frac{\partial w_z}{\partial r} = \left( \frac{w_r}{w_z} - \frac{w_r}{w_z} \right) w_r \frac{\partial w_z}{\partial r} + w_r \frac{\partial w_z}{\partial r} = \frac{w_r}{w_z} w_r \frac{\partial w_z}{\partial r} + \left( 1 - \frac{w_r}{w_z} \right) w_r \frac{\partial w_z}{\partial r} \tag{247}$$

So that

$$\begin{aligned}
-\frac{dp}{dz}\Big|_{r\theta z} = & \rho \left[ \frac{w_r}{w_z} \left( -\omega^2 r + \left( \frac{1}{r} - 1 \right) w_\theta^2 + \left( w_r \frac{\partial w_r}{\partial r} + w_\theta \frac{\partial w_\theta}{\partial r} + w_r \frac{\partial w_z}{\partial r} \right) \right) + \left( 1 - \frac{w_r}{w_z} \right) w_r \frac{\partial w_z}{\partial r} \right. \\
& + \omega r \frac{\partial v_\theta}{\partial z} + \frac{1}{2} \frac{\partial (v_r^2 + v_\theta^2 + v_z^2)}{\partial z} \\
& \left. - g f_{g_z} \right]
\end{aligned} \tag{248}$$

Which is equal to (using product rule).

$$\begin{aligned}
-\frac{dp}{dz}\Big|_{r\theta z} = & \rho \left[ \frac{w_r}{w_z} \left( -\omega^2 r + \left( \frac{1}{r} - 1 \right) w_\theta^2 + \frac{1}{2} \frac{\partial w^2}{\partial r} \right) + \left( 1 - \frac{w_r}{w_z} \right) w_r \frac{\partial w_z}{\partial r} \right. \\
& \left. + \omega r \frac{\partial v_\theta}{\partial z} + \frac{1}{2} \frac{\partial v^2}{\partial z} - g f_{g_z} \right]
\end{aligned} \tag{249}$$

We still consider the change of tangential velocity with respect to z zero, therefore the fourth term can be neglected. We rewrite here

$$\begin{aligned}
-\frac{dp}{dz}\Big|_{r\theta z} = & \rho \left[ \frac{w_r}{w_z} \left( -\omega^2 r + \left( \frac{1}{r} - 1 \right) w_\theta^2 + \frac{1}{2} \frac{\partial w^2}{\partial r} \right) + \left( 1 - \frac{w_r}{w_z} \right) w_r \frac{\partial w_z}{\partial r} \right. \\
& \left. + \frac{1}{2} \frac{\partial v^2}{\partial z} - g f_{g_z} \right]
\end{aligned} \tag{250}$$

In the considered 3-dimensional space we know that from linearization

$$\Delta w^2 \stackrel{\text{def}}{=} \frac{\partial w^2}{\partial r} \Delta r + \frac{\partial w^2}{\partial \theta} \Delta \theta + \frac{\partial w^2}{\partial z} \Delta z \tag{251}$$

We divide by  $\Delta r$ , assume  $\frac{\Delta \theta}{\Delta r} = 0$  and let  $\Delta$  go to zero to find

$$\frac{dw^2}{dr} = \frac{\partial w^2}{\partial r} + \frac{\partial w^2}{\partial z} \frac{dz}{dr} \tag{252}$$

Similarly, for v

$$\Delta v^2 \stackrel{\text{def}}{=} \frac{\partial v^2}{\partial r} \Delta r + \frac{\partial v^2}{\partial \theta} \Delta \theta + \frac{\partial v^2}{\partial z} \Delta z \tag{253}$$

We divide by  $\Delta z$ , assume  $\frac{\Delta \theta}{\Delta z} = 0$  and let  $\Delta$  go to zero to find

$$\frac{dv^2}{dz} = \frac{\partial v^2}{\partial r} \frac{dr}{dz} + \frac{\partial v^2}{\partial z} \tag{254}$$

We also conclude that  $\frac{\partial v_\theta}{\partial z} = 0$  because of axisymmetrical flow. Hence substitutions reduce Eq. (204) to (using  $\frac{w_r}{w_z} = \frac{dr}{dz}$ )

$$\begin{aligned}
-\frac{dp}{dz}\Big|_{r\theta z} = & \rho \left[ \frac{w_r}{w_z} \left( -\omega^2 r + \left( \frac{1}{r} - 1 \right) w_\theta^2 + \left( \frac{1}{2} \frac{dw^2}{dr} - \frac{1}{2} \frac{\partial w^2}{\partial z} \frac{dz}{dr} \right) \right) \right. \\
& + \left( 1 - \frac{w_r}{w_z} \right) w_r \frac{\partial w_z}{\partial r} + \left( \frac{1}{2} \frac{dv^2}{dz} - \frac{1}{2} \frac{\partial v^2}{\partial r} \frac{dr}{dz} \right) \\
& \left. - g f_{g_z} \right]
\end{aligned} \tag{255}$$

Rewriting and changing sign

$$\begin{aligned}
-\frac{dp}{dz}\Big|_{r\theta z} = & \rho \left[ \frac{w_r}{w_z} \omega^2 r + \frac{w_r}{w_z} \left(1 - \frac{1}{r}\right) w_\theta^2 - \frac{w_r}{w_z} \frac{1}{2} \frac{dw^2}{dr} + \frac{w_r}{w_z} \frac{1}{2} \frac{\partial w^2}{\partial z} \frac{dz}{dr} \right. \\
& + \left. \left(\frac{w_r}{w_z} - 1\right) w_r \frac{\partial w_z}{\partial r} - \frac{1}{2} \frac{dv^2}{dz} + \frac{1}{2} \frac{\partial v^2}{\partial r} \frac{dr}{dz} \right. \\
& \left. + gf_{gz} \right] \quad (256)
\end{aligned}$$

Or rewritten

$$\begin{aligned}
-\frac{dp}{dz}\Big|_{r\theta z} = & \rho \left[ \frac{w_r}{w_z} \omega^2 r - \frac{w_r}{w_z} \frac{1}{2} \frac{dw^2}{dr} - \frac{1}{2} \frac{dv^2}{dz} \right. \\
& + \frac{w_r}{w_z} \left(1 - \frac{1}{r}\right) w_\theta^2 + \frac{w_r}{w_z} \frac{1}{2} \frac{\partial w^2}{\partial z} \frac{dz}{dr} + \left(\frac{w_r}{w_z} - 1\right) w_r \frac{\partial w_z}{\partial r} + \frac{1}{2} \frac{\partial v^2}{\partial r} \frac{dr}{dz} \left. \right. \\
& \left. + gf_{gz} \right] \quad (257)
\end{aligned}$$

The pressure along a stage of the streamline from  $r_1$  to  $r_2$  can be found as (multiply by  $dz$ )

$$\begin{aligned}
\int_{stage} dp = & \rho \left[ \omega^2 \int_{stage} r dz - \frac{w_r}{w_z} \frac{dz}{dr} \frac{1}{2} \int_{stage} dw^2 - \frac{1}{2} \int_{stage} dv^2 \right. \\
& + \frac{w_r}{w_z} \frac{dz}{dr} \frac{1}{2} \int_{stage} \frac{\partial w^2}{\partial z} dz + \left(\frac{w_r}{w_z} - 1\right) w_r \int_{stage} \frac{\partial w_z}{\partial r} dz + \frac{1}{2} \frac{dr}{dz} \int_{stage} \frac{\partial v^2}{\partial r} dz \left. \right. \\
& \left. + \int_{stage} gf_{gz} dr \right] \quad (258)
\end{aligned}$$

This is simplified using known ratios to

$$\begin{aligned}
\int_{stage} dp = & \rho \left[ \omega^2 \int_{stage} r dz - \frac{1}{2} \int_{stage} dw^2 - \frac{1}{2} \int_{stage} dv^2 \right. \\
& + \frac{1}{2} \int_{stage} \frac{\partial w^2}{\partial z} dz + \left(\frac{w_r}{w_z} - 1\right) w_r \int_{stage} \frac{\partial w_z}{\partial r} dz + \frac{1}{2} \frac{dr}{dz} \int_{stage} \frac{\partial v^2}{\partial r} dz \left. \right. \\
& \left. + \int_{stage} gf_{gz} dr \right] \quad (259)
\end{aligned}$$

Which yields for the pressure related to the potential head along one streamline stage in the axial direction?!

$$p_2 - p_1 = \rho \left[ \omega^2 \frac{r_2^2 - r_1^2}{2} + \frac{w_1^2 - w_2^2}{2} + \frac{v_1^2 - v_2^2}{2} + gf_g(r_2 - r_1) \right] \quad (260)$$

## E Simple derivation of affinity law for pump pressure

A more simplistic derivation of the affinity law for pump pressure  $p$  [Pa] can be obtained from force equilibrium in a pump.

Simulating a pump effect for the cutter head requires an expression for the force that is exerted by the fluid on the hypothetical volute chamber. This centrifugal force for a rotating mass is given in equation (261).

$$F_{cf} = 2\Psi \frac{mu^2}{D} \quad (261)$$

Where  $m$  is the fluid mass ( $\rho\pi/4D^2b$ ) inside the cutter [kg] and  $\Psi$  is the dimensionless head [-], a coefficient that scales the centroid of the fluid mass. The meridional exit area  $A$  [m<sup>2</sup>] of the virtual volute chamber equals  $\pi Db$ , hence the internal pressure  $p^-$  [Pa] that is exerted on the volute chamber can be found by again substituting  $u = \omega D/2$ . The affinity law for pump pressure is then found according to equation (262).

$$p = \frac{1}{8}\Psi\rho\omega^2D^2 = \hat{\Psi}\rho\omega^2D^2 \quad (262)$$

## F Expansion of the model's continuity equation

### F.1 Derivation of actual radial specific flow for disc 1 and 2

Restating the affinity laws

$$q_{r_i} = \frac{\Phi_i}{\hat{\Psi}_i} 2\pi \frac{1}{\omega \rho_i} f_{\gamma_i} \Delta p_{blade_i} \quad (263)$$

Or reversely

$$\Delta p_{blade_i} = \frac{\Psi_i}{\Phi_i} \frac{1}{2\pi f_{\gamma_i}} \omega \rho_i \hat{q}_{r_i} \quad (264)$$

We say

$$q_{r_2} = \frac{\Phi_2}{\hat{\Psi}_2} 2\pi \frac{1}{\omega \rho_w} f_{\gamma_2} \Delta p_{discs_2} = \frac{\Phi_2}{\hat{\Psi}_2} 2\pi \frac{1}{\omega \rho_w} f_{\gamma_2} (\Delta p_{blade_1} - \Delta p_{blade_2}) \quad (265)$$

Substituting equation (264)

$$\begin{aligned} q_{r_2} &= \frac{\Phi_2}{\hat{\Psi}_2} 2\pi \frac{1}{\omega \rho_w} f_{\gamma_2} \Delta p_{discs_2} \\ &= \frac{\Phi_2}{\hat{\Psi}_2} 2\pi \frac{1}{\omega \rho_w} f_{\gamma_2} \left( \frac{\Psi_1}{\Phi_1} \frac{1}{2\pi f_{\gamma_1}} \omega \rho_m \hat{q}_{r_1} - \frac{\Psi_2}{\Phi_2} \frac{1}{2\pi f_{\gamma_2}} \omega \rho_m \hat{q}_{r_2} \right) \end{aligned} \quad (266)$$

Simplify to find

$$q_{r_2} = \frac{\Phi_2}{\hat{\Psi}_2} \frac{1}{\rho_w} f_{\gamma_2} \left( \frac{\Psi_1}{\Phi_1} \frac{1}{f_{\gamma_1}} \rho_m \hat{q}_{r_1} - \frac{\Psi_2}{\Phi_2} \frac{1}{f_{\gamma_2}} \rho_m \hat{q}_{r_2} \right) \quad (267)$$

Which can be written as

$$q_{r_2} = \left( \frac{\Psi_1 \rho_m \Phi_2 f_{\gamma_2}}{\hat{\Psi}_2 \rho_w \Phi_1 f_{\gamma_1}} \hat{q}_{r_1} - \hat{q}_{r_2} \right) \quad (268)$$

Suppose

$$\rho_m = c_{vs}(\rho_q - \rho_w) + \rho_w = \left( \frac{c_c Q_c}{Q_{r_1} + Q_d + Q_{a_m}} (\rho_q - \rho_w) + \rho_w \right) \quad (269)$$

Then

$$\frac{\rho_m}{\rho_w} = c_{vs} \left( \frac{\rho_q}{\rho_w} - 1 \right) + 1 = \left( \frac{c_c Q_c}{Q_{r_1} + Q_d + Q_{a_m}} \left( \frac{\rho_q}{\rho_w} - 1 \right) + 1 \right) \quad (270)$$

Hence

$$q_{r_2} = \left( \frac{\Psi_1 \Phi_2}{\hat{\Psi}_2 \Phi_1} \left( \frac{c_c Q_c}{Q_{r_1} + Q_d + Q_{a_m}} \left( \frac{\rho_q}{\rho_w} - 1 \right) + 1 \right) \frac{f_{\gamma_2}}{f_{\gamma_1}} \hat{q}_{r_1} - \hat{q}_{r_2} \right) \quad (271)$$

Knowing

$$\hat{q}_{r_1} = \Phi_1 2\pi \omega r_{t,1}^2 f_{\gamma_1} \quad (272)$$

$$\hat{q}_{r_2} = \Phi_2 2\pi\omega r_{t,2}^2 f_{\gamma_2} \quad (273)$$

Also

$$q_{r_1} = \hat{q}_{r_1} = \hat{\Phi}_1 2\pi\omega r_{t,1}^2 f_{\gamma_1} \quad (274)$$

Then the radial velocity for disc 2 is given as

$$q_{r_2} = \frac{\Psi_1 \Phi_2}{\Psi_2 \Phi_1} \left( \frac{c_c Q_c}{q_{r_1} b_1 + Q_d + Q_{am}} \left( \frac{\rho_q}{\rho_w} - 1 \right) + 1 \right) \frac{f_{\gamma_2}}{f_{\gamma_1}} \hat{\Phi}_1 2\pi\omega r_{t,1}^2 f_{\gamma_1} - \hat{\Phi}_2 2\pi\omega r_{t,2}^2 f_{\gamma_2} \quad (275)$$

Or

$$q_{r_2} = 2\pi\omega \left[ \frac{\Psi_1 \Phi_2}{\Psi_2 \Phi_1} \left( \frac{c_c Q_c}{\hat{\Phi}_1 2\pi\omega r_{t,1}^2 f_{\gamma_1} b_1 + Q_d + Q_{am}} \left( \frac{\rho_q}{\rho_w} - 1 \right) + 1 \right) f_{\gamma_2} \Phi_1 r_{t,1}^2 - \Phi_2 r_{t,2}^2 f_{\gamma_2} \right] \quad (276)$$

## F.2 Derivation of polynomial for disc height 1

De volumetric flow rate at disc 2 is obtained from equation (276).

$$Q_{r_2} = 2\pi\omega \left( \frac{f_{\gamma_2} c_c Q_c}{2\pi\omega f_{\gamma_1} b_1 + \frac{Q_d}{\Phi_1 r_{t,1}^2} + \frac{Q_{am}}{\Phi_1 r_{t,1}^2}} \left( \frac{\rho_q}{\rho_w} - 1 \right) + f_{\gamma_2} \Phi_1 r_{t,1}^2 - \Phi_2 r_{t,2}^2 f_{\gamma_2} \right) b_2 \quad (277)$$

Split

$$Q_{r_2} = 2\pi\omega \left( \frac{f_{\gamma_2} c_c Q_c}{2\pi\omega f_{\gamma_1} b_1 + \frac{Q_d}{\Phi_1 r_{t,1}^2} + \frac{Q_{am}}{\Phi_1 r_{t,1}^2}} \left( \frac{\rho_q}{\rho_w} - 1 \right) + f_{\gamma_2} \Phi_1 r_{t,1}^2 - \Phi_2 r_{t,2}^2 f_{\gamma_2} \right) b \quad (278)$$

$$- 2\pi\omega \left( \frac{f_{\gamma_2} c_c Q_c}{2\pi\omega f_{\gamma_1} b_1 + \frac{Q_d}{\Phi_1 r_{t,1}^2} + \frac{Q_{am}}{\Phi_1 r_{t,1}^2}} \left( \frac{\rho_q}{\rho_w} - 1 \right) + f_{\gamma_2} \Phi_1 r_{t,1}^2 - \Phi_2 r_{t,2}^2 f_{\gamma_2} \right) b_1$$

Rewrite

$$Q_{r_2} = 2\pi\omega \left( \frac{f_{\gamma_2} c_c Q_c}{2\pi\omega f_{\gamma_1} b_1 + \frac{Q_d}{\Phi_1 r_{t,1}^2} + \frac{Q_{am}}{\Phi_1 r_{t,1}^2}} \left( \frac{\rho_q}{\rho_w} - 1 \right) + \Phi \left( f_{\gamma_2} r_{t,1}^2 - r_{t,2}^2 f_{\gamma_2} \right) \right) b \quad (279)$$

$$- 2\pi\omega \left( \frac{f_{\gamma_2} c_c Q_c}{2\pi\omega f_{\gamma_1} b_1 + \frac{Q_d}{\Phi_1 r_{t,1}^2} + \frac{Q_{am}}{\Phi_1 r_{t,1}^2}} \left( \frac{\rho_q}{\rho_w} - 1 \right) + \Phi \left( f_{\gamma_2} r_{t,1}^2 - r_{t,2}^2 f_{\gamma_2} \right) \right) b_1$$

Or

$$Q_{r_2} = 2\pi\omega \left( \frac{f_{\gamma_2} c_c Q_c}{2\pi\omega f_{\gamma_1} b_1 + \frac{Q_d}{\Phi r_{t,1}^2} + \frac{Q_{a_m}}{\Phi r_{t,1}^2}} \left( \frac{\rho_q}{\rho_w} - 1 \right) + \Phi (f_{\gamma_2} r_{t,1}^2 - r_{t,2}^2 f_{\gamma_2}) \right) b$$

$$- 2\pi\omega \left( \frac{f_{\gamma_2} c_c Q_c}{2\pi\omega f_{\gamma_1} b_1 + \frac{Q_d}{\Phi r_{t,1}^2} + \frac{Q_{a_m}}{\Phi r_{t,1}^2}} \left( \frac{\rho_q}{\rho_w} - 1 \right) + \Phi (f_{\gamma_2} r_{t,1}^2 - r_{t,2}^2 f_{\gamma_2}) \right) b_1 \quad (280)$$

The volumetric flow rate at disc 1 is obtained from equation (274).

$$Q_{r_1} = q_{r_1} b_1 = \Phi_1 2\pi\omega r_{t,1}^2 f_{\gamma_1} b_1 \quad (281)$$

The volumetric flow rate balance is taken

$$Q_{a_{nose}} + Q_c + Q_{r_2} - Q_{r_1} - Q_d - Q_{a_m} = 0 \quad (282)$$

So

$$2\pi\omega \left( \frac{f_{\gamma_2} c_c Q_c}{2\pi\omega f_{\gamma_1} b_1 + \frac{Q_d}{\Phi r_{t,1}^2} + \frac{Q_{a_m}}{\Phi r_{t,1}^2}} \left( \frac{\rho_q}{\rho_w} - 1 \right) + \Phi (f_{\gamma_2} r_{t,1}^2 - r_{t,2}^2 f_{\gamma_2}) \right) b$$

$$- 2\pi\omega \left( \frac{f_{\gamma_2} c_c Q_c}{2\pi\omega f_{\gamma_1} b_1 + \frac{Q_d}{\Phi r_{t,1}^2} + \frac{Q_{a_m}}{\Phi r_{t,1}^2}} \left( \frac{\rho_q}{\rho_w} - 1 \right) + \Phi (f_{\gamma_2} r_{t,1}^2 - r_{t,2}^2 f_{\gamma_2}) \right) b_1 \quad (283)$$

$$+ Q_{a_{nose}} + Q_c - Q_d - Q_{a_m} = \Phi_1 2\pi\omega r_{t,1}^2 f_{\gamma_1} b_1$$

Rewrite

$$\frac{f_{\gamma_2} c_c Q_c}{2\pi\omega f_{\gamma_1} b_1 + \frac{Q_d}{\Phi r_{t,1}^2} + \frac{Q_{a_m}}{\Phi r_{t,1}^2}} \left( \frac{\rho_q}{\rho_w} - 1 \right) 2\pi\omega b + \Phi (f_{\gamma_2} r_{t,1}^2 - r_{t,2}^2 f_{\gamma_2}) 2\pi\omega b$$

$$- \frac{f_{\gamma_2} c_c Q_c}{2\pi\omega f_{\gamma_1} b_1 + \frac{Q_d}{\Phi r_{t,1}^2} + \frac{Q_{a_m}}{\Phi r_{t,1}^2}} \left( \frac{\rho_q}{\rho_w} - 1 \right) 2\pi\omega b_1 - \Phi (f_{\gamma_2} r_{t,1}^2 - r_{t,2}^2 f_{\gamma_2}) 2\pi\omega b_1 \quad (284)$$

$$+ Q_{a_{nose}} + Q_c - Q_d - Q_{a_m} = \Phi_1 2\pi\omega r_{t,1}^2 f_{\gamma_1} b_1$$

So

$$f_{\gamma_2} c_c Q_c \left( \frac{\rho_q}{\rho_w} - 1 \right) 2\pi\omega b + \Phi (f_{\gamma_2} r_{t,1}^2 - r_{t,2}^2 f_{\gamma_2}) 2\pi\omega b \left( 2\pi\omega f_{\gamma_1} b_1 + \frac{Q_d}{\Phi r_{t,1}^2} + \frac{Q_{a_m}}{\Phi r_{t,1}^2} \right)$$

$$- f_{\gamma_2} c_c Q_c \left( \frac{\rho_q}{\rho_w} - 1 \right) 2\pi\omega b_1 - \Phi (f_{\gamma_2} r_{t,1}^2 - r_{t,2}^2 f_{\gamma_2}) 2\pi\omega b_1 \left( 2\pi\omega f_{\gamma_1} b_1 + \frac{Q_d}{\Phi r_{t,1}^2} + \frac{Q_{a_m}}{\Phi r_{t,1}^2} \right) \quad (285)$$

$$+ \left( 2\pi\omega f_{\gamma_1} b_1 + \frac{Q_d}{\Phi r_{t,1}^2} + \frac{Q_{a_m}}{\Phi r_{t,1}^2} \right) (Q_{a_{nose}} + Q_c - Q_d - Q_{a_m}) = \left( 2\pi\omega f_{\gamma_1} b_1 + \frac{Q_d}{\Phi r_{t,1}^2} + \frac{Q_{a_m}}{\Phi r_{t,1}^2} \right) \Phi_1 2\pi\omega r_{t,1}^2 f_{\gamma_1} b_1$$

Is

$$\begin{aligned}
& f_{\gamma_2} c_c Q_c \left( \frac{\rho_q}{\rho_w} - 1 \right) 2\pi\omega b \\
& + \Phi \left( f_{\gamma_2} r_{t,1}^2 - r_{t,2}^2 f_{\gamma_2} \right) 2\pi\omega b \left( 2\pi\omega f_{\gamma_1} b_1 + \frac{Q_d}{\Phi r_{t,1}^2} + \frac{Q_{a_m}}{\Phi r_{t,1}^2} \right) \\
& - f_{\gamma_2} c_c Q_c \left( \frac{\rho_q}{\rho_w} - 1 \right) 2\pi\omega b_1 \\
& - \Phi \left( f_{\gamma_2} r_{t,1}^2 - r_{t,2}^2 f_{\gamma_2} \right) 2\pi\omega b_1 \left( 2\pi\omega f_{\gamma_1} b_1 + \frac{Q_d}{\Phi r_{t,1}^2} + \frac{Q_{a_m}}{\Phi r_{t,1}^2} \right) \\
& + \left( 2\pi\omega f_{\gamma_1} b_1 + \frac{Q_d}{\Phi r_{t,1}^2} + \frac{Q_{a_m}}{\Phi r_{t,1}^2} \right) (Q_{a_{nose}} + Q_c - Q_d - Q_{a_m}) \\
& = \left( 2\pi\omega f_{\gamma_1} b_1 + \frac{Q_d}{\Phi r_{t,1}^2} + \frac{Q_{a_m}}{\Phi r_{t,1}^2} \right) \Phi_1 2\pi\omega r_{t,1}^2 f_{\gamma_1} b_1
\end{aligned} \tag{286}$$

Separate terms

$$\begin{aligned}
& f_{\gamma_2} c_c Q_c \left( \frac{\rho_q}{\rho_w} - 1 \right) 2\pi\omega b \\
& + \Phi \left( f_{\gamma_2} r_{t,1}^2 - r_{t,2}^2 f_{\gamma_2} \right) 2\pi\omega b 2\pi\omega f_{\gamma_1} b_1 + \Phi \left( f_{\gamma_2} r_{t,1}^2 - r_{t,2}^2 f_{\gamma_2} \right) 2\pi\omega b \left( \frac{Q_d}{\Phi r_{t,1}^2} + \frac{Q_{a_m}}{\Phi r_{t,1}^2} \right) \\
& - f_{\gamma_2} c_c Q_c \left( \frac{\rho_q}{\rho_w} - 1 \right) 2\pi\omega b_1 \\
& - \Phi \left( f_{\gamma_2} r_{t,1}^2 - r_{t,2}^2 f_{\gamma_2} \right) 2\pi\omega b_1 2\pi\omega f_{\gamma_1} b_1 - \Phi \left( f_{\gamma_2} r_{t,1}^2 - r_{t,2}^2 f_{\gamma_2} \right) 2\pi\omega b_1 \left( \frac{Q_d}{\Phi r_{t,1}^2} + \frac{Q_{a_m}}{\Phi r_{t,1}^2} \right) \\
& + (Q_{a_{nose}} + Q_c - Q_d - Q_{a_m}) 2\pi\omega f_{\gamma_1} b_1 + (Q_{a_{nose}} + Q_c - Q_d - Q_{a_m}) \left( \frac{Q_d}{\Phi r_{t,1}^2} + \frac{Q_{a_m}}{\Phi r_{t,1}^2} \right) \\
& = \Phi_1 2\pi\omega r_{t,1}^2 f_{\gamma_1} b_1 2\pi\omega f_{\gamma_1} b_1 + \Phi_1 2\pi\omega r_{t,1}^2 f_{\gamma_1} b_1 \left( \frac{Q_d}{\Phi r_{t,1}^2} + \frac{Q_{a_m}}{\Phi r_{t,1}^2} \right)
\end{aligned} \tag{287}$$

Rewrite

$$\begin{aligned}
& -\Phi \left( f_{\gamma_2} r_{t,1}^2 - r_{t,2}^2 f_{\gamma_2} \right) 2\pi\omega 2\pi\omega f_{\gamma_1} b_1^2 - \Phi_1 2\pi\omega r_{t,1}^2 f_{\gamma_1} 2\pi\omega f_{\gamma_1} b_1^2 \\
& + \Phi \left( f_{\gamma_2} r_{t,1}^2 - r_{t,2}^2 f_{\gamma_2} \right) 2\pi\omega b 2\pi\omega f_{\gamma_1} b_1 + (Q_{a_{nose}} + Q_c - Q_d - Q_{a_m}) 2\pi\omega f_{\gamma_1} b_1 \\
& - f_{\gamma_2} c_c Q_c \left( \frac{\rho_q}{\rho_w} - 1 \right) 2\pi\omega b_1 - \Phi \left( f_{\gamma_2} r_{t,1}^2 - r_{t,2}^2 f_{\gamma_2} \right) 2\pi\omega \left( \frac{Q_d}{\Phi r_{t,1}^2} + \frac{Q_{a_m}}{\Phi r_{t,1}^2} \right) b_1 \\
& + f_{\gamma_2} c_c Q_c \left( \frac{\rho_q}{\rho_w} - 1 \right) 2\pi\omega b + \Phi \left( f_{\gamma_2} r_{t,1}^2 - r_{t,2}^2 f_{\gamma_2} \right) 2\pi\omega b \left( \frac{Q_d}{\Phi r_{t,1}^2} + \frac{Q_{a_m}}{\Phi r_{t,1}^2} \right) \\
& + (Q_{a_{nose}} + Q_c - Q_d - Q_{a_m}) \left( \frac{Q_d}{\Phi r_{t,1}^2} + \frac{Q_{a_m}}{\Phi r_{t,1}^2} \right) \\
& - \Phi_1 2\pi\omega r_{t,1}^2 f_{\gamma_1} b_1 \left( \frac{Q_d}{\Phi r_{t,1}^2} + \frac{Q_{a_m}}{\Phi r_{t,1}^2} \right) = 0
\end{aligned} \tag{288}$$

Or

$$\begin{aligned}
& \Phi \left( f_{\gamma_2} r_{t,1}^2 - r_{t,2}^2 f_{\gamma_2} \right) 2\pi\omega 2\pi\omega f_{\gamma_1} b_1^2 + \Phi_1 2\pi\omega r_{t,1}^2 f_{\gamma_1} 2\pi\omega f_{\gamma_1} b_1^2 \\
& - \Phi \left( f_{\gamma_2} r_{t,1}^2 - r_{t,2}^2 f_{\gamma_2} \right) 2\pi\omega b 2\pi\omega f_{\gamma_1} b_1 - (Q_{a_{nose}} + Q_c - Q_d - Q_{a_m}) 2\pi\omega f_{\gamma_1} b_1 \\
& + f_{\gamma_2} c_c Q_c \left( \frac{\rho_q}{\rho_w} - 1 \right) 2\pi\omega b_1 + \Phi \left( f_{\gamma_2} r_{t,1}^2 - r_{t,2}^2 f_{\gamma_2} \right) 2\pi\omega \left( \frac{Q_d}{\Phi r_{t,1}^2} + \frac{Q_{a_m}}{\Phi r_{t,1}^2} \right) b_1 \\
& - f_{\gamma_2} c_c Q_c \left( \frac{\rho_q}{\rho_w} - 1 \right) 2\pi\omega b - \Phi \left( f_{\gamma_2} r_{t,1}^2 - r_{t,2}^2 f_{\gamma_2} \right) 2\pi\omega b \left( \frac{Q_d}{\Phi r_{t,1}^2} + \frac{Q_{a_m}}{\Phi r_{t,1}^2} \right) \\
& - (Q_{a_{nose}} + Q_c - Q_d - Q_{a_m}) \left( \frac{Q_d}{\Phi r_{t,1}^2} + \frac{Q_{a_m}}{\Phi r_{t,1}^2} \right) \\
& + \Phi_1 2\pi\omega r_{t,1}^2 f_{\gamma_1} b_1 \left( \frac{Q_d}{\Phi r_{t,1}^2} + \frac{Q_{a_m}}{\Phi r_{t,1}^2} \right) = 0
\end{aligned} \tag{289}$$

Combine

$$\begin{aligned}
& \left( \Phi \left( f_{\gamma_2} r_{t,1}^2 - r_{t,2}^2 f_{\gamma_2} \right) 2\pi\omega 2\pi\omega f_{\gamma_1} + \Phi_1 2\pi\omega r_{t,1}^2 f_{\gamma_1} 2\pi\omega f_{\gamma_1} \right) b_1^2 \\
& - \Phi \left( f_{\gamma_2} r_{t,1}^2 - r_{t,2}^2 f_{\gamma_2} \right) \left( 2\pi\omega b 2\pi\omega f_{\gamma_1} - 2\pi\omega \left( \frac{Q_d}{\Phi r_{t,1}^2} + \frac{Q_{a_m}}{\Phi r_{t,1}^2} \right) \right) b_1 \\
& + \left( f_{\gamma_2} c_c Q_c \left( \frac{\rho_q}{\rho_w} - 1 \right) - (Q_{a_{nose}} + Q_c - Q_d - Q_{a_m}) 2\pi\omega f_{\gamma_1} \right) 2\pi\omega b_1 \\
& - \left( f_{\gamma_2} c_c Q_c \left( \frac{\rho_q}{\rho_w} - 1 \right) + \Phi \left( f_{\gamma_2} r_{t,1}^2 - r_{t,2}^2 f_{\gamma_2} \right) \left( \frac{Q_d}{\Phi r_{t,1}^2} + \frac{Q_{a_m}}{\Phi r_{t,1}^2} \right) \right) 2\pi\omega b \\
& - (Q_{a_{nose}} + Q_c - Q_d - Q_{a_m}) \left( \frac{Q_d}{\Phi r_{t,1}^2} + \frac{Q_{a_m}}{\Phi r_{t,1}^2} \right) \\
& + \Phi 2\pi\omega r_{t,1}^2 f_{\gamma_1} \left( \frac{Q_d}{\Phi r_{t,1}^2} + \frac{Q_{a_m}}{\Phi r_{t,1}^2} \right) b_1 = 0
\end{aligned} \tag{290}$$

Divide by  $2\pi\omega$

$$\begin{aligned}
& \left( \Phi \left( f_{\gamma_2} r_{t,1}^2 - r_{t,2}^2 f_{\gamma_2} \right) 2\pi\omega f_{\gamma_1} + \Phi_1 r_{t,1}^2 f_{\gamma_1} 2\pi\omega f_{\gamma_1} \right) b_1^2 \\
& - \Phi \left( f_{\gamma_2} r_{t,1}^2 - r_{t,2}^2 f_{\gamma_2} \right) \left( b 2\pi\omega f_{\gamma_1} - \left( \frac{Q_d}{\Phi r_{t,1}^2} + \frac{Q_{a_m}}{\Phi r_{t,1}^2} \right) \right) b_1 \\
& + \left( f_{\gamma_2} c_c Q_c \left( \frac{\rho_q}{\rho_w} - 1 \right) - (Q_{a_{nose}} + Q_c - Q_d - Q_{a_m}) 2\pi\omega f_{\gamma_1} \right) b_1 \\
& - \left( f_{\gamma_2} c_c Q_c \left( \frac{\rho_q}{\rho_w} - 1 \right) + \Phi \left( f_{\gamma_2} r_{t,1}^2 - r_{t,2}^2 f_{\gamma_2} \right) \left( \frac{Q_d}{\Phi r_{t,1}^2} + \frac{Q_{a_m}}{\Phi r_{t,1}^2} \right) \right) b \\
& - (Q_{a_{nose}} + Q_c - Q_d - Q_{a_m}) \frac{1}{2\pi\omega} \left( \frac{Q_d}{\Phi r_{t,1}^2} + \frac{Q_{a_m}}{\Phi r_{t,1}^2} \right) \\
& + \Phi r_{t,1}^2 f_{\gamma_1} \left( \frac{Q_d}{\Phi r_{t,1}^2} + \frac{Q_{a_m}}{\Phi r_{t,1}^2} \right) b_1 = 0
\end{aligned} \tag{291}$$

Rewrite

$$\begin{aligned}
& (\Phi f_{\gamma_2} r_{t,1}^2 f_{\gamma_1} - \Phi r_{t,2}^2 f_{\gamma_2} f_{\gamma_1} + \Phi_1 r_{t,1}^2 f_{\gamma_1} f_{\gamma_1}) 2\pi\omega b_1^2 \\
& - \Phi \left[ (f_{\gamma_2} r_{t,1}^2 - r_{t,2}^2 f_{\gamma_2}) \left( 2\pi\omega f_{\gamma_1} b - \left( \frac{Q_d}{\Phi r_{t,1}^2} + \frac{Q_{a_m}}{\Phi r_{t,1}^2} \right) \right) - r_{t,1}^2 f_{\gamma_1} \left( \frac{Q_d}{\Phi r_{t,1}^2} + \frac{Q_{a_m}}{\Phi r_{t,1}^2} \right) \right] b_1 \\
& + \left( f_{\gamma_2} c_c Q_c \left( \frac{\rho_q}{\rho_w} - 1 \right) - (Q_{a_{nose}} + Q_c - Q_d - Q_{a_m}) 2\pi\omega f_{\gamma_1} \right) b_1 \\
& - \left( f_{\gamma_2} c_c Q_c \left( \frac{\rho_q}{\rho_w} - 1 \right) + \Phi (f_{\gamma_2} r_{t,1}^2 - r_{t,2}^2 f_{\gamma_2}) \left( \frac{Q_d}{\Phi r_{t,1}^2} + \frac{Q_{a_m}}{\Phi r_{t,1}^2} \right) \right) b \\
& - (Q_{a_{nose}} + Q_c - Q_d - Q_{a_m}) \frac{1}{2\pi\omega} \left( \frac{Q_d}{\Phi r_{t,1}^2} + \frac{Q_{a_m}}{\Phi r_{t,1}^2} \right) \\
& = 0
\end{aligned} \tag{292}$$

Rewrite again

$$\begin{aligned}
& \Phi 2\pi\omega \left[ (f_{\gamma_2} f_{\gamma_1} + f_{\gamma_1}^2) r_{t,1}^2 - f_{\gamma_2} f_{\gamma_1} r_{t,2}^2 \right] b_1^2 \\
& - \left[ \Phi 2\pi\omega f_{\gamma_1} f_{\gamma_2} (r_{t,1}^2 - r_{t,2}^2) b - \left( f_{\gamma_1} + f_{\gamma_2} \left( 1 - \frac{r_{t,2}^2}{r_{t,1}^2} \right) \right) (Q_d + Q_{a_m}) \right] b_1 \\
& + \left[ f_{\gamma_2} c_c Q_c \left( \frac{\rho_q}{\rho_w} - 1 \right) - 2\pi\omega f_{\gamma_1} (Q_{a_{nose}} + Q_c - Q_d - Q_{a_m}) \right] b_1 \\
& - f_{\gamma_2} \left[ \left( \frac{\rho_q}{\rho_w} - 1 \right) c_c Q_c + \left( 1 - \frac{r_{t,2}^2}{r_{t,1}^2} \right) (Q_d + Q_{a_m}) \right] b \\
& - \frac{1}{\Phi 2\pi\omega r_{t,1}^2} (Q_{a_{nose}} + Q_c - Q_d - Q_{a_m}) (Q_d + Q_{a_m}) \\
& = 0
\end{aligned} \tag{293}$$

And on

$$\begin{aligned}
& \Phi 2\pi\omega \left[ (f_{\gamma_2} f_{\gamma_1} + f_{\gamma_1}^2) r_{t,1}^2 - f_{\gamma_2} f_{\gamma_1} r_{t,2}^2 \right] b_1^2 \\
& - 2\pi\omega f_{\gamma_1} \left[ \Phi f_{\gamma_2} (r_{t,1}^2 - r_{t,2}^2) b + (Q_{a_{nose}} + Q_c - Q_d - Q_{a_m}) \right] b_1 \\
& + \left[ f_{\gamma_2} c_c Q_c \left( \frac{\rho_q}{\rho_w} - 1 \right) + \left( f_{\gamma_1} + f_{\gamma_2} \left( 1 - \frac{r_{t,2}^2}{r_{t,1}^2} \right) \right) (Q_d + Q_{a_m}) \right] b_1 \\
& - f_{\gamma_2} \left[ \left( \frac{\rho_q}{\rho_w} - 1 \right) c_c Q_c + \left( 1 - \frac{r_{t,2}^2}{r_{t,1}^2} \right) (Q_d + Q_{a_m}) \right] b \\
& - \frac{1}{\Phi 2\pi\omega r_{t,1}^2} (Q_{a_{nose}} + Q_c - Q_d - Q_{a_m}) (Q_d + Q_{a_m}) \\
& = 0
\end{aligned} \tag{294}$$

## G Geometry descriptions

There are multiple methods to describe the geometry of the cutter head. A preliminary model may overlay the cutter with a truncated cone as demonstrated in appendix G.1. An advanced geometrical description goes into further detail as presented in

### G.1 Cutter (preliminary)

In order to describe the flows in this model, the control volume is heavily simplified by reducing the cutter head geometry to a segmented cylinder geometry. First, the geometry is reduced to a truncated cone shape. Next, the cylinder diameters are found through linear interpolation within the truncated cone. These diameters are representative for the flow through the full heights  $b_1$  [m] and  $b_2$  [m] of the respective discs of the cutter as depicted in Figure G.1: Simplification of the cutter geometry and expressed in equations (295) and (296).

$$D_1 = D_{ring} - \frac{b_1}{2 \tan \kappa} \quad (295)$$

$$D_2 = D_{top} - \frac{b - b_1}{2 \tan \kappa} \quad (296)$$

Where  $D_1$  is the average diameter of segment 1 [m],  $D_2$  is the average diameter of segment 2 [m],  $D_{ring}$  is the diameter of the cutter ring [m],  $D_{top}$  is the diameter of the cutter top [m] and  $\kappa$  represents the angle between the truncated cone and the cutter ring [deg]. Figure G.1 depicts the shape of the truncated cone.

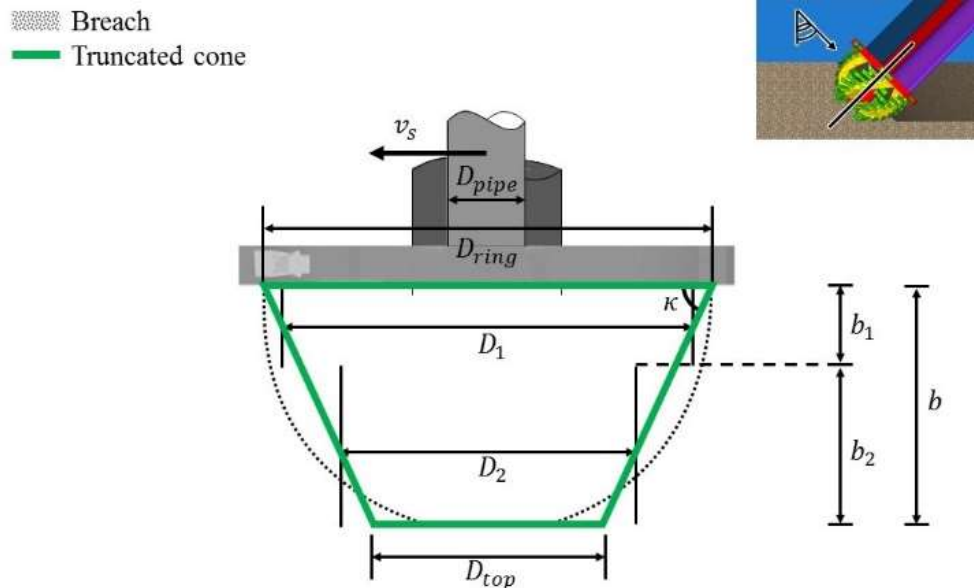


Figure G.1: Simplification of the cutter geometry.

## G.2 Bank (preliminary)

For simplicity purposes, the cutterhead is considered penetrated in the bank under an angle  $\lambda$  [deg] into an equally inclined bank angle of 45 degrees. In reality, this is highly uncommon since the high suction mouth placement induces rapid redeposition. Figure G.1: Simplification of the cutter geometry depicts the cutter placement for this model. The cut off area of the bank  $A_{cut}$  [m<sup>2</sup>] is related to the placement of the cutter and can be mapped onto the segmented cutterhead shape by introducing the effective bank height  $\hat{h}$  [m], i.e. the height of the bank in the coordinate system of the cutter. Choosing a lower bank height  $h$  [m] and thus effective bank height allows for the distribution of cut face towards segment 1 of the simplified shape. It is assumed that the tip of the simplified cutter geometry can be identified as the lower end of the effective bank height of segment 2  $\hat{h}_2$  [m].

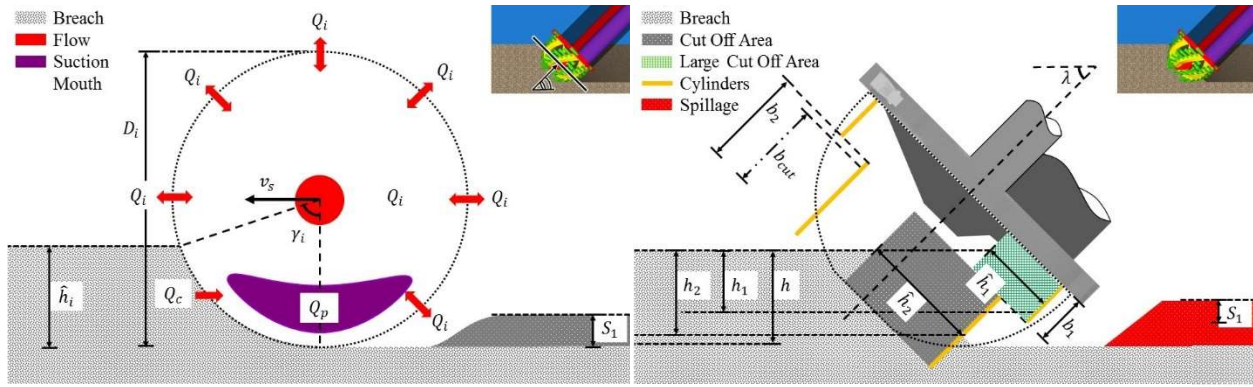


Figure G.2: Schematic visualization of the bank contact angle (left) and the relation between bank height and effective bank height (right).

As depicted in Figure G.2, the angle  $\gamma_i$  [rad] associated with the intersecting circumference of the cutter and the bank geometry can be expressed as a function of the cutter diameter and effective bank height as evidenced in equation (297). Note that this equation is only valid when the bank and ladder angle are equal and for  $2\hat{h}_i \leq D_i$ . Additional geometry formulations are necessary for larger bank heights.

$$\hat{h}_i = \frac{D_i}{2}(1 - \cos \gamma_i) \Leftrightarrow \gamma_i = \cos^{-1} \left( 1 - \frac{2\hat{h}_i}{D_i} \right) \quad (297)$$

Discretization of the cutterhead requires a geometry criterion to determine segment contributions to the cut face. Equation (298) relates a linearized estimation of the cut depth to the cut off area.

$$b_{cut} = \frac{A_{cut}}{\hat{h}} \quad (298)$$

Where  $b_{cut}$  is an estimate for the depth of the cut for the given bank-cutter interaction. Consequently, a sequence of geometry expressions allow for the computation of the parameters relevant to the cutting contributions of segment 1 and 2 for any given  $D_1$  and  $D_2$  as outlined in equation (299) and (300).

$$\widehat{h}_2 = \begin{cases} \frac{A_{cut}}{b_2}, & b_{cut} < b_2 \\ \widehat{h}, & b_{cut} \geq b_2 \end{cases} \quad (299)$$

$$\widehat{h}_1 = \begin{cases} 0, & b_{cut} < b_2 \\ \frac{A_{cut} - \widehat{h}_2 b_2}{b_1}, & b_{cut} \geq b_2 \end{cases} \quad (300)$$

Where  $\widehat{h}_1$  is de effective bank height of segment 1 [m]. Since flows through soil are neglected, the active flow contribution areas of segment 1 and 2 are found using the bank contact angle  $\gamma_i$  [rad] (see Figure G.2 (left)). The bank contact angle is used to determine the dimensionless factor  $f_{\gamma_i}$  [-] that was introduced to account for the free flow factor of the impeller exit area as shown below

$$f_{\gamma_i} = 1 - \frac{\gamma_i}{2\pi} \quad (301)$$

### G.3 Cutter (adcanvcd)

The following geometrical descriptions of the leading edge radius of the cutter and the blade angle at the leading and trailing edge respectively, supplement the advanced geometrical descriptions given in the main report.

$$\begin{aligned} r_l &= r_{l,z_0} + f_{r_{l_1}} z^2 + f_{r_{l_2}} z \\ f_{r_{l_2}} &= -\frac{r_{l,z_0} - r_{l,z_b}}{b} - f_{r_{l_1}} \\ f_{r_{l_1}} &= -0.15 \\ r_{l,z_0} &= \frac{D_{ring}}{2} \frac{3}{3.5} \\ r_{l,z_b} &= \frac{D_{nose}}{2} \frac{1}{3.5} \end{aligned} \quad (302)$$

$$\begin{aligned} \beta_t &= \beta_{t,z_0} + f_{\beta_{t_1}} z^2 + f_{\beta_{t_2}} z \\ f_{\beta_{t_2}} &= -\frac{\beta_{t,z_0} - \beta_{t,z_b}}{b} - f_{\beta_{t_1}} \\ f_{\beta_{t_1}} &= -10 \\ \beta_{t,z_0} &= 155 \\ \beta_{t,z_b} &= 100 \end{aligned} \quad (303)$$

$$\begin{aligned} \beta_l &= \beta_{l,z_0} + f_{\beta_{l_1}} z^2 + f_{\beta_{l_2}} z \\ f_{\beta_{l_2}} &= -\frac{\beta_{l,z_0} - \beta_{l,z_b}}{b} - f_{\beta_{l_1}} \\ f_{\beta_{l_1}} &= -15 \\ \beta_{l,z_0} &= 170 \\ \beta_{l,z_b} &= 60 \end{aligned} \quad (304)$$

## H Literature Notes

### H.1 Den Burger (2003)

#### 1. Goal

“A better understanding of the occurrence of spillage when using a cutter suction dredge”

- a. Mostly looking at hard formations
- b. Not necessarily reducing spillage

#### 2. Spillage Definition

“the soil that is cut during the dredging process, but is not sucked up by the suction pipe.

- a. Spillage resulting from the cutting process
  - i. Violent cutting
    1. Chips are thrown away immediately
- b. Spillage resulting from the mixture forming process
  - i. Particles (chips) enter cutter head but leave for some reason. Influenced by
    1. Geometry of cutter head
    2. Shape of the suction mouth
    3. Operational parameters
      - a. Rotational velocity
      - b. Mixture velocity
      - c. Swing/Haul velocity

#### 3. Consequences of Spillage

- a. Reduces productivity of the CSD
  - i. Digging deeper than required
- b. Increase uncertainty with regards to production estimates because difficult to estimate
  - i. Increases risk involved in obtaining dredging work
- c. Over-depth cutting required
  - i. Increases wear
  - ii. More energy consumption
    1. All together more costly operation

#### 4. Reduce spillage options

- a. Optimize cutter geometry
  - i. Very much iterative process, trial and error
- b. Adjusting operational parameters
  - i. Hard to obtain feedback
  - ii. Density meters in the suction pipe only indicate production. Far from cutter head, so delay in feedback. Additionally, Difficulties when
    1. Large parameters
    2. Flow fluctuations
    3. Slip between water and particles

#### 5. General

- a. Trailing suction hopper dredge dominates market
- b. CSD advantages
  - i. Wide range of soil type cutting

- ii. Precision
  - c. Disadvantages
    - i. Dredging depth limited
  - d. Applications
    - i. Dredging of harbors and fairways
    - ii. Land fill projects
- 6. Set-up
  - a. Ladder provides weight on the cutter head so teeth can penetrate the soil
    - i. Practice, maximum ladder angle is about 45 degrees. The larger the angle, the larger spillage.
  - b. Teeth/Chisels are mounted on adapters, which are mounted on the blades.
    - i. Easy replacement when teeth are worn out
    - ii. Ensures teeth are always positioned correctly
  - c. Blades
    - i. Thick, to ensure high cutting forces
  - d. Drive shaft
    - i. Connected to the head by means of a screw joint
  - e. Conical back plate
    - i. Distance of the breach to the suction mouth becomes smaller, beneficial for productivity.
  - f. Suction pipe
    - i. Mounted on the ladder. Sticks through conical back plate.
  - g. Spud carriage
    - i. Center of rotation for vessel
    - ii. Rotation performed by winches that are fastened by cables to side anchors
    - iii. Typically 30 degrees per side, 60 in total
    - iv. Working spud
      - 1. Fixed to the bottom, center of rotation
    - v. Auxiliary spud is down in the corners. Spud carriage is moved back towards the front of the ship. Then working spud is lowered again and auxiliary spud is lifted.
  - h. Height of cutter head
    - i. Has big influence on productivity (Slotta 1984). **Taller heads are less productive** due to distance of suction mouth.
    - ii. Suction force only significant in vicinity of suction mouth.
  - i. Skirts
    - i. Have **positive effect** on productivity. Decrease probability of particles leaving the cutter head.
    - ii. Simple steel plates, welded on the blades at the trailing edge.
- 7. Working
  - a. Hard formations: Head is typically halfway the breach to reduce cutting forces
  - b. Soft formations: Head can be deeper
  - c. Two functions that may set contradictory demands to the design of a cutter head
    - i. Mechanical cutting
      - 1. Goal: optimum between required power and wear

2. Literature reference: Roxborough 1975, Deketh 1995, Verhoef 1997.
- ii. Mixing (water/soil mixture) for suction pipe suck up
  1. Goal: minimize spillage
- d. Over-cut
  - i. Teeth of the cutter head start to cut at the top of the breach/bank working their way down
- e. Under-Cut
  - i. Teeth start at the bottom and work way up
  - ii. Practice: when cutting rock, in the under-cut situation the production is about two to three times higher than in over-cut stituation
8. Soft formations:
  - a. Particles will follow the water flow more easily than hard formations.
  - b. For sand there is a distinct relationship between productivity of a cutter head and the ratio of the suction flow and the rotational velocity of the cutter head.
  - c. ratio of suction flow and rotational velocity of the cutter head determines the flow inside the cutter head. Steinbusch first to introduce a flow number  $Q_m/(\omega \cdot R)$ . This flow number assumes **uniformity of flow**.
    - i. (Mol1977a and Moret1997a)
    - ii. Steinbusch et al al. (1999) and Dekker et al. (1999).
9. Hard formations:
  - a. Particles will be larger and consequently have a certain freedom of motion with respect to water flow.
  - b. Large particles: gravitational and inertial forces are expected to be more dominant in comparison with the cutting of sand. In that case, **spillage is determined by the indivudal values of the suction flow and the rotational velocity of the cutter head (and particle diameter and density) rather than the flow number only** (as verified in chapter 6).
10. WATER tests
  - a. For every suction flow there is a transition value for the angular velocity of the cutter head. Below the transition value, there is an ingoing flow along the entire contour head that equals **the suction flow**.
  - b. If angular velocity of cutter head is larger, an outgoing flow starts to develop. Incoming = outgoing flow + suction flow.
  - c. The ratio of angular velocity and mixture flow appeared fairly constant.
11. Flow origin
  - a. Due to shape of blades near the hub, due to screw propeller. Sucks in water from the front.
  - b. If axial flow is increased beyond suction flow, then water will leave the cutter near the ring. Particles that are dragged along cause spillage. This is considered **the centrifugal pump effect**.
  - c. The centrifugal pump effect amplifies the axial pump effect.
  - d. The pump effect caused by the blades is considered negligible to the under pressure caused by the suction flow.
  - e. The pump effect **does not refer to a pressure rise inside the cutter head**.

- f. Flow inside cutter head is governed by the Navier-Stokes equations and trajectory of a particle by its equations of motion.
    - i. See appendix A
    - ii. Dimensionless equations of motion for a particle show that for prototype scale
      - 1. Inertia of particles plays an important role when particle relaxation time is approximately of the same order of magnitude as the characteristic time scale of the fluid.
      - 2. Particle Reynolds number is well within the turbulent or Newton range ( $1 \times 10^3 < Re < 2 \times 10^5$ ). Drag coefficient is independent of  $Re_p$ . In this range, the particle drag coefficient will vary between 0.5 for spherical particles and 1.1 for sand-like particles (van Rijn, 1984).
  - g. Den Burger (2003) focuses mainly on **1 particle**. Is assumed representative for a large number of particles, with strong assumptions of
    - i. neglecting particle-particle interactions
    - ii. neglecting flow disturbance due to particles
  - h. Residence time of particles are calculated and trajectories filmed (Chapter 4)
  - i. Simulate trajectory of particle in CSD (chapter 5)
    - i. Forced vortex to represent the rotation of the fluid and a sink (suction flow)
  - j. Cutting tests (rock) and influence of inclination angle (chapter 6)
  - k. Results
    - i. Production curves have optimum
      - 1. Initial increase in angular velocity increases production
    - ii. Influence of cutter geometry on production (chapter 7)
      - 1. Verified with a model (chapter 8)
  - l. Conclusions (chapter 9)
12. Prototype tests are hard
- a. Because expensive
  - b. Difficult to perform
13. Therefore model tests
- c. Reduces number of experiments that have to be performed
  - d. Scaling tests give similar insights
14. Disadvantages
- e. Certain process may be scaled incorrectly and the consequence should be evaluated
15. Types of similarities
- f. Geometrical similarity
    - i. Equal geometrical ratios
  - g. Kinematic similarity
    - i. Similarity of time as well as geometry
      - 1. Velocity-scale ratio will be same on model and prototype scale
  - h. Dynamic similarity
    - i. Similarity of geometry, time and force
16. Literature conclusions:
- i. External force on the soil particles is gravitational in origin: Froude is appropriate scaling (Joanknecht 1976)

- i. Ratio of fall velocity and suction velocity should be equal on all scales (no physical argument given), but **still we use NS** because more appropriate

17. Viscous stresses

- j. Appendix A shows that Reynolds number is large enough to neglect the viscous stresses.
- k. Therefore NS reduces to dimensionless Euler equation
  - i. Characteristic scales
    - 1. T: time scale is either residence time of a fluid particle (applicable when the suction flow is dominant) or a specific time based on the cycle of the cutter head (when rotational velocity of the cutter head is dominant).  
Residence time =  $t = \frac{V_c}{Q_i}$

18. Operational parameters

- l. Typical values, on prototype scale, for the rotational velocity of the cutter head and mixture velocity are 30 RPM and 5m/s.
- m. Rock density between 2000 kg/m<sup>3</sup> and 2650 kg/m<sup>3</sup>.

Regarding spillage:

- 19. Cutter head works axial + centrifugal pump: sucks in water from the front and accelerates it towards the back plate (axial pump effect). Near the back plate or cutter ring the centrifugal pump effect becomes important, by which water is thrown out of the cutter head.
- 20. Every mixture flow showed a transition value where an outflow started to develop near the cutter ring. The flow increased with increasing rotational velocity.
- 21. The ratio of the transition value for the rotational velocity and the mixture velocity was fairly constant.  
 $\frac{\omega R}{v} = 0.42$ . Almost identical in both under-cut and over-cut scenario (perhaps relate transition value to transition of Reynolds to Froude number?)
- 22. Flow field inside the cutter head in under-cut situation clearly differed from the flow field in over-cut situation. (This explains why Hayes' model was a bad fit). The flow fields (patterns) were very similar with varying mixture velocities as well as rotational velocities. (moret, 1977a).
- 23. **Interesting:** placed in a water, the transition value was higher, so in the bank water actually escapes the cutter head more easily!!! This might be caused by the limitation effect of the breach.
- 24. **Mol 1977a:** the influence of the haul velocity could be accounted for by the superposing the haul velocity on the flow field of the stationary situation. Haul velocity facilitated the fluid flow out of the cutter head near the cutter ring. Important metric.
- 25. **Plastic tests** in a stationary cutter showed that the trajectory of the particles depended on the velocity ratio.
- 26. Irregardless of overcut / undercut, the amount of particles sucked up depended on the velocity ratio. Production trend followed.
- 27. **Important:** heavier particles (D50 = 1800 micrometer), deviated more from streamlines of the fluid than the paths of the smaller particles.
- 28. **In Under-cut:** the drag force and the gravitational force might cancel each other out in some parts of the cutter head.

29. In over-cut situation, the gravitational force always had a negative influence on the number of particles that was sucked up.

### H.2 Slotta (1976)

- Experiments to scale up to 2.5 [m] cutterhead Buckingham PI theory
- Non-dimensional relation for velocity using a set of dimensionless groups of variables

$$\frac{Q_p}{v_p D_{head}} = f \left( \underbrace{\left( \frac{d_n}{D_{head}} \right)^m}_{\text{diameter ratio}}, \underbrace{\left( \frac{\omega D_{head}}{D_{head}} \right)^n}_{\text{normalized velocity}}, \underbrace{\left( \frac{g D_{head}}{v_p^2} \right)^r}_{\text{inverse Froude number}}, \underbrace{\left( \frac{\mu}{v_p D_{head} \rho_p} \right)^s}_{\text{inverse Reynolds number}}, \underbrace{\left( \frac{\Delta p}{\rho v_p} \right)^t}_{\text{Euler's number}} \right) \quad (305)$$

With  $\mu$  = viscosity,  $v_p$  = velocity at suction nozzle

Principles of dimensional analysis: which of dynamic forces is dominant?

- If the same fluid is used in both model and prototype, then strict similitude can be found for only one force.
- If flow is turbulent and gravity dominant, then scale according to equal Froude numbers
- If viscous forces are dominant (laminar flow), then scale according to equal Reynolds numbers
- If both gravity and viscosity dominate, model becomes very sensitive to density and viscosity

For CSD, Reynolds scaling seems appropriate from the correlations found, even though you might expect Froude.

### H.3 Joanknecht (1976)

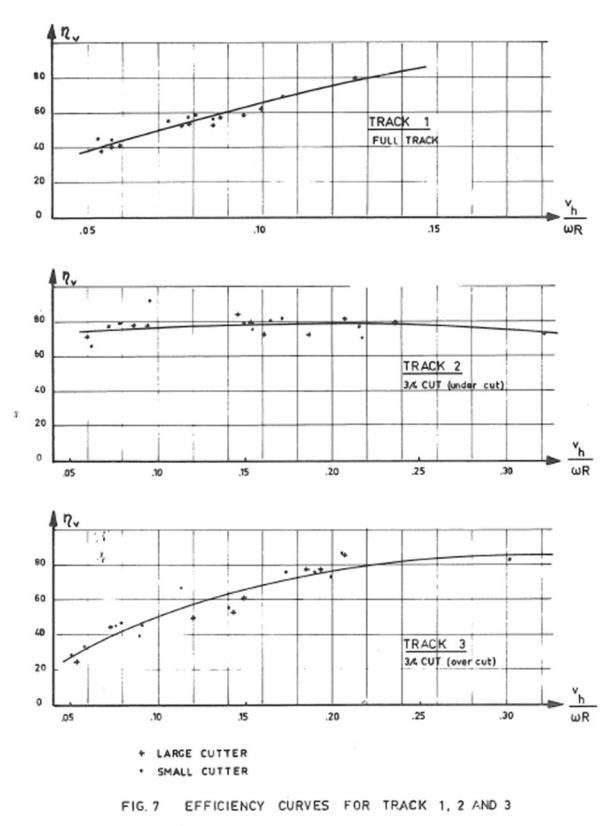
Efficiency set out against a dimensionless number

$$\eta = \frac{Q_{eff}}{Q_{th}} \quad (306)$$

The dominant parameter for kinematic similarity between model and prototype is the number of Froude based on grain size.

- For dynamic similarity, the ratio of the entrance velocity into the suction mouth and the terminal velocity of the soil cuttings should be equal in model and prototype.
- Similarity rules also by Joanknecht
- Sub-division between the cutting process and the transportation of particles towards the suction mouth.
- $d_{50} = 200$  micrometer.

- Used Froude scaling for cutting process
- Used ratio of terminal velocity and mixture velocity for transportation of particles
- Spillage:



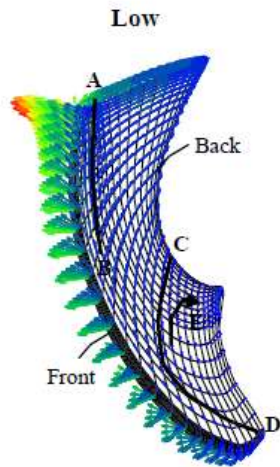
#### H.4 Steinbusch (1999)

- For low flow number rotation dominates the flow and spillage occurs near the cutter ring. For high flow number the suction flow dominates the flow, but this does not result in spillage. For nominal flow number there is a balance between rotation and suction flow. A simplified case is considered with water only. When the Reynolds number is large, and the initial flow conditions are irrotational, the Navier-Stokes equations can be simplified to the incompressible potential flow model [2] (Remember: Reynolds is most active for the suction inlet) Non-dimensional flow number characterizes an important ratio between angular velocity and the fluid velocity in the suction mouth

$$\theta = \frac{Q}{\Omega R^3} \quad (307)$$

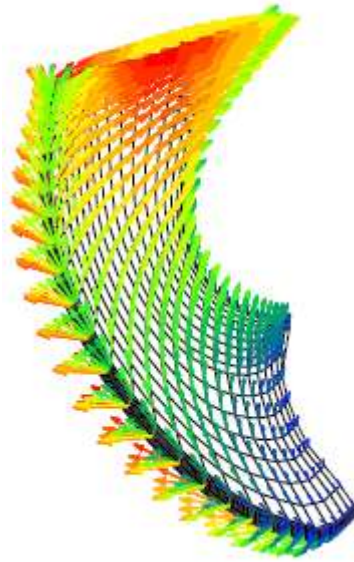
- This number was plotted horizontally and vertically the velocities were plotted. Basically two dimensional numbers plotted against each other.
- Relative velocities are plotted.

- For high flow number the suction flow induced by the pump dominates the flow. No Spillage is pre-dicted, but the flow no longer is neatly aligned with the blade.
- The computed flow patterns on the blade of the cutter head are shown in Figure 4 for three
- flow numbers, low, nominal and high. These figures show the *relative* velocity, i.e. the velocity
- seen by an observer that rotates with the cutter head. In addition a figure is given that shows
- the orientation of the blade with respect to the cutter ring in these plots.



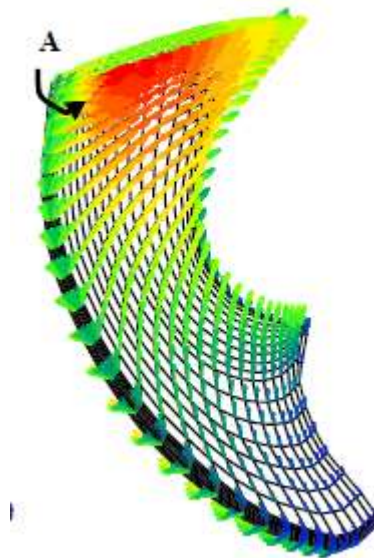
- For the low flow number, the flow is directed outward left of the line  $AB$ . There the flow leaves the cutter head (spillage). At the front of the blade near the cutter ring, the velocities are high. In between the line  $CD$  and the hub the velocity is low and recirculation is found, see the arrow  $E$ . For the low flow number, the flow induced by the rotation dominates the flow.

### Nominal



- 
- For the nominal flow number **no outflow is observed (no spillage)**. Flow velocities are roughly uniform, although lower velocities are found near the hub. For the nominal flow number there is an balance between rotation and suction induced flows.

### High



- No actual flow number is given for these graphs

## H.5 Hayes (2000)

- Operating characteristics, sediment properties, site characteristics and environmental conditions are identified
- Dimensional analysis for numbers
- Parameters correlated with observed sediment rates.
- Lots of research on suspended sediment transport, but requires information about sediment resuspension at dredging operation (mass generation rate or a concentration distribution)
- "One TGU corresponds to the quantity of turbidity generated when a unit of quantity of bed material is dredged." Hayes (2000) about Nakai (1978)

$$TGU = \frac{KBHuC_r}{Q_p} \quad (308)$$

- $R_{74}$  = fraction by weight of particles finer than 74 micrometer
- $R_0$  = fraction by weight of particles smaller than the diameter of a particle whose critical resuspension velocity equals the measured current velocity
- $Q_p$  = volume rate of dredged materials [ $m^3/s$ ] ??? denoted as  $Q_s$  in paper but expected to be  $Q_p$
- $B$  is the width of the turbid area [m]
- $H$  = depth of water [m]
- $u$  = unidirectional tidal current velocity
- $C_r$  = net concentration of suspended solids generated by dredging [ $kg/m^3$ ].
- Relation assumes uniform vertical and horizontal sediment distributions in the water column and a constant, unidirectional velocity.

**Hayes (1986) found this relation from correlation to dimensionless variables**

*Data: - Calumet Harbour III*

$$C_r = 0.150 \left( \frac{v_s}{v_p} \right)^{2.869} \left( \frac{v_{rt}}{v_p} \right)^{1.027} \quad (309)$$

- $v_s$  = swing velocity [m/s]
- $v_p$  = suction intake velocity [m/s]
- $v_{rt}$  = tangential velocity at top of the rotation **relative to surrounding water** [m/s]
- The  $R^2$  statistic for multiple determination of 0.72 ( $n=12, p=3$ ). The cut thickness (face) is approximately equal to cutter diameter, but since equal, was **not taken into account** in the regression. Elliptical cutterhead is assumed. Note that

$$v_{rt} = \begin{cases} |v_s + v_t|, & \text{starboard - to - port} \\ |v_s - v_t|, & \text{port - to - starboard} \end{cases} \quad (310)$$

## H.6 Andrassy and Herbich (1988)

Examined the relationship between dredging operational parameters and observed sediment resuspension concentrations from many field and laboratory studies. Including data from Brahme (1983) and Herbich and DeVries (1986).

Parameters were:

- rotational velocity
- suction velocity
- swing velocity
- thickness of cut
- ladder angle
- sediment size
- cutterhead size

**No statistically significant relationships** were identified in the study.

Field data were:

- James River
- Savannah River
- Calumet Harbor
- Port Kanda (Japan)
- lab data (Brahme)
- lab data (Herbich deVries)

**Collins (1995) performed a regression analysis similar to Hayes 1986, but included data from**

- Calumet Harbor
- James River
- Savannah River

(More dredge sizes, operating parameters and sediment characteristics)

A new relation for  $C_r$

$$\frac{C_r}{\rho} = 10^6 F_F F_D \left( \frac{v_s}{v_p} \right)^{2.848} \left( \frac{v_t}{v_p} \right)^{1.022} \quad (311)$$

$F_f$  and  $F_d$  regression parameters for (cutter size) and (thickness of cut relative to the cutter).

(Note: the latter term can be rewritten to make it simpler. But since the absolute velocities are used and always have a positive value, they are indistinguishable. Low swing speed equals high swing speed with counter velocity!

### Empirical relations for spillage estimation type 1

In essence, sediment dislodged by the cutter head can be differentiated with respect to three flow rates (Hayes, 2000) as formulated in Equation (312).

$$\dot{m}_S = \dot{m}_P + \dot{m}_G + \dot{m}_D \quad (312)$$

where  $\dot{m}_S$  is the rate of in situ sediment dislodged by the cutter head [kg/m<sup>3</sup>]  $\dot{m}_P$ , is the rate of sediment removal via the suction mouth [kg/s],  $\dot{m}_G$  is the rate of sediment that is suspended and immediately redeposited by the cutter [kg/s],  $\dot{m}_D$  is the rate of sediment brought into suspension by the cutter and transported away [kg/s]. Neglecting the spillage source from the violent nature of the cutting process (type 1), it can be assumed that

$$\dot{m}_S = c_c A_c * v_s \quad (313)$$

$C_c$  = concentration of the cut

The surface of the cut is dependent of the cutter geometry and commonly estimated rudimentarily using  $A_c = L_c t_c$ , where  $L_c$  and  $t_c$  are the length of the cutterhead and thickness of the cut respectively [m].

According to Hayes,  $\dot{m}_S$  as well as  $\dot{m}_P$  can be estimated with reasonable accuracy

$$\dot{m}_P = c_p Q_p \quad (314)$$

Field data suggest  $\dot{m}_S \gg \dot{m}_D$  and  $\dot{m}_P \gg \dot{m}_D$

Hayes expects that sediment resuspension results from fine sediment particles adhering to the cutter blades as they pass through the sediment

If so, sediment resuspension should be related to the rotational surface area exposed to the

washing mechanism of the water, i.e., while they are out of the bottom sediment and exposed to erosional forces associated with water passing across the blade surface. Thus, the total surface area exposed to washing (The disturbed mass of air or water pushed aft (or fore when in reverse) by the) can be estimated as

$$A_E = A_F + A_T \quad (315)$$

$A_E$ =exposed area

$A_F$ =surface area on the forward face of the cutter exposed to washing action

$A_T$ =exposed cutter area on the trailing side of the cutter

Very elaborate derivation of surface area for washing is presented (Crocket 1933)

$$\dot{m}_D = c_D L_c H_D v_s \quad (316)$$

$H_D$ =height above newly dredged elevation  $\sim 2D_c$

$m_D$ = [kg/h]

Hayes estimated that resuspended solid concentration decreases to background concentrations at approximately two cutter head diameters above the postdredging bottom. Conservative estimate. Very limited field observations. "Values for  $C_r$  were first adjusted for background total suspended solids

concentration and, thus, reflect only the resuspended sediment resulting from the dredging operations.”

Parameters were made non-dimensional. A stepwise linear regression analysis was conducted. ‘g’ replaced  $\dot{m}_D$  to annotate predicted values.

Correlation was found:

$$g = 10^{5.666} v_{rt}^{1.864} \left( \frac{A_E}{A_C} \right)^{14.143} \quad (317)$$

g= predicted value

$$R^2 = 0.572$$

This relation was shown to be a better predictor than the mean values (RMSE/S<sub>m</sub>). It was seen that the effect of swing velocity was obscured by other variables. Also,  $\widehat{\dot{m}_D}$  was not yet included. This can be rewritten to dimensional function

$$g = 1.3147 |V_s \pm n\pi D_{head}|^{1.864} \left( \frac{A_E}{D_{head} L_c} \right)^{14.143} \quad (318)$$

Dimensional analysis yielded significance of variables. Now Dimensionless numbers are considered.

Buckingham Π theory (Buckingham, 1995)) was used to reduce the number of independent solutions to be investigated.

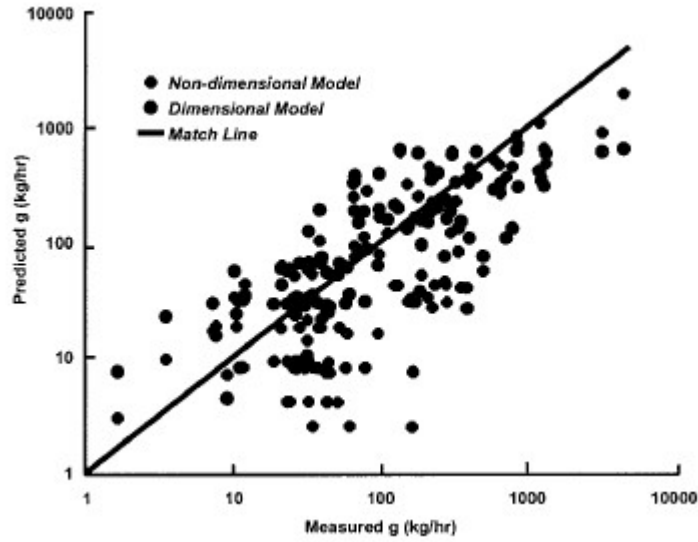
$$\underbrace{\frac{\dot{m}_D}{\dot{m}_S}}_{\pi_1} = f \left( \underbrace{\frac{\dot{m}_S}{\dot{m}_P}}_{\pi_2}, \underbrace{\frac{v_s}{v_p} \frac{A_E}{A_C}}_{\pi_3}, \underbrace{\frac{A_E}{A_C}}_{\pi_4}, \underbrace{\frac{v_{rt}}{v_p}}_{\pi_5} \right) \quad (319)$$

Buckingham Π analysis yielded

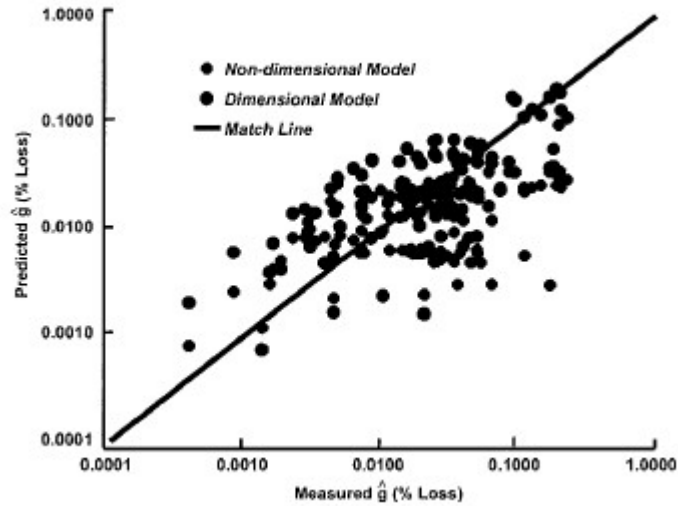
$$\pi_1 = 10^{-5.812} \pi_3^{1.804} \pi_5^{1.966} \quad (320)$$

Or

$$g = \frac{c_c t_c D_{head}^{1.966} L_c^{2.966} V_s^{2.804} A_E^{1.804} |V_s \pm n\pi D_{head}|^{1.966}}{30.5 Q^{3.770}} \quad (321)$$



The dimensionless model and dimensional model are compared.



Rewrite to % loss using formula above for mD and mS for dimensional

$$\hat{g} = \frac{|V_s \pm n\pi D_{head}|^{1.864}}{27.4c_c V_s t_c L_c^{15.143}} \left( \frac{A_E}{D_{head}} \right)^{14.143} \quad (322)$$

Dimensionless

$$\hat{g} = \frac{(L_c D_{head})^{1.966} (v_s A_E)^{1.804} |V_s \pm n\pi D_{head}|^{1.966}}{1.099Q^{3.770}} \quad (323)$$

n= [rps], Q=volumetric flow rate through the cutter.

	DM	NDM
Adjusted correlation coefficient $r$	0.76	0.72
$S_e$ (kg/hr)	0.42	0.94
RMSE/ $S_e$	0.63	<b>0.54</b>

Bold = best prediction

However, sensitivity important with such power equations. Specific variables are:

cutter diameter =  $D_{head} = 1.07$  m

$L_c = 0.91$  m

flow rate =  $0.6$  m<sup>3</sup>/s

dredging depth =  $6.1$  [m]

ladder angle =  $23.6$  [deg]

When not the dependent variables, these were values: (so buckingham theory rotates dependent variables)

$n = 0.25$  rps (0.15 rpm)

$v_s = 0.305$

$tc/D_f = 1$

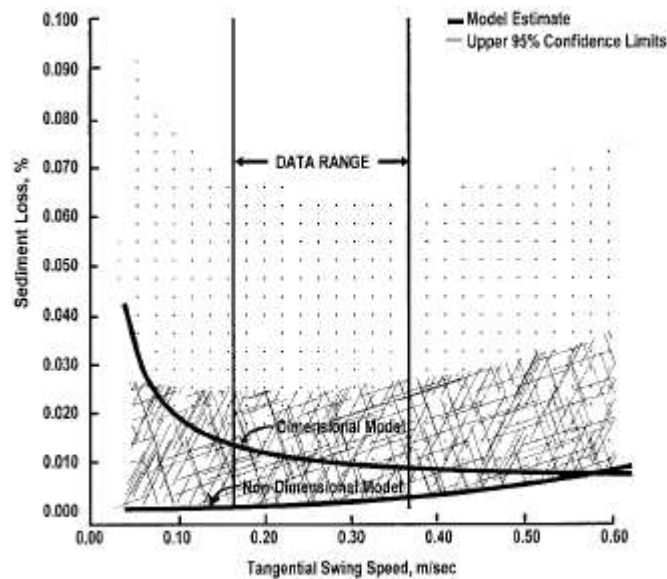


FIG. 3. Model Sensitivity to Swing Speed  $V_s$

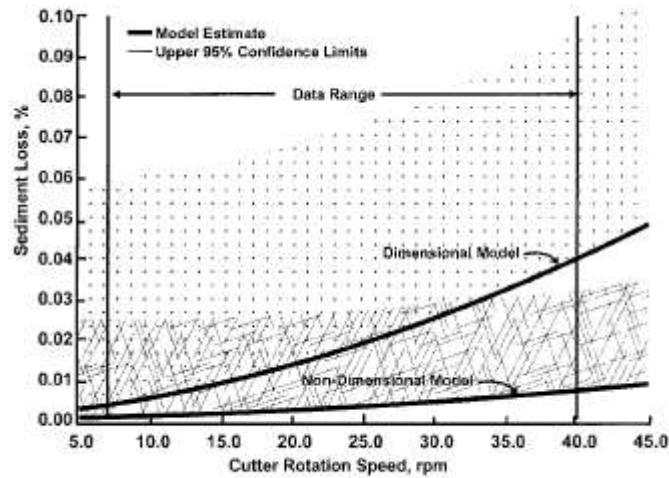


FIG. 4. Model Sensitivity to Cutter Rotation Speed  $\alpha$

Careful:

- Most applicable for similar models
- only apply to dredges within the range of operating characteristics
- application was tried against Acushnet River data, but initial models did not explain resuspended sediment variations very well. Better models needed.
- 0.0035% LOSS

### H.7 Empirical relations for spillage estimation type 1

In essence, sediment dislodged by the cutter head can be differentiated with respect to three flow rates (Hayes, 2000) as formulated in Equation (312).

$$\dot{m}_S = \dot{m}_P + \dot{m}_G + \dot{m}_D \quad (324)$$

where  $\dot{m}_S$  is the rate of in situ sediment dislodged by the cutter head [kg/m<sup>3</sup>],  $\dot{m}_P$  is the rate of sediment removal via the suction mouth [kg/m<sup>3</sup>],  $\dot{m}_G$  is the rate of sediment that is suspended and immediately redeposited by the cutter [kg/m<sup>3</sup>],  $\dot{m}_D$  is the rate of sediment brought into suspension by the cutter and transported away [kg/m<sup>3</sup>]. Neglecting the spillage source from the violent nature of the cutting process (type 1), it can be assumed that

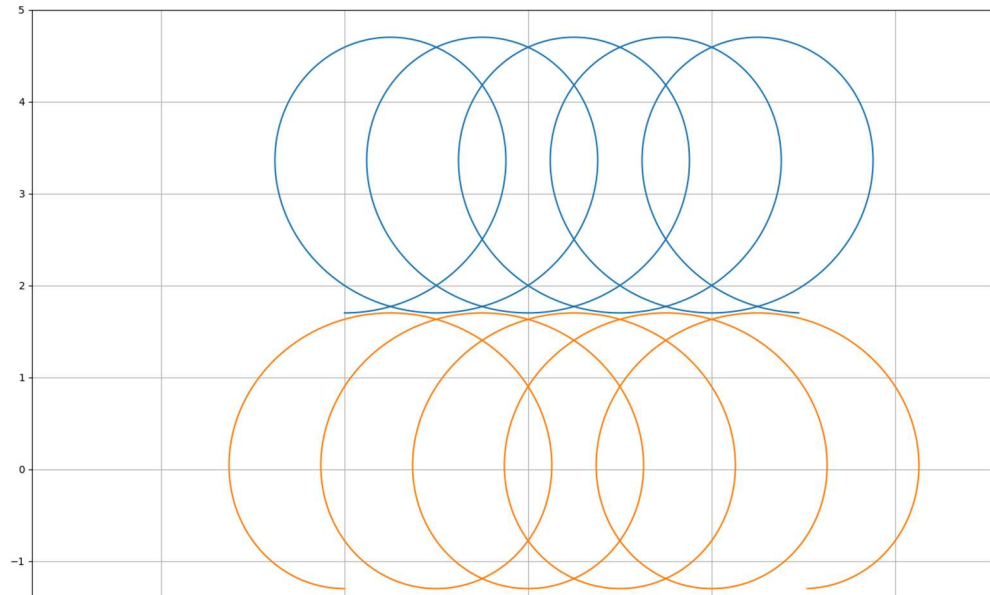
$$\dot{m}_S = C_S A_C * v_S \quad (325)$$

The surface of the cut is dependent of the cutter geometry and commonly estimated rudimentarily using  $A_C = L_C t_C$ , where  $L_C$  and  $t_C$  are the length of the cutterhead and thickness of the cut respectively [m].

According to Hayes,  $\dot{m}_S$  as well as  $\dot{m}_P$  can be estimated with reasonable accuracy

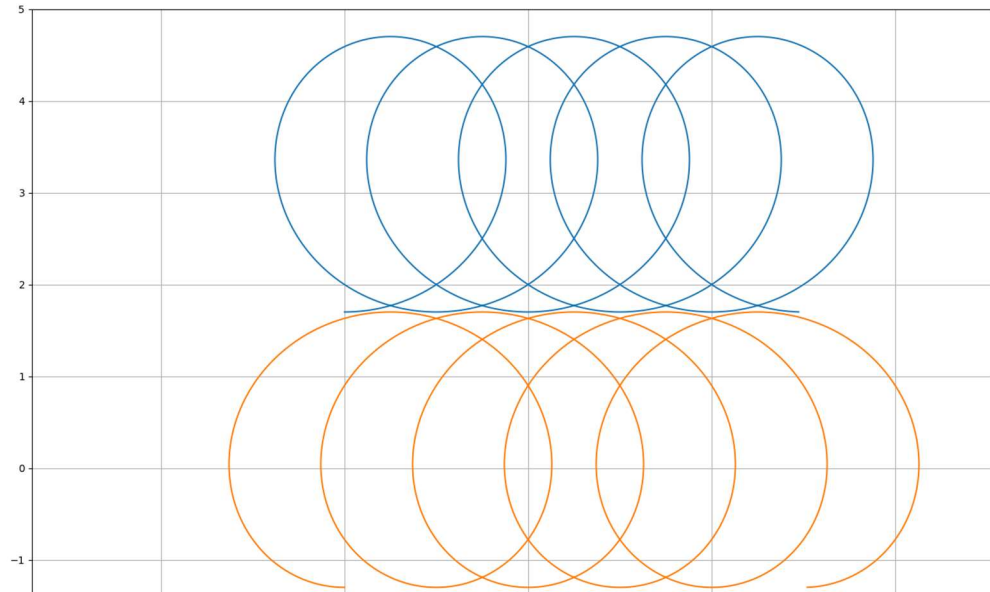
# I Cutter tip trajectory

Cutter tip trajectories for a single bladed cutter head.



**Cutter tip trajectories for dig-swing (top) and back swing (bottom)**

Cutter tip trajectories for a six-bladed cutter head.



**Cutter tip trajectories for dig-swing (top) and back swing (bottom)**

## J Reference Implementation (Python)

### SRCSM.py

```
# -*- coding: utf-8 -*-
"""
Created on Mon Jun 11 14:01:51 2018

@author: jwerkhoven
@version: Python 2.7
"""

# Import functions
from __future__ import division
import numpy as np
import tkMessageBox
import time
import matplotlib.pyplot as plt

#%% Define Sand-Rock Cutting Spillage Model (Version 1)
def M_SRCSM(speed,vrbls,geometry,nvrnmnt,ii):

    # Geometrical variables
    D_ring      = geometry.D_ring
    r_ring      = D_ring/2
    D_nose      = geometry.D_nose
    r_nose      = D_nose/2
    b           = geometry.b_cutter
    b_1start    = 0.25*b # Estimate width for iteration
    D_pipe      = geometry.D_pipe
    xideg       = geometry.xi_deg

    # Environmental variables
    h           = nvrnmnt.h_bank
    lambddeg    = nvrnmnt.lambda_deg
    c_c         = nvrnmnt.c_c
    v_s         = nvrnmnt.v_s
    l_step      = nvrnmnt.l_step

    # Cutting variables
    v_m         = vrbls.v_m_index[ii]
    Phi         = vrbls.Phi
    f_d         = vrbls.f_d
    f_c_d       = vrbls.f_c_d
    f_d_type    = vrbls.f_d_type
    particle    = vrbls.particle
    omegarad   = vrbls.omega_rad

    # Compute penetration depth
    lambdarad  = np.deg2rad(lambddeg)
    xirad      = np.deg2rad(xideg)
    z_pen      = l_step * np.cos(lambdarad)

    # Input particle-specific parameters
    if particle == 1: #Sand
        v_ts    = 0.02
        rho_q   = 2650
        rho_b   = 1700
        rho_w   = 1025
    elif particle == 0: #rock
        v_ts    = 0.73
        rho_q   = 2200
        rho_b   = 1700
        rho_w   = 1025

    #%% Improved Geometry

    # Trailing edge radii ring (0) and nose (b) (given)
    r_t_0 = D_ring/2
```

```

r_t_b = D_nose/2
r_t_0_fit1 = -0.1
r_t_0_fit2 = -(r_t_0 - r_t_b)/b - r_t_0_fit1*b
def r_t_function(z):
    r_t = r_t_0 + r_t_0_fit1*z**2 + r_t_0_fit2*z
    return r_t

# Leading edge radii at ring (0) and nose (b) (from drawings)
r_l_0 = r_t_0 * 3.0/3.5
r_l_b = r_t_b * 1.0/3.5
r_l_0_fit1 = -0.15
r_l_0_fit2 = -(r_l_0 - r_l_b)/b - r_l_0_fit1*b
def r_l_function(z):
    r_l = r_l_0 + r_l_0_fit1*z**2 + r_l_0_fit2*z
    return r_l

# Leading edge blade angles at ring (0) and nose (b) (from drawings)
B_t_0 = 155
B_t_b = 100
B_t_0_fit1 = -10
B_t_0_fit2 = -(B_t_0 - B_t_b)/b - B_t_0_fit1*b
def B_t_function(z):
    B_t = B_t_0 + B_t_0_fit1*z**2 + B_t_0_fit2*z
    return B_t

# Trailing edge blade angles at ring (0) and nose (b) (from drawings)
B_l_0 = 170
B_l_b = 60
B_l_0_fit1 = -25
B_l_0_fit2 = -(B_l_0 - B_l_b)/b - B_l_0_fit1*b
def B_l_function(z):
    B_l = B_l_0 + B_l_0_fit1*z**2 + B_l_0_fit2*z
    return B_l

# Optional check
def r_t_derivative(z):
    r_t_d = -2*r_t_0_fit1*z - r_t_0_fit2
    return r_t_d

### Bank contact parameters

# Apply condition for z_tip
z_tip = -1/2 * (np.tan(lambdarad)+r_t_0_fit2)/r_t_0_fit1
if z_tip < b:
    z_tip = z_tip
else:
    z_tip = b

z_0 = 0
z_2 = b-z_pen
r_t_z_2 = r_t_function(z_2)
r_t_z_pen = r_t_function(z_pen)
r_t_z_tip = r_t_function(z_tip)
Delta_r = abs(-r_t_z_tip - (-r_t_z_2 + (z_tip-z_2)*np.tan(lambdarad)))
h_pen = Delta_r*np.cos(lambdarad)
z_1 = z_2 - Delta_r * np.tan(np.pi/2-xirad-lambdarad)

r_b_z_2 = -r_t_z_2
r_b_z_1 = -r_t_z_2 - Delta_r
r_b_z_0 = r_b_z_1 - z_1*np.tan(lambdarad)

h_hat = h/np.sin(xirad)
h_hat_2 = h_pen*np.sin(xirad)
h_hat_3 = h_hat-h_hat_2

# Apply condition for z_3
z_3 = h_hat_3*np.sin(np.pi/2-xirad-lambdarad) + z_2
if b <= z_3:
    z_3 = b
elif b < z_3:

```

```

z_3 = z_3

r_b_z_3 = -r_t_z_2 + np.sqrt(h_hat_3**2 + (z_3-z_2)**2)
z_4 = b
r_b_z_4 = r_b_z_3 + (z_4-z_3)*np.tan(lambdarad)
delta_z_hat_pen = (z_2-z_1)/np.cos(lambdarad)
r_t_z_4 = r_t_function(z_4)

### Compute cut area
a_s = h_hat # verified
b_s = h/np.cos(np.pi/2 - lambdarad)
c_s = (z_3-z_1)/np.cos(lambdarad) # verified
s = (a_s+b_s+c_s)/2

# Apply condition for A_cut_triangle in case lambda == xi
if c_s == 0:
    A_cut_triangle = 0
elif 0 < c_s:
    A_cut_triangle = np.sqrt(s*(s-a_s)*(s-b_s)*(s-c_s))

A_cut_parallelogram = h*(z_4-z_3)/np.cos(lambdarad) # verified
A_cut = A_cut_triangle + A_cut_parallelogram

### Determine outflow angle
def gamma_function(z,r_t_z,r_b_z):
    if r_b_z <= -r_t_z:
        gamma = 0
    elif -r_t_z < r_b_z <= r_t_z:
        if r_b_z <= 0:
            Delta_r_b_z = r_t_z - abs(r_b_z)
        elif 0 < r_b_z:
            Delta_r_b_z = r_t_z + r_b_z
        x_z_squared_1 = -Delta_r_b_z**2 + np.sqrt(1/2*Delta_r_b_z**2 + \
            4*r_t_z**2*Delta_r_b_z**2)
        x_z_squared_2 = -Delta_r_b_z**2 - np.sqrt(1/2*Delta_r_b_z**2 + \
            4*r_t_z**2*Delta_r_b_z**2)
        x_z_squared = max(x_z_squared_1,x_z_squared_2)
        x_z = np.sqrt(x_z_squared)
        gamma = 2*np.arctan(r_b_z/x_z)
    elif r_t_z < r_b_z:
        gamma = 1
    return gamma

def r_b_function(z):
    if z < z_1:
        r_b_z = r_b_z_0 + z*np.tan(lambdarad)
    elif z_1 <= z < z_3:
        r_b_z = r_b_z_2 + (z-z_2)*np.tan(lambdarad+xirad)
    elif z_3 <= z:
        r_b_z = r_b_z_3 + (z-z_3)*np.tan(lambdarad)
    return r_b_z

### Checking geometry

# x = np.linspace(0, b, 100)
# fig = plt.figure()
# plt.plot(x, r_t_function(x))
# plt.plot(x, -r_t_function(x))
# plt.plot([z_0,z_1,z_2,z_3,z_4], [r_b_z_0,r_b_z_1,r_b_z_2,r_b_z_3,r_b_z_4])
# plt.xlim(0, 6)
# plt.ylim(-4, 2)
# plt.gca().set_aspect('equal', adjustable='box')
# plt.show

### Iteration model

# Iteration starter
jj = 0

# Specify iteration parameters

```

```

relax      = speed.relax          # Determine iteration step
threshold  = speed.threshold      # Determine required accuracy
error      = 1                    # Start value for error

# Iterate under accuracy condition
while error > threshold:
    jj=jj+1

    # Compute iteration geometry
    b_2      = b-b_1start          # Height of disc 2
    r_ext_1  = r_t_function(b_1start) # Radius of disc 1
    r_ext_2  = r_t_function(b_1start + b_2/2) # Radius of disc 2

    %% Bank contact area and parameters (Simple geometry)
    if geometry.version == 1:

        # Simple geometry does not take into account the shape of the bank
        b_cut    = A_cut/h_hat
        h_hat    = h/np.sin(xirad)
        kapparad = np.arctan(b/((D_ring-D_nose)/2))
        D_1      = D_ring-b_1start/np.tan(kapparad)
        D_2      = D_nose+(b_2)/np.tan(kapparad)

        # Verify condition for h
        if 2*h_hat <= D_1:
            h_hat = h_hat
        else:
            tkinter.showerror('Geometry error', 'h_hat < D_z/2')

        if b_cut < b_2:
            h_hat_2 = A_cut/b_2
            h_hat_1 = 0
        elif b_cut > b_2:
            h_hat_2 = h_hat
            h_hat_1 = (A_cut-h_hat_2*b_2)/b_1start

        if h_hat_1 < D_1/2:
            gamma_1 = np.arccos(1-(2*h_hat_1/D_1))
        else:
            gamma_1 = np.arcsin(2*h_hat_1/D_1-1+np.pi/2)

        if h_hat_2 < D_2/2:
            gamma_2 = np.arccos(1-(2*h_hat_2/D_2))
        else:
            gamma_1 = np.arcsin(2*h_hat_2/D_2-1+np.pi/2)

    %% Bank contact area and parameters (Advanced geometry)
    elif geometry.version == 2:

        # Linearized geometry for the computation of outflow parameter
        r_t_1 = r_t_function(b_1start/2)
        r_t_2 = r_t_function(b_1start+b_2/2)
        r_b_1 = r_b_function(b_1start/2)
        r_b_2 = r_b_function(b_1start+b_2/2)
        gamma_1 = gamma_function(b_1start/2,r_t_1,r_b_1)
        gamma_2 = gamma_function(b_1start+b_2/2,r_t_2,r_b_2)

    elif geometry.version == 3:

        # Take average of a series of slices to determine average gamma
        n_slices = 10

        # For disc 1
        gamma_collect_1 = []
        x = np.linspace(0, b_1start, n_slices)
        for ii in x:
            r_t_1 = r_t_function(ii)
            r_b_1 = r_b_function(ii)
            gamma = gamma_function(ii,r_t_1,r_b_1)

```

```

        gamma_collect_1 = np.hstack([[gamma_collect_1,gamma]])

# For disc 2
gamma_collect_2 = []
x = np.linspace(b_1start, b, n_slices)
for ii in x:
    r_t_2 = r_t_function(ii)
    r_b_2 = r_b_function(ii)
    gamma = gamma_function(ii,r_t_2,r_b_2)
    gamma_collect_2 = np.hstack([[gamma_collect_2,gamma]])

# Take averages
gamma_1 = sum(gamma_collect_1)/n_slices
gamma_2 = sum(gamma_collect_2)/n_slices

# Coefficients
f_gamma_1 = 1-gamma_1/(2*np.pi)
f_gamma_2 = 1-gamma_2/(2*np.pi)

# Blade angle at the trailing edge
B_t_1 = B_t_function(b_1start/2) # Pre Green Light version

### SRCSM start

# Centrifugal advection, volumetric flow rate disc 1 (estimate)
Q_r_1 = Phi*2*np.pi*omegarad*r_ext_1**2*f_gamma_1*b_1start

# In situ volumetric dredge flow rate
Q_c = A_cut*v_s

# Axial volumetric flow rate at the suction pipe
Q_a_m = 1/4*np.pi*D_pipe**2*v_m

# Axial volumetric flow rate at the nose
Q_a_nose = Q_a_m*nvrnmnt.Q_a_nose

#
if vrbls.version == 1: # WODCONXXII version

    Q_a_nose = 0

elif vrbls.version == 2: # Post Green Light Version

    if gamma_2 <= np.pi:
        x_2 = r_t_2 * np.sin(gamma_2)

# Compute radial component of v at theta = pi/2,
# half penetration depth
v_ts_r = v_ts/np.cos(lambdarad)
v_r_thalfpihalfzpen_hat = v_ts_r # _hat because approximation

# Compute axial component of v at theta = pi/2, half penetration
# depth
v_z_thalfpihalfzpen_hat = v_m # _hat because approximation

# Compute velocity
u_thalfzpen = omegarad*r_t_2
v_ratio_hat = v_r_thalfpihalfzpen_hat/(v_z_thalfpihalfzpen_hat)

# Apply minimum criterium for the downwards velocity
v_theta_thalfpihalfzpen = v_ts_r + f_d_type*f_d*u_thalfzpen
if v_theta_thalfpihalfzpen > 0:
    v_theta_thalfpihalfzpen = v_theta_thalfpihalfzpen
elif v_theta_thalfpihalfzpen <= 0:
    v_theta_thalfpihalfzpen = 0

r_t_ref = r_ext_2
A_d = abs(x_2)*b_2
Q_d = A_d *v_theta_thalfpihalfzpen *(v_ratio_hat)**2 \
    *(b-z_pen/2)/h_hat

```

```

# Compute new value for b_ltrue
# This calculation method prioritizes simplicity over runtime and can
# be adapted for speed improvements
b_ltrue = (f_gamma_2*r_ext_1**2*c_c*Q_c / \
           (Phi**2*np.pi*omegarad*r_ext_1**2*f_gamma_1*b_lstart + \
            Q_d + Q_a_m)* \
           ((rho_q/rho_w)-1) \
           + f_gamma_2*r_ext_1**2 - r_ext_2**2*f_gamma_2)/ \
           r_ext_1**2*f_gamma_1 \
           +(Q_a_nose + Q_c - Q_d - Q_a_m)/ \
           (Phi**2*np.pi*omegarad*r_ext_1**2*f_gamma_1)

# b_l cannot be negative
b_ltrue = max(b_ltrue,0)

# Convergence criterium
error = abs(b_ltrue - b_lstart)
b_lstart = b_lstart*(1-relax)+b_ltrue*relax
b_l = b_ltrue

# Centrifugal advection, volumetric flow rate disc 1 (iterated)
Q_r_1 = Phi**2*np.pi*omegarad*r_ext_1**2*f_gamma_1*b_l

# Radial volumetric flow rate at disc 2
Q_r_2 = Q_d + Q_a_m + Q_r_1 - Q_a_nose - Q_c

# Concentration at the bank
c_c = (rho_b - rho_w)/(rho_q - rho_w)

# Concentration in the cutter (disc 1 specifically)
c_vs = c_c*Q_c/(Q_a_m + Q_r_1 + Q_d) # Average in disc 1
c_r = c_vs # Centrifugal Advection

# Determine rapid redeposition
if Q_d == 0:
    c_d_max = 0
    c_d = 0
elif Q_d > 0:
    c_d_max = min((c_c*Q_c - c_vs*Q_r_1)/Q_d,c_c) # When Q_a_m = 0
    c_d = f_c_d*c_vs+(c_d_max-c_vs)* v_ratio_hat**2
elif Q_d < 0:
    tkMessageBox.showerror('Q_d turns negative', 'Q_d < 0')

# Determine concentrations
c_m = (c_c*Q_c - c_r*Q_r_1 - c_d*Q_d)/Q_a_m; # Suction flow
c_c = c_c

# Compute Spillage
SpillageR = c_r*Q_r_1/(c_c*Q_c)
SpillageD = c_d*Q_d/(c_c*Q_c)
Spill_rate = SpillageR+SpillageD
Prod_rate = 1-Spill_rate
theta_hat = omegarad*(r_ring)**3/Q_a_m

# Collect and return
collect = np.array([Spill_rate,Prod_rate,theta_hat,Q_c,Q_a_m,Q_r_1, \
                   Q_r_2,b_l,b_2,c_r,c_m,c_d_max,c_d,f_gamma_1, \
                   f_gamma_2,SpillageR,SpillageD,Q_d,Q_a_nose, \
                   A_cut,c_c])

# Debug Mode
# import pdb
# pdb.set_trace()

return collect

```

## K Model analysis tool (Python)

### Control\_panel.py

```
# -*- coding: utf-8 -*-
"""
"Analyzing CSD Spillage Models"
@author: jwerkhoven
"""

%% Establish framework
from __future__ import division # Required since 2.7 divides integers to floor
# raw_input("Press Enter to continue...")

from IPython import get_ipython
get_ipython().magic('reset -sf')

%% Start-up and importing
import datetime
import os
unused_variable = os.system("cls") # on windows
import pandas as pd
import numpy as np
import matplotlib.pyplot as plt
plt.close('all')

%% Speed considerations
class speed:
    relax      = 1E-2
    threshold  = 1E-4

%% Specific variables
# These variables should be taken from a file or project
class geometry:
    D_ring     = 3.11
    D_nose     = 2.12
    b_cutter   = 2.5
    D_pipe     = 0.95
    xi_deg     = 45
    version    = 3 # choose 1 for simple, 2 intermediary, 3 for advanced

%% Define cutting variables
class nvrnmnt:
    h_bank     = 1 # 1 for A_cut =1.4
    l_step     = 1.4 # 1 for A_cut=1.4
    v_s        = 0.2
    c_c        = 0.4
    lambda_deg = 45
    Q_a_nose   = 0 # factor to determine relative size of Q_a_nose

%% Calibration Data

# NEW VERSION
xlsxnumpy = pd.read_excel("SpillageDataMiltenburg.xlsx")
Cal_Data = np.array(xlsxnumpy)

#How to select data for calibration
# Data = Data[Data[:,8] == 1] # Find all rows for the long cutter
# Data = Data[Data[:,8] == 0] # Find all rows for the short cutter
# Data = Data[Data[:,9] == 1] # Find all rows for under-cutting
# Data = Data[Data[:,9] == 0] # Find all rows for over-cutting
# Data = Data[Data[:,10] == 30] # Find all rows for non-rotated mouth
# Data = Data[Data[:,10] == 30] # Find all rows for forward rotated mouth
# Data = Data[Data[:,10] == -30] # Find all rows for backward rotated mouth
# Data = Data[Data[:,14] == 1] # Find all rows for sand
# Data = Data[Data[:,14] == 0] # Find all rows for rock
# Data = Data[Data[:,15] == 1] # take simple
# Data = Data[Data[:,15] == 0] # take sensitivity data

# OLD VERSION
```

```

class clbrtn:
    theta_hat = np.array([ 7, 6.5, 6, 5.5, 5, 4.5, 4, 3.5, 3, 2.5, \
                          2, 1.5, 1, 0.5, 0], dtype=float)
    prod_rate = np.array([30, 35, 40, 45, 51, 58, 64, 73, 81, 97, \
                          99, 100, 100, 100, 100], dtype=float)
    spill_rate = 100-prod_rate
    name = 'Miltenburg (1983)'
    pythonexample = 1

###      Model Name   Phi    under=1 long=1  suc_m  gmtry  simple?  Sand=#1,
models = [['SRCSM',   0.58,  1,    1,    0,    1,    1,    1],
          ['SRCSM',   0.92,  1,    1,    0,    1,    1,    0],
          ['WCSM',   0.58,  1,    1,    0,    1,    1,    1],
          ['WCSM',   0.92,  1,    1,    0,    1,    1,    0]]

f_d      = 0.012 #0.012
f_c_d    = 20    #20
f_d_type = -1 # udercut =-1, overcut = 1

for mm in range(len(models)):
    exec("import %s" % (str(models[mm][0])))

### Options
rotate      = 5          # Which sensitivity analysis to perform? See list below
model_index = np.array([0,1]) # Which models to be evaluated?
sens_rotate = 1          # Which model on display in the graphs? 1 is middle
D_rotate    = 3.11      # Rotate the diameter for which to display Q_m

### Independent variables
class vrbls:
    v_m_index = np.array([2.25, 2.375, 2.5, 2.626, 2.75, 3, 3.25, 3.25, \
                          3.5, 3.75, 4, 4.5, 5, 5.5, 6, 6.5, 7, 7.5, 8, 8.5])
    omega_rpm = 30
    omega_rad = omega_rpm*2*np.pi/60 # = (pi) [rad/s]
    Q_m_index = np.array([11, 8, 7, 6, 5, 4, 3, 2])
    D_ring_index = np.ones(shape=[1,8])*D_rotate # indexii for default conversion to Q_m
    theta_hat_index = omega_rad*(D_ring_index/2)**3/Q_m_index
    version = 2 # choose 1 for WODCONXXII paper, 2 for final version

### Define variables to rotate for sensitivity analysis
mutation = 0.01
s_min    = 1-mutation
s_plus   = 1+mutation

class snstvt:
    s0 = np.array([s_min*(geometry.xi_deg-1), geometry.xi_deg-1, \
                  s_plus*(geometry.xi_deg-1)]) # xi_deg
    n0 = 'geometry.xi_deg'
    s1 = np.array([s_min*nvrnmnt.v_s, nvrnmnt.v_s, s_plus*nvrnmnt.v_s])
    n1 = 'nvrnmnt.v_s'
    s2 = np.array([s_min*nvrnmnt.c_c, nvrnmnt.c_c, s_plus*nvrnmnt.c_c])
    n2 = 'nvrnmnt.c_c'
    s3 = np.array([s_min*nvrnmnt.h_bank, nvrnmnt.h_bank, s_plus*nvrnmnt.h_bank])
    n3 = 'nvrnmnt.h_bank'
    s4 = np.array([s_min*nvrnmnt.l_step, nvrnmnt.l_step, s_plus*nvrnmnt.l_step])
    n4 = 'nvrnmnt.l_step'
    s5 = np.array([s_min*(nvrnmnt.lambda_deg-1), nvrnmnt.lambda_deg-1, \
                  s_plus*(nvrnmnt.lambda_deg-1)]) # lambda_deg
    n5 = 'nvrnmnt.lambda_deg'
    s6 = np.array([s_min*geometry.D_ring, geometry.D_ring, s_plus*geometry.D_ring])
    n6 = 'geometry.D_ring'
    s7 = np.array([s_min*geometry.D_nose, geometry.D_nose, s_plus*geometry.D_nose])
    n7 = 'geometry.D_nose'
    s8 =
np.array([s_min*geometry.b_cutter, geometry.b_cutter, s_plus*geometry.b_cutter])
    n8 = 'geometry.b_cutter'
    s9 = np.array([s_min*geometry.D_pipe, geometry.D_pipe, s_plus*geometry.D_pipe])
    n9 = 'geometry.D_pipe'
    s10 = np.array([s_min*vrbls.omega_rad, vrbls.omega_rad, s_plus*vrbls.omega_rad])
    n10 = 'vrbls.omega_rad'
    s11 = np.array([1,1,1]) #placeholder

```

```

n11      = 'vrbls.f_d_type'
s12      = np.array([s_min*nvrnmnt.Q_a_nose,nvrnmnt.Q_a_nose,s_plus*nvrnmnt.Q_a_nose])
n12      = 'nvrnmnt.Q_a_nose'

#

### Loop through cutting variables

n_v_m    = len(vrbls.v_m_index)          # should be universal, number of
                                         # variable changes to loop through

n_models = len(model_index)
n_sens   = len(eval('snstvt.s'+str(rotate)))
var_number = 21                          # how many variables expected to attract
                                         # from function file

# Collect matrix with model results
Data_collect = np.zeros(shape=[n_v_m, var_number, n_sens, n_models]) # open collection matrix
for mm in range(n_models):

    #What models do you want to run?
    model_rotate= model_index[mm] # select the mm'th model from model_index
    vrbls.Phi    = models[model_rotate][1] # for now, find Phi number
    vrbls.f_d    = f_d
    vrbls.f_c_d  = f_c_d
    vrbls.f_d_type = f_d_type
    vrbls.particle=models[model_rotate][7] #

    # Exception for f_d_type
    snstvt.s11 = np.array([1,-1,-1])
    snstvt.n11 = 'vrbls.f_d_type'

    labels0    = []
    sens_collect= np.zeros(shape=[n_v_m, var_number, 0])
    for kk in range(n_sens):

        if rotate == 0:
            geometry.xi_deg = snstvt.s0[kk]
        elif rotate == 1:
            nvrnmnt.v_s = snstvt.s1[kk]
        elif rotate == 2:
            nvrnmnt.c_c = snstvt.s2[kk]
        elif rotate == 3:
            nvrnmnt.h_bank = snstvt.s3[kk]
        elif rotate == 4:
            nvrnmnt.l_step = snstvt.s4[kk]
        elif rotate == 5:
            nvrnmnt.lambda_deg = snstvt.s5[kk]
        elif rotate == 6:
            geometry.D_ring = snstvt.s6[kk]
        elif rotate == 7:
            geometry.D_nose = snstvt.s7[kk]
        elif rotate == 8:
            geometry.b_cutter = snstvt.s8[kk]
        elif rotate == 9:
            geometry.D_pipe = snstvt.s9[kk]
        elif rotate == 10:
            vrbls.omega_rad = snstvt.s10[kk]
        elif rotate == 11:
            vrbls.f_d_type = snstvt.s11[kk]
        elif rotate == 12:
            nvrnmnt.Q_a_nose = snstvt.s12[kk]

        sens_analysis = eval('snstvt.n'+str(rotate))
        print('Variable rotation = '+sens_analysis+'['+str(kk)+']')

        var_collect = np.zeros(shape=[0, var_number])
        for ii in range(n_v_m):
            collect = eval(models[mm][0]+' .M_'+models[mm][0]+' \
                '(speed,vrbls,geometry,nvrnmnt,ii)')
            # print(Model_collect)
            var_collect=np.vstack((var_collect,collect))

```

```

sens_collect = np.dstack((sens_collect,var_collect))
print('Variable Number = '+str(kk)+'/'+str(n_sens-1))

Data_collect[:, :, :, mm] = sens_collect

### Plotting Data

x0_start      = 0.5
x0_end        = 7.5
y0_start      = 0
y0_end        = 100
y5_start      = -25
y5_end        = 25

#use different shapes for graphs
markers = ['o', 's', '^']

# Workaround operations
theta_hat_index1 = np.insert(vrbls.theta_hat_index,0,x0_start)
theta_hat_index1 = np.append(theta_hat_index1,x0_end)
Q_m_index1 = vrbls.Q_m_index.tolist()
Q_m_index1.append('')
Q_m_index1.insert(0,'')

datetime_object = datetime.datetime.now()

### Graph mark-up
label_size     = 16
title_size     = 12

from matplotlib import rcParams
rcParams['mathtext.fontset'] = 'stix'
rcParams['font.family'] = 'STIXGeneral'

# Collect values for specific location of theta
for mm in range(n_models):

    r_plus= (Data_collect[14,15,2,mm]-Data_collect[14,15,1,mm])\
Data_collect[14,15,1,mm]*100
    d_plus= (Data_collect[14,16,2,mm]-Data_collect[14,16,1,mm])\
Data_collect[14,16,1,mm]*100
    t_plus= (Data_collect[14,0,2,mm] -Data_collect[14,0,1,mm])\
Data_collect[14,0,1,mm]*100
    r_min = (Data_collect[14,15,0,mm]-Data_collect[14,15,1,mm])\
/Data_collect[14,15,1,mm]*100
    d_min = (Data_collect[14,16,0,mm]-Data_collect[14,16,1,mm])\
Data_collect[14,16,1,mm]*100
    t_min = (Data_collect[14,0,0,mm] -Data_collect[14,0,1,mm])\
Data_collect[14,0,1,mm]*100

    Data_collect[14,2,2,mm]
    if mm == 0:
        d_plus = 0
        d_min = 0

    print(t_min,t_plus)

### PLOT data if condition is met

markers_colorst = ['darkcyan','c','cyan']
markers_colorsc = ['k','k','k']
markers_colorsr = ['darkred','r','salmon']
markers_colorsd = ['darkgreen','g','lightgreen']
markers_colorsm = ['b','b','b']

plotting = 1
if plotting == 1:

    ### PLOT 1

```

```

for mm in range(n_models):

    Data = Cal_Data
    Data = Data[Data[:,9] == models[mm][2]] # Find all rows for under-cutting
    Data = Data[Data[:,8] == models[mm][3]] # Find all rows for the long cutter
    Data = Data[Data[:,10] == models[mm][4]] # Find all rows for non-rotated mouth
    Data = Data[Data[:,15] == models[mm][6]] # take simple
    Data = Data[Data[:,14] == models[mm][7]] # Find all rows for sand (1) or rock (0)
    Data = Data[np.argsort(Data[:,13])]
    theta_hat = Data[:,13]
    spill_rate= Data[:,3]

    theta_hat = map(float,theta_hat)
    theta_hat = np.asarray(theta_hat)

    spill_rate = map(float,spill_rate)
    spill_rate= np.asarray(spill_rate)

    $$$ Create overview figure
    fig1, axarr = plt.subplots(1,2,figsize=(14,6))

    if mm % 2 == 0: # sand
        data_label = '$d_{50} = 180E^{-3} [mm]$ (Miltenburg, 1983)'
        d50 = '$d_{50} = 180E^{-3} [mm]$\''
    elif mm % 2 == 1:
        data_label = '$d_{50} = 80 [mm]$ (Den Burger, 2003)'
        d50 = '$d_{50} = 80 [mm]$\''
    axarr[0].plot(theta_hat,spill_rate,'kx', label = data_label)

    legend_title = d50+' , $\Phi$='+str(models[mm][1])
    title_add = ('$'+eval('snstvt.n'+str(rotate)).split('.')[1].split('_')[0]+ \
        '_'+eval('snstvt.n'+str(rotate)).split('.')[1].split('_')[-1]+ \
        ')'+str(eval('snstvt.s'+str(rotate))[kk])+'$')

    for kk in range(n_sens):

        if kk == sens_rotate:

            var = format(eval('snstvt.s'+str(rotate))[kk], '.23')
            var_value = str(var)
            var_name = '$'+(eval('snstvt.n'+str(rotate)).split('.')[1].split('_')[0]+ \
                '_'+eval('snstvt.n'+str(rotate)).split('.')[1].split('_')[-1]+ \
                ')'+'$')
            total_spillage_label = var_name+'='+var_value+ \
                ', Total spillage'
            centrifugal_advection_label = var_name+'='+var_value+ \
                ', Centrifugal advection'
            rapid_redeposition_label = var_name+'='+var_value+ \
                ', Rapid redeposition'

            x_given = Data_collect[:,2,2,mm]
            y_given = Data_collect[:,2,0,mm]
            x_find = theta_hat
            y_find = np.interp(x_find,x_given,y_given)
            delta_y_find = 100*y_find-spill_rate

            # Spillage Plot
            axarr[0].set_xlabel(r'$\theta = \frac{\omega R_{ring}^3}{Q_m}$', \
                fontsize=label_size+2)
            axarr[0].set_ylabel(r'Spillage rate [%]', fontsize=label_size)
            axarr[0].plot(Data_collect[:,2,2,mm],Data_collect[:,0,2,mm]*100, \
                color=markers_colorst[kk], \
                markerfacecolor=markers_colorst[kk],linestyle='-', \
                marker=markers[kk], label='Total spillage')
            axarr[0].plot(Data_collect[:,2,2,mm],Data_collect[:,15,2,mm]*100, \
                color=markers_colorsr[kk], \
                markerfacecolor=markers_colorsr[kk], linestyle='--', \
                marker=markers[kk], label= 'Centrifugal Advection')
            axarr[0].plot(Data_collect[:,2,2,mm],Data_collect[:,16,2,mm]*100, \
                color=markers_colorsd[kk], \

```

```

        markerfacecolor=markers_colorsd[kk], linestyle='-.', \
        marker=markers[kk], label='Rapid redeposition')
axarr[0].set_xlim([x0_start, x0_end])
axarr[0].set_ylim([y0_start, y0_end])
axarr[0].grid(which='major',axis='both', linestyle=':', linewidth=0.5)

# Add second horizontal axis
axadd = axarr[0].twinx()
axadd.set_xlabel(r'$Q_{m}$ $[m^3/s]$, $D_{ring}$='+str(D_rotate)+' \
[m]', fontsize=label_size) # de facto title
axadd.set_xticks(theta_hat_index1.tolist(), minor=False) # create second axis
axadd.set_xlim([x0_start, x0_end])
axadd.set_xticklabels(Q_m_index1) # set the labels to display at those ticks
axadd.grid(which='major',axis='x', color='k', linestyle='--', \
linewidth=0.5)

# Delta vs theta_hat
axarr[1].plot(x_find,delta_y_find, color=markers_colorst[kk], \
markerfacecolor=markers_colorst[kk], \
linestyle='-', marker=markers[kk], label='Total spillage')
axarr[1].set_xlabel(r'$\hat{\theta} = \frac{\omega r_{ring}^3}{Q_m}$', \
fontsize=label_size+2)
axarr[1].set_ylabel(r'Spillage rate error [pp]', fontsize=label_size)
axarr[1].set_xlim([x0_start, x0_end])
axarr[1].set_ylim([y5_start, y5_end])
axarr[1].grid(which='major',axis='both', linestyle=':', linewidth=0.5)
# axarr[1].legend(labels5, title=legend_title)

# Add second horizontal axis
axadd = axarr[1].twinx()
axadd.set_xlabel(r'$Q_{m}$ $[m^3/s]$, $D_{ring}$='+str(D_rotate)+' [m]', \
fontsize=label_size)
axadd.set_xticks(theta_hat_index1.tolist(), minor=False) # create second axis
axadd.set_xticklabels(Q_m_index1) # set the labels to display at those ticks
axadd.set_xlim([x0_start, x0_end])
axadd.set_xticklabels(Q_m_index1) # set the labels to display at those ticks
axadd.grid(which='major',axis='x', color='k', linestyle='--', linewidth=0.5)

axarr[0].legend(loc='upper center', ncol=2, title=legend_title)
axarr[1].legend(loc='upper center', ncol=2, title=legend_title)

axarr[1].axhline(y=-5, color='r', linestyle='-.')
axarr[1].axhline(y=5, color='r', linestyle='-.')
axarr[1].axhline(y=-10, color='k', linestyle='--')
axarr[1].axhline(y=10, color='k', linestyle='--')

axarr[0].axvline(x=1.7, color='tab:purple', linestyle='-.')
axarr[0].axvline(x=3.6, color='tab:purple', linestyle='-.')
axarr[1].axvline(x=1.7, color='tab:purple', linestyle='-.')
axarr[1].axvline(x=3.6, color='tab:purple', linestyle='-.')

# Save plot
timestamp = str(datetime_object)
if mm==0:
    p = 'Sand'
elif mm == 1:
    p = 'Rock'
filename='PlotTotals/'+p+'.'+timestamp+'fig1.png'
filename=filename.replace(':', '.')

fig1.savefig(filename,dpi=200)

### PLOT 2
for mm in range(n_models):

    if mm % 2 == 0: # sand
        data_label = '$d_{50} = 180E^{-3}$ [mm]$ (Miltenburg, 1983)'
        d50 = '$d_{50} = 180E^{-3}$ [mm]$'
    elif mm % 2 == 1:
        data_label = '$d_{50} = 80$ [mm]$ (Den Burger, 2003)'
        d50 = '$d_{50} = 80$ [mm]$'

```

```

$$$ Create overview figure
fig2, axarr = plt.subplots(1,2,figsize=(14,6))

# plt.tight_layout()
legend_title = d50+' $^{\Phi}$'+str(models[mm][1])
title_add = ('$'+eval('snstvt.n'+str(rotate)).split('.')[1].split('_')[0]+ \
    '{'+eval('snstvt.n'+str(rotate)).split('.')[1].split('_')[-1]+ \
    }'+str(eval('snstvt.s'+str(rotate))[kk])+'$')

model_name = models[mm][0]
phi_name = '$^{\Phi}$'+str(models[mm][1])

for kk in range(n_sens):

    var = format(eval('snstvt.s'+str(rotate))[kk], '.23')
    var_value = str(var)
    var_name = '$'+(eval('snstvt.n'+str(rotate)).split('.')[1].split('_')[0]+ \
        '{'+eval('snstvt.n'+str(rotate)).split('.')[1].split('_')[-1]+ \
        }'+str(eval('snstvt.s'+str(rotate))[kk])+'$')
    size = str(mutation*100)

    # Volumetric Flow Rates
    if kk == sens_rotate:
        axarr[0].stackplot(Data_collect[:,2,kk,mm], +Data_collect[:,6,kk,mm], \
            +Data_collect[:,3,kk,mm], \
            +Data_collect[:,18,kk,mm], colors=['m','k','y'])
        axarr[0].stackplot(Data_collect[:,2,kk,mm], -Data_collect[:,4,kk,mm], \
            -Data_collect[:,5,kk,mm], \
            -Data_collect[:,17,kk,mm], colors=['b','r','g'])
        axarr[0].set_xlabel(r'$^{\theta} = \frac{\omega r_{ring}^3}{Q_m}$', \
            fontsize=label_size+2)
        axarr[0].set_ylabel(r'Volumetric Flow Rates [m^3/s]', \
            fontsize=label_size) # de facto title
        axarr[0].set_xlim([x0_start, x0_end])
        axarr[0].set_ylim([-8, 8])
        axarr[0].grid(which='major',axis='both', linestyle=':', linewidth=0.5)

        # Add second horizontal axis
        axadd = axarr[0].twinx()
        axadd.set_xlabel(r'$Q_m$ [m^3/s], $D_{ring}$'+str(D_rotate)+' [m]', \
            fontsize=label_size) # de facto title
        axadd.set_xticks(theta_hat_index1.tolist(), minor=False) # create second axis
        axadd.set_xticklabels(Q_m_index1) # set the labels to display at those ticks
        axadd.set_xlim([x0_start, x0_end])
        axadd.set_xticklabels(Q_m_index1) # set the labels to display at those ticks
        axadd.grid(which='major',axis='x', color='k', linestyle='--', linewidth=0.5)

        # Ceoncentrations
        axarr[1].plot(Data_collect[:,2,kk,mm],Data_collect[:,20,kk,mm], \
            color=markers_colorsc[kk], \
            markerfacecolor=markers_colorsc[kk], linestyle='-', \
            marker=markers[kk], label='$c_{c}$')
        axarr[1].plot(Data_collect[:,2,kk,mm],Data_collect[:,10,kk,mm], \
            color=markers_colorsm[kk], \
            markerfacecolor=markers_colorsm[kk], linestyle=':', \
            marker=markers[kk], label='$c_{m}$')
        axarr[1].plot(Data_collect[:,2,kk,mm],Data_collect[:,9,kk,mm], \
            color=markers_colorsr[kk], \
            markerfacecolor=markers_colorsr[kk], linestyle='--', \
            marker=markers[kk], label='$Q_{r_1}$')
        axarr[1].plot(Data_collect[:,2,kk,mm],Data_collect[:,12,kk,mm], \
            color=markers_colorsd[kk], \
            markerfacecolor=markers_colorsd[kk], linestyle='-.', \
            marker=markers[kk], label='$Q_{d}$')
        axarr[1].set_xlabel(r'$^{\theta} = \frac{\omega r_{ring}^3}{Q_m}$', \
            fontsize=label_size+2)
        axarr[1].set_ylabel(r'Concentrations [-]', fontsize=label_size) # de facto
title
        axarr[1].set_xlim([x0_start, x0_end])
        axarr[1].set_ylim([-0.1, 0.65])

```

```

axarr[1].grid(which='major',axis='both', linestyle=':', linewidth=0.5)

# Add second horizontal axis
axadd = axarr[1].twinx()
axadd.set_xlabel(r'$Q_{m}$ $[m^3/s]$, $D_{ring}$'+str(D_rotate)+\
' [m]', fontsize=label_size) # de facto title
axadd.set_xticks(theta_hat_index1.tolist(), minor=False) # create second axis
axadd.set_xticklabels(Q_m_index1) # set the labels to display at those ticks
axadd.set_xlim([x0_start, x0_end])
axadd.set_xticklabels(Q_m_index1) # set the labels to display at those ticks
axadd.grid(which='major',axis='x', color='k', linestyle='--', \
linewidth=0.5)

lg = axarr[0].legend(['$Q_{r_{2}}$','$Q_{c}$','$Q_{a_{nose}}$','$Q_{a_{m}}$','$Q_{r_{1}}$','$Q_{d}$'],\
loc='upper center',ncol=2, title=legend_title)
lg.get_title().set_fontsize(title_size)
lg = axarr[1].legend(ncol=2, title=legend_title)
lg.get_title().set_fontsize(title_size)

axarr[0].axvline(x=1.7, color='tab:purple', linestyle='-.')
axarr[0].axvline(x=3.6, color='tab:purple', linestyle='-.')
axarr[1].axvline(x=1.7, color='tab:purple', linestyle='-.')
axarr[1].axvline(x=3.6, color='tab:purple', linestyle='-.')

# Save plot
timestamp = str(datetime_object)
if mm==0:
    p = 'Sand'
elif mm == 1:
    p = 'Rock'
filename='PlotTotals/'+p+'.'+timestamp+'fig2.png'
filename=filename.replace(':', '.')

fig2.savefig(filename,dpi=200)

### PLOT 3
for mm in range(n_models):

    if mm % 2 == 0: # sand
        data_label = '$d_{50} = 180E^{-3}$ [mm]$ (Miltenburg, 1983)'
        d50 = '$d_{50} = 180E^{-3}$ [mm]$\
    elif mm % 2 == 1:
        data_label = '$d_{50} = 80$ [mm]$ (Den Burger, 2003)'
        d50 = '$d_{50} = 80$ [mm]$\

### Create overview figure
fig3, axarr = plt.subplots(1,2,figsize=(14,6))

for kk in range(n_sens):

    model_name = models[mm][0]
    phi_name = '$\^{\Phi}$'+str(models[mm][1])

    if kk == sens_rotate:

        var = format(eval('snstvt.s'+str(rotate))[kk], '.23')
        var_value = str(var)
        var_name = '$'+(eval('snstvt.n'+str(rotate)).split('.')[1].split('_')[0]+ \
'_{'+eval('snstvt.n'+str(rotate)).split('.')[1].split('_')[-1]+ \
'}')+ '$'
        size = str(mutation*100)

        # Concentrations
        axarr[0].plot(Data_collect[:,2,1,mm],\
            (Data_collect[:,15,0,mm]-Data_collect[:,15,1,mm])/\
            Data_collect[:,15,1,mm]*100, \
            color=markers_colorsr[kk-1], markerfacecolor=markers_colorsr[kk-1], \
            linestyle='-.', \
            marker=markers[kk-1], label=var_name+' -'+size+'[%]')

```

```

axarr[0].plot(Data_collect[:,2,1,mm],\
              (Data_collect[:,15,2,mm]-Data_collect[:,15,1,mm])/\
              Data_collect[:,15,1,mm]*100, \
              color=markers_colorsr[kk+1], markerfacecolor=markers_colorsr[kk+1], \
              linestyle='-', \
              marker=markers[kk+1], label=var_name+' '+size+'[%]')
axarr[0].set_xlabel(r'$\hat{\theta} = \frac{\omega r_{ring}^3}{Q_m}$', \
                   fontsize=label_size+2)
axarr[0].set_ylabel(r'Change in centrifugal advection-induced spillage rate
[%]', \
                   fontsize=label_size)
axarr[0].set_xlim([x0_start, x0_end])
axarr[0].grid(which='major',axis='both', linestyle=':', linewidth=0.5)

# Add second horizontal axis
axadd = axarr[0].twinx()
axadd.set_xlabel(r'$Q_m$ $[m^3/s]$, $D_{ring}$='+str(D_rotate)+' [m]', \
                fontsize=label_size)
axadd.set_xticks(theta_hat_index1.tolist(), minor=False) # create second axis
axadd.set_xticklabels(Q_m_index1) # set the labels to display at those ticks
axadd.set_xlim([x0_start, x0_end])
axadd.set_xticklabels(Q_m_index1) # set the labels to display at those ticks
axadd.grid(which='major',axis='x', color='k', linestyle='--', linewidth=0.5)

axarr[1].plot(Data_collect[:,2,1,mm],\
              (Data_collect[:,16,0,mm]-Data_collect[:,16,1,mm])/\
              Data_collect[:,16,1,mm]*100, \
              color=markers_colorsd[kk-1], markerfacecolor=markers_colorsd[kk-1], \
              linestyle='-', \
              marker=markers[kk-1], label=var_name+' '+size+'[%]')
axarr[1].plot(Data_collect[:,2,1,mm],\
              (Data_collect[:,16,2,mm]-Data_collect[:,16,1,mm])/\
              Data_collect[:,16,1,mm]*100, \
              color=markers_colorsd[kk+1], markerfacecolor=markers_colorsd[kk+1], \
              linestyle='-', \
              marker=markers[kk+1], label=var_name+' '+size+'[%]')
axarr[1].set_xlabel(r'$\hat{\theta} = \frac{\omega r_{ring}^3}{Q_m}$', \
                   fontsize=label_size+2)
axarr[1].set_ylabel(r'Change in rapid redeposition-induced spillage rate [%]', \
                   fontsize=label_size)
axarr[1].set_xlim([x0_start, x0_end])
axarr[1].grid(which='major',axis='both', linestyle=':', linewidth=0.5)

# Add second horizontal axis
axadd = axarr[1].twinx()
axadd.set_xlabel(r'$Q_m$ $[m^3/s]$, $D_{ring}$='+str(D_rotate)+' [m]', \
                fontsize=label_size)
axadd.set_xticks(theta_hat_index1.tolist(), minor=False) # create second axis
axadd.set_xticklabels(Q_m_index1) # set the labels to display at those ticks
axadd.set_xlim([x0_start, x0_end])
axadd.set_xticklabels(Q_m_index1) # set the labels to display at those ticks
axadd.grid(which='major',axis='x', color='k', linestyle='--', linewidth=0.5)

lg = axarr[0].legend(ncol=2, title=d50+' '+phi_name+'\n'+Sensitivity for '\
+var_name, fontsize=title_size)
lg.get_title().set_fontsize(title_size)
lg = axarr[1].legend(ncol=2, title=d50+' '+phi_name+'\n'+Sensitivity for '\
+var_name, fontsize=title_size)
lg.get_title().set_fontsize(title_size)

axarr[0].axvline(x=1.7, color='tab:purple', linestyle='-.')
axarr[0].axvline(x=3.6, color='tab:purple', linestyle='-.')
axarr[1].axvline(x=1.7, color='tab:purple', linestyle='-.')
axarr[1].axvline(x=3.6, color='tab:purple', linestyle='-.')

# Save plot
timestamp = str(datetime_object)
if mm==0:
    p = 'Sand'

```

```

elif mm == 1:
    p = 'Rock'
    filename='PlotTotals/'+p+'.'+timestamp+'fig3.png'
    figname=filename.replace(':', '.')

    fig3.savefig(figname,dpi=200)

$$$ PLOT 4 # Variety of data
if mm == 0:

    Data = Cal_Data
    Data = Data[Data[:,9] == models[mm][2]] # Find all rows for under-cutting
    Data = Data[Data[:,8] == models[mm][3]] # Find all rows for the long cutter
    Data = Data[Data[:,10] == models[mm][4]] # Find all rows for non-rotated mouth
    Data = Data[Data[:,15] == 0] # take scattered data
    Data = Data[Data[:,14] == models[mm][7]] # Find all rows for sand (1) or rock (0)
    Data = Data[np.argsort(Data[:,13])]
    theta_hat = Data[:,13]
    spill_rate= Data[:,3]

    theta_hat = map(float,theta_hat)
    theta_hat = np.asarray(theta_hat)
    spill_rate = map(float,spill_rate)
    spill_rate= np.asarray(spill_rate)

    $$$ Create overview figure
    fig4, axarr = plt.subplots(1,2,figsize=(14,6))

    legend_title = d50+' $^{\Phi}$'+str(models[mm][1])
    title_add = ('$'+eval('snstvt.n'+str(rotate)).split('.')[1].split('_')[0]+ \
        '_'+eval('snstvt.n'+str(rotate)).split('.')[1].split('_')[-1]+ \
        '')+str(eval('snstvt.s'+str(rotate))[kk])+'$')

    if mm % 2 == 0: # sand
        data_label = '$d_{50} = 180E^{-3}$ [mm]$ (Miltenburg, 1983)'
        d50 = '$d_{50} = 180E^{-3}$ [mm]$'
    elif mm % 2 == 1:
        data_label = '$d_{50} = 80$ [mm]$ (Den Burger, 2003)'
        d50 = '$d_{50} = 80$ [mm]$'

    axarr[0].plot(theta_hat,spill_rate,'kx', label = data_label)
    z = np.polyfit(theta_hat, spill_rate, 2)
    axarr[0].plot(z)

    plt.show()

    for kk in range(n_sens):

        var = format(eval('snstvt.s'+str(rotate))[kk], '.23')
        var_value = str(var)
        var_name = '$'+(eval('snstvt.n'+str(rotate)).split('.')[1].split('_')[0]+ \
            '_'+eval('snstvt.n'+str(rotate)).split('.')[1].split('_')[-1]+ \
            '))+ '$'
        total_spillage_label = var_name+'='+var_value+', Total spillage'
        centrifugal_advection_label = var_name+'='+var_value+', Centrifugal advection'
        rapid_redeposition_label = var_name+'='+var_value+', Rapid redeposition'

        if kk == sens_rotate:

            x_given = Data_collect[:,2,2,mm]
            y_given = Data_collect[:,0,2,mm]
            x_find = theta_hat
            y_find = np.interp(x_find,x_given,y_given)
            delta_y_find = 100*y_find-spill_rate

            # Spillage Plot
            axarr[0].set_xlabel(r'$^{\theta} = \frac{\omega R_{ring}^3}{Q_m}$', \
                fontsize=label_size+2)
            axarr[0].set_ylabel(r'Spillage rate [%]', fontsize=label_size) # de facto title
            axarr[0].plot(Data_collect[:,2,2,mm],Data_collect[:,0,2,mm]*100, \
                color=markers_colorst[kk], \

```

```

        markerfacecolor=markers_colorst[kk],linestyle='-', \
        marker=markers[kk], label='Total spillage')
axarr[0].plot(Data_collect[:,2,kk,mm],Data_collect[:,15,kk,mm]*100, \
        color=markers_colorsr[kk], \
        markerfacecolor=markers_colorsr[kk], linestyle='--', \
        marker=markers[kk], label='Centrifugal Advection')
axarr[0].plot(Data_collect[:,2,kk,mm],Data_collect[:,16,kk,mm]*100, \
        color=markers_colorsd[kk], \
        markerfacecolor=markers_colorsd[kk], linestyle='-.', \
        marker=markers[kk], label='Rapid redeposition')
axarr[0].set_xlim([x0_start, x0_end])
axarr[0].set_ylim([y0_start, y0_end])
axarr[0].grid(which='major',axis='both', linestyle=':', linewidth=0.5)

# Add second horizontal axis
axadd = axarr[0].twinx()
axadd.set_xlabel(r'$Q_m$ $[m^3/s]$, $D_{ring}$='+str(D_rotate)+' [m]', \
        fontsize=label_size) # de facto title
axadd.set_xticks(theta_hat_index1.tolist(), minor=False) # create second axis
axadd.set_xlim([x0_start, x0_end])
axadd.set_xticklabels(Q_m_index1) # set the labels to display at those ticks
axadd.grid(which='major',axis='x', color='k', linestyle='--', \
        linewidth=0.5)

# Delta vs theta_hat
axarr[1].plot(x_find,delta_y_find, color=markers_colorst[kk], \
        markerfacecolor=markers_colorst[kk], \
        linestyle='-', marker=markers[kk], label='Total spillage')
axarr[1].set_xlabel(r'$\hat{\theta} = \frac{\omega r_{ring}^3}{Q_m}$', \
        fontsize=label_size+2)
axarr[1].set_ylabel('Spillage rate error [pp]', fontsize=label_size)
axarr[1].set_xlim([x0_start, x0_end])
axarr[1].set_ylim([y5_start, y5_end])
axarr[1].grid(which='major',axis='both', linestyle=':', linewidth=0.5)
# axarr[1].legend(labels5, title=legend_title)

# Add second horizontal axis
axadd = axarr[1].twinx()
axadd.set_xlabel(r'$Q_m$ $[m^3/s]$, $D_{ring}$='+str(D_rotate)+' [m]', \
        fontsize=label_size) # de facto title
axadd.set_xticks(theta_hat_index1.tolist(), minor=False) # create second axis
axadd.set_xticklabels(Q_m_index1) # set the labels to display at those ticks
axadd.set_xlim([x0_start, x0_end])
axadd.set_xticklabels(Q_m_index1) # set the labels to display at those ticks
axadd.grid(which='major',axis='x', color='k', linestyle='--', linewidth=0.5)

axarr[0].legend(loc='upper center', bbox_to_anchor=(0.5, -0.2), ncol=2, \
        title=legend_title, frameon=False)
axarr[1].legend(loc='upper center', bbox_to_anchor=(0.5, -0.2), ncol=2, \
        title=legend_title, frameon=False)

axarr[1].axhline(y=-5, color='r', linestyle='-.')
axarr[1].axhline(y=5, color='r', linestyle='-.')
axarr[1].axhline(y=-10, color='k', linestyle='--')
axarr[1].axhline(y=10, color='k', linestyle='--')

axarr[0].axvline(x=1.7, color='tab:purple', linestyle='-.')
axarr[0].axvline(x=3.6, color='tab:purple', linestyle='-.')
axarr[1].axvline(x=1.7, color='tab:purple', linestyle='-.')
axarr[1].axvline(x=3.6, color='tab:purple', linestyle='-.')

# Save plot
timestamp = str(datetime_object)
if mm==0:
    p = 'Sand'
elif mm == 1:
    p = 'Rock'
filename='PlotTotals/'+p+'.'+timestamp+'fig4.png'
#fig.savefig(filename,dpi=1000)
filename=filename.replace(':','.')

```

```

fig4.savefig(figname,dpi=200)

$$$ PLOT 5, Multiple spillage plots
for mm in range(n_models):

    Data = Cal_Data
    Data = Data[Data[:,9] == models[mm][2]] # Find all rows for under-cutting
    Data = Data[Data[:,8] == models[mm][3]] # Find all rows for the long cutter
    Data = Data[Data[:,10] == models[mm][4]] # Find all rows for non-rotated mouth
    Data = Data[Data[:,15] == models[mm][6]] # take simple
    Data = Data[Data[:,14] == models[mm][7]] # Find all rows for sand (1) or rock (0)
    Data = Data[np.argsort(Data[:,13])]
    theta_hat = Data[:,13]
    spill_rate= Data[:,3]

    theta_hat = map(float,theta_hat)
    theta_hat = np.asarray(theta_hat)
    spill_rate = map(float,spill_rate)
    spill_rate= np.asarray(spill_rate)

    $$$ Create overview figure
    fig5, axarr = plt.subplots(1,2,figsize=(14,6))

    legend_title = d50+'', '$^\Phi$'+str(models[mm][1])
    title_add = ('$'+eval('snstvt.n'+str(rotate)).split('.')[1].split('_')[0]+ \
        '_'+eval('snstvt.n'+str(rotate)).split('.')[1].split('_')[-1]+ \
        '')+str(eval('snstvt.s'+str(rotate))[kk])+'$')

    if mm % 2 == 0: # sand
        data_label = '$d_{50} = 180E^{-3}$ [mm]$(Miltenburg, 1983)'
        d50 = '$d_{50} = 180E^{-3}$ [mm]$\''
    elif mm % 2 == 1:
        data_label = '$d_{50} = 80$ [mm]$(Den Burger, 2003)'
        d50 = '$d_{50} = 80$ [mm]$\''
    axarr[0].plot(theta_hat,spill_rate,'kx', label = data_label)

    for kk in range(n_sens):

        var = format(eval('snstvt.s'+str(rotate))[kk], '.23')
        var = round(float(var), 3)
        var_value = str(var)
        var_name = '$'+(eval('snstvt.n'+str(rotate)).split('.')[1].split('_')[0]+ \
            '_'+eval('snstvt.n'+str(rotate)).split('.')[1].split('_')[-1]+ \
            '))+ '$'
        total_spillage_label = var_name+'='+var_value+', Total spillage'
        centrifugal_advection_label = var_name+'='+var_value+', Centrifugal advection'
        rapid_redeposition_label = var_name+'='+var_value+', Rapid redeposition'

        x_given = Data_collect[:,2,kk,mm]
        y_given = Data_collect[:,0,kk,mm]
        x_find = theta_hat
        y_find = np.interp(x_find,x_given,y_given)
        delta_y_find = 100*y_find-spill_rate

        # Spillage Plot
        axarr[0].set_xlabel(r'$^\theta = \frac{\omega R_{ring}^3}{Q_m}$', \
            fontsize=label_size+2)
        axarr[0].set_ylabel(r'Spillage rates [%]', fontsize=label_size) # de facto title
        axarr[0].plot(Data_collect[:,2,kk,mm],Data_collect[:,0,kk,mm]*100, \
            color=markers_colorst[kk], \
            markerfacecolor=markers_colorst[kk],linestyle='-', marker=markers[kk], \
            label=total_spillage_label)
        axarr[0].plot(Data_collect[:,2,kk,mm],Data_collect[:,15,kk,mm]*100, \
            color=markers_colorsr[kk], \
            markerfacecolor=markers_colorsr[kk], linestyle='--', marker=markers[kk], \
            label=centrifugal_advection_label)
        axarr[0].plot(Data_collect[:,2,kk,mm],Data_collect[:,16,kk,mm]*100, \
            color=markers_colorsd[kk], \
            markerfacecolor=markers_colorsd[kk], linestyle='-.', marker=markers[kk], \
            label=rapid_redeposition_label)

```

```

axarr[0].set_xlim([x0_start, x0_end])
axarr[0].set_ylim([y0_start, y0_end])
axarr[0].grid(which='major',axis='both', linestyle=':', linewidth=0.5)

# Add second horizontal axis
axadd = axarr[0].twinx()
axadd.set_xlabel(r'$Q_{m}$ $[m^3/s]$, $D_{ring}$='+str(D_rotate)+' [m]', \
                fontsize=label_size) # de facto title
axadd.set_xticks(theta_hat_index1.tolist(), minor=False) # create second axis
axadd.set_xlim([x0_start, x0_end])
axadd.set_xticklabels(Q_m_index1) # set the labels to display at those ticks
axadd.grid(which='major',axis='x', color='k', linestyle='--', linewidth=0.5)

# Delta vs theta hat
axarr[1].plot(x_find,delta_y_find, color=markers_colorst[kk], \
             markerfacecolor=markers_colorst[kk], \
             linestyle='-', marker=markers[kk], label=total_spillage_label)
axarr[1].set_xlabel(r'$\theta = \frac{\omega r_{ring}^3}{Q_m}$', \
                  fontsize=label_size+2)
axarr[1].set_ylabel(r'Spillage rate errors [pp]', fontsize=label_size) # de facto
title

axarr[1].set_xlim([x0_start, x0_end])
axarr[1].set_ylim([y5_start, y5_end])
axarr[1].grid(which='major',axis='both', linestyle=':', linewidth=0.5)
# axarr[1].legend(labels5, title=legend_title)

# Add second horizontal axis
axadd = axarr[1].twinx()
axadd.set_xlabel(r'$Q_{m}$ $[m^3/s]$, $D_{ring}$='+str(D_rotate)+' [m]', \
                fontsize=label_size) # de facto title
axadd.set_xticks(theta_hat_index1.tolist(), minor=False) # create second axis
axadd.set_xticklabels(Q_m_index1) # set the labels to display at those ticks
axadd.set_xlim([x0_start, x0_end])
axadd.set_xticklabels(Q_m_index1) # set the labels to display at those ticks
axadd.grid(which='major',axis='x', color='k', linestyle='--', linewidth=0.5)

axarr[0].legend(loc='upper center', bbox_to_anchor=(0.5, -0.2), ncol=2, \
               title=legend_title, frameon=False)
axarr[1].legend(loc='upper center', bbox_to_anchor=(0.5, -0.2), ncol=2, \
               title=legend_title, frameon=False)

axarr[1].axhline(y=-5, color='r', linestyle='-.')
axarr[1].axhline(y=5, color='r', linestyle='-.')
axarr[1].axhline(y=-10, color='k', linestyle='--')
axarr[1].axhline(y=10, color='k', linestyle='--')

axarr[0].axvline(x=1.7, color='tab:purple', linestyle='-.')
axarr[0].axvline(x=3.6, color='tab:purple', linestyle='-.')
axarr[1].axvline(x=1.7, color='tab:purple', linestyle='-.')
axarr[1].axvline(x=3.6, color='tab:purple', linestyle='-.')

timestamp = str(datetime_object)
if mm==0:
    p = 'Sand'
elif mm == 1:
    p = 'Rock'
figname='PlotTotals/'+p+'.'+timestamp+'fig5.png'
figname=figname.replace(':', '.')

fig5.savefig(figname,dpi=200)

```

